Theoretical Insights into Cathode Designing and Working Mechanism in Aluminium Batteries

Ph.D. Thesis

by

PREETI BHAURIYAL

DISCIPLINE OF CHEMISTRY

INDIAN INSTITUTE OF TECHNOLOGY INDORE

DECEMBER 2019

Theoretical Insights into Cathode Designing and Working Mechanism in Aluminium Batteries

A THESIS

Submitted in partial fulfillment of the

requirements for the award of degree

of

DOCTOR OF PHILOSOPHY

by

PREETI BHAURIYAL

DISCIPLINE OF CHEMISTRY

INDIAN INSTITUTE OF TECHNOLOGY INDORE

DECEMBER 2019

INDIAN INSTITUTE OF TECHNOLOGY INDORE

CANDIDATE'S DECLARATION

I hereby certify that the work which is being presented in the thesis entitled **Theoretical Insights into Cathode Designing and Working Mechanism in Aluminium Batteries** in the partial fulfillment of the requirements for the award of the degree of **DOCTOR OF PHILOSOPHY** and submitted in the **DISCIPLINE OF CHEMISTRY, INDIAN INSTITUTE OF TECHNOLOGY INDORE**, is an authentic record of my own work carried out during the time period from JULY 2015 to DECEMBER 2019 under the supervision of **Dr. BISWARUP PATHAK**, Associate Professor, Discipline of Chemistry, IIT Indore.

The matter presented in this thesis has not been submitted by me for the award of any other degree of this or any other institute.

Preeti **13.12.2019**

Signature of the student with date

(PREETI BHAURIYAL)

This is to certify that the above statement made by the candidate is correct to the best of my knowledge.

BPathak **13.12.2019**

Signature of Thesis Supervisor with date

(Dr. BISWARUP PATHAK)

PREETI BHAURIYAL has successfully given her Ph.D. Oral Examination held on **18.05.2020.**

Parimalkar

Signature of Chairperson (OEB)

Date: 18-05-2020

Signature of External Examiner

Date:

डॉ. जी. नरहरि शास्त्री/Dr. G. Narahari Sastry
निदेशक / DIRECTOR
सी एस आई आर-उत्तर पूर्व विज्ञान तथा प्रौद्योगिकी संस्थान
CSIR-NORTH EAST INSTITUTE OF SCIENCE & TECHNOLOGY
जोरहाट-785006, असम, भारत Jorhat- 785006, Assam, India

BPathak

Signature(s) of Thesis Supervisor(s)

Date: 18-05-2020

Preeti

Signature of PSPC Member #1

Date: 18.05.2020

Venkatesh. C

Signature of PSPC Member #2

Date: 18-05-2020

Tushar kanti Mukherjee

Signature of Convener, DPGC

Date: 18-05-2020

BPathak

Signature of Head of Discipline

Date: 18-05-2020

Acknowledgements

It is my immense pleasure to express my sincere respect and most heartfelt gratitude to my supervisor, Dr. Biswarup Pathak for his constant guidance and encouragement throughout my work. I am significantly obligated for his support, motivation and better understanding. His vision and dedication in presenting the projects has a remarkable influence on me.

I am thankful to my PSPC members, Dr. Chelvam Venkatesh and Dr. Preeti A. Bhobe for their guidance and valuable suggestions during my work.

I would like to thank my experimental collaborator, Prof. Dr. Maksym V. Kovalenko and Dr. Kostiantyn Kravchyk for their guidance and scientific discussion during all the collaborative projects.

I wish to express my gratitude to Prof. Pradeep Mathur, Director, IIT Indore for his continuous support in every aspect.

I would like to thank IIT Indore for providing laboratory, computational facilities, and financial support during my work.

I would also like to thank Dr. Satya S. Bulusu, Dr. Apurba K. Das, Dr. Tushar Kanti Mukherjee, Dr. Sampak Samanta, Dr. Shaikh M. Mobin, Dr. Rajneesh Misra, Dr. Tridib Kumar Sarma, Dr. Chelvam Venkatesh, Dr. Anjan Chakraborty, Dr. Amrendra Kumar Singh, Dr. Abhinav Raghuvanshi and Dr. Dipak Kumar Roy for their guidance and help during various activities in the department.

I extend my deep appreciations to my group members Mr. Arup Mahata, Ms. Indrani Choudhuri, Mr. Kuber Singh Rawat, Ms. Priyanka Garg, Mr. Sourabh Kumar, Ms. Gargee Bhattacharya, Mr. Chiranjit Mondal, Mr. Akhil S Nair, Mr. Shyama Charan Mandal, and Mr. Rameshwar Lal Kumawat, Mr. Sandeep Das, Mr. Arunendu Das, Mr. Surya Sekhar Manna, Mr. Amitabha Das, Mr. Samir Kumar Nayak, Mr. Sumit Kumar and Mr. Hariom Saini for their generous help and co-operation to make my work successful.

I would also like to thank Mr. Dhiraj Vijayvargiya, Mr. Yogendra Singh, Mr. Manish Kushwaha, Ms. Vinita Kothari and Mr. Rameshwar Dauhare for their technical support. I would also like to thank Ms. Anjali Bandiwadekar, Mr. Rajesh Kumar, Mr. Lala Ram Ahirwar and other library staffs for their constant help, whenever required.

I am personally very much grateful to my friends, Ms. Dixita, Ms. Disha, Ms. Nirali, who were always there to constantly support me during my Ph.D. period. Here, it is specially to be mentioned that, it has been a wonderful experience to work with many friends at IIT Indore during my PhD who really helped me in many aspects.

I would like to take this opportunity to express my respect, love and gratitude to all the teachers and friends who were part of my life for their kind love and support and teaching me in some and other ways to lead me to the right path.

Finally, I would like to express my deep gratitude towards my family for their support. First of all I am thankful to my lovable parents Mrs. Geeta Bhauriyal, Mr. Rajendra Singh Bhauriyal, and my brothers Mr. Anuj Bhauriyal and Mr. Sagar Dasila for their selfless love and motivation. My forever interested, encouraging and always enthusiastic grandfathers Mr. Trilok Singh Bhauriyal and Mr. Daleep Singh Dasila, who are always excited to know what I am doing. My grandmothers Mrs. Manuli Dasila and Mrs. Khimuli Bhauriyal for showering blessings and all my family members for their love and encouragement in my Ph.D. and in my life in general.

I also place on record, my sense of gratitude to one and all, who directly or indirectly, have played role in this venture.

PREETI BHAURIYAL

Dedicated to

My Parents

and

Grandparents

Abstract

The increasing energy demands of the world is resulting in exploration of renewable and clean alternative fuels capable of replacing the current energy sources efficiently. In this context, rechargeable batteries have been recognized as one of the capable clean energy sources due to their several advantages like concise size, high efficiency, and simple maintenance and are potentially consist of reversible cell reactions. Especially, Aluminium (Al) metal-based batteries with highly abundant Al metal, and higher volumetric capacity (~8040 mAh/cm^3) are emerging as the next alternate provider of energy. The marketing of Al battery technology is also anticipated to be much safer, because of the small expected size, low cost, and more environmental inertness of Al batteries compared to thermal runway and explosion sensitive Li-ion batteries.

However, the field of Al batteries being in its initial phase of development require lots of understanding and efforts to make it a reliable choice. One of the very famous Al based batteries are Al-dual-ion batteries involving active participation of ionic liquid electrolytes during the charge/discharge reactions and overall output results. In Al-dual-ion batteries, which show huge advantages in terms of higher average voltage, fast charge/discharge rates, and efficient cycle stability with constant energy density, the choice of the cathode plays a quite important role in determining the overall battery efficiency. Therefore, choosing a suitable cathode which can deliver higher voltage and efficient storage capacity as well as maintaining the structural stability with a fast charge/discharge rate is the primary aim of Al batteries.

Along with this, the rechargeable aluminium-sulfur (Al-S) battery, which has been proposed very recently (year 2016), stand out as the promising alternative of commercial batteries as they have the benefit of low cost, and eco-friendly sulfur cathode offering a maximum theoretical capacity (1675 mAh/g), which is the highest of all known solid cathode materials.

Overall, Al-S batteries can deliver high energy density of 1300 Wh/Kg with the theoretical voltage of 1.27 V. For the better development of this promising field of Al-S batteries, it is very necessary to understand the complex electrochemical reactions occurring during charge/discharge process, as well as designing new cathode support which can not only serves to facilitate the electrochemical reaction, but also to improve the reversibility of S during charge/discharge.

Therefore, the joint ventures of both experimental and theoretical effort are very necessary to understand the working mechanism of Al-dual-ion batteries as well as Al-S batteries which further help us to develop more efficient cathode systems furnishing higher voltage and storage capacity.

The contents of each chapter included in the thesis are discussed briefly as follows:

1. Introduction

In this chapter, we have briefly discussed the developing field of rechargeable aluminum (Al) batteries giving more emphasis on the working behavior of non-aqueous Al-dual-ion batteries and Al-sulfur batteries. A detailed discussion is presented about the non-aqueous chemistry of ionic-liquid electrolytes in driving the research filed to develop more efficient and cost-effective Al batteries. Along with the exploration of the reaction mechanisms of both Al dual-ion batteries and Al-S batteries, the role of cathode material in improving the electronic as well as electrochemical properties has also been studied. In addition, we have also reviewed the recent advancements, which have been suggested experimentally and theoretically to build potential cathode materials along with discussing the ideas to develop more advanced cathodes by relative comparison with Li batteries.

Our thesis work involves the density functional theory (DFT) calculations to investigate the reaction mechanism and cathode applicability in Al batteries. Therefore, this chapter also includes a brief discussion of DFT and its importance in theoretical exploration of batteries as well as supporting the experimental data. This chapter also covers the computational techniques, which are used to explain the results of the computation.

2. Staging Mechanism of $AlCl_4^-$ into Graphite and Electron-Rich Graphite-like Electrode and Investigation of the Stability vs. Voltage for Aluminium Batteries

This chapter offers a detailed investigation of the staging mechanism of $AlCl_4^-$ anion intercalation to form graphite intercalation compounds (GIC) by carrying out systematic study of the structure, stability, electronic properties, theoretical capacity and average voltage of the $AlCl_4$ anion intercalated graphite electrodes (Figure 1). The geometrical preference of $AlCl_4$ anion inside cathode is observed to be tetrahedral and overall stability of $AlCl_4$ anion intercalated graphite is confirmed with the help of energetic as well as thermal stability calculations. The significant amount of charge transfer from C-atoms of host intercalating layers to the four Cl-atoms of $AlCl_4$ indicates the electrochemical oxidation of graphitic carbons on $AlCl_4$ intercalation, confirming that the intercalation of $AlCl_4$ is a charging process. Four stages (stage-4 to stage-1) are modelled to study the step by step stage formation during $AlCl_4$ anion intercalation and de-intercalation processes. The activation behaviour attributed to an opening process of graphite galleries on anion intercalation for the very first anion intercalation step is observed with the help of energetic studies. The calculated net average voltage and storage capacity values are also observed to be in accordance with the experimental values.

Moreover, a detailed discussion of voltage vs. stability of $AlCl_4$ intercalated systems is carried by examining the applicability of electron rich graphite-like C_3N cathode for Al batteries. By carrying out the similar modelling procedure as of graphite to understand the staging behavior of anion intercalation into graphite, we have evaluated the stability, specific capacity, and voltage profile diagram of $AlCl_4$-intercalated C_3N system. Our results demonstrate that electron-deficient system with adequate stability towards $AlCl_4$ intercalation can be a superior choice to obtain high voltage in Al batteries when compared to graphite cathode. Therefore, the present study is quite helpful in understanding the working mechanism of Al batteries and the development of high-voltage Al battery electrodes with adequate stability.

3. Graphene/hBN Heterostructures as High-Capacity Cathodes with High Voltage for Next-Generation Aluminium Batteries

In this chapter, we have proposed the 2D graphene/hexagonal boron nitride heterostructure (G/hBN) as a suitable cathode material for Al batteries. The heterostructure of graphene (G) and hBN is quite important as it exhibits rich physical properties that include a tunable band gap, ultrahigh electron mobility, and the demonstration of controllable hyperbolic metamaterial characteristics. Also, the thought behind investigating G/hBN heterostructure, is to get high voltage as the hBN layer can induce moderately low binding with $AlCl_4$ because of electron deficient B and electronegative N atoms, and at the same time, the graphene along with maintaining constant conductivity can also help in providing the overall stability to the system. By means of comparative analysis of structural and binding studies, we observe that the binding energy of $AlCl_4$ incorporation into G/hBN is significantly improved compared to pristine graphene and hBN. Moreover, we observe that the G/hBN heterostructure can show a diffusion barrier as small as 0.01 eV for the outer hBN surface diffusion, which is comparatively lower than the experimentally studied graphite electrode. The voltage of 2.14 V and an efficient storage capacity of 183 mA h/g obtained in the G/hBN heterostructure (Figure 2) are larger than that obtained in monolayer graphene which provides high storage capacity (248 mA h/g) but with small voltage (1.99 V) and monolayer hBN imparting a voltage of 2.23 V, while having very less capacity (120 mA h/g). All these results suggest that the G/hBN heterostructure could be an ideal cathode material choice for Al batteries, and other 2D heterostructures should also be examined for Al batteries.

4. A Computational Study of Single-walled Carbon Nanotube Based Ultrafast High Capacity Aluminium Battery

This chapter includes the exploration of 1D single-walled carbon nanotubes (SNNTs) as the potential cathode materials for the high capacity Al dual-ion batteries. Here, the idea is to overcome the activation of partially closed interlayer spaces of bulk cathode for the very first charging step by allowing the trouble-free $AlCl_4$ adsorption into the spacious intra as well as inter-tube space. By means of structural studies, we have concluded that $AlCl_4$ adsorbs in its stable tetrahedral geometry, and an AIMD study showed that the $AlCl_4$ adsorbed SWNT system is stable over a temperature range 300–600 K. Moreover, our results show that the SWNT has very small diffusion barriers of 0.003 and 0.006 eV for $AlCl_4$ diffusion on inner and outer tube surface, respectively, which signifies excellent charge/discharge rates for an Al battery. We have also examined the effect of varying SWNT diameters on the average open-circuit voltage and specific capacity of SWNT based Al batteries and concluded that the average open-circuit voltage and $AlCl_4$ storage capacity increases with increasing SWNT diameter and can be as high as 1.96 V and 275 mAh/g in (25,25) SWNT relative to graphite (70 mAh/g) (Figure 3). Overall, it is confirmed that the 1D SWNT systems have better cathode applicability as compared to traditional graphite cathode for Al dual-ion batteries.

5. Investigation of Charge and Discharge Processes in Aluminium Sulfur Batteries

This chapter provides a detailed understanding of the involved charging and discharging processes in Al-S battery with the help of ab initio molecular dynamics (AIMD) simulations. The solid-electrolyte interface (SEI) is modelled by constructing the interfacial systems between the ionic liquid electrolyte ($AlCl_3$ with 1-ethyl-3-methylimidazoliumchloride (EMIC)) and the most stable (001) surfaces of S_8 and Al_2S_3 to study the discharging and charging, respectively. During the discharging process, the reduction of S_8 follows layer by layer mechanism and involves the formation of various cationic and anionic intermediate species which drives the formation of Al polysulfides during the course of discharging process. The evolution of discharge voltage profile studied over a limited timescale shows two voltage domains, first corresponding the reduction of S_8 rings to higher order polysulfides and later domain to conversion to lower order polysulfides. We also observe the diffusion of these higher order Al polysulfides to electrolyte, which is in accordance with the experimentally observed solvation of higher order Al poylsulfides into electrolyte. The evolution of atomistic structure and reaction voltage during charging shows similar layer by layer reaction pattern as of discharging process.

6. Superior Anchoring Effect of Cu-benzenehexathial MOF as Aluminium-Sulfur Battery Cathode Host

In this chapter, the 2D Cu-benzenehexathial (Cu-BHT) metal organic framework has been proposed to be a more potential cathode host for Al-S batteries as compared to carbonaceous host such as graphene. The favorable electrical conductivity of Cu-BHT eliminates the insulating nature of most sulfur-based electrode and is helpful in supporting the cathode charge/discharge processes. The results of binding study show that while graphene has low adsorption energies towards Al polysulfides, the Cu-BHT furnishes improved adsorption of Al polysulfides because of the presence of copper and sulfur, which results into increased charge transfer to Al polysulfides. The synergic dual interaction based on the Al-S (of sulfur host) bond and S (of Al polysulfide)-Cu bond also lead to uniform deposition of insoluble Al_2S_3 over the Cu-BHT surface, improving the utilization of the active cathode host. Moreover, it is also observed that the Al polysulfides adsorption is much stronger than their interaction with the electrolytes, thus decreasing the overall dissolution of Al polysulfide into electrolyte to increase the net cycle performance in Al-S batteries. With these desirable properties, it is expected that Cu-BHT can be used as a promising anchoring cathode host compared to graphene in Al-S batteries.

4. Conclusions

The conclusions of the thesis can be outlined as follows:

1. The Al dual-ion batteries follow the staging mechanism of $AlCl_4$ intercalation stabilizing $AlCl_4$ in its tetrahedral geometry. The understanding of voltage vs. stability concept concludes that an electron deficient graphite-like material can make a high voltage cathode for Al dual-ion batteries.
2. The 2D heterostructure of graphene and h-BN acts as a more efficient cathode material offering a voltage of 2.14 V and an efficient storage capacity of 183 mAh/g compared to pure graphene (1.99 V, 248 mA h/g) and h-BN (2.23 V, 120 mA h/g).
3. The one-dimensional single walled carbon nanotube systems offer improved cathode applicability for Al dual-ion batteries allowing the trouble-free $AlCl_4$ adsorption for the very first charging step, better charge/discharge rates and quite high storage capacities.
4. The charging and discharging processes in aluminium-sulfur batteries show layer by layer reaction mechanism, and formation of various cationic and anionic intermediate species depending upon the local Al

concentration, which drives the formation and conversion of Al polysulfides.

5. The 2D Cu-benzenehexathial (BHT) shows superior anchoring effect as the sulfur host in aluminium-sulfur battery compared to carbonaceous graphene.

List of Publications

1) **Bhauriyal P.**, Das S., Pathak B. (2020), Theoretical insights into the charge and discharge processes in aluminium-sulfur batteries, J. Phys. Chem. C, (DOI:10.1021/acs.jpcc.0c01358)

2) **Bhauriyal P.**, Pathak B. (2019), Identification of non-carbonaceous cathodes in Al batteries: Potential applicability of black and blue phosphorene monolayers, Chem. Asian J., 14, 2831-2837 (DOI: 10.1002/asia.201900693)

3) **Bhauriyal P.**, Bhattacharyya G., Rawat K. S., Pathak B. (2019), Graphene/hBN heterostructure as high capacity cathode with high voltage for next generation aluminium batteries, J. Phys. Chem. C, 123, 3959-3967 (DOI: 10.1021/acs.jpcc.8b10550)

4) **Bhauriyal P.**, Rawat K. S., Bhattacharyya G., Garg, P., Pathak B. (2018), First-principles study of magnesium peroxide nucleation for Mg-air battery, Chem. Asian J., 13, 3198-3203 (DOI: 10.1002/asia.201801057)

5) **Bhauriyal P.**, Garg P., Patel M., Pathak B. (2018), Electron-rich graphite-like electrode: Stability vs. voltage for Al batteries, J. Mater. Chem. A, 6, 10776-10786 (DOI: 10.1039/c8ta01820k)

6) **Bhauriyal P.**, Mahata A., Pathak B. (2018), Graphene-like carbon-nitride monolayer: A potential anode material for Na and K-ion batteries, J. Phys. Chem. C, 122, 2481-2489 (DOI: 10.1021/acs.jpcc.7b09433)

7) **Bhauriyal P.**, Mahata, A., Pathak B. (2017), A computational study of single-walled carbon nanotube based ultrafast high

capacity Al battery, Chem. Asian J., 12, 1944-1951 (DOI: 10.1002/asia.201700570)

8) **Bhauriyal P.**, Mahata A., Pathak B. (2017), Hexagonal BC_3 electrode for a high-voltage Al-ion battery. J. Phys. Chem. C, 121, 9748–9756 (DOI: 10.1021/acs.jpcc.7b02290)

9) **Bhauriyal P.**, Mahata A., Pathak B. (2017), The staging mechanism of AlCl4 intercalation in graphite electrode for aluminium-ion battery. Phys. Chem. Chem. Phys., 19, 7980–7989 (DOI: 10.1039/c7cp00453b)

10) **Bhauriyal P.**, Pathak B. (2020), Superior anchoring effect of Cu-benzenehexathial MOF as aluminium-sulfur battery cathode host, (Manuscript to be submitted)

11) Das S., **Bhauriyal P.**, Pathak B. (2020), Theoretical insights into solid electrolyte interphase formation in an Al anode dual-ion battery, J. Phys. Chem. C, 124, 7634–7643 (DOI: 10.1021/acs.jpcc.9b11421)

12) Choudhuri I., **Bhauriyal P.**, Pathak B. (2019), Recent advances in graphene-like 2D materials for spintronics applications, Chem. Mater., 20, 8260-8285 (DOI: 10.1021/acs.chemmater.9b02243)

13) Singh S. K., **Bhauriyal P.**, Pathak B. (2019), Computational insights into working mechanism of $LiPF_6$-graphite dual-ion battery, J. Phys. Chem. C, 123, 23863-23871 (DOI: 10.1021/acs.jpcc.9b07046)

14) Bhattacharyya G., Garg P., **Bhauriyal P.**, Pathak B. (2019), Density functional theory study of defect induced ferromagnetism and half-metallicity in CaI_2 based monolayer

for spintronics applications, ACS Appl. Nano Mater., (DOI: 10.1021/acsanm.9b00967)

15) Rawat K. S., Mandal S. C., **Bhauriyal P.**, Garg P., Pathak B. (2019), Catalytic upgrading of ethanol to n-butanol using aliphatic Mn-PNP complex: Theoretical insights on reaction mechanisms and product selectivity, Catal. Sci. Technol., 9, 2794-2805 (DOI: 10.1039/C9CY00501C)

16) Rawat K. S., Garg P., **Bhauriyal P.**, Pathak B. (2019), Metal-ligand bifunctional based Mn-catalysts for CO_2 hydrogenation reaction, Molecular Catal., 468, 109-116 (DOI: 10.1016/j.mcat.2019.02.017) (Impact Factor: 3.89)

17) Garg P., **Bhauriyal P.**, Mahata A., Rawat K. S., Pathak B. (2019), Role of dimensionality for photocatalytic water splitting: CdS nanotube versus bulk structure, ChemPhysChem, 20, 383-391 (DOI: 10.1002/cphc.201801051)

18) Garg P., Bhattacharyya G., **Bhauriyal P.**, Pathak B. (2019), Enhanced Lewis acid-base adducts in doped stanene: Sensing and photocatalysis, Appl. Surf. Sci., 478, 946-958 (DOI: 10.1016/j.apsusc.2019.02.048)

19) Bhattacharyya G., Choudhuri I., **Bhauriyal P.**, Garg P., Pathak B. (2018), Ferromagnetism in magnesium chloride monolayer with an unusual large spin-up gap, Nanoscale, 10, 22280-22292 (DOI: 10.1039/C8NR07429A)

20) Kravchyk K., **Bhauriyal P.**, Piveteau L., Guntlin C., Pathak B. Kovalenko M. (2018), High-energy-density dual-ion battery for stationary storage of electricity using concentrated potassium fluorosulfonylimide, Nature Commun., 9, 4469 (DOI: 10.1038/s41467-018-06923-6)

21) Mahata A., Garg P., Rawat K. S., **Bhauriyal P.**, Pathak B. (2017), Free-standing platinum monolayer as an efficient and selective catalyst for oxygen reduction reaction, J. Mater. Chem. A, 5, 5303-5313 (DOI: 10.1039/C7TA00685C)

22) Mahata A., **Bhauriyal P.**, Rawat K. S., Pathak B. (2016), Pt_3Ti (Ti19@Pt60) based cuboctahedral core-shell nanocluster favours direct over indirect oxygen reduction reaction, ACS Energy Lett., 1, 797-805 (DOI: 10.1021/acsenergylett.6b00385)

Table of Contents

Chapter 1: Introduction

Chapter 2: Staging Mechanism of $AlCl_4^-$ into Graphite and Electron-Rich Graphite-like Electrode and Investigation of the Stability vs. Voltage for Aluminium Batteries

Chapter 3: Graphene/hBN Heterostructures as High-Capacity Cathodes with High Voltage for Next-Generation Aluminium Batteries

Chapter 4: A Computational Study of Single-walled Carbon Nanotube Based Ultrafast High Capacity Aluminium Battery

Chapter 5: Investigation of Charge and Discharge Processes in Aluminium-Sulfur Batteries

Chapter 6: Superior Anchoring Effect of Cu-benzenehexathial MOF as Aluminium-Sulfur Battery Cathode Host

Chapter 7: Scope for Future Work

List of Figures

Chapter 1

Chapter 2

Chapter 3

Chapter 4

Chapter 5

Chapter 6

List of Tables

Chapter 1

Chapter 2

Chapter 3

Chapter 4

Chapter 5

Chapter 6

Acronyms

LIB	Lithium-ion battery
AIB	Aluminium-ion battery
DIB	Dual-ion battery
2D	Two-dimensional
3D	Three dimensional
VB	Valence band
CB	Conduction band
BO	Born-Oppenheimer
HF	Hartree-Fock
SCF	Self-Consistent Field
DFT	Density functional theory
LDA	Local density approximation
GGA	Generalized gradient approximation
PBE	Perdew-Burke-Ernzerhof
PAW	Projector augmented wave
B3LYP	Becke, three-parameter, Lee-Yang-Parr
VASP	Vienna ab initio simulation package
AIMD	Ab initio molecular dynamics
VESTA	Visualization of electronic and structural analysis
DOS	Density of states
PDOS	Projected density of states
CDD	Charge density difference
SWNT	Single walled nanotube

Chapter 1

Introduction

1.1. Rechargeable Batteries

With the continuous growth and development of world’s economy, the consumption and supply of energy becomes very important factors to look for. Presently, most of world energy needs is being satisfied using the fossil fuel with the supply of over 85% of the growing energy demand of world. However, these fossil fuels are non-sustainable because the limited reserves and also are accompanied by potential environmental pollutions. The energy dependence of world on fossil fuels is one of the major reasons of increasing amounts of carbon dioxide and other greenhouse gas (GHG) in the atmosphere rising concerns about the global climate change. Therefore, it is necessary to flourish energy sources, which involve lower environmental pollution, and in this regard the renewable energies are becoming the centre of interest, which are crucial to reduce the carbon dioxide emissions. The renewable as well as sustainable energy sources such as wind, solar, and tide seem quite good options *[1–3]*. However, till present their utilization is still very much restricted by intermittent and diffuse natures of these renewable sources making them an inconvenient option to be directly utilized along with the definite need of devices to store the generated electric energy by these power plants for further utilization *[4-6]*. All of these criteria lead to look for new and efficient energy storage and conversion systems. These necessary energetic choices place electrochemical energy management as one of the major technological developments for the 21st century. The most popular energy storage and conversion devices are batteries, which are electrochemical energy storage systems *[7-9]*. Roughly, batteries can be categorized in two types, primary batteries which are non-rechargeable and suitable for one time usage, and secondary batteries, which can be recharged for some certain charge/discharge cycles.

Nowadays, the electrical energy storage is attracting huge market interest and has significantly catalyzed the growth of consumer electronics market. The consumer market has expanded for pronounced usage of batteries more significantly for grid storage of energy, portable electronics, and the electrification of the transportation sector due to commercialization of battery-driven auto-mobiles. With the ongoing miniaturization of electronic devices comes the desire to increase the capacity density and also the specific capacity of current battery systems. From over a century, various kinds of secondary batteries such as lead–acid *[10-11]*, nickel metal hydride *[12-13]*, nickel–cadmium *[14-15]*, and lithium ion batteries (LIBs) *[16-20]* are being actively used in a variety of applications in portable electronic devices and automobiles. Especially for portable electronics, LIBs provide much higher energy density than other rechargeable batteries (Figure 1.1). Presently, rechargeable LIBs are leading choice of the wireless battery market to produce cell phones, digital cameras, laptop, computers, etc., and are also being considered to be a suitable choice for future electric vehicles and large scale energy storage systems *[16-20]*. Having all these useful characteristics, the application of current Li ion technology is still limited due to their energy density and storage capacity as the their working mechanism is based on intercalation-type anode-cathode systems, as well as the increased cost of Li for long term usage *[21-22]*. Therefore, as the demand of renewable sources is increasing for efficient electricity storage, electrical vehicles, and the functionalities of the portable electronics becoming more sophisticated, there is an urgent need of the development of more advanced rechargeable batteries. The increase in energy density can be achieved by either improving the charge storage capacity or increasing the cell voltage or increasing both. In this context, some of the most important parameters which need be considered are the cost, safety, energy and power, cycle stability, and environmental friendliness. Therefore, looking for options beyond the LIB has become very important and alternatives with different chemistries have to be suggested.

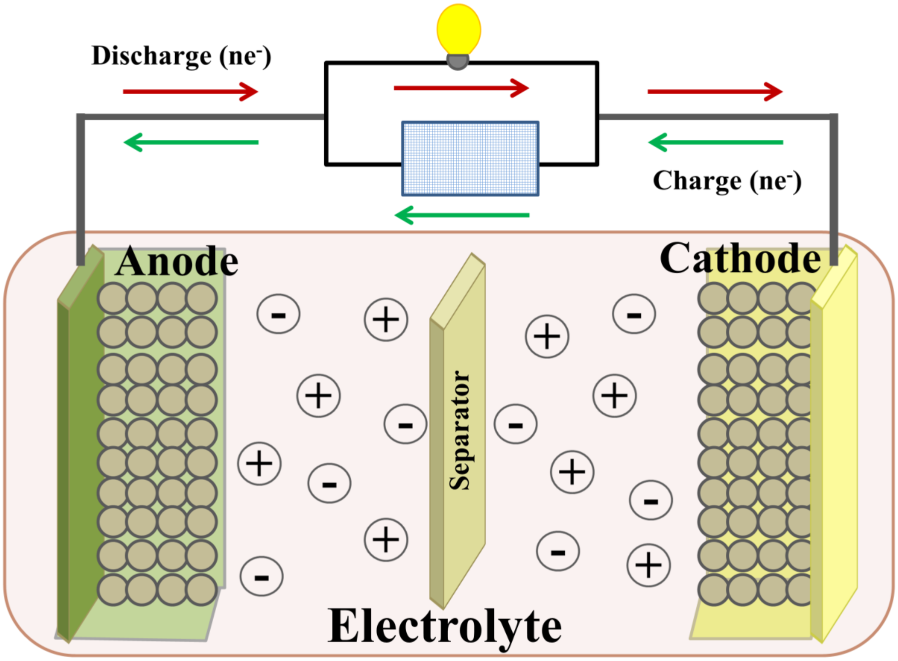

Figure 1.1: Schematic representation of a rechargeable battery.

1.2. Aluminium Based Batteries

Aluminium (Al) being the third most abundant element in the earth crust along with furnishing $3e^-$ redox reactions draws a huge attention of scientific community *[23-24]*. Particularly in field of batteries various positive factors of Al support the renewed interest towards Al batteries as shown in Figure 1.2. Al batteries show improved safety due to the environmental inertness and easier handling of Al metal. The involvement of $3e^-$ exchange reactions lead to higher volumetric capacity (8046 mAh/cm^3) *[25-26]* than monovalent LIBs (2062 mAh/cm^3) *[27]* and divalent magnesium-ion batteries (3833 mAh/cm^3) *[28-29]*, respectively, which indicates that the Al metal based batteries can store higher amount of energy on a per volume basis compared to other metal-ion based batteries *[30, 31]*. Moreover, Al batteries commonly involve the usage of ionic liquid electrolyte, which is nonvolatile and nonflammable in nature and can form a quite safe battery system. Based on these advantages, Al batteries are expected to have an easier market penetration. As consequence, the an ambitious project entitled as “ALION” was launched by European Commission in 2015 for the development of aluminium-batteries for energy storage applications in decentralized electricity generation systems *[32]*.

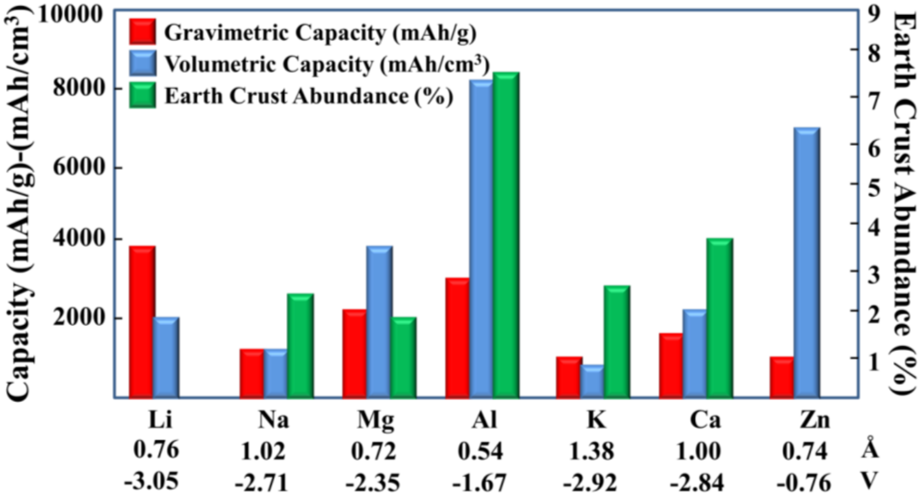

Figure 1.2: Comparison of various metal anodes. Figure adapted with permission from Ref. 33. Copyrights 2019, Wiley-VCH.

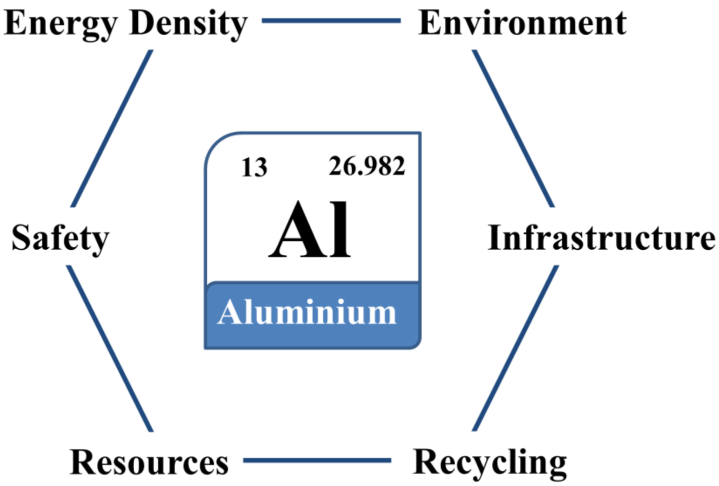

Figure 1.3: Strengths of using Al as anode in batteries. Adapted with permission from Ref. 34. with permission from ref 202. Published by Frontiers with Creative Commons Attribution 4.0 International License: https://creativecommons.org/licenses/by/4.0/. Copyright 2019.

1.3. Non-Aqueous Al Batteries

As the name suggests, the nonaqueous Al batteries consist of a non-aqueous chloroaluminate-based ILs electrolytes alongside an aluminum anode. These nonaqueous electrolyte systems are show more suitability for Al batteries than aqueous electrolytes because in aqueous system, due to the relatively low standard reduction potential of Al (−1.662 V vs SHE), there occurs the generation of hydrogen before Al could plate in the process of reduction, thus decreasing the overall efficiency of the Al anode. For Al batteries, the most studied ionic liquid electrolyte system usually contains $AlCl_3$ with substituted imidazolium chloride salt, i.e. 1-ethyl-3-methylimidazolium chloride (EMIC) and 1-butyl-3-methylimidazolium chloride (BMIC) *[28, 35]*. These room temperature ionic liquids form a new class of electrolyte which offers tunable properties, such as high ionic conductivity, low volatility leading to reduced flammability and high electrochemical and chemical stabilities. The variation in ratio of $AlCl_3$:imidazolium salt tunes the Lewis acidity in such systems, which affects the Al plating *[36-38]*. The system becomes acidic for $AlCl_3$ > ILs molar ratio and the dominant species is $Al_2Cl_7^-$ along with $AlCl_4^-$, the system is neutral for $AlCl_3$ = ILs with the only anionic $AlCl_4^-$ species, and in basic system $AlCl_3$ < ILs, $AlCl_4^-$ and Cl^- species coexist. This ratio plays a major factor in influencing the electrochemical reaction taking place in the cell. At higher mole ratios of 1.3-2.0, the cathodic limit is given by the reversible electrochemical process of aluminum deposition whereas for lower mole ratios of 0.8, 1 and 1.1 are associated with the irreversible reduction of the ionic liquid’s organic cation *[39]*. On the other hand, the anodic stability limit is governed by evolution of chlorine at the cathode side, which can follow any of the three different routes (shown in equations) depending on the main anionic species present in the electrolyte, and thus can result into the different electrolyte anodic stability values *[39]*.

$$2Cl^- \rightarrow Cl_2 + 2e^- \quad (1.1)$$

$$4AlCl_4^- \rightarrow Cl_2 + 2Al_2Cl_7^- + 2e^- \quad (1.2)$$

$$6Al_2Cl_7^- \rightarrow Cl_2 + 4Al_3Cl_{10}^- + 2e^- \quad (1.3)$$

Out of these systems, the acidic system is suitable for the reversible electroplating/stripping of Al according to the following reversible reaction *[40]*.

$$4Al_2Cl_7^- + 3e^- \rightarrow Al + AlCl_4^- \quad (1.4)$$

1.4. Cathode Materials for Aluminum Batteries

In nonaqueous Al batteries, different types of electron transfer processes can lead to different reaction mechanisms of charging and discharging. Overall, the reactions mechanisms can be categorized into two reversible energy storage mechanisms: intercalation reactions and conversion reactions as presented in Figure 1.3. As the chloroaluminate ionic liquid electrolyte consists of Al ion in the form of both cation and anions, so both Al^{3+} and $AlCl_4^-$ can intercalate in the respective cathode systems to undergo intercalation reaction in certain Al batteries. For the case of rocking chair type Al batteries, which involve intercalation of Al^{3+} into cathodes, various metal oxides *[41-47]* and sulfides *[48-50]* cathodes materials have been reported. These Al batteries are reported to furnish high capacity, however are limited by their small cycle life, coulombic efficiency and cell voltage range (~0.6 V). Whereas, Al batteries involving the intercalation of $AlCl_4^-$ are famously known as Al dual-ion batteries, which deliver higher voltage of ~2.00 V and fast charge/discharge rates *[35, 51-62]*. On the other hand, the Al batteries with conversion mechanism involve the reversible conversion of cathode systems containing multivalent elements species to discharge products containing Al^{3+} ion, which are anticipated to acquire higher-energy capacities because of involvement these multi-electron redox reactions *[63-71]*. Such conversion based reaction mechanisms are now being well studied for Al batteries involving sulfur based cathode systems *[68-71]*.

Having the similar non-aqueous electrolyte, the difference in the reaction mechanisms of Al batteries arises due to the choice of different cathode materials. Various cathode materials have been explored till present showing either intercalation or conversion reaction mechanisms depending upon their structural and electronic characteristics. For intercalation mechanism, cathode materials involving the intercalation of $AlCl_4^-$ anion are more advantageous *[35]*, whereas sulfur cathodes for conversion cathodes *[70-71]*. Therefore, the previously studied intercalation and conversion type cathode materials are summarized in Figure 1.4 and discussed in two sections along with discussion of the reaction mechanisms of Al-dual ion batteries and Al-S batteries.

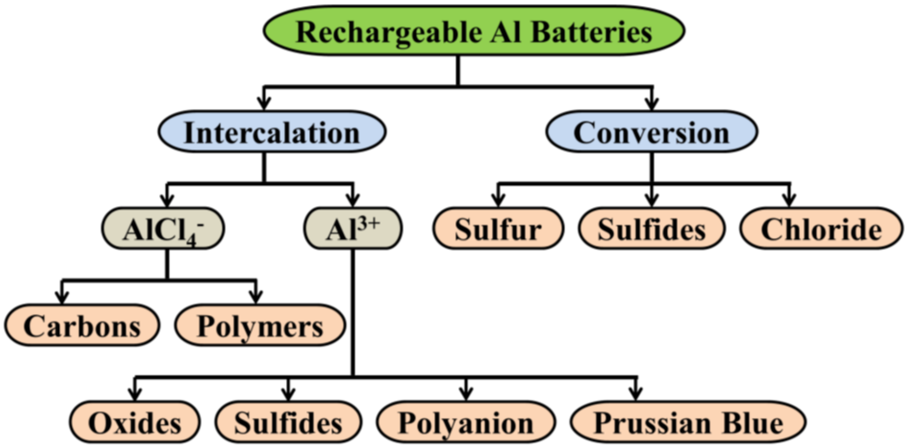

Figure 1.4: Classification of cathode materials with different reaction mechanisms in non-aqueous Al batteries.

1.4.1. Al Dual-Ion Batteries: Intercalation of $AlCl_4^-$

1.4.1.1. Traditional Graphite and Its Structural Forms

The graphite based cathode systems have hugely contributed towards the betterment of rechargeable Al batteries by offering excellent electrochemical performances such as improved cycle life, fast rate capability and high cell voltage *[35, 57]*. Graphite is one of the widely used anode for Li-ion batteries, and the first electrochemical intercalation of $AlCl_4^-$ into graphite was demonstrated in year 1979 by Armand et al., making a setup with Al anode and NaCl-$AlCl_3$ (in melted state at 175 °C) as the electrolyte *[72]*. However, practically graphite was first utilized as a cathode in Al-DIB in year 2015 by two independent research groups in form of 3D-graphite foam and carbon paper respectively *[35, 57]*. Having the [EMIm]Cl-$AlCl_3$ ionic liquid electrolyte, two major charge/discharge voltage plateaus were observed at 2.0~2.4 V and 1.9~1.6 with ultrahigh rate performance upto 5000 mA/g along with 66 mAh/g storage capacity. Besides, the appealing electrochemical performance, for the first time $AlCl_4^-$ was proposed as the active agent to undergo intercalation reaction into graphite. After that various forms of graphite derivatives were used to improve the rate performance and capacity. In this respect, pre-intercalated $AlCl_4$ graphene foam was used to increase the ion diffusion *[51]*, whereas to increase the electron conductivity, a high-temperature-annealed defect-free graphene aerogel was used *[52]*. Also some few layered graphene *[53]* and a graphene mesh network *[73]* were also reported to increase the rate performance in Al batteries. Whereas in terms of capacity, defect containing graphene nanoribbons (~120 mAh/g) *[59]*, as well as high-quality crystalline natural graphite with fewer defects also achieved a high capacity of ~110 mAh/g *[74]*.

The commercial graphite can be used as a high working voltage cathode material in a RTIL electrolyte but is limited by the structural disintegration, volume expansion and high self-discharge rates *[35, 57]*. Moreover, apart from the intercalation mechanism, the information regarding the intercalation capacity as well as the interaction approach of the intercalant $AlCl_4$ with graphite is also needs to be clearly understood. The geometry of intercalated $AlCl_4$ is not clearly resolved as some of the studies say that $AlCl_4$ is planar *[75]*, whereas other reports favor the stability of the tetrahedral geometry inside graphite *[61, 76]*. Moreover, it is also quite important to have better understanding about the stability of the $AlCl_4$ intercalated graphite electrode, migration behaviour of $AlCl_4$ into graphite, and voltage variations during the course of charge/discharge reactions, and their dependency on the different staging patterns of $AlCl_4$ formed during intercalation and deintercalation processes. Thus, in this thesis, we have studied the intercalation mechanism by analyzing the $AlCl_4$ intercalation into the graphite electrode in staging manner, which is an intrinsic feature of graphite intercalation compounds. Moreover, we have also discussed how the voltage and the stability of $AlCl_4$ intercalated cathode system are related to each other and what could be the innovative ideas to increase the efficiency of Al dual-ion batteries.

1.4.1.2. Other than graphite: Exploration of Low Dimensional Cathodes

With the progressive investigations in the field of Al batteries, the structural and electrochemical limitations of graphite and its derivatives are also a point of interest. In this respect, various other kinds of cathode materials are also explored. One of such report was presented by Hudak et al. where, polypyrrole and polythiophene, chloroaluminate-doped conducting polymers were used as cathode materials with $AlCl_3$:[EMIm]Cl (molar ratio 2:1) electrolyte and a coulombic efficiency of 100% was attained *[62]*. However, because of the dissolution of the active polymer in electrolyte, lower capacities were achieved.

Therefore, the cathode designing for Al dual-ion batteries requires more striking ideas, and such motivations can be taken from the trials of the previously studied metal-ion batteries. The introduction of some variations on elemental level such as doping the sites with other elements or replacing with other cathode materials, and changes on structural levels like preferential selection of low dimensional materials, which have been proved to be successful to overcome certain limitations of metal-ion batteries can also be applied for Al-dual-ion batteries. In this regard, one strategy could be doping of boron or nitrogen sites in the experimentally used graphite cathode, which can change the electronic structure and can produce locally accessible active sites in the graphite lattice to improve the activity. The B and N atoms behave as a p-type and n-type dopants by decreasing and increasing the number of electrons in the system, respectively. One of such B doped system, BC_3 which is of great interest to material scientists and physicists since it was reported *[77]*. Various studies have compared the potential applicability of BC_3 with traditional graphite cathode for metal-ion batteries and observed that BC_3 offers higher intercalation capacity due to its relatively light mass and higher energy density, and also improves voltage stability during the course of reaction *[78-82]*. On the other hand, another candidate to be studied is C_3N *[83-85]*, which is also similar to graphite in its structural and stacking pattern, and can also be studied towards its cathode applicability for Al batteries. Therefore, it will be interesting to analyze that how an electron deficient system BC_3 and electron-rich system C_3N (compared to that of graphite) can affect the stability and electrochemical properties of Al batteries. Hence, all of this work has been discussed in our thesis (Figure 1.5).

Moreover, the exploration of low dimensional materials compared to bulk graphite cathode can also lead to improved Al dual-ion battery efficiency. When compared to their parent bulk systems from which they are exfoliated, the low dimensional materials show many structural dependent advantages such as surface areas with more active sites to allow increased storage capacity, decreased diffusion paths to have increased rate performance and improved cycle stabilities *[85-87]*. Because of all these mentioned advantages, the low dimensional electrodes such as 2D monolayer and few layered systems *[88-91]*, 2D heterostructures *[92-95]*, 1D nanotube *[96-99]* and nanoribbon *[100-103]* systems are widely studied for various metal-ion batteries. However, for Al batteries exploration of such systems is very limited. In this regard, 2D heterostructure of graphene with a hexagonal boron nitride (h-BN) could be quite interesting to be explored towards its Al dual-ion battery cathode applicability due to exhibiting rich physical properties such as high electron mobility and tunable band gap *[104-109]*. This graphene/h-BN heterostructure can offer improved voltage due to presence of electron deficient B and electronegative N atoms and improved stability and conductivity because of the presence of graphene. Therefore, graphene/h-BN heterostructure is examined in this thesis for potential Al battery cathode. Other than the 2D systems, 1D materials such nanotubes, especially carbon nanotubes (CNTs) having superior electronic and structural properties can also be explored as building blocks for future Al batteries. CNTs with hollow structures are observed to offer high-storage capacity than graphite because having large surface area, more guest binding sites, and easy diffusion of ions *[110-113]*. Moreover, the tubular structure of CNTs can be a host for $AlCl_4$ anions, and the hollow interior cavities of CNT are superior to avoid any strain which can associated to the structural changes as a consequence of repeated ion intercalation/deintercalation, thus increasing the overall cycle life of Al dual-ion batteries. One of such study employing CNT is recently reported, an aluminum asymmetric capacitor is studies involving intercalation/ deintercalation of $AlCl_4$ anion into multiwalled carbon nanotubes during charging/discharging of the capacitor *[114]*. This study further initiates the exploration of CNTs for Al battery cathodes. Therefore, we have also investigated the potential applicability of these above reviwed electrodes such as C_3N, CNTs, and graphene/h-BN heterostructure towards their potential cathode applications in Al dual-ion batteries (Figure 1.5).

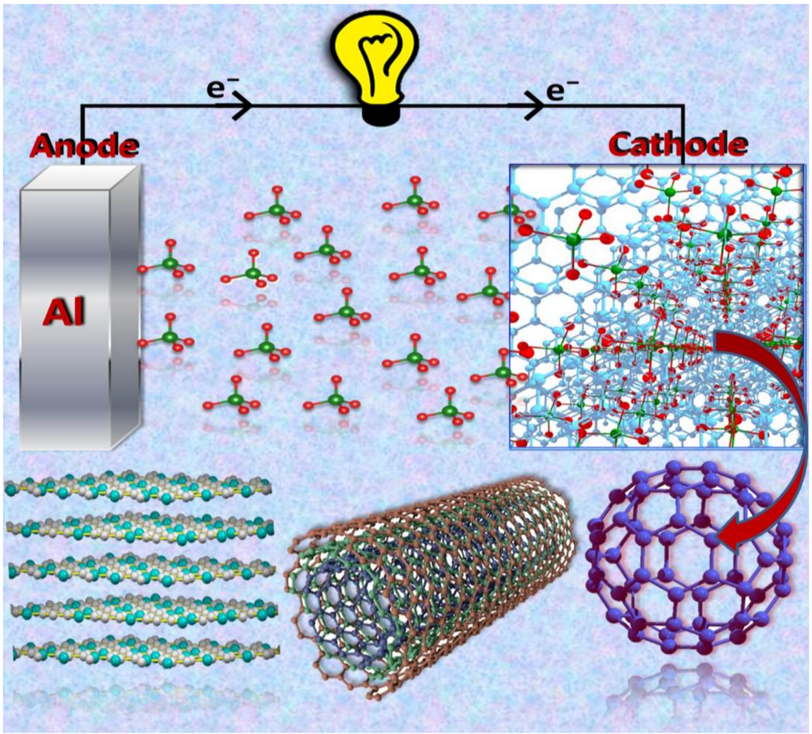

Figure 1.5: Exploration of possible cathode materials for Al batteries other than bulk graphite.

1.4.2. Al-S Batteries: Conversion Mechanism

The sulfur based batteries like Li-S, Na-S, K-S, Mg-S, and Ca-S batteries have drawn considerable interest having the earth-abundant sulfur as a low cost and high-capacity (1675 mAh/g) cathode material. In a similar way, Al-S stand out as the most advantageous ones because of the high abundance, small atomic weight and trivalent oxidation state of aluminium to furnish higher gravimetric (2.90 Ah/g) and volumetric capacity (3.80 Ah/g) as Al metal anode. Overall, Al-S batteries can provide high energy density of 1300 Wh/Kg with the theoretical voltage of 1.30 V providing a low cost application in electric vehicles and grid-scale energy storage. Especially, Al-S batteries with nonaqueous ionic-liquid electrolyte *[66-69]* show huge advantages over aqueous electrolytes *[115]* in terms of reversibility. Al-S batteries follow the rocking-chair reaction mechanism involving Al^{3+} intercalation at sulfur cathode, where the overall concentration of electrolyte remains constant during the course of reaction.

The overall involved reactions during discharge process can be given as follows,

Anode: $2Al + 14AlCl_4^- \leftrightarrow 8Al_2Cl_7^- + 6e^-$ (1.5)

Cathode: $8Al_2Cl_7^- + 6e^- + 3S \leftrightarrow Al_2S_3 + 14AlCl_4^-$ (1.6)

Overall: $2Al + 3S \leftrightarrow Al_2S_3$ (1.7)

At cathode, the involved reaction steps resulting into the final discharge product Al_2S_3 are proposed to undergo similar polysulfide sequence formation as of Li-S batteries that are S_x^{2-} $1 \leq x < 6$ as shown in Figure 1.6 *[70-71]*. The characteristic of Al-S battery voltage profile is a two voltage plateau, the higher plateau associated with conversion of elemental sulfur to higher order polysulfides whereas, the lower voltage plateau is associated with the conversion of higher to lower order polysulfides *[70-71]*. The Al-S batteries suffer with certain limitations in their practical application, as the sulfur cathode undergoes dissolution in the electrolyte and the oxidation kinetics of AlS_x during charging is quite slow *[69-71]*. Till present, very limited number of studies have been investigated on Al-S batteries and the complex reaction mechanism is still in the initial stage of understanding. In this respect, the Ab Initio molecular dynamics (AIMD) simulations could be very helpful, which have already successfully contributed having a clear understanding of Li-S batteries *[116-118]*. Therefore, in this thesis, we have we have used AIMD simulations to evaluate the complex electrochemical reactions occurring during charging and discharging processes.

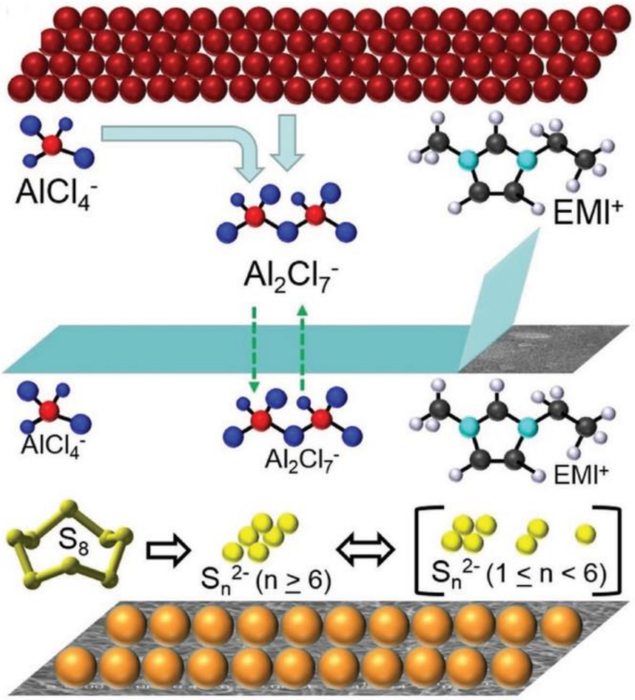

Figure 1.6: Schematic summary of the electrochemical discharge–charge mechanism of the Al-S battery. Figure reprinted with permission from Ref. 70. Copyrights 2017, WILEY-VCH.

1.4.2.1. Exploration of Cathode Host Materials

The role of a cathode is quite important for Al-S batteries, not only in improving the electrochemical properties such as capacity and voltage but also increasing the sustainability and rate performance of the battery. The very first reversible Al-S battery is recently proposed by Gao et al., using activated carbon cloth/sulfur as cathode (pore size <2 nm) in ILs to reversibly encapsulate sulfur *[68]*. This battery has shown a high capacity of 1000 mAh/g with excellent reversibility of 20 cycle life. The proposed Al-S battery involves an ionic liquid electrolyte $AlCl_3$:EMIC with sulfur undergoing a solid-state conversion reaction *[68]*. After that a more advanced reversible Al-S battery was studied working at ambient-temperature with a well thought out sulfur cathode, a single-walled carbon nanotube (SWCNT) coated on the glass fiber close to the sulfur cathode side, which helps to reduce the effects from the diffusion of Al polysulfide intermediates and reduces the polarization of the cell *[70]*. With this strategically designed cathode, the cycling performance of the Al–S system has certainly improved. After that another approach was proposed by Yu et al. for developing more reversible Al-S battery working at room-temperature by adding lithium salt into the ionic liquid electrolyte *[71]*, which improved the reaction kinetics of Al-S battery by alleviating Al polysulfide dissolution into electrolyte. And, they could obtain ~1,000 mAh/g initial capacity with maintaining a capacity of 600 mAh/g even after 50 cycles. Very recently, a composite of sulfur on a carbonized HKUST-1 matrix (S@HKUST-1-C) is analyzed for Al–S batteries cathode *[119]*, which observed to offer a high reversible capacity of 600 mAh/g at the 75th cycle and 460 mAh/g at the 500th cycle with a Coulombic efficiency of around 95%. The better efficiency of this battery is credited to the presence of copper (Cu) metal, which participates in the electrochemical process by forming an ionic cluster with Al polysulfide which drives the electrochemical reaction and improves the reversibility of sulfur during charge and discharge processes. Moreover, Cu also increases the electronic conductivity of HKUST-1-C/S interface. Such Cu based MOF have also been investigated for the development of more efficient Li-S batteries, both experimentally and theoretically *[118, 120-123]*. Therefore, for the effective growth of Al-S batteries, it is necessary to take inspiration from more developed L-S batteries as Al-S batteries also follow the similar kind of working mechanism. Hence, in this thesis, we have explored the applicability of a Cu-metal based MOF as Al-S battery cathode and understand the involved reaction mechanism in details.

1.5. Theory

In this part, we have discussed the essential theory and computing techniques used in our studies. In general, solid state materials have the periodic arrangement of atoms. Therefore, the properties of these materials are highly dependent on the atomic arrangements in the system. Hence, the following sections discuss the interaction between the electron and nucleus particles for the calculation of the atomic properties of the solid state material.

1.5.1. Schrödinger Equation

In general, the time independent Schrödinger Equation is used for the estimation of the electronic structural properties of the materials and molecules. This time independent Schrödinger equation can be expressed as equation 1.8,

$$\mathrm{H}\Psi(\mathrm{r},\mathrm{R}) = \mathrm{E}\Psi(\mathrm{r},\mathrm{R}) \tag{1.8}$$

Here, H is the Hamiltonian operator, which defines all the properties of the system, Ψ is the wave function of the system containing all the information about the nuclei and electrons, and E is the total energy of the system. The Hamiltonian operator can also be expressed by equation 1.9 as follows,

$$H = -\frac{h^2}{2m_e}\sum_i \nabla_i^2 - \sum_I \frac{h^2}{2M_I}\nabla_I^2 + \frac{1}{2}\sum_{i\neq j}\frac{e^2}{|\boldsymbol{r_i}-\boldsymbol{r_j}|} + \frac{1}{2}\sum_{I\neq J}\frac{Z_I Z_J e^2}{|\boldsymbol{R_I}-\boldsymbol{R_J}|} - \sum_{i,I}\frac{Z_I e^2}{|\boldsymbol{r_i}-\boldsymbol{R_I}|} \tag{1.9}$$

In this case, m_e is the mass of the electron and r_i is the position of the electron. Moreover, M_I is the mass of the nuclei, R_I is the position of the nuclei and Z_I is the nuclear charge of the considered system. In the above equation, the first and second terms represent the kinetic energies of the electron and nuclei, respectively. Moreover, the following three terms correspond to the electron-electron repulsion, nuclei-nuclei repulsion and electrons-nuclei attractive interaction, respectively. Therefore, placing the Hamiltonian operator in the Schrödinger equation gives the properties of the system.

In case of solid state materials, number of nuclei and electrons are very high, leading to a complex Hamiltonian operator. Hence, exact solvation of the Schrödinger equation for many body systems is practically impossible. Therefore, it is highly important to employ some approximations, and in this context, the Born-Oppenheimer (BO) approximation is quite useful *[124]*.

1.5.1.1. Born-Oppenheimer (BO) Approximation

The BO approximation is used for the approximation of the Schrödinger equation of the solid state materials. In this approximation, we consider the speed of the nuclei and electron *[124]*. The nuclei speed is very less compared to the electron as the nucleus is 1836 times heavier than the mass of the electron. Therefore, the nucleus is presumed to be stationary with respect to electron and kinetic energy of the nuclei can be neglected from the Hamiltonian operator. Hence, the Hamiltonian operator is as follows,

$$H = -\frac{h^2}{2m_e}\sum_i \nabla_i^2 + \frac{1}{2}\sum_{i\neq j}\frac{e^2}{|\boldsymbol{r_i}-\boldsymbol{r_j}|} + \frac{1}{2}\sum_{I\neq J}\frac{Z_I Z_J e^2}{|\boldsymbol{R}_I-\boldsymbol{R}_J|} - \sum_{i,I}\frac{Z_I e^2}{|\boldsymbol{r}_i-\boldsymbol{R}_I|} \qquad (1.10)$$

For the system having only one nucleus, the Hamiltonian operator can be rewritten as equation 1.11,

$$H = -\frac{h^2}{2m_e}\sum_i \nabla_i^2 + \frac{1}{2}\sum_{i\neq j}\frac{e^2}{|\boldsymbol{r}_i-\boldsymbol{r}_j|} - \sum_{i,I}\frac{Z_I e^2}{|\boldsymbol{r}_i-\boldsymbol{R}_I|} \qquad (1.11)$$

This BO approximation is not enough to completely solve of the Schrödinger equation of solid state materials systems. So, the equation requires further modifications. In this context, other approximations like Hartree-Fock theory (HF theory), density functional theory (DFT) etc. are extremely useful. Therefore, we have discussed about Hartree-Fock theory (HF theory) and density functional theory (DFT) in the next section of the thesis.

1.5.2. Hartree-Fock Theory (HF Theory)

In this method, Hamiltonian operator is considered to be made up of two parts. In one-part, core Hamiltonian describes the kinetic energy of the electrons with potential of electron-nuclei attraction, whereas another one part describes the electron-electron repulsion. Therefore, the Hamiltonian operator is written as the equation 1.12.

$$H = H^{C} + \frac{1}{2}\sum_{i\neq j}\frac{e^2}{|\mathbf{r}_i - \mathbf{r}_j|} \qquad (1.12)$$

In the above equation, H^C can be represented as follows,

$$H^{C} = -\frac{h^2}{2m_e}\sum_i \nabla_i^2 - \sum_{i,I}\frac{Z_I e^2}{|\mathbf{r}_i - \mathbf{R}_I|} \qquad (1.13)$$

The core part of the Hamiltonian operator (H^C) can be exactly solved, whereas repulsion of electrons cannot be treated properly. In this case the electron-electron repulsion is considered in the average manner, where electron is considered independently.

Now, considering the single Slater determinant (Φ_{SD}), one can get the lowest possible state of the energy. Here, optimization of the orbital (χ_i) by the variational method on Φ_{SD} gives the lowest possible energy. This forms the HF equation and the solution of the HF equation can be obtained from the spin orbitals, when energy (E) reaches to the lowest value.

$$f_i\chi_i = \epsilon_i\chi_i \qquad (1.14)$$

In the above equation, χ_i is the eigen function of f_i, and ϵ_i is the eigen value of the operator f_i. The operator and eigen values termed as the Fock operator and orbital energy of the system, respectively. This Fock operator (f_i) behaves like one electron operator, which can be represented as equation 1.15.

$$f_i = H^c + V_{HF}(i) \tag{1.15}$$

where, $V_{HF}(i)$ is known as the HF potential describing the average repulsive potential energy of an electron with other (N – 1) electrons (in as system having N number of electrons). Therefore, the HF potential can be replaced by the following term.

$$V_{HF}(\mathrm{i}) = \sum_{\mathrm{i,I}} \frac{\mathrm{Z_I e^2}}{|\mathbf{r}_\mathrm{i} - \mathbf{R}_\mathrm{I}|} \tag{1.16}$$

Consideration of this above term in the Hamiltonian operator makes Schrödinger equation very complex to solve. However, equating the average repulsive potential as equation 1.17 simplifies the solution of the Schrödinger equation.

$$V_{HF}(i) = \sum_i [J_i(x_i) - K_i(x_i)] \tag{1.17}$$

Here, J_i gives the potential of an electron at x_i due to its average distribution of charges from another electron, whereas K_i is the exchange variable of two different spin orbitals. The equation 1.17 can solved via two different methods. For system having even numbers of electrons which are paired, equation 1.17 is solved by the Restricted Hartree-Fock formalism (RHF formalism), whereas even electrons or odd electrons present in unpaired form are solved using Unrestricted Hartree-Fock formalism (UHF formalism).

One should know the value of χ_i for the calculation of $V_{HF}(i)$. Therefore, an iterative self-consistent field method (SCF method) is required to solve the equation. At first, an arbitrary $V_{HF}(i)$ value is considered to calculate χ which is followed getting a new $V_{HF}(i)$. This process continues until two of the successive potentials become identical.

In this method, the calculated energy is always higher than the real energy of the system as electrons are considered in the average electronic field.

Here, the energy and other properties are obtained from the wave function. The number of variables are quite large for many body systems, making the HF method difficult to be used for many body systems. Hence, a different approach is required to find out real energy of the systems and this encountered density functional theory (DFT).

1.5.3. Density Functional Theory (DFT)

Density functional theory a quantum-mechanical approach, which is used to find out the electronic structure and properties of the particular many body system by consideration of its electron density. This method is dependent only on three positional coordinates and hence, avoids the complexity of the wavefunction. This innovative idea is presented by Thomas-fermi, where ideal free electron gaseous molecules are used in the non-interacting system. Moreover, Hohenberg-Kohn have also proposed two theorems which are highly useful for the DFT calculations *[125-126]*. In the following sections we will discuss the overview of the DFT.

1.5.3.1.The Hohenberg-Kohn Theorems

Theorem 1: The first theorem of Hohenberg and Kohn states that the ground state properties of the many electron systems can be evaluated by the electron density $n(\boldsymbol{r})$ of the interacting electrons moving under the external potential of $V_{ext}(\boldsymbol{r})$. Here, the ground-state energy of the Schrödinger’s equation is a unique functional of the electron density $n_0(\boldsymbol{r})$.

Theorem 2: The second theorem talks about the universal total energy functional $E[\rho(r)]$ in terms of particle density $\rho(r)$ under the external potential of $V_{ext}(r)$. The functional is written as equation 1.18,

$$E[\rho(r)] = E_{HK}[\rho(r)] + \int V_{ext}(r)\rho(r)dr \tag{1.18}$$

where, $E_{HK}[\rho(\boldsymbol{r})]$ represents the internal and kinetic energies of the all interacting particles of the system. From the above equation it is clear that the ground state energy of the many body system is obtained, if electron density functional is less as it minimizes the energy of the system. However, the exact form of the functional for a given electron density is not clear from the theorems. Therefore, further improvement of the theory is required.

1.5.3.2. Kohn-Sham Equations

Further, Kohn-Sham have proposed a new equation for the description of the Hohenberg- Kohn theorems. Kohn-Sham equations consider the many body problem as a simple single problem, which being non-interacting in nature. The effective potential of the simple single particle is given by $V(r_i)$, known as the Kohn-Sham potential. In this context, the energy of the system can be calculated as follows,

$$E[\rho(r)] = T_0[\rho(r)] + \frac{1}{2}\iint \frac{\rho(r)\rho(r)' dr dr'}{|r-r'|} + \int V_{ext}(r)\rho(r)dr + E_{xc}[\rho(r)dr] + E_{II} \tag{1.19}$$

where, the first term $T_0[\rho(r)]$ represents the kinetic energy of the simple single non-interacting electron, second term $\frac{1}{2}\iint \frac{\rho(r)\rho(r)' dr dr'}{|r-r'|}$ represents the electron-electron Coulombic interaction, the third term $\int V_{ext}(r)\rho(r)dr$ represents the potential energy of the valence and the core electrons and the fourth term $E_{xc}[\rho(r)dr]$ is for the exchange-correlation interaction that considers all non-classical many-body effects between electrons. The last term E_{II} denotes the nuclei-nuclei interactions. However, the above Kohn-Sham equation can be further reduced as using equation 1.20 as follows,

$$\left[-\frac{1}{2}\nabla^2 + V_{eff}(r)\right]\Psi_i(r) = E_i\Psi_i(r) \tag{1.20}$$

Here, $\Psi_i(r)$ represents the Kohn-Sham orbitals, and V_{eff} is the addition of Coulomb interaction ($V_{Hartree}$), external potential (V_{ext}) and exchange correlation (V_{xc}).

$$V_{eff} = V_{Hartree} + V_{ext} + V_{xc} \tag{1.21}$$

Therefore, the effective potential of the simple non-interaction single particle can be shown in the form of the Coulomb interaction, external potential and exchange correlation. The above equation 1.12 can be solved exact, if exchange correlation potential is known. However, it is not easy to find out the exact exchange correlation potential, and different approximations are further developed for this purpose. Most of the approximations proposed for the solvation of the equation 1.20 and 1.21 are extensively used during the simulation of molecular and solid state problems *[127]*.

1.5.3.3. Exchange-Correlation Functional

The unknown parameter, exchange correlation potential functional in the Kohn-Sham equation can be divided into two parts. One is exchange and another is correlation part (equation 1.22).

$$E_{xc}(n(\boldsymbol{r})) = E_x(n(\boldsymbol{r})) + E_c(n(\boldsymbol{r})) \tag{1.22}$$

In the equation 1.22, $E_{xc}(n(\boldsymbol{r}))$ is the exchange-correlation functional, $E_x(n(\boldsymbol{r}))$ and $E_c(n(\boldsymbol{r}))$ represent the exchange and correlation part of the system. This exchange correlation functional $E_{xc}(n(\boldsymbol{r}))$ can be approximated using some local functional, which are discussed below.

1.5.3.4. Local Density Approximation (LDA)

Local density approximation (LDA) can be used for the derivation of the exchange correlation functional $E_{xc}(n(\boldsymbol{r}))$ *[126-127]*. In this approximation, a homogeneous electron gas is considered, which can be defined as follows,

$$E_{xc}^{LDA} = \int d^3r\, n(\boldsymbol{r})\, \mathcal{E}_{xc}^{hom}(n(\boldsymbol{r})) \tag{1.23}$$

In this equation 1.23, $\mathcal{E}_{xc}^{hom}(n(\boldsymbol{r}))$ is the exchange-correlation energy per particle with the electron density $n(\boldsymbol{r})$ in the homogeneous gas. This approximation is mostly useful for finding the ground state of the solid state materials, where density varies very slowly. However, this approximation is unable to find out exact cohesive energy, formation energy, bond dissociation energy and adsorption energies when compared with the experimental values. Moreover, it can also not calculate the exact band gap of semiconductor and insulator *[130]*.

1.5.3.5. Generalized Gradient Approximation (GGA)

Generalized gradient approximation (GGA) has been proposed as LDA approximation is unable to find out some of the important properties of the materials. In case of the GGA, electron density gradient is used for the calculation of the exchange correlation functional. Here, the exchange correlation functional is written as equation 1.24,

$$E_{xc}^{GGA} = \int d^3r\, n(\boldsymbol{r})\, \mathcal{E}_{xc}^{GGA}\left(n(\boldsymbol{r}), \nabla n(\boldsymbol{r})\right) \tag{1.24}$$

where, $\mathcal{E}_{xc}^{GGA}\left(n(\boldsymbol{r}), \nabla n(\boldsymbol{r})\right)$ is the exchange-correlation energy per electron gradient. This GGA approximation is useful for the systems, where density varies very rapidly. Moreover, it is found to provide accurate results during calculation of the total, cohesive, formation, and adsorption energies along with correct determination of lattice parameters etc. In this context, the most commonly used GGA approximation is developed by Perdew, Burke and Ernzerhof known as GGA-PBE functional. In this functional, the exchange energy of the system can be evaluated as follows,

$$E_x^{PBE} = \int d^3r \, n(\boldsymbol{r}) \, \mathcal{E}_x^{PBE}\big(n(\boldsymbol{r}), s(\boldsymbol{r})\big) \tag{1.25}$$

In the equation 1.25, the PBE exchange energy is the product form of the enhancement factor F_x^{PBE} and the LDA exchange as shown in equation 1.26.

$$\mathcal{E}_x^{PBE}\big(n(\boldsymbol{r}), s(\boldsymbol{r})\big) = \mathcal{E}_x^{LDA}\big(n(\boldsymbol{r})\big) * F_x^{PBE}\ \big(s(\boldsymbol{r})\big) \tag{1.26}$$

Moreover, some other GGA approximations are also available for the calculation of the exchange correlation energy of the system e.g. Perdew and Wang (PW91), revised PBE, PBEsol etc. *[131-133]*.

1.5.3.6. Projector Augmented Wave (PAW) Method

The electronic nature of a system is not same as core electrons and valence electrons positions are different from the nuclei i.e. the electronic wave function behaves differently for the core and valance electrons. The wave function of the core electrons oscillates very rapidly, whereas the wave function for the valence electrons are very smooth. In general, the valence electrons are represented by the plane wave basis set, which are conventional basis set. However, the plane wave basis sets are not considered for the core region electrons because of complex wave function. Therefore, the partial wave expansion is used for the description of the electrons, which are in the augmented region and the method is known as the projector augmented-wave method (PAW) *[135-137]*.

This method is based on the linear transformation operator (T). Here, all the electron wave functions Ψ_{n} are transferred to a pseudo wave function

$\widetilde{\Psi}_n$ and the pseudo wave function $\widetilde{\Psi}_n$ will be a function of the original electron wave functions Ψ_n as follows,

$$|\Psi_n\rangle = T|\widetilde{\Psi}_n\rangle \tag{1.27}$$

In the equation 1.27, T is the transformation operator. Here, both the wave functions $\widetilde{\Psi}_n$ and Ψ_n can be denoted by the linear combination of partial waves for each augmentation regions.

$$|\Psi_n\rangle = \sum_i c_i|\phi_i\rangle \tag{1.28}$$

$$|\widetilde{\Psi}_n\rangle = \sum_i c_i|\tilde{\phi}_i\rangle \tag{1.29}$$

Therefore, the transformation operator T is wriiten as equation 1.30,

$$T = 1 + \sum_i(|\phi_n\rangle - |\tilde{\phi}_n\rangle)\langle\tilde{p}_i| \tag{1.30}$$

where, $\langle\tilde{p}_i|$ is the projection function. This pseudopotential easily solves the problems for the core electrons, and can transform the rapidly oscillating wave function to a smooth wave function. This is a highly useful method for the investigation of the properties of the solid state materials. Moreover, the PAW method has also been combined with the ultra-soft pseudopotentials and linear augmented-plane-wave features. In this thesis, we have used the PAW method, which is combined with the Vienna *ab-initio* simulation package (VASP) *[138]*.

1.5.4. Dispersion in Density Functional Theory

All the above discussed cases are unable to provide the details of the dispersion, which is dependent on interactions at distance R. In general, the Coulombic interaction and exchange interactions are dependent on the electron transition density of the fragments which are interacting.

$$E_{Disp}^{(2)} = \sum_{ia} \sum_{jb} \frac{(ia|jb)[(ia|jb)-(ja|ib)]}{\varepsilon_a + \epsilon_b - \varepsilon_i - \varepsilon_j} \qquad (1.31)$$

Here, addition of all the particles hole excitation between orbitals $i \rightarrow a$ and $j \rightarrow b$ is localized on A and B fragments, respectively. Moreover, E is the corresponding energy of the orbital. These excitations are not present for standard DFT. Therefore, DFT is unable to calculate the long-range dispersion interaction *[139]*. In most of these cases dispersion correction performs empirical corrections. However, the highly useful dispersion correction method is the Grimme's DFT-D_n method. The general for for this Grimme's DFT-D_n is as follow *[140]*,

$$E_{Disp}^{DFT-D} = -\sum_{AB} \sum_{n=6,8,10\ldots} S_n \frac{C_n^{AB}}{R_{AB}^n} f_{damp}(R_{AB}) \qquad (1.32)$$

Here, C_n^{AB} is the dispersion coefficient for AB, R_{AB} is the distance between A and B, S_n is the adjusted correction for the repulsion *[141]* and $f_{damp}(R_{AB})$ is double counting effect of correlation used at intermediate distances *[142]*.

In this thesis, we have used Grimme's DFT-D3 for most of the DFT calculations, which considers the triplets atoms for three body effects. This dispersion effect does not change any molecular property i.e. wave function, but contributes on the basis of the atomic forces, which can give different geometry during optimization of the system with respect to the non-correction based optimization.

1.5.5. Other Computational Tools

In this thesis, some other computational tools have also been used along with the VASP package to understand the properties of the solid state materials, such as Ab initio molecular dynamics (AIMD) simulation, nudged elastic band (NEB) method, Bader charge analysis, etc. All of these have been discussed one after another for more detail.

1.5.5.1. *Ab initio* Molecular Dynamics (AIMD) Simulation

In practical work, different reactions are performed in different temperature and it is highly essential to find out the effect of temperature on the considered solid state material. In this context, Ab initio molecular dynamics (AIMD) simulation is a highly useful computational technique for the investigation of the effects of the temperature on the dynamical behavior of the considered material. In case of the classical molecular dynamics (CMD) atomic forces are obtained from the generated model potentials, whereas in AIMD atoms use the forces obtained from the DFT calculations *[143]*. However, computational cost of the AIMD simulation is very high, therefore, the uses of this AIMD simulation is limited to very few number of atoms. In this thesis, all the AIMD simulations have been performed by the canonical ensemble (NVT) at different temperature with a time step of 1 femtosecond. Moreover, the control of the temperature is done by the Nosé thermostat model *[144]*.

1.5.5.2. Nudged Elastic Band (NEB) Method

The kinetic nature and diffusion pathways of the reaction are two important factors in chemistry. And, can be find out by the NEB method, which is implemented in VASP in the area of theoretical chemistry and condensed matter physics. This method finds the saddle point of the minimum energy path (MEP) between the reactant and product of a reaction. In this method the harmonic approximation of transition state theory (hTST) *[145]* is used and the rate constant of the reaction for the transition around the saddle points is denoted as follows,

$$k^{hTST} = \frac{\prod_i^{3N} v_i^{init}}{\prod_i^{3N-1} v_i^{\ddagger}} e^{-(E^{\ddagger}-E^{init})/k_B T} \tag{1.33}$$

In the equation 1.33, $E^{\ddagger}$ and E^{init} are the energies of the saddle point and initial state i.e. reactant, and v_i^{init} and $v_i^{\ddagger}$ are the normal mode of frequencies for initial state and the saddle point, respectively. In general, NEB optimizes a number of intermediates within reactant and product. This intermediate optimization is done by adding spring forces along the band between images. In our calculations, we have used a code developed by Henkelmann for the formation of the images *[146]*.

1.5.5.3. Bader Charge

In Bader charge analysis, molecules are divided into the atoms for the calculation of the charges of the atoms within the molecules. This process is based on the Bader partitioning scheme *[147]*, where electronic charge density is considered for the analysis. Moreover, the partitioning of the density is determined by the 2-D surface, where density of the charge is in the minimum perpendicular to the surface i.e. zero-flux surfaces. By the calculation of the Bader charge analysis, one can easily determine the multipole moments of interacting atoms or molecules.

In this thesis, we have used Henkelman group developed algorithm for the calculation of the Bader atomic charges of the molecules *[148]*. This algorithm is very fast which operates on the basis of the charge density grid. Moreover, it is presented for the decomposition of electronic charge density of the molecule into its atomic contributions.

1.6. References

1. Larcher D., Tarascon J. (2015), Towards greener and more sustainable batteries for electrical energy storage, Nat. Chem. 7, 19-29 (DOI: 10.1038/nchem.2085)
2. Müller-Buschbaum, P. (2017), Solar Technologies go Hybrid, Adv. Energy Mater. 7, 1701977 (DOI: 10.1002/aenm.201701977)

3. Y. Lei (2016), Functional Nanostructuring for Efficient Energy Conversion and Storage, Adv. Energy Mater. 6, 1600461(DOI: 10.1002/aenm.201600461)
4. Zhao M., Yuan K., Wang Y., Li G., Guo J., Gu L., Hu W. Zhao H., Tang Z. (2016), Metal–organic frameworks as selectivity regulators for hydrogenation reactions, Nature, 539, 76-80 (DOI: 10.1038/nature19763)
5. Kim J. H., Choi S. Y., Choi M. Gershon T., Lee Y. S., Wang W., Shin B., Chung S. Y. (2016), Atomic scale observation of oxygen substitution and its correlation with hole transport barriers in $Cu_2ZnSnSe_4$ thin film solar cells, Adv. Energy Mater., 6, 1501902 (DOI: 10.1002/aenm.201501902)
6. Lee W. J., Lim J., Kim S. O. (2016), Nitrogen dopants in carbon nanomaterials: defects or a new opportunity? Small Methods, 1, 1600014 (DOI: 10.1002/smtd.201600014)
7. Lu J., Chen Z., Ma Z., Pan F., Curtiss L. A., Amine K. (2016), The role of nanotechnology in the development of battery materials for electric vehicles Nat. Nanotechnol., 11, 1031-1038 (DOI: 10.1038/nnano.2016.207)
8. Zhang G., Zhang Z. W., Peng H. J., Huang J. Q., Zhang Q. (2017) A toolbox for lithium–sulfur battery research: methods and protocols, Small Methods, 1, 1700134 (DOI: 10.1002/smtd.201700134)
9. Hu J., Jiang, Y., Cui S., Duan Y., Liu T., Guo H., Lin L., Lin Y., Zheng J., Amine K., Pan F. (2016), Lithium -ion batteries: 3D-printed cathodes of LiMn1−xFexPO4 nanocrystals achieve both ultrahigh rate and high capacity for advanced lithium-ion battery, Adv. Energy Mater., 6, 1670105 (DOI: 10.1002/aenm.201670105)
10. Krieger E. M., Cannarella J., Arnold C. B. (2013), A comparison of lead-acid and lithium-based battery behavior and capacity fade in off-grid renewable charging applications, Energy, 60, 492-500 (DOI: 10.1016/j.energy.2013.08.029)

11. May G. J., Davidson A., Monahov B. (2018), Lead batteries for utility energy storage : A review, J. Energy Storage, 15, 145–157 (DOI: 10.1016/j.est.2017.11.008)
12. Pierozynski B. (2011), On the low temperature performance of nickel-metal hydride (NiMH) batteries, Int. J. Electrochem. Sci., 6, 860 – 866
13. Paxton B., Newman J. (1997), Modeling of Nickel/Metal Hydride Batteries, J. Electrochem. Soc., 144, 11, 3818-3831 (DOI: 10.1149/1.1838098)
14. Yazvinskaya N. N., Galushkin1 N. E., Galushkin D. N., Galushkina I. A. (2016), Analysis of thermal runaway after effects in nickel-cadmium batteries, Int. J. Electrochem. Sci., 11, 10287 – 10295 (DOI: 10.20964/2016.12.44)
15. Zahran M. B. A., Atef A. (2006), Electrical and thermal properties of NiCd battery for low earth orbit satellite's applications, WSEAS Transactions on Electronics, 3, 340-348
16. Jin Y., Zhu B., Lu Z., Liu N., Zhu J. (2017), Challenges and recent progress in the development of Si anodes for lithium-ion battery, Adv. Energy Mater., 7, 1700715 (DOI: 10.1002/aenm.201700715)
17. Nam K. T., Kim D. W., Yoo P. J., Chiang C. Y., Meethong N., Hammond P. T., Chiang, Y. M., Belcher A. M. (2006), Virus-enabled synthesis and assembly of nanowires for lithium ion battery electrodes, Science, 312, 885 (DOI: 10.1126/science.1122716)
18. Whittingham M. S. (2004), Lithium batteries and cathode materials, Chem. Rev., 104, 4271-4302 (DOI: 10.1021/cr020731c)
19. Wang H., Dai H. (2013), Strongly coupled inorganic–nano-carbon hybrid materials for energy storage, Chem. Soc. Rev., 42, 3088-3113 (DOI: 10.1039/C2CS35307E)
20. Park K., Yu B. C., Goodenough J. B. (2016), Li_3N as a cathode additive for high energy density lithium-ion batteries, Adv. Energy Mater., 6, 1502534 (DOI: 10.1002/aenm.201502534)

21. Chae S., Kim N., Ma J., Cho J., Ko M. (2017), Lithium-ion batteries: one to one comparison of graphite blended negative electrodes using silicon nanolayer embedded graphite versus commercial benchmarking materials for high energy lithium-ion batteries, Adv. Energy Mater., 7, 1700071 (DOI: 10.1002/aenm.201700071)
22. Girishkumar G., McCloskey B., Luntz A. C., Swanson S., Wilcke W. (2010), Lithium−air battery: promise and challenges, J. Phys. Chem. Lett., 1 , 2193-2203 (DOI: 10.1021/jz1005384)
23. Wedepohl K. H. (1995), The composition of the continental crust, Geochim. Cosmochim. Acta, 59, 1217-1232 (DOI: 10.1016/0016-7037(95)00038-2)
24. Yaroshevsky A. A. (2006), Abundances of chemical elements in the earth's crust, Geochem. Int., 44, 48-55 (DOI: 10.1134/S001670290601006X)
25. Chiku M., Takeda H., Matsumura S., Higuchi E. (2015), Amorphous vanadium oxide/Carbon composite positive electrode for rechargeable aluminum battery, ACS Appl. Mater. Interfaces, 7, 24385-24389 (DOI: 10.1021/acsami.5b06420)
26. Chiku M., Takeda H., Yamaguchi Y., Higuchi E., Inoue H. (2013), Study on the electrolyte containing AlBr3 and KBr for rechargeable aluminum batteries, Int. J. Chem., 5, 1 (DOI: 10.5539/ijc.v5n4p1)
27. Muldoon C. B. B. J., Gregory T. (2014), Quest for nonaqueous multivalent secondary batteries: magnesium and beyond, Chem. Rev., 114, 11683-11720 (DOI: 10.1021/cr500049y)
28. Li Q., Bjerrum N. J. (2002), Aluminum as anode for energy storage and conversion: a review, J. Power Sources, 110, 1-10 (DOI: 10.1016/S0378-7753(01)01014-X)
29. Xia S., Zhang X.-M., Huang K., Chen Y.-L., Wu Y.-T. J. (2015), Ionic liquid electrolytes for aluminium secondary battery: Influence of organic solvents, J. Electroanal. Chem., 757, 167 (DOI: 10.1016/j.jelechem.2015.09.022)

30. U. S. Geological Survey, U.S. Geol. Surv. Miner. Commod. Summ., 2015, 196.
31. Fleischer M. (1953), Recent estimates of the abundances of the elements in the earth's crust, Geol. Surv. Circ., 285 (DOI: https://doi.org/10.3133/cir285)
32. High specific energy alumnium-ion rechargeable decentralized electricity generation sources, http://cordis.europa.eu/project/rcn/197095_en.html.
33. Yang H., Li H., Li J., Sun Z., He K., Cheng H.-M., Li F., (2019), The rechargeable aluminum battery: opportunities and challenges, Angew. Chem. Int. Ed., 58, 11978 (DOI: 10.1002/anie.201814031)
34. Leisegang T., Meutzner F., Zschornak M., Münchgesang W., Schmid R., Nestler T., Eremin R. A., Kabanov A. A., Blatov V. A., Meyer D. C. (2019), The aluminum-ion battery: A sustainable and seminal concept? Front. Chem., 7, 268 (DOI: 10.3389/fchem.2019.00268)
35. Lin M. C., Gong M., Lu B., Wu Y., Wang D. Y., Guan M., Angell M., Chen C., Yang J., Hwang B. J., Dai,H. (2015), An ultrafast rechargeable aluminium-ion battery, Nature, 520, 325-328 (DOI: 10.1038/nature14340)
36. Gale R. J., Osteryoung, R. A. (2015), Potentiometric investigation of dialuminum heptachloride formation in aluminum chloride-1-butylpyridinium chloride mixtures, Inorg. Chem., 18, 1603-1605 (DOI: 10.1021/ic50196a044)
37. Jiang T., Brym M. J. C., Dubé G., Lasia A., Brisard G. M. (2006), Electrodeposition of aluminium from ionic liquids: Part I-electrodeposition and surface morphology of aluminium from aluminium chloride ($AlCl_3$)–1-ethyl-3-methylimidazolium chloride ([EMIm]Cl) ionic liquids, Surf. Coatings Technol., 201, 1-9 (DOI: 10.1016/j.surfcoat.2005.10.046)
38. Jiang T., Chollier Brym M. J., Dubé G., Lasia A., Brisard G. M. (2006), E Electrodeposition of aluminium from ionic liquids: Part II -

studies on the electrodeposition of aluminum from aluminum chloride ($AlCl_3$) - trimethylphenylammonium chloride (TMPAC) ionic liquids, Surf. Coatings Technol., 201, 10-18 (DOI: 10.1016/j.surfcoat.2005.10.046)

39. Wang H., Gu S., Bai Y., Chen S., Zhu N., Wu C., Wuab F. (2015), Anion-effects on electrochemical properties of ionic liquid electrolytes for rechargeable aluminum batteries J. Mater. Chem. A, 3, 22677-22686 (DOI: 10.1039/c5ta06187c)
40. Weaving J. S., Orchard S. W. (1991), Experimental studies of transition metal chloride electrodes in undivided cells using molten NaAlCl4 electrolyte, J. Power Sources, 36, 537-546 (DOI: 10.1016/0378-7753(91)80079-D)
41. Chiku M., Takeda H., Matsumura S., Higuchi E., Inoue H. (2015), Amorphous vanadium oxide/carbon composite positive electrode for rechargeable aluminum battery, ACS Appl. Mater. Interfaces, 7, 24385-24389 (DOI: 10.1021/acsami.5b06420)
42. Wang H., Bai Y., Chen S., Luo X., Wu C., Wu F., Lu J., Amine K. (2015), Binder-free V2O5 cathode for greener rechargeable aluminum battery, ACS Appl. Mater. Interfaces, 7, 80-84 (DOI: 10.1021/am508001h)
43. Wang H., Bi X., Bai Y., Wu C., Gu S., Chen S., Wu F., Amine K., Lu J. (2017), Open-structured V2O5·nH2O nanoflakes as highly reversible cathode material for monovalent and multivalent intercalation batteries, Adv. Energy Mater., 7, 1602720 (DOI: 10.1002/aenm.201602720)
44. González J. R., Nacimiento F., Cabello M., Alcántara R., Lavela P., Tirado J. L. (2016), Reversible intercalation of aluminium into vanadium pentoxide xerogel for aqueous rechargeable batteries, RSC Adv., 6, 62157-62164 (DOI: 10.1039/C6RA11030D)
45. Wang W., Jiang B., Xiong W., Sun H., Lin Z., Hu L., Tu J., Hou J., Zhu H., Jiao S. (2013), A new cathode material for super-valentbattery

based on aluminium ionintercalation and deintercalation, Sci. Rep., 3, 3383 (DOI: 10.1038/srep03383)

46. Jiang J., Li H., Huang J., Li K., Zeng J., Yang Y., Li J., Wang Y., Wang J., Zhao J. (2017), Investigation of the reversible intercalation/deintercalation of Al into the novel Li3VO4@C microsphere composite cathode material for aluminum-ion batteries, ACS Appl. Mater. Interfaces, 9, 28486-28494 (DOI: 10.1021/acsami.7b07503)
47. Kaveevivitchai W., Huq A., Wang S., Park M. J., Manthiram A. (2017), Rechargeable aluminum-ion batteries based on an open-tunnel framework, Small, 13, 1701296 (DOI: 10.1002/smll.201701296)
48. Mei L., Xu J., Wei Z., Liu H., Li Y., Ma J., Dou S. (2017), Chevrel phase Mo_6T_8 (T = S, Se) as electrodes for advanced energy storage, Small, 13, 1701441 (DOI: 10.1002/smll.201701441)
49. Lee B., Lee H. R., Yim T., Kim J. H., Lee J. G., Chung K. Y., Cho B. W., Oha S. H. (2016), Investigation on the structural evolutions during the insertion of aluminum ions into Mo6S8 chevrel phase, J. Electrochem. Soc., 163, A1070-A1076 (DOI:10.1149/2.0011607)
50. Geng L., Scheifers J. P., Fu C., Zhang J., Fokwa B. P. T., Guo J. (2017), Titanium sulfides as intercalation-type cathode materials for rechargeable aluminum batteries, ACS Appl. Mater. Interfaces, 9, 21251-21257 (DOI: 10.1021/acsami.7b04161)
51. Wu Y., Gong M., Lin M. C., Yuan C., Angell M., Lu H., Wang D -Y., Zhang X. Yang J., Hwang B.-J., Dai H. (2016), 3D graphitic foams derived from chloroaluminate anion intercalation for ultrafast aluminum ion battery, Adv. Mater., 28, 9218-9222 (DOI: 10.1002/adma.201602958)
52. Chen F., Guo H., Liu Y., Huang T., Zheng B., Ananth N., Xu Z., Gao W., Gao C. (2017), A defect-free principle for advanced graphene cathode of aluminum-ion battery, Adv. Mater., 29, 1605958 (DOI: 10.1002/adma.201605958)

53. Zhang L., Chen L., Luo H., Zhou X., Liu Z. (2017), Large sized few layer graphene enables an ultrafast and long life aluminum-ion battery, Adv. Energy Mater., 7, 1700034 (DOI: 10.1002/aenm.201700034)
54. Wang S., Kravchyk K. V., Krumeich F., Kovalenko M. V. (2017), Kish graphite flakes as a cathode material for an aluminum chloride–graphite battery, ACS Appl. Mater. Interfaces, 9, 28478-28485 (DOI: 10.1021/acsami.7b07499)
55. Kravchyk K. V., Wang S., Piveteau L., Kovalenko M. V. (2017), Efficient aluminum chloride–natural graphite battery, Chem. Mater., 29, 4484-4492 (DOI: 10.1021/acs.chemmater.7b01060)
56. Jiao S., Lei H., Tu J., Zhu J., Wang J., Mao X. (2016), An industrialized prototype of the rechargeable Al/AlCl3-[EMIm]Cl/graphite battery and recycling of the graphitic cathode into graphene, Carbon, 109, 276-281 (DOI: 10.1016/j.carbon.2016.08.027)
57. Sun H., Wang W., Yu Z., Yuan Y., Wang S., Jiao S. (2015), A new aluminium-ion battery with high voltage, high safety and low cost, Chem. Commun., 51, 11892-11895 (DOI: 10.1039/C5CC00542F)
58. Rani J. V., Kanakaiah V., Dadmal T., Rao M. S., Bhavanarushi S. (2013), Fluorinated natural graphite cathode for rechargeable ionic-liquid based aluminum–ion battery, J. Electrochem. Soc., 160, A1781-A1784 (DOI: 10.1149/2.072310jes)
59. Yu X., Wang B., Gong D., Xu Z., Lu B. (2017), Graphene nanoribbons on highly porous 3D graphene for high capacity and ultrastable Al-ion batteries, Adv. Mater., 29, 1604118 (DOI: 10.1002/adma.201604118)
60. Childress A. S, Parajuli P., Zhu J., Podila R., Rao A. M. N. (2017), A Raman spectroscopic study of graphene cathodes in high-performance aluminum ion batteries, Nano Energy, 39, 69-76 (DOI: 10.1016/j.nanoen.2017.06.038)
61. Jung S. C., Kang Y.-J., Yoo D.-J., Choi J. W., Han Y.-K. (2016), Flexible few-layered graphene for the ultrafast rechargeable

aluminum-ion battery, J. Phys. Chem. C, 120, 13384-13389 (DOI: 10.1021/acs.jpcc.6b03657)

62. Hudak N. S. (2014), Chloroaluminate-doped conducting polymers as positive electrodes in rechargeable aluminum batteries, J. Phys. Chem. C, 118, 5203-5215 (DOI: 10.1021/jp500593d)
63. Sutoa K., Nakata A., Murayamab H., Hirai T., Yamaki J.-Y., Ogumi Z. (2016), Electrochemical properties of Al/vanadium chloride batteries with $AlCl_3$-1-Ethyl-3-methylimidazolium chloride electrolyte, J. Electrochem. Soc., 163, A742-A747 (DOI: 10.1149/2.0991605jes)
64. Wang S., Jiao S., Wang J., Chen H. S., Tian D., Lei H., Fang D. N. (2017), High-performance aluminum-ion battery with CuS@C microsphere composite cathode, ACS Nano, 11, 469 (DOI: 10.1021/acsnano.6b06446)
65. Yu Z., Kang Z., Hu Z., Lu J., Zhou Z., Jiao S. (2016), Hexagonal NiS nanobelts as advanced cathode materials for rechargeable Al-ion batteries, Chem. Commun., 52, 10427-10430 (DOI: 10.1039/C6CC05974K)
66. Wang S., Yu Z., Tu J., Wang J., Tian D., Liu Y., Jiao S. (2016), A novel aluminum-ion battery:Al/AlCl3/[EMIm]Cl/Ni3S2@graphene, Adv. Energy Mater., 6, 1600137 (DOI:10.1002/aenm.201600137)
67. Mori T., Orikasa Y., Nakanishi K., Kezheng C., Hattori M., Ohta T., Uchimoto Y. (2016), Discharge/charge reaction mechanisms of FeS2 cathode material for aluminum rechargeable batteries at 55°C, J. Power Sources, 313, 9-14 (DOI: 10.1016/j.jpowsour.2016.02.062)
68. Gao T., Li X., Wang X., Hu J., Han, F., Fan X., Suo L., Pearse A. J., Lee S. B., Rubloff G. W., Gaskell K. G., Noked M., Wang C. (2016), A rechargeable Al/S battery with an ionic liquid electrolyte, Angew. Chem. Int. Ed., 55, 9898–9901 (DOI: 10.1002/anie.201603531)

69. Cohn G., Ma L., Archer L. A. (2015), A novel non-aqueous aluminum sulfur battery, J. Power Sources, 283, 416 – 422 (DOI: 10.1016/j.jpowsour.2015.02.131)
70. Yu X., Manthiram A., (2017), Electrochemical energy storage with a reversible nonaqueous room-temperature aluminum–sulfur chemistry, Adv. Energy Mater., 7, 1700561 (DOI: 10.1002/aenm.201700561)
71. Yu X., Boyer M. J., Hwang G. S., Manthiram A. (2017), Room-temperature aluminum-sulfur batteries with a lithium-ion-mediated ionic liquid electrolyte, Chem., 4, 586–598 (DOI: 10.1016/j.chempr.2017.12.029)
72. Foljletier M., Armand M. (1979), Electrochemical method for characterization of graphite-aluminium chloride intercalation compounds, Carbon, 17, 427-429 (DOI: 10.1016/0008-6223(79)90059-9)
73. Yang G. Y., Chen L., Jiang P., Guo Z. Y., Wang W., Liu Z. P. (2016), Fabrication of tunable 3D graphene mesh networkwith enhanced electrical and thermal properties forhigh-rate aluminum-ion battery application, RSC Adv., 6, 47655-47660 (DOI: 10.1039/c6ra06467a)
74. Wang D.-Y., Wei C.-Y., Lin M.-C., Pan C.-J., Chou H.-J., Chen H.-A., Gong M., Wu Y., Yuan C., Angell M., Hsieh Y.-J., Chen Y.-H., Wen C. Y., Chen C.-W., Hwang B. -J., Chen C. C., Dai H. (2017), Advanced rechargeable aluminium ion battery with a high-quality natural graphite cathode, Nat. Commun., 8, 1-7 (DOI: 10.1038/ncomms14283)
75. Wu M. S., Xu B., Chen L. Q., Ouyang C. Y. (2016), Geometry and fast diffusion of AlCl4 cluster intercalated in graphite, Electrochim. Acta, 195, 158-165 (DOI: 10.1016/j.electacta.2016.02.144)
76. Jung S. C., Kang Y. J., Han Y. K. (2017), Commentson“ Geometry and fast diffusion of AlCl4 cluster intercalated in graphite [Electrochim.Acta195(2016)158–165]”, Electrochim. Acta, 223, 135–136 (DOI:10.1016/j.electacta.2016.11.040)

77. Kouvetakis J., Kaner R., Sattler M., Bartlett N. (1986), A novel graphite-like material of composition BC 3, and nitrogen−carbon graphites, J. Chem. Soc., Chem. Commun., 24, 1758−1759 (DOI: 10.1039/C39860001758)
78. Kuzubov A. A.; Fedorov A. S., Eliseeva N. S., Tomilin F. N., Avramov P. V., Fedorov D. G. (2012), High-capacity electrode material BC3 for lithium batteries proposed by ab initio simulations. Phys. Rev. B: Condens. Matter Mater. Phys., 85, 195415 (DOI: 10.1103/PhysRevB.85.195415)
79. King T. C., Matthews P. D., Glass H., Cormack J. A., Holgado J. P., Leskes M., Griffin J. M., Scherman O. A., Barker P. D., Grey C. P. et al. (2015), Theory and Practice: Bulk Synthesis of C3B and its H2- and Li-Storage Capacity, Angew. Chem. Int. Ed., 54, 5919−5923 (DOI: 10.1002/anie.201412200)
80. Stadie N. P., Billeter E., Piveteau L., Kravchyk K. V., Döbeli M. (2017), Kovalenko, M. V. Direct Synthesis of Bulk Boron-Doped Graphitic Carbon, Chem. Mater., 29, 3211 (DOI: 10.1021/acs.chemmater.7b00376)
81. Liu Y., Artyukhov V. I., Liu M., Harutyunyan A. R., Yakobson B. I. (2013), Feasibility of lithium storage on graphene and its derivatives, J. Phys. Chem. Lett., 4, 1737−1742 (DOI: 10.1021/jz400491b)
82. Joshi R. P., Ozdemir B., Barone V., Peralta J. E. (2015), Hexagonal BC3: A robust electrode material for Li, Na, and K ion batteries, J. Phys. Chem. Lett., 6, 2728−2732 (DOI: 10.1021/acs.jpclett.5b01110)
83. Mahmood J., Lee E. K., Jung M., Shin D., Choi H. J., Seo J. M., Jung S. M., Kim D., Li F., Lah M. S., Park N., Shin H. J., Oh J. H., Baek J. B. (2016), Two-dimensional polyaniline (C3N) from carbonized organic single crystals in solid state, Proc. Natl. Acad. Sci. U. S. A., 113, 7414 (DOI: 10.1073/pnas.1605318113)
84. Yang S., Li W., Ye C., Wang G., Tian H., Zhu C., He P., Ding G., Xie X., Liu Y., Lifshitz Y., Lee S. T., Kang Z., Jiang M. (2017), C3N—A

2D Crystalline, Hole Free, Tunable Narrow Bandgap Semiconductor with Ferromagnetic Properties, Adv. Mater., 29, 1605625 (DOI: 10.1002/adma.201605625)

85. Yu X. Y., Yu L., Lou X. W. (2016), Metal sulfide hollow nanostructures for electrochemical energy storage, Adv. Energy Mater, 6, 1501333 (DOI: 10.1002/aenm.201501333)
86. Nai J., Lou X. W. (2018), Hollow structures based on prussian blue and its analogs for electrochemical energy storage and conversion, Adv. Mater., 31, 1706825 (DOI: 10.1002/adma.201706825)
87. Yu L., Yu X. Y., Lou X. W. (2018), The design and synthesis of hollow micro-/ nanostructures: present and future trends, Adv. Mater., 30, 1800939 (DOI: 10.1002/adma.201800939)
88. Yang E., Ji H., Jung Y. (2015), Two-dimensional transition metal dichalcogenide monolayers as promising sodium ion battery anodes, J. Phys. Chem. C, 119, 26374−26380 (DOI: 10.1021/acs.jpcc.5b09935)
89. Er D., Li J., Naguib M., Gogotsi Y., Shenoy V. B. (2014), Ti3C2MXene as a high capacity electrode material for metal (Li, Na,K, Ca) ion batteries, ACS Appl. Mater. Interfaces, 6, 11173−11179 (DOI: 10.1021/am501144q)
90. Ishikawa R., Watanabe S., Yamazaki O., Oya T., Tsuboi N. (2019), Perovskite/graphene solar cells without a hole-transport layer, ACS Appl. Energy Mater, 2, 932−955 (DOI: 10.1021/acsaem.8b01606)
91. Xia H., Xu Q., Zhang J. (2018), Recent progress on two-dimensional nanoflake ensembles for energy storage applications, Nano-Micro Lett.,10, 66 (DOI: 10.1007/s40820-018-0219-z)
92. Guo G.-C., Wang D., Wei X.-L., Zhang Q., Liu H., Lau W.- M., Liu L.-M. (2015), First-principles study of phosphorene and graphene heterostructure as anode materials for rechargeable Li batteries, J. Phys. Chem. Lett., 6, 5002−5008 (DOI: 10.1021/acs.jpclett.5b02513)
93. Li Q., Yang J., Zhang L. (2018), Theoretical prediction of blue phosphorene/borophene heterostructure as a promising anode material

for lithium-ion batteries, J. Phys. Chem. C, 122, 18294−18303 (DOI: 10.1021/acs.jpcc.8b06742)

94. Mikhaleva N. S., Visotin M. A., Kuzubov A. A., Popov Z. I. (2017), VS2/graphene heterostructures as promising anode material for Li-oon batteries, J. Phys. Chem. C, 121, 24179−24184 (DOI: 10.1021/acs.jpcc.7b07630)
95. Shi L., Zhao T. S., Xu A., Xu J. B. (2016), Ab initio prediction of a silicene and graphene heterostructure as an anode material for Li- and Na-ion batteries, J. Mater. Chem. A, 4, 16377−16382 (DOI: 10.1039/C6TA06976B)
96. Sehrawat P., Julien C., Islam S.S. (2016), Carbon nanotubes in Li-ion batteries: A review, Mater. Sci. Eng. B, 213, 12–40 (DOI: 10.1016/j.mseb.2016.06.013)
97. Centi G., Perathoner P. (2011), Carbon nanotubes for sustainable energy applications, ChemSusChem, 4, 913 – 925 (DOI: 10.1002/cssc.201100084)
98. Tian L. X., Yang C.-L., Wang M.-S., Ma X. G. (2011), High-efficiency storage of lithium with single-walled carbon nanotubes, Comput. Theor. Chem., 966, 105–112 (DOI: 10.1016/j.comptc.2011.02.020)
99. Fang R., Chen K., Yin L., Sun Z., Li F., Cheng H.-M. (2019), Lithium batteries: the regulating role of carbon nanotubes and graphene in lithium-ion and lithium–sulfur batteries, Adv. Energy Mater., 31, 1970066 (DOI: 10.1002/adma.201970066)
100. Li S. N., Liu J. B., Liu B. X. (2016), First principles study of nanostructured TiS2 electrodes for Na and Mg ion storage, J. Power Sources, 320, 322-331 (DOI: 10.1016/j.jpowsour.2016.04.122)
101. Li Y. S., Ao X., Liao J.-L., Jiang J., Wang C., Chiang W. C. (2017), Sub-10-nm graphene nanoribbons with tunable surface functionalities for lithium-ion batteries, Electrochimica Acta, 249, 404–412 (DOI: 10.1016/j.electacta.2017.07.183)

102. Shoorideh, G., Ko B., Berry A., Divvela M. J., Kim Y. S., Li Z., Patel B., Chakrapani S., Joo Y. L. (2018), Harvesting interconductivity and intraconductivity of graphene nanoribbons for a directly deposited, high-rate silicon-based anode for li-Ion batteries, ACS Appl. Energy Mater., 1, 1106−1115 (DOI: 10.1021/acsaem.7b00228)

103. Cui C., Li M., Zhang X. (2018), In-situ cutting of graphene into short nanoribbons with applications to Ni-Zn batteries, 8, 5657 (DOI: 10.1038/s41598-018-23944-9)

104. Wang J., Ma F., Liang W., Sun M. (2017), Electrical properties and applications of graphene, hexagonal boron nitride (h-BN), and graphene/h-BN heterostructures, Mater. Today Phys., 2, 6−34 (DOI: 10.1016/j.mtphys.2017.07.001)

105. Shirodkar S. N., Kaxiras E. (2016), Li intercalation at graphene/ hexagonal boron nitride interfaces, Phys. Rev. B: Condens. Matter Mater. Phys., 93, 245438 (DOI: 10.1103/PhysRevB.93.245438)

106. Wang J., Ma F., Sun M. (2017), Graphene, hexagonal boron nitride, and their heterostructures: properties and applications, RSC Adv., 7, 16801−16822 (DOI:10.1039/C7RA00260B)

107. Oshima C., Itoh A., Rokuta E., Tanaka T., Yamashita K., Sakurai T. (2000), A hetero-epitaxial-double-atomic-layer system of monolayer graphene/monolayer h-BN on Ni(111), Solid State Commun., 116, 37−40 (DOI: 10.1016/S0038-1098(00)00268-4)

108. Giovannetti G., Khomyakov P. A., Brocks G., Kelly P. J., van den Brink J. (2007), Substrateinduced band gap in graphene on hexagonal boron nitride: ab initio density functional calculations, Phys. Rev. B: Condens. Matter Mater. Phys., 76, 073103 (DOI: 10.1103/PhysRevB.76.073103)

109. Fan Y., Zhao M., Wang Z., Zhang X., Zhang H. (2011), Tunable electronic structures of graphene/boron nitride heterobilayers, Appl. Phys. Lett., 98, 083103 (DOI: 10.1063/1.3556640)

110. Zhao Q., Nardelli M. B., Bernholc J. (2002), Ultimate strength of carbon nanotubes: A theoretical study, Phys. Rev. B, 65, 144105 (DOI: 10.1103/PhysRevB.65.144105)

111. Lee S. W., Yabuuchi N., Gallant B. M., Chen S., Kim B. S., Hammond P. T., Shao-Horn Y. (2010), High-power lithium batteries from functionalized carbon-nanotube electrodes, Nat. Nanotechnol., 5, 531–537 (DOI: 10.1038/nnano.2010.116)

112. Gao B., Bower C., Lorentzen J. D., Fleming L., Kleinhammes A., Tang X. P., Mcneil L. E., Wu Y., Zhou O. (2000), Enhanced saturation lithium composition in ball-milled single-walled carbon nanotubes, Chem. Phys. Lett., 327, 69–75 (DOI: 10.1016/S0009-2614(00)00851-4)

113. Gao B., Kleinhammes A., Tang X. P., Bower C., Fleming L., Wu Y., Zhou O (1999), Electrochemical intercalation of single-walled carbon nanotubes with lithium, Chem. Phys. Lett., 307, 153–157 (DOI: 10.1016/S0009-2614(99)00486-8)

114. Jiao H., Wang J., Tu J., Lei H., Jiao S. (2016), Aluminum-ion asymmetric supercapacitor incorporating carbon nanotubes and an ionic liquid electrolyte: Al/AlCl$_3$-[EMIm]Cl/CNTs, Energy Technol., 4, 1112–1118 (DOI: 10.1002/ente.201600125)

115. Licht S. (1997), A high capacity Li-ion cathode: The Fe(III/VI) super-iron cathode, J. Electrochem. Soc., 144, 133-136 (DOI: 10.3390/en3050960)

116. Arneson C., Wawrzyniakowski Z. D., Postlewaite J. T., Ma Y. (2018), Lithiation and delithiation processes in lithium–sulfur batteries from ab Initio molecular dynamics simulations, J. Phys. Chem. C, 122, 16, 8769-8779 (DOI: 10.1021/acs.jpcc.8b00478)

117. Ma Y., Garofalini S. H. (2017), Reactive molecular dynamics simulations of the conversion and reconversion reactions in Fef2 nanoparticles, J. Phys. Chem. C, 121, 15002−15007 (DOI: 10.1021/acs.jpcc.7b02412)

118. Ma Y., Garofalini S. H. (2012), Atomisticinsights into the conversion reaction in iron fluoride: A dynamically adaptive force field approach, J. Am. Chem. Soc., 134, 8205−8211 (DOI: 10.1021/ja301637c)

119. Guo, Y., Jin, H., Qi, Z., Hu, Z., Ji, H., Wan, L.-J. (2019), Carbonized-MOF as a sulfur host for aluminum–sulfur batteries with enhanced capacity and cycling life, Adv. Funct. Mater, 29, 1807676 (DOI: 10.1002/adfm.20180767)

120. Wang, Z., Wang, B., Yang, Y., Cui, Y., Wang, Z., Chen, B., Qian, G. (2015), Mixed-metal−organic framework with effective Lewis acidic sites for sulfur confinement in high-performance lithium−sulfur batteries, ACS Appl. Mater. Interfaces, 7, 20999−21004 (DOI: 10.1021/acsami.5b07024)

121. Hao G. P., Tang C., Zhang E., Zhai P.-Y., Yin J., Zhu W., Zhang Q., Kaskel S., (2017), Thermal exfoliation of layered metal–organic frameworks into ultrahydrophilic graphene stacks and their applications in Li–S batteries, Adv. Mater., 29, 1702829 (DOI:10.1002/adma.201702829)

122. Mao Y., Li G., Guo Y., Li Z., Liang C., Peng X., Lin Z., (2017), Foldable interpenetrated metal-organic frameworks/carbon nanotubes thin film for lithium–sulfur batteries, Nat. Commun., 8, 14628 (DOI: 10.1038/ncomms14628)

123. Zhou J., Li R., Fan X., Chen Y., Han R., Li W., Zheng J., Wang B., Li X., (2014), Rational design of a metal–organic framework host for sulfur storage in fast, long-cycle Li–S batteries, Energy Environ. Sci., 7, 2715-2724 (DOI:10.1039/C4EE01382D)

124. Born M., Oppenheimer J. (1927), Zur quantentheorie der molekeln, J. Ann. Physik, 84, 457 (DOI: 10.1002/andp.19273892002)

125. Hohenberg P., Kohn W. (1964), Inhomogeneous electron gas, Phys. Rev. B, 136, B864-B871 (DOI: 10.1103/PhysRev.136.B864)

126. Kohn W., Sham L. J. (1965), Self-consistent equations including exchange and correlation effects, Phys. Rev., 140, A1133-A1138 (DOI: 10.1103/PhysRev.140.A1133)

127. Xia B. Y., Wu H. B., Wang X., Lou X. W. (2013), Index facets and enhanced electrocatalytic properties, Angew. Chem. Int. Ed., 52, 12337-12340 (DOI: 10.1002/anie.201307518)

128. Martin, R. M. (2012), Electronic structure: basic theory and practical methods, Cambridge University press, ISBN: 9780511805769 (DOI: 10.1017/CBO9780511805769)

129. Ceperley D. M., Alder B. (1980), Ground State of the Electron Gas by a Stochastic Method, Phys. Rev. Lett., 45, 566-569 (DOI: 10.1103/PhysRevLett.45.566)

130. van de Walle A., Ceder G. (1999), Correcting over binding in local-density-approximation calculations, Phys. Rev. B, 59, 14992-15001 (DOI: 10.1103/PhysRevB.59.14992)

131. Perdew J. P., Burke K., Ernzerhof M. (1996), Generalized gradient approximation made simple, Phys. Rev. Lett., 77, 3865-3868 (DOI: 10.1103/PhysRevLett.77.3865)

132. Perdew J. P., Wang Y. (1992), Accurate and simple analytic representation of the electron-gas correlation energy, Phys. Rev. B, 45, 13244-13249 (DOI: 10.1103/PhysRevB.45.13244)

133. Perdew J. P., Ruzsinszky A., Csonka G. I., Vydrov O. A., Scuseria G. E., Constantin L. A., Zhou X., Burke K. (2008), Restoring the density-gradient expansion for exchange in solids and surfaces, Phys. Rev. Lett., 100, 136406 (DOI: 10.1103/PhysRevLett.100.136406)

134. Vanderbilt D. **(**1990), Soft self-consistent pseudopotentials in a generalized eigenvalue formalism, Phys. Rev. B, 41, 7892-7895 (DOI: 10.1103/PhysRevB.41.7892)

135. Blochl P. E. (1994), Projector augmented-wave method, Phys. Rev. B, 50, 17953-17979 (DOI: 10.1103/PhysRevB.50.17953)

136. Andersen, O. K. (1975), Linear methods in band theory, Phys. Rev. B., 12, 3060-3083 (DOI: 10.1103/PhysRevB.12.3060)

137. Hamann D. R., Schlüter M., Chiang C. (1979), Norm-conserving pseudopotentials, Phys. Rev. Lett., 43, 1494-1497 (DOI:10.1103/PhysRevLett.43.1494)

138. MillsG., Jónsson H. (1994), Quantum and thermal effects in H2 dissociative adsorption: Evaluation of free energy barriers in multidimensional quantum systems, Phys. Rev. Lett. 72, 1124. (DOI:10.1103/PhysRevLett.72.1124)

139. Grimme S., Antony J., Ehrlich S., Krieg H. (2010), A consistent and accurate ab initio parametrization of density functional dispersion correction (DFT-D) for the 94 elements H-Pu, J. Chem. Phys. 132, 154104 (DOI: https://doi.org/10.1063/1.3382344)

140. Grimme S. (2011), Density functional theory with Londondispersion corrections, WIREs Comput. Mol. Sci., 1, 211-228 (DOI: 10.1002/wcms.30)

141. Grimme S. (2004), Accurate description of van der Waals complexes by density functional theory including empirical corrections, J. Comput. Chem., 25, 1463-1473 (DOI:10.1002/jcc.20078)

142. Chai J. D., Head-Gordon M. (2008), Long-range corrected hybrid density functionals with damped atom-atom dispersion corrections, Phys. Chem. Chem. Phys., 10, 6615-6620 (DOI: 10.1039/B810189B)

143. Paquet E., Viktor H. L. (2018), Computational Methods for Ab Initio Molecular Dynamics, Advances in Chemistry, 2018, 14 pages (DOI: 10.1155/2018/9839641)

144. Nosé S. (1984), A unified formulation of the constant temperature molecular dynamics methods, J. Chem. Phys., 81, 511-519 (DOI: 10.1063/1.447334)

145. Mills G., Jónsson H. (1994), Quantum and thermal effects in H2 dissociative adsorption: Evaluation of free energy barriers in

multidimensional quantum systems, Phys. Rev. Lett. 72, 1124 (DOI: 10.1103/PhysRevLett.72.1124)

146. Henkelman G., Jonsson H. **(**2000), A climbing image nudged elastic band method for finding saddle points and minimum energy paths, J. Chem. Phys., 113, 9978-9985 (DOI: 10.1063/1.1329672)

147. Bader, R. F. W. (1994), Atoms in Molecules: A Quantum Theory; Oxford University Press: USA.

148. Henkelman G., Arnaldsson A., Jonsson H. (2006), A fast and robust algorithm for Bader decomposition of charge density, Comput. Mater. Sci., 36, 354-360 (DOI: 10.1016/j.commatsci.2005.04.010)

Chapter 2

Staging Mechanism of $AlCl_4^-$ into Graphite and Electron-Rich Graphite-like Electrode and Investigation of the Stability vs. Voltage for Aluminium Batteries

2.1. Introduction

With the growing demand for energy, it is highly necessary to look for energy sources which are more abundant and can meet high-energy demand *[1, 2]*. In this context, metal-ion batteries have attracted more attention than other energy sources due to their several advantages like concise size, high efficiency, and simple maintenance *[3, 4]*. Metal ion batteries have emerged as a source for various energy applications, from personal electronics to grid storage *[5]*. Electrical energy storage in the form of metal ion batteries can be used not only as a back-up energy source for the national electric grid and smart grids, but also as an energy source for transportation, defence, or space research applications, as well as for small-scale devices such as electronics, medical implants and power tools *[6]*. Different kinds of metal ion batteries like Li- *[7–11]*, Na- *[12–14]*, Mg- *[15, 16]*, and Zn-ion *[17, 18]* batteries have been developed in recent years. Among these metal-ion batteries, some have emerged as very good potential candidates due to their high energy densities, better discharge voltage, and high capacities *[7]*. However, there are still some limitations in terms of safety, production cost, availability, and reactivity (interaction of electrode with electrolyte at a higher voltage) *[19–23]*. In recent years, Al rechargeable batteries have emerged as a promising type of rechargeable battery due to their high abundance, high gravimetric density, lower reactivity and easier handling *[24]*. Unlike Li and Na-ion batteries, an Al rechargeable battery involves three-electron-redox properties during the electrochemical charging and discharging processes leading to high capacity *[25, 26]*. Besides, the volumetric charge storage capacity of aluminium metal is 8.0 Ah/cm^3, which is about four times the capacity of lithium 2.06 Ah/cm^3 *[27]*. Even having such desirable characteristics, there are still some limitations regarding suitable cathode materials, electrolytes *[28]*, inadequate cycle life, degradation of cathode materials, and decreasing capacity rate. Moreover, Al rechargeable batteries undergo corrosion in aqueous electrolyte and form a passive surface layer on the electrode that reduces the cell voltage and efficiency *[24, 29, 30]*. But in recent years, with the advancement of Al-ion batteries, various cathode materials in ionic liquid/$AlCl_3$ electrolyte have been studied theoretically and experimentally, such as V_2O_5 *[31]*, fluorinated natural graphite *[32]*, VO_2 *[33]*, and polymers *[27]* that do not suffer from passive layer formation and have less internal resistance compared to aqueous electrolyte-based batteries. But, all of them suffer from low capacity, low voltage or short cycle life.

Very recently, Lin et al. developed a new kind of Al-ion battery where graphite is used as a cathode with an Al anode and an ionic liquid electrolyte that contains 1-ethyl-3-methylimidazolium chloride ([EMIm]Cl) and anhydrous aluminium chloride ($AlCl_3$) *[34]*. It is accepted that the chloroaluminate anion ($AlCl_4$) reversibly intercalates and deintercalates between the graphite layers in aluminium ion batteries, unlike other metal ion batteries where the intercalating guest is a metal cation. Graphite being the redox amphoteric material can form both donor and acceptor graphite intercalation compounds (GICs) by electrochemical intercalation of cations and anions respectively *[35, 36]*. Alkali metal cation intercalated graphite compounds are well reported as negative electrodes in metal-ion batteries and are well studied both theoretically and experimentally *[37]*. There is also a broad range of different anions capable of forming acceptor-type GICs, such as fluoride guest species (PF_6, AsF_6, BF_4), chlorides ($AlCl_4$, $GaCl_4$ or $TaCl_6$), and oxides (SO_4, NO_3, ClO_4) *[38]*. Lin et al. have demonstrated the reversible intercalation of $AlCl_4$ using XPS and high spatial resolution AES elemental mapping *[34]*. During the discharge process, on the anode side, $AlCl_4$ reacts with the Al electrode to generate Al_2Cl_7 and electrons while on the cathode side, deintercalation of $AlCl_4$ occurs from the $AlCl_4$ intercalated graphite layers. The reverse reactions take place during the charging process. The complete reactions during charging and discharging can be written as,

$$\mathrm{Al} + 7\mathrm{AlCl}_4^- \rightleftharpoons 4\mathrm{Al}_2\mathrm{Cl}_7^- + 3\mathrm{e}^- \qquad \text{(anode)} \qquad (2.1)$$

$$\mathrm{C}_\mathrm{n}[\mathrm{AlCl}_4] + \mathrm{e}^- \rightleftharpoons \mathrm{C}_\mathrm{n} + \mathrm{AlCl}_4^- \qquad \text{(cathode)} \qquad (2.2)$$

In the discharge process $3e^-$ are transferred to the external circuit leading to high capacity. The reaction mechanism is quite different from that of typical Li-ion batteries; firstly, because the electrolyte anions also participate in the reaction and, secondly, because a large anion $AlCl_4^-$ intercalates between the layers compared to the small Li^+ during the charging process instead of during discharging. The proposed battery takes about a minute for complete charging, and that ultrafast naturemust be related to the intercalationmechanism, migration of $AlCl_4^-$ within the layers and the nature of the bonding between graphite and $AlCl_4^-$.

Therefore, apart from the intercalation mechanism, there is a lack of clear understanding about the intercalation capacity and intercalated species. Some recent studies have talked about the planar geometry of $AlCl_4$ *[39]*, whereas other reports say that the tetrahedral geometry is more stable inside graphite *[40, 41]*. Therefore, the geometry of $AlCl_4$ during intercalation and deintercalation has yet to be understood. Moreover, none of the previous studies have paid attention to the systematic staging mechanism of $AlCl_4$ intercalation, which is undoubtedly the deciding factor behind the ultrafast nature of the Al-ion battery. In fact, it is very necessary to examine the stability of the graphite electrode, diffusion of $AlCl_4$, theoretical capacity and voltage profile diagrams of $AlCl_4$ intercalation into graphite, which are very much dependent on the different staging patterns of $AlCl_4$. Therefore in the present study, we have investigated the intercalation mechanism by considering the staging manner of $AlCl_4$ intercalation into the graphite electrode, which is a characteristic feature of GICs. First-principles calculations are performed for a systematic study of the structure, stability, electronic properties, theoretical capacity and average voltage of the $AlCl_4$ intercalated graphite electrodes. In addition, Ab Initio Molecular Dynamics (AIMD) *[42]* has been performed to investigate the thermal stability of graphite after $AlCl_4$ intercalation at the temperature range of 300 to 600 K. Furthermore, a detailed investigation has been done to understand the diffusion pathways of $AlCl_4$ inside the graphite layer. Our results are compared with the recent experimental findings on Al-ion batteries. We have studied the $AlCl_4$ intercalated graphite system to understand the anion intercalation mechanism in graphite, which in turn can be very helpful for designing better electrodes in the near future.

Another concept, which is quite interesting to increase the efficiency of electrode materials in batteries, is the introduction of some changes on elemental (doping the sites or replacing with other substitute cathode material). One of such strategy is doping N sites in graphite structure, which can alter electronic structure and increase the reactivity by producing locally accessible active sites in the graphite lattice as result of hybridization of nitrogen lone pair electrons with the p electrons in the carbon *[43, 44]*. The presence of N atoms increases the number of electrons in a system and behaves as n-type (electron-donating) dopants *[45]*. Nitrogen doped graphene has a tendency to release electrons easier than graphene, which could be beneficial for Al battery that works on the mechanism of charge transfer from system to the intercalant $AlCl_4$. Therefore, choosing a nitrogen doped graphene cathode can benefit the overall stability of the system by stabilizing the $AlCl_4$ inside the cathode. Very recently, a 25 % N doped graphite like, C_3N has been synthesized possessing a two-dimensional (2D) AB-stacked layered structure *[46, 47]*. The structure of 2D C_3N is quite interesting, because it contains uniformly distributed nitrogen atoms at 1,4-positions for multi-functionality. C_3N having the similar structural and stacking pattern like graphite, could act as a potential cathode for Al battery. Moreover, a systematic knowledge associated with an electron rich system and Al batteries are still in their early stages, therefore it would be interesting to examine the effect of electronically rich C_3N electrode (compared to graphite) on the stability and electrochemical properties of Al battery and to check how the dimensional change in C_3N influences the output in Al batteries. In this regard, as proposed by Shi et al. multi-scale computational methods can play very important role in determining the crucial properties such as crystal structure, electronic/ionic properties, activation energy, and the electrochemical characteristics, such as capacity, thermal and cycle stability which determine the applicability of secondary battery energy storage materials *[48]*. Therefore, we have used First principle calculations to carry out a detailed study on 3D C_3N to compare the influence of electron rich N and electron deficient B containing systems on the stability and voltage of Al batteries.

In this paper, we investigate the applicability of C_3N electrode as a suitable cathode material for Al batteries. We have initiated the study by examining the intercalation behaviour and stabilization of $AlCl_4$ intercalant in C_3N system, followed by the analysis of electronic properties such as total and projected density of states, charge density difference and Bader charge calculations. We have also performed the detailed investigation to evaluate the diffusion behaviour of $AlCl_4$ in the corresponding systems. The voltage profile diagram of C_3N system has been discussed in details to determine the voltage and storage capacities. In addition, we have conducted a detailed discussion on how the working mechanism of Al battery is different from metal-ion batteries and why the output voltage is dependent on the stability of $AlCl_4$ intercalated cathode. We have also discussed about the electrode systems which can certainly increase or decrease the output voltage and what are the parameters based on which, we can chose an electrode for maximum stability and voltage.

2.2. Computational Details

The first-principles calculations are performed using a projected augmented wave (PAW) method as implemented in the Vienna Ab initio Simulation Package (VASP) *[49, 50]*. The exchange-correlation potential is described by using the generalized gradient approximation of Perdew-Burke-Ernzerhof (GGA-PBE) *[51]*. The Projector augmented-wave (PAW) method is employed to treat interactions between ion cores and valance electrons *[52]*. An energy cutoff of 470 eV is used for the plane waves. All the optimized structures are obtained by fully relaxing both atomic and lattice positions until the Hellmann-Feynman forces on all atoms are smaller than 0.012 eV/Å. The Brillouin zone is sampled with Gamma centered k-point grid of 6 × 6 × 2 for unit cell and 2 × 2 × 2 for supercell calculations of graphite, whereas for a 2 × 2 × 1 supercell of C_3N the Brillouin zone is sampled with a 2 × 2 × 2 Monkhorst-Pack grid. All the systems are fully optimized, where the convergence criteria for total energy are set at 10^{-3} eV. The van der Waals interactions play a very crucial role for the layered systems. Therefore, we have used the DFT-D3 approach for the correction of van der Waals interactions that adds the vdW correction for potential energy and interatomic forces *[53]*. The optimized interlayer spacing of pristine graphite (3.34 Å) is in close agreement with experimentally reported value (3.33 Å) *[54]*.

The Ab Initio Molecular Dynamic Simulation (AIMD) is performed using the canonical ensemble with fixed volume, temperature, and particle number. AIMD simulations are performed at 300-600 K with the time step of 1 fs for 5 ps time steps. For the calculation of electronic structure, the Brillouin zone is sampled with a k-point grid of 19 × 19 × 11 for graphite and 11 × 11 × 11 for C_3N. The 3 × 3 × 1 supercell of 36 carbon atoms is used for both DOS and AIMD calculations in graphite. Bader charge analysis is performed *[55-57]* with the help of the Henkelman programme *[58]* using near-grid algorithm refine-edge method to understand the charge transfer process between the atoms. We have calculated the diffusion barriers using the nudged elastic band (CI-NEB) method *[59]*. The minimum energy paths (MEP) are initialized by considering six image structures between fully optimized initial and final structural geometries, and the energy convergence criteria of each image is set to 10^{-3} eV.

Activation barriers are calculated by the energy differences between the transition and initial states and the entropy corrections and Zero point energy (ZPE) correction are included while calculating the diffusion barriers. The ZPE is calculated as: $\mathrm{ZPE} = \sum_i \frac{h\nu_i}{2}$, where h is Planck's constant and ν_i is vibrational frequency. The ZPE of the system is calculated by considering only the degrees of freedom of intercalated $\mathrm{AlCl_4}$.

2.3. Results and Discussion

2.3.1. Section A: Graphite Electrode

2.3.1.1. $AlCl_4$ Intercalation

We start by examining the most stable geometry of $AlCl_4$ in graphite because there are still controversies about the exact geometry of $AlCl_4$ in graphite based systems, whether it is planar or tetrahedral (Figure 2.1(a-b)) *[39, 40]*. In graphite, the tetrahedral $AlCl_4$ structure is 0.73 eV more stable than the square-planar $AlCl_4$ structure. This is very much in agreement with our gas phase calculations too, where we find that the tetrahedral $AlCl_4$ molecule is 0.88 eV more stable than the square planar geometry. In addition, the tetrahedral geometry is well supported by a recent theoretical study, where various dispersion-corrected DFT methods such as DFT-D2, DFT-D3(zero- damping), vdW-DF(revPBE), vdW-DF(optPBE), vdW-DF2 (PW88), vdW-DF2 (PW86b), and vdW-DF2 (PW86R) have been employed to confirm that the tetrahedral $\mathrm{AlCl_4}$ intercalated graphite is more stable by 0.36–0.77 eV, when compared to the planar $\mathrm{AlCl_4}$ intercalated graphite *[41]*. Therefore, the tetrahedral $AlCl_4$ intercalated structure is considered for our further study. It is observed that the tetrahedral geometry of $AlCl_4$ gets slightly distorted after intercalation as <Cl-Al-Cl bond angle is in the range of 104.42°-113.42° and Al-Cl bond length is in the range of 2.158-2.159 Å compared to 109.27° <Cl-Al-Cl bond angle and 2.151 Å Al-Cl bond length in the tetrahedral geometry of $AlCl_4$. Such kind of distortion is also observed experimentally in $AlCl_4$

intercalated graphite structure *[34]*. The distortion is the outcome of the van der Waals forces between the graphite layers, reducing the graphite interlayer distance by compressing the size of tetrahedral $AlCl_4$, giving it a distorted geometry. Further, our calculations suggest that the ABA stacking pattern of graphite does not change even after $AlCl_4$ intercalation, and such retention of ABA stacking is also observed in another acceptor type of GICs *[60]*.

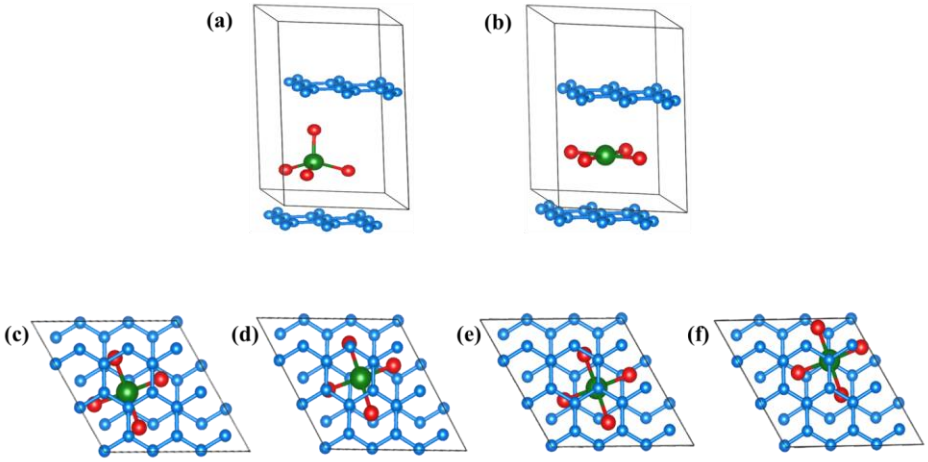

Figure 2.1: $AlCl_4$ intercalated geometries: (a) tetrahedral and (b) planar. Optimized structures (top view) of $AlCl_4$ intercalation at four different intercalation sites: (c) B1, (d) B2, (e) H, and (f) T. Al and Cl atoms are shown by green and red spheres, respectively, and the graphite carbon atoms are shown by blue spheres.

We have carefully investigated all possible intercalation sites for $AlCl_4$ in graphite. We find that there are four preferential intercalation sites (Figure 2.1c-f) for $AlCl_4$ in graphite: (i) bridge 1 (B1), (ii) bridge 2 (B2), (iii) hexagonal (H), and (iii) top (T) sites. In the B1 site, the Al atom occupies at the bridge position of a C-C bond, whereas in the B2 site, the Al occupies the bridging position between two non-bonded carbon atoms (Figure 2.1d). The H and T sites refer to the centre of the hexagons (C_6) and top position of a C atom, respectively. Our relative energetic study shows (Table 2.1) that all four sites are very much favourable and very close in energy. Among these, B2 is the most stable site for $AlCl_4$ intercalation.

Table 2.1: Geometrical parameters for the $AlCl_4$ intercalated structure at different sites; relative energy (ΔE) with respect to the B2 site, C-C bond lengths (d^{C-C}) and interlayer spacing between graphite layers.

Sites	ΔE (eV)	d^{C-C} (Å)	d (Å)
B1	0.009	1.423	8.639
B2	0.000	1.423	8.594
H	0.013	1.422	8.633
T	0.006	1.423	8.622

The AIMD simulations are carried out to check the thermal stability of $AlCl_4$ intercalated graphite structures (Figure 2.2). For graphite system, we have considered the most stable B2-site bounded $AlCl_4$ to carry out the simulations. First, the structure is heated at 300 K with the time scale of 1 fs for 5 ps, and we observe that the AB stacking of graphite as well as the distorted tetrahedral geometry of $AlCl_4$ stay unaltered with little shifting of the intercalated $AlCl_4$ from the B2 site. Furthermore, simulation using an NVT ensemble is carried out at 400, 500 and 600 K with a time step of 1 fs for 5 ps. However, the results of the simulations at 500 K and 600 K are little different in terms of the relative position of $AlCl_4$ and graphite host layers. The distorted tetrahedral geometry of $AlCl_4$ is preserved but the orientation and position of intercalation site of $AlCl_4$ is now slightly changed from the optimized structure. The bond lengths and bond angles do not change significantly. Therefore, we can say that AIMD simulations (300-600 K) do not change the geometry of $AlCl_4$ and thus the structure does not undergo any other minima. Other than this, another important point can also be concluded from this study that the $AlCl_4$ diffusion could be fast into graphite as $AlCl_4$ does not involve any change in the nature of chemical bonding of $AlCl_4$.

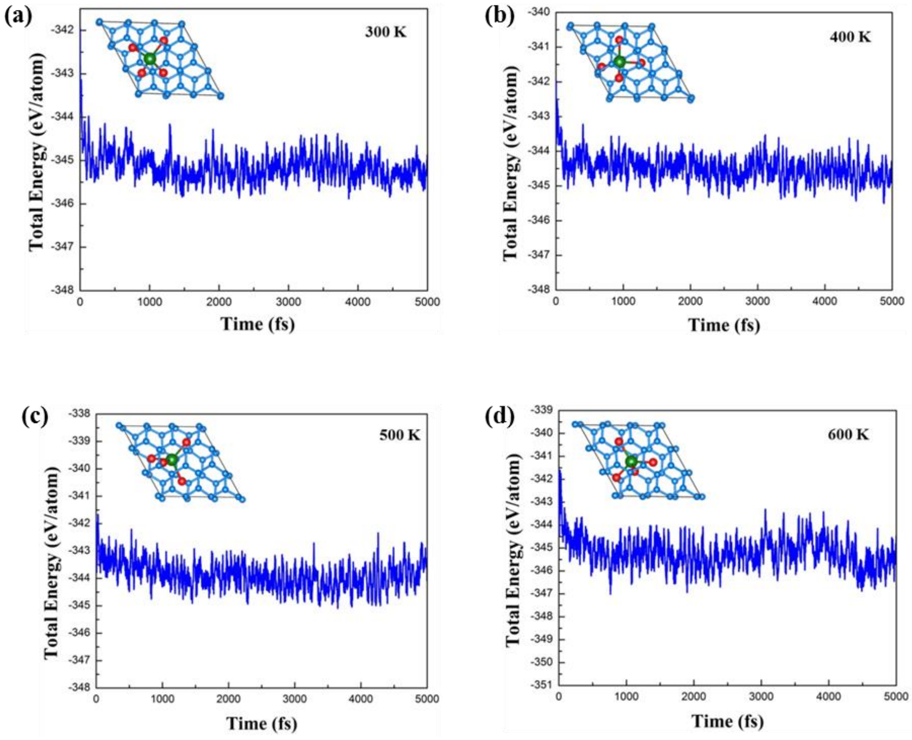

Figure 2.2: Molecular dynamics simulation analysis at different temperatures as a function of time step and the obtained structures, (a) 300K, (b) 400 K, (c) 500 K and (d) 600 K.

2.3.1.2. System Setup

In Al-ion battery, it has been reported that anions ($AlCl_4$) are being intercalated and deintercalated during the charging and discharging process, respectively *[34]*. The characteristic feature of GICs is a staging phenomenon where intercalant forms periodic sequence between graphite layers *[35-36, 61]*. It is well known that the process of guest species intercalation does not proceed in every layer simultaneously. The guest molecule (anions) must overcome the cohesive van der Waal attraction between the adjacent graphite layers. In addition, the electrostatic repulsion between different intercalant layers also forces further intercalation within the same graphite gallery contrary to further intercalation into another unoccupied layer *[62-65]*. Based on these forces, different stages (extent of intercalation) are expected to occur during the charging and discharging process, and this has been observed experimentally *[66-68]*, and also studied theoretically *[69]*. The different stages of intercalation into graphite can be represented with respect to the number of graphite layers or the number of empty galleries between the intercalant guest layers *[35, 70]*, where stage-n corresponds to the structure with n number of graphite layer or n-1 number of empty galleries in between the intercalated layers. Therefore in stage-1, all galleries are occupied. Interestingly, such different stages have been reported for anion intercalation in graphite *[38, 70]*, and stage-4, in particular, is observed for $AlCl_4$ ion intercalation in graphite *[34]*. For this, we have modelled four different stages (stage 1-4) of intercalation as shown in Figure 2.2, and four different concentrations are used for each of these stages. A 6 × 6 × 2 supercell of 288 carbon atoms is constructed for stage-1 (Figure 2.3a), stage-2 (Figure 2.3b) and stage-4 (Figure 2.3d) calculations and another one with a 6 × 6 × 3 supercell of 432 atoms is constructed for stage-3 (Figure 2.3c) calculations. It should be noted that we have modelled our system by taking the pure graphite AB stacked structure having four and six graphitic layers with 3.34 Å interlayer spacing, which is completely different from few layers of graphene (where the AB stack is not maintained) *[40]*. Therefore, we believe that the graphite model is more appropriate to mimic the real experimental observations in ultrafast Al-ion battery.

Four different $AlCl_4$ stoichiometries are considered for the stage-1 intercalation, which can form $[(\mathrm{AlCl}_4)_n\mathrm{C}_{288}]$ with n values of 4, 8, 12, 16. Therefore, within the each gallery of stage-1, the minimum and maximum numbers of intercalated $AlCl_4$ molecules are **1** and **4**. Hence, the minimum and maximum numbers of $AlCl_4$ molecules that can be intercalated in stage-1 are $[(\mathrm{AlCl}_4)_4\mathrm{C}_{288}]$ and $[(\mathrm{AlCl}_4)_{16}\mathrm{C}_{288}]$. Two more representations are also considered in between the minimum and maximum values, which are $(\mathrm{AlCl_4})_8\mathrm{C}_{288}$ and $(\mathrm{AlCl_4})_{12}\mathrm{C}_{288}$ respectively. Similarly different $AlCl_4$ stoichiometries are considered containing the formula unit of $(\mathrm{AlCl_4})_\mathrm{n}\mathrm{C}_{288}$, with n values of 2, 4, 6 to 8 for stage-2 and n = 1, 2, 3, 4 for stage-4. Stage-3 is studied with a formula unit of $(\mathrm{AlCl_4})_\mathrm{n}\mathrm{C}_{432}$, where n values are 2, 4, 6, 8.

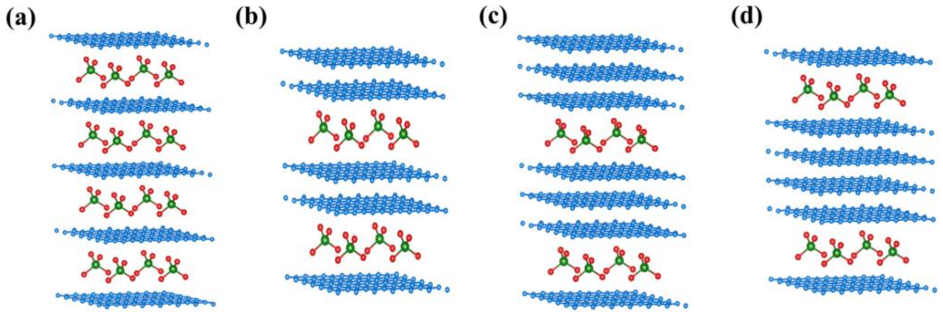

Figure 2.3: Schematic representations (side view) of the optimized structures of the four different intercalated stages: (a) stage-1, (b) stage-2, (c) stage-3 and, (d) stage-4.

2.3.1.3. Binding Energy

To evaluate the stability of the intercalated compounds, we have first calculated the binding energy of $AlCl_4$ using the relation,

$$\mathrm{E_{binding}} = \frac{\mathrm{E_{[AlCl_4]_xCathode}} - \mathrm{E_{Cathode}} - \mathrm{xE_{AlCl_4}}}{\mathrm{x}} \qquad (2.3)$$

where $\mathrm{E_{[AlCl_4]_xCathode}}$, $\mathrm{E_{Cathode}}$ and $\mathrm{E_{AlCl_4}}$ are the total energy of $AlCl_4$ intercalated graphite, bulk graphite and $AlCl_4$. Here, a more negative binding energy value indicates that intercalation of $AlCl_4$ into graphite is favourable (exothermic) and $AlCl_4$ tends to bind with graphite. The binding energies calculated for all stages are listed in Table 2.1 for graphite.

We observe that for graphite intercalation compounds, the calculated binding energies are negative for all the cases except for the first intercalation step, suggesting that the intercalation into graphite is not favourable at lower $AlCl_4$ concentrations, whereas it becomes easier with the increase in concentration of $AlCl_4$. This is because of the comparatively large size of $AlCl_4$ than that of graphite interlayer spacing which makes the intercalation of $AlCl_4$ difficult. At lower concentrations the interaction between intercalated $AlCl_4$ and host graphite layers is not strong enough to overcome the van der Waals attractive forces between the graphite layers. At higher concentrations intercalation becomes easier in the already increased graphite host galleries. Our calculated binding energy of intercalated species clearly supports the results of intercalation voltage where also the first intercalation step is different from the subsequent steps of $AlCl_4$ intercalation. It can be seen that the $AlCl_4$ binding energy of bulk graphite increases with increase in the number of $AlCl_4$, whereas for the given concentration of $AlCl_4$ the higher order stage (stage-3, stage-4) is more stable than lower order stage (stage-1, stage-2). The calculated binding energies are consistent with previously reported results for Al-ion battery with graphite electrode *[40]*. A good cathode material for Al-ion battery requires a fair binding strength of $AlCl_4$ as well as suitable interlayer spacing. Therefore, graphite, having both characteristics makes it a potential cathode for Al-ion batteries. The average interlayer distance is calculated as follows,

$$\text{Average interlayer distance} = \frac{total\ height\ of\ the\ stage{-}n\ having\ n{-}1\ galleries\ or\ n\ graphite\ layers}{n{-}1\ galleries\ or\ n\ graphite\ layers} \tag{2.4}$$

Table 2.2: Average interlayer distance (Å), Voltage (V), and binding energy (eV) per $AlCl_4$ for all stages with different stoichiometries considered. The average interlayer distance term is used to differentiate the total height of the four stages considered upon intercalation.

Stages	No of $AlCl_4$	Interlayer distance	Voltage	Binding energy
stage-1	4	8.36	3.47	+0.39
	8	8.52	2.30	-0.77
	12	8.69	2.00	-1.08
	16	8.76	1.87	-1.20
stage-2	2	6.07	3.64	+0.57
	4	6.09	2.04	-1.04
	6	6.12	1.75	-1.31
	8	6.11	1.66	-1.41
stage-3	2	5.11	3.91	+0.24
	4	5.16	2.13	-0.94
	6	5.20	1.74	-1.33
	8	5.22	1.65	-1.43
stage-4	1	4.72	3.66	+0.59
	2	4.74	2.01	-1.07
	3	4.76	1.65	-1.42
	4	4.78	1.58	-1.50

2.3.1.4. Staging Mechanism

We have first studied the structural deformation in graphite due to the $AlCl_4$ intercalation. We find that the interlayer spacing in $AlCl_4$ intercalated graphite is larger than that in pure graphite. In fact, the interlayer spacing of pure graphite (3.34 Å) is lower than the size of $AlCl_4$ (5.28 Å) *[71]*. Therefore, as $AlCl_4$ intercalates, the interlayer spacing profoundly increases during the first intercalation step and increases in a limited range on further intercalations. This is because the first intercalation step is a kind of opening process for the partially closed galleries of graphite to accommodate large anions and once the graphite is activated, further intercalation becomes smooth into the expanded graphite galleries. Similar kind of opening process is observed for intercalation of others anions vastly studied in dual-ion cells *[68]*. The average gallery height expansion in graphite after $AlCl_4$ intercalation is in the range of 150% - 160% that is comparable with expansion values (130%-140%) of PF_6 and TFSI [bis(trifluoromethane)sulphonamide] anions intercalation respectively *[72]*. For the reported ultrafast Al-ion battery, it is experimentally obtained that the increase in interlayer spacing upon $AlCl_4$ intercalation does not result into exfoliation phenomenon, yet the battery shows current density of 4,000 mA/g possessing more than 7,500 cycles without capacity decay *[34]*. The average optimized interlayer spacing for all four stages with different $AlCl_4$ stoichiometries has been given in Table 2.1. The expansion of interlayer spacing is advantageous for the easier diffusion of $AlCl_4$ into graphite. For stage-1, the structure deformation is maximum as $AlCl_4$ intercalates into each gallery. For other stages, stage-2, 3 and 4, each graphite gallery does not act as a host for $AlCl_4$ leading to small structural deformation. It is minimum for stage-4, where $AlCl_4$ intercalates after every three empty galleries.

The distance between two graphite host layers i.e the intercalant gallery height (d_i), nearly remains constant (8.36 - 8.76 Å) for all the stages with the varying $AlCl_4$ concentrations. Previous studies on GICs *[73]* justify our results that for the given intercalant, d_i remains essentially independent of the intercalation stages. However, the experimentally reported value of d_i is very low 5.7 Å *[34]*. In fact, the van der Waals size of $AlCl_4$ can be approximated to 5.95 Å *[74]* and the minimum C-Cl distance should be 3 Å to avoid the substantial energy increase due to the repulsive exchange interaction between the Cl ions of intercalated $AlCl_4$ and graphite layers

[40, 75]. Therefore, from the $AlCl_4$ size and C-Cl distance, it is clear that the intercalant gallery height should be more than 8 Å. Furthermore, such large interlayer distances for $AlCl_4$ intercalated graphite are also supported by the XRD results. Interestingly, the gallery heights (8.36 - 8.76 Å) and C-Cl distances (3.15 - 3.25 Å) of our calculations agree well with the previous observations *[40]*. In comparison with the intercalant gallery height value of 9.5 Å for $AlCl_3$ intercalation into graphite *[71]*, the observed values for $AlCl_4$ intercalation are lower, which can be because of the distortion of tetrahedral geometry of $AlCl_4$ after intercalation. The average interlayer spacing is in the range of 4.75 Å that is very close to the experimentally obtained 4.55 Å average interlayer spacing *[76]*. Moreover, Lin et al. has also observed a stage-4 graphite intercalation compound where host gallery that intercalates $AlCl_4$ in distorted tetrahedral geometry has an interlayer spacing of 5.70 Å *[34]*.

To further verify the staging mechanism of anion intercalation, we have compared the relative stabilities of stage-1, stage-2 and stage-4 having same $AlCl_4$concentration. The optimized structures of the most stable configurations for stage-1, stage-2 and stage-4 are shown in Figure 2.4 with relative energetics. The stage-4 system containing four $AlCl_4$ is the most stable, followed by stage-2 and stage-1. This observation supports the fact that the intercalation into a single gallery is favoured until it reaches its maximum occupancy before starting to fill adjacent empty galleries. This behaviour can be understood on the basis of ion-ion Coulomb repulsion and interlayer van der Waals attraction. We believe that during intercalation, the intercalant overcomes the cohesive van der Waals attractions between two adjacent graphite layers. If the Coulomb repulsion is smaller compared to the energy requirement for the expansion of interlayer spacing, intercalation occurs within the same gallery instead of further intercalation into other unoccupied galleries. Similar staging patterns have been reported for TFSI anion intercalation into graphite where ex-situ and in-situ X-ray diffraction techniques have been used for systematic study of the staging transitions and compositions of the staged phases at different cut-off potentials and temperatures and it has been observed that the first intercalation stage starts with stage-4 followed by stage-3 and then the maximum intercalated stage-1 reached with stoichiometry ranging between C_{19}TFSI and C_{20}TFSI *[68, 70]*. However, during de-intercalation reverse-staging transitions occurs from stage-1 to stage-2 followed by stage-3. In addition, experimental and theoretical studies of alkali metal intercalation also verify this type of sequential staging pattern *[63-67]*. Therefore, we believe that among the four considered stages, the intercalation of $AlCl_4$ will first start into stage-4, and the filling continues in stage-4 until it reaches its maximum occupancy. Further intercalation forms stage-3, followed by stage-2 and stage 1 as inferred by the relative energy calculations.

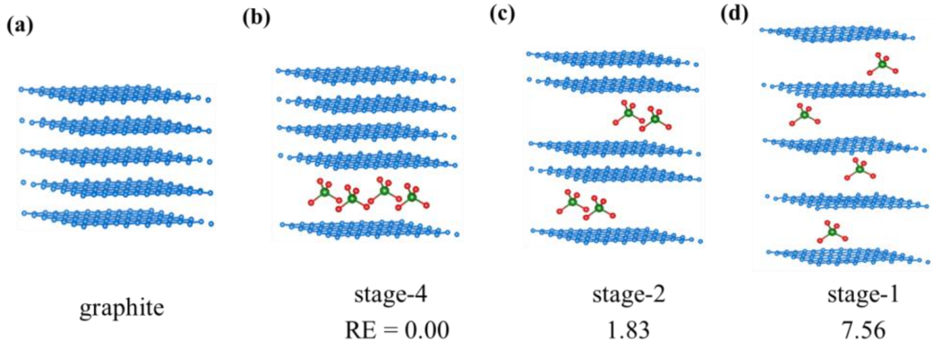

Figure 2.4: Systematic illustration of staging mechanism for (a) graphite, (b) stage-4, (c) stage-2 and, (d) stage-1. RE (in eV) is the relative energetics for same concentrations.

2.3.1.5. Electronic Properties

To gain a deep understanding on the nature of interaction between $AlCl_4$ and graphite, we have calculated the total density of states (TDOS) and projected density of states (PDOS) for $AlCl_4$ intercalated graphite (Figure 2.5). $AlCl_4$ intercalated graphite is metallic in nature with considerable electronic states at the Fermi level and the metallic nature arises due to the contribution of *2p* orbitals of C. There is some overlap between the *3p* electronic states of Cl and *2p* electronic states of C and this suggests that some interaction occurs between the carbon atoms of graphite and Cl atoms of intercalated $AlCl_4$.

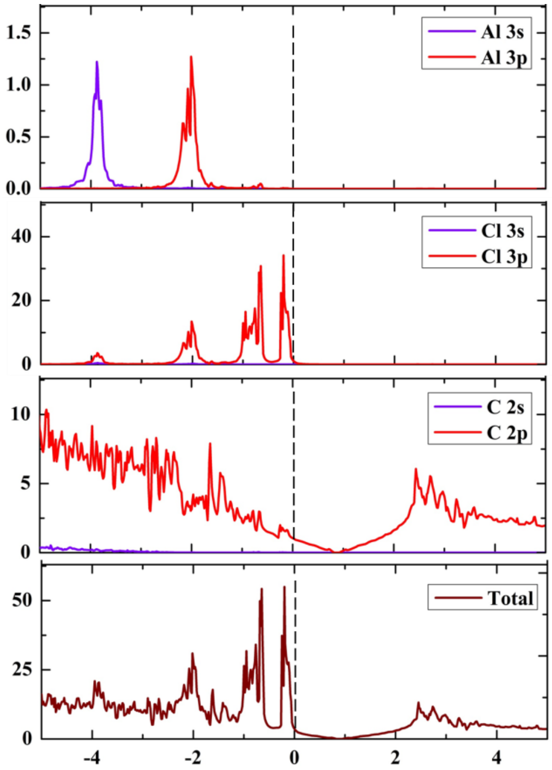

Figure 2.5: Total DOS and projected DOS of (a) $AlCl_4$ intercalated graphite. The Fermi level is set at zero.

Bader charge analysis is performed to obtain the net charges on Al, Cl of $AlCl_4$ and C of graphite. The net accumulated charge after $AlCl_4$ intercalation in graphite is compared with the charge on gaseous $AlCl_4$. The net negative charge on each Cl atom increases from -0.587 |e| to -0.801 |e| and the net positive charge on Al atom (+2.347 to +2.345) practically remains the same. Our optimized structures show that each Cl atom of $AlCl_4$ optimizes nearly at the center of hexagons and it is in close proximity of six carbon atoms. Each of the six C-atoms equally contributes towards the charge transfer after $AlCl_4$ intercalation and the negative charge on each C-atoms decreases from -0.009 |e| to +0.028 |e|. The net charge transfer (+0.214 |e|) suggests a significant amount of electron transfer from nearest C-atoms to one Cl atom. The Bader charge analysis is qualitatively consistent with our PDOS calculations. Therefore, one $AlCl_4$ molecule accepts an amount of -0.856 |e| from the neighbouring carbon atoms. This clearly indicates about the electrochemical oxidation of graphite by $AlCl_4$ intercalation, and confirming the intercalation of $AlCl_4$ during the charging process which is in good agreement with the Lin et al. work where they have shown using XPS that the 284.8 eV C 1s peak of pristine graphite broadened to a shoulder at higher energy of 285.9 eV after the charging process.[34] Lin et al. further confirmed the anionic intercalation (chloroaluminate anion) using AES elemental mapping. These observations give a very valuable insight into the desirable properties of the future electrode materials that can be developed for Al-ion batteries. We predict layered materials with the similar properties like graphite but with more electron donating ability can easily undergo oxidation upon anion intercalation and can secure stable oxidized structures. Therefore, it might be interesting to study n-doped graphene analogues or more electron efficient graphene analogues as cathode materials for Al-ion batteries.

2.3.1.6. Diffusion Pathways of $AlCl_4$

The ultrafast charging rate is one of the important characteristic of the proposed graphite based Al-ion battery. The charging/discharging rate of batteries is related to the diffusion of the intercalated species through the electrodes. Therefore, to study the $AlCl_4$ diffusion mechanism in graphite electrode, we have calculated barriers for finding out the energetically favourable diffusion paths. Here, similar to Li diffusion in Li-GICs, the diffusion of $AlCl_4$ is restricted to the 2-dimensional path along the ab plane *[77, 78]*. As previously studied the B2 site is comparatively stable compared to other sites. Hence, in this work four favourable diffusion paths have been studied from a B2 site to a neighboring B2 site. The first diffusion path, path 1is from site B2 to its nearest B2 site passing through a B1 site (B2-B1-B2), the second is path 2 from site B2 to another nearest site B2 via site H (B2-H-B2) and the third, path 3 involves the $AlCl_4$ diffusion from site B2 to another B2 site via site T (B2-T-B2). The fourth diffusion path is path 4 that covers the distance from one B2 site to other B2 site. Figure 2.6 shows the four diffusion paths investigated and the diffusion barriers involved. The results clearly demonstrate that the diffusion energy barrier is very small for all the four cases ~ 0.01 eV, which could be due to the large interlayer spacing (8.26 to 8.76 Å) of host graphite galleries that helps in the trouble free diffusion of $AlCl_4$. Secondly, throughout the diffusion process of $AlCl_4$ inside graphite, there is no change in the chemical bonding of $AlCl_4$ and the third driving force could be the comparable binding energy of $AlCl_4$ at the different binding sites along the diffusion path, helping in lowering the diffusion barrier for $AlCl_4$ diffusion. The results of our study justify the experimentally observed ultrafast charging process of graphite based Al-ion battery.

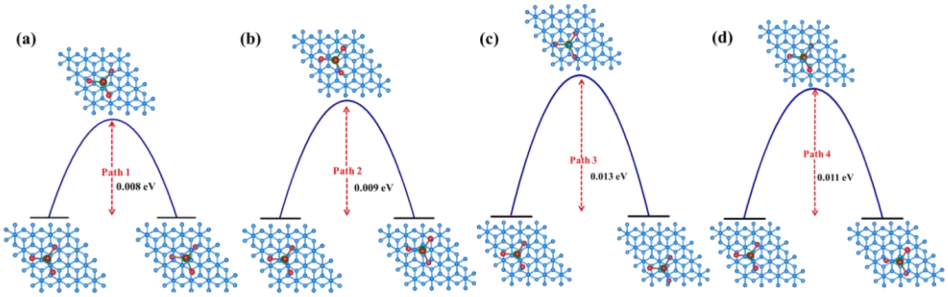

Figure 2.6: Schematic representation of the diffusion barriers for the four pathways, where (a) to (d) correspond to Path 1 to Path 4.

2.3.1.7. Electrochemical Properties

The open circuit voltage (OCV) is a valuable measure of battery's performance. It can be calculated using the following complete cell reaction,

$$3/x[(AlCl_4)_xC_n] + (EMI^+AlCl_4^-) + Al \leftrightarrow 3/x(C_n) + 4(EMI^+Al_2Cl_7^-) \tag{2.5}$$

where, x is the number of $AlCl_4$ intercalated into graphite. The average voltage (V) during this process can be written in the form of change in Gibbs free energy (ΔG_f) *[79, 80],*

$$V = -\frac{\Delta G_f}{zF} \tag{2.6}$$

where, z and F are the number of valence electrons during the intercalation process and the Faraday constant, respectively; ΔG_f is the change in Gibbs free energy during the intercalation process which is defined as,

$$\Delta G_f = \Delta E + P\Delta V - T\Delta S \tag{2.7}$$

$P\Delta V$ is on the order of 10^{-5} eV and the term $T\Delta S$ is comparable to 26 meV at room temperature; thus, the entropy and pressure terms are negligible *[79]*. ΔG_f is then approximately equal to the total energy change (ΔE) involved in system, which is defined as,

$$\Delta E = \left\{{}^{3}\!/_{x}\, E_{C_n} + 4E_{[EMI^{+}Al_2Cl_7^{-}]}\right\} - \left\{{}^{3}\!/_{x}\, E_{[(AlCl_4)_x C_n]} + 4E_{[EMI^{+}AlCl_4^{-}]} + E_{Al}\right\} \tag{2.8}$$

where $E_{[(AlCl_4)_x C_n]}$, $E_{[EMI^{+}AlCl_4^{-}]}$ and $E_{[EMI^{+}Al_2Cl_7^{-}]}$ are the total energies of the $AlCl_4$ intercalated graphite system, $EMI^{+}AlCl_4^{-}$ and $EMI^{+}Al_2Cl_7^{-}$, respectively. E_{Al} is the total energy of a single Al atom in a bulk BCC structure and E_{Cn} is the total energy of graphite system. $E_{[EMI^{+}AlCl_4^{-}]}$ and $E_{[EMI^{+}Al_2Cl_7^{-}]}$ are calculated by optimizing the $EMI^{+}AlCl_4^{-}$ and $EMI^{+}Al_2Cl_7^{-}$, respectively as a molecular species due to non-availability of their crystal structures.

Therefore the average voltage for the system is given by,

$$V = \left(\frac{\{{}^{3}/_{x} E_{[(AlCl_4)_x C_n]} + 4E_{[EMI^+ AlCl_4^-]} + E_{Al}\} - \{{}^{3}/_{x} E_{C_n} + 4E_{[EMI^+ Al_2Cl_7^-]}\}}{z} \right) \tag{2.9}$$

The voltage profile diagrams (Figure 2.7) represent the variation of average voltage with the weight percentage (wt%) of $AlCl_4$ for all four stages (stages 1-4) and the calculated value for different stoichiometries are listed in Table 2.1. It is very interesting to find that for each stage the average voltage (total energy change of the system) of first intercalation step is quite large than the other successive intercalation steps. We believe that the reason could be the interlayer spacing of pure graphite (3.34 Å), which is far lower than the size of $AlCl_4$ (5.27 Å) and therefore the graphite layer resists the first intercalation and large energy change is involved to achieve the interlayer distance in the range of $AlCl_4$, resulting into a comparatively higher voltage value (Figure 2.7). Other successive intercalation steps become easy in the already expanded graphite host galleries, resulting into subsequently constant voltage values. Similar observations are also reported for TFSI and PF_6 anions intercalation in graphite, where the voltage profile of first intercalation cycle differs from the next intercalation cycles *[70, 72]*. This kind of activation behaviour is attributed to an opening process of graphite galleries. Besides, such electrode expansion is also observed for TFSI and PF_6 anion intercalation after the first cycle *[70]* and similar outcomes are shown by Lin et al. using XPS and AES techniques for $AlCl_4$ intercalation.

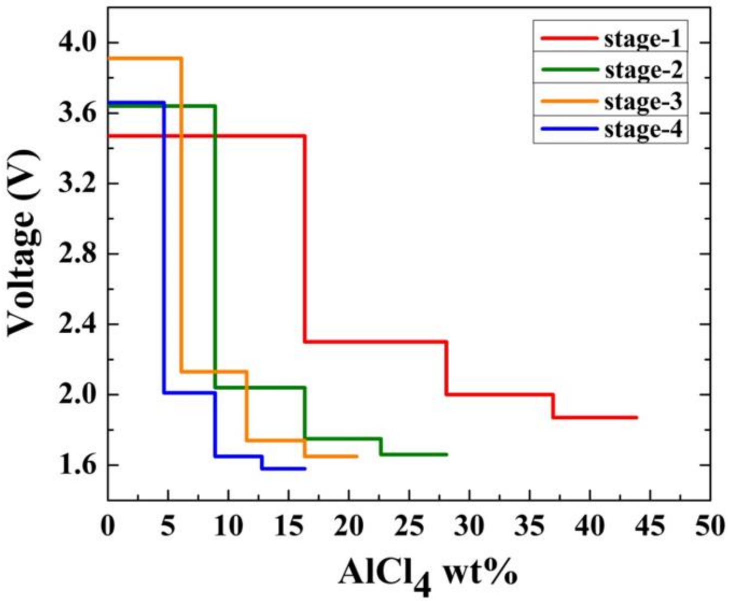

Figure 2.7: Voltage profile diagram of $AlCl_4$ intercalated (a) graphite and (b) BC_3 systems against Al/Al^{3+}.

From the Figure 2.7, we find that the $AlCl_4$ average voltage varies in a range of 1.58 V to 3.91. The voltage averaged over 0 to 44 wt% of $AlCl_4$ is 2.01 V, 2.13 V, 2.04 V and 2.3 V for stage-4, stage-3, stage-2 and stage-1, respectively. These values are in very much agreement with the experimentally reported voltage plateaus of 2.25-2.00 V and 1.90-1.50 V.

We further calculated the specific capacity of each stage using the following expression,

$$C = \frac{nxF}{M_f} \tag{2.10}$$

where, n is the number of electrons transferred per formula unit, x is the number of $AlCl_4$ intercalated, F is the Faraday constant, and M_f is the mass of formula unit. Our calculated gravimetric capacities for the stage-1 and stage-4 GICs are 69.62 and 25.94 mAh/g, which is very close to experimentally reported values of 65 and 30 mAh/g at the end and the start of the charging process, respectively. These observations support our work that initial charging process starts with stage-4 graphite intercalation system showing 25.94 mAh/g capacity and reaches its completely charged state that is stage-1 intercalated graphite with 69.62 mAh/g capacity at the end of charging process. Therefore, based on our findings and other experimental observations, we predict that it will be better to explore graphite-like layered materials as cathode materials which have larger interlayer spacing and greater flexibility. The intercalation and deintercalation of $AlCl_4$ will become easy in such large host galleries, which can increase the efficiency and life time of the battery because the structural deformation will be negligible and even the first intercalation step could be an easier one.

2.3.2. Section B: C_3N Electrode

2.3.2.1. Stability

Previous experimental and theoretical studies have reported that out of the two possible $AlCl_4$ geometries (tetrahedral and planar), $AlCl_4$ preferentially intercalates with the tetrahedral geometry into the bulk phase graphite *[81]*, and BC_3 electrodes *[82]*, 2D flexible graphene electrodes *[83]*, and 1D carbon nanotubes (CNT) *[84]*. Here also C_3N follows the same trend and preferentially stabilize the tetrahedral geometry of $AlCl_4$ than the planar structure (Figure 2.8). The relative energy difference between tetrahedral and planar $AlCl_4$ intercalated is 0.95 eV and 0.88 eV for C_3N bulk and bilayer, respectively, which is more than that in graphite (0.73 eV), and BC_3 (0.68 eV) *[82]*, which indicates towards the stronger binding of tetrahedral $AlCl_4$ in 3D and 2D C_3N phases. On considering all the possible binding sites, we observe that only four sites, B-NC, B-CC, T-NC, and T-CC are stable for $AlCl_4$ binding in C_3N bulk as shown in Figure 2.8. The binding energy ($\mathrm{E_{binding}}$) is calculated using the equation,

$$\mathrm{E_{binding}} = (\mathrm{E_{C_3N+AlCl_4}} - \mathrm{E_{C_3N}} - \mathrm{E_{AlCl_4}}) \qquad (2.11)$$

where, $E_{C_3N+AlCl_4}$ and E_{C_3N} are the total energies of C_3N phase bulk with and without $AlCl_4$, respectively and E_{AlCl_4} is the total energy of one $AlCl_4$ molecule in the box. According to this definition, a more negative binding energy would suggest a thermodynamically favourable intercalation of $AlCl_4$. We observe that the T-NC with -2.45 eV binding energy. Moreover, in case of structurally rigid C_3N bulk, the interaction between intercalant $AlCl_4$ and C_3N layers leads to the change in the structural preference of C_3N bulk form AB to AA stacking (Figure 2.8) on intercalation of $AlCl_4$ having a interlayer spacing of 8.23 Å. Overall, we can say that C_3N is able to provide overall stability of the battery system with continuous charge/discharge cycles.

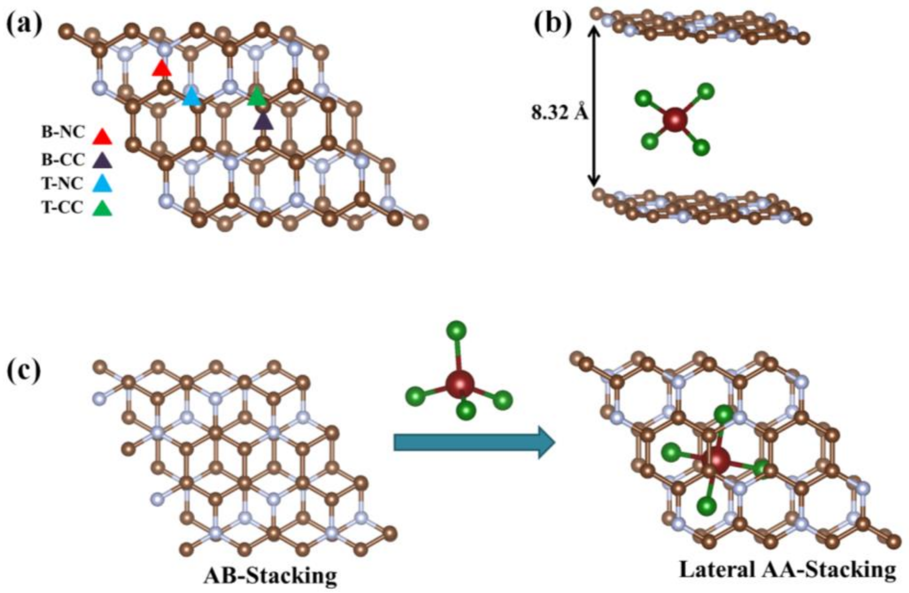

Figure 2.8: Schematic representation of possible adsorption sites and $AlCl_4$ (tetrahedral) intercalated structures: (a) bulk C_3N (3D), (b) C_3N bilayer (2D), and (c) C_3N-NT (1D).

2.3.2.2. Electronic Structure

Apart from the binding study, the electronic properties are also important to get deeper insight into the electrode material for a battery development. Therefore, we have performed the total and projected density of state calculations for all the C_3N bulk before as well as after $AlCl_4$ binding as shown in Figure 2.9. The C_3N bulk is metallic in nature, and on $AlCl_4$ intercalation it retains its metallic character with the shifting of Fermi level towards the valence band. In $AlCl_4$ intercalated/adsorbed C_3N, there is significant overlap between the 2p orbitals of C and N, and 3p orbital of Cl in the -5 to -2 eV energy range of the valence band, indicating towards a strong interaction between $AlCl_4$ and C_3N layers, further supporting the calculated binding energy values. Therefore, the 3D C_3N systems ensure constant electronic conductivity when used as Al battery cathodes. Another important tool to understand the interaction between $AlCl_4$ and C_3N systems is the charge density difference analysis, which can be possibly observed in the spatial distribution of charge density difference (ρ_{CDD}) plot shown in Figure 2.9.

$$\rho_{CDD} = \rho^{total} - \sum_i \rho_i^{fragments} \tag{2.12}$$

where, the ρ^{total} is the total charge density of the system and $\rho_i^{fragments}$ is the charge density of the individual fragments by which the system is made of. Here the charge density of the fragments ($\rho_i^{fragments}$) is calculated by a pseudo structure in which fragment part retains the same structure as in the total system but other parts are deleted. Here, ρ^{total} is calculated for intercalated 3D C_3N systems and the corresponding plots are shown in Figure 2.9. There is a net gain of electronic charge around each Cl atom of $AlCl_4$ molecule and a net loss of electronic charge on neighbouring C atoms of C_3N surface, indicating the mechanism of charge transfer from C_3N layers towards the Cl atoms of $AlCl_4$ molecule and oxidation of C_3N after $AlCl_4$ adsorption. Further, the Bader charge analysis *[55-58]* shows that in pure C_3N bulk, each carbon atom is positively charged with a net effective charge of 0.43 |e|, whereas, each N atom acquire a net effective charge of 1.28 |e|. However, on intercalation of $AlCl_4$, both neighbouring C and N atoms lose some charge to more electronegative Cl atoms of $AlCl_4$ and a whole of 0.90 |e| charge is transferred from C_3N bulk to $AlCl_4$. The amount of charge transfer in C_3N is more compared to that in the previously studied graphite (0.85 |e|) and BC_3 (0.70 |e|) electrodes *[82]*, which is in agreement with the strong binding of $AlCl_4$ with C_3N compared to graphite.

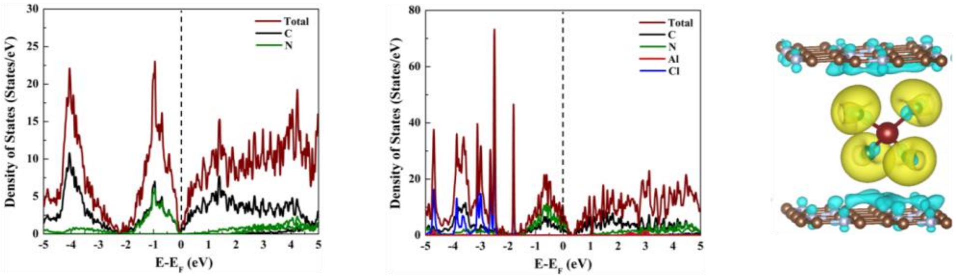

Figure 2.9: Density of states plots of C_3N phases before and after $AlCl_4$ binding, and the corresponding charge density difference plot.

2.3.2.3. Diffusion Characteristics

One of the crucial characteristic for determining the suitability of an electrode material for rechargeable batteries is the charge/discharge rate and it can be related with the diffusion properties of intercalating species. Therefore, we have examined the diffusion rate of $AlCl_4$ into C_3N bulk. The diffusion pathways are identified in all the three systems as shown in Figure 2.10. We have taken a 3×3×1 supercell for the diffusion calculations in C_3N bulk and the diffusion is restricted in xy-plane (Figure 2.10) as established in graphite *[77, 78]*. The associated energy barriers along these paths are calculated and the energy profiles are shown in Figure 2.10.

For the C_3N bulk, three diffusion paths have been considered with high structural symmetry between the two nearest neighboring T-NC sites, depicted as path-1, path-2, and path-3. The minimum diffusion barrier 0.15 eV is obtained for path-1, compared to 0.17 eV and 0.23 eV for path-2, and path-3, respectively. It is worth noting that the minimum diffusion barrier is less than the barrier of tetrahedral $AlCl_4$ into bulk graphite (0.33 eV) *[83]*, and BC_3 (0.38 eV) *[82]*. The $AlCl_4$ diffusivity is calculated using the given equation,

$$D = a^2 \nu e^{-E_b/k_B T} \tag{2.13}$$

where, a is the hopping distance, υ is the vibrational prefactor (10^{12} Hz) *[85, 86]*, E_b is $AlCl_4$ diffusion energy barrier, k_B is the Boltzmann constant, and T is the temperature.

The resultant diffusivity 5.5×10^{-6} cm^2s^{-1} for bulk C_3N is higher than that reported for graphite 2.2×10^{-9} cm^2s^{-1} *[83]*, which means C_3N bulk can diffuse $AlCl_4$ at much faster rate than that in the graphite electrode making it a potential electrode material. Overall, we can say that C_3N system is capable of providing trouble-free diffusion not only for small metal ions Na, and K but also for comparatively large anions like $AlCl_4$.

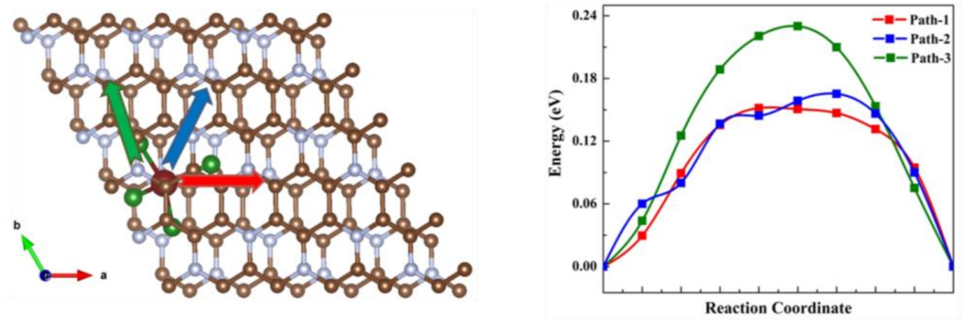

Figure 2.10: Schematic representation of the top view of the considered diffusion paths for $AlCl_4$ diffusion and the corresponding diffusion barrier profiles for 3D C_3N bulk system.

2.3.2.4. Electrochemical Properties

In order to examine the suitability of 3D C_3N as electrode material for Al batteries, we next evaluate the crucial electrochemical characteristics such as voltage and specific capacity.

For x number of $AlCl_4$ intercalated on C_3N system the net reaction can be expressed as,

$$3/x[(AlCl_4)_xC_3N] + 4(EMI^+AlCl_4^-) + Al \leftrightarrow$$
$$3/xC_3N + 4(EMI^+Al_2Cl_7^-) \quad (2.14)$$

The cell voltage can be determined by the Nernst equation *[79, 80]*,

$$V = -\frac{\Delta G_{cell}}{zF} \quad (2.15)$$

where z is the number of valence electrons during the intercalation process and F is the Faraday constant, respectively; ΔG_{cell} is the change in Gibbs free energy for chemical reaction of Al battery, which can be approximated to the internal energy ($\Delta G_f = \Delta E + P\Delta V - T\Delta S$) at 0 K due to negligible contribution of entropy and volume effect on the cell voltage. Thus, the cell voltage can be calculated by computing the corresponding internal energy change as,

$$\Delta E = \{{}^{3}/_{x}\, E_{[(AlCl_4)_xC_3N]} + 4E_{[EMI^+AlCl_4^-]} + E_{Al}\} - \{{}^{3}/_{x}\, E_{C_3N} +$$
$$4E_{[EMI^+Al_2Cl_7^-]}\} \quad (2.16)$$

where, $E_{[(AlCl_4)_xC_3N]}$, $E_{[EMI^+AlCl_4^-]}$ and $E_{[EMI^+Al_2Cl_7^-]}$ are the total energies of the $AlCl_4$ intercalated C_3N system, $EMI^+AlCl_4^-$ and $EMI^+Al_2Cl_7^-$, respectively. E_{Al} is the energy per atom in the bulk Al metal and E_{C_3N} is the total energy of C_3N. $E_{[EMI^+AlCl_4^-]}$ and $E_{[EMI^+Al_2Cl_7^-]}$ are calculated by optimizing the $EMI^+AlCl_4^-$ and $EMI^+Al_2Cl_7^-$, respectively as a molecular species due to non-availability of their crystal structures.

Therefore the average voltage (V_{ave}) for the system can be calculated using equation (2.16), where z is the electronic charge.

$$V_{ave} = -\left(\frac{\left\{{}^{3}/_{x}E_{C_3N} + 4E_{[EMI^{+}Al_2Cl_7^{-}]}\right\} - \left\{{}^{3}/_{x}E_{[(AlCl_4)_x C_3N]} + 4E_{[EMI^{+}AlCl_4^{-}]} + E_{Al}\right\}}{z}\right) \tag{2.17}$$

To determine the voltage and capacity, we first determine the maximum $AlCl_4$ intercalated 3D C_3N systems. For C_3N bulk, the stage-1, where all galleries are occupied, is the maximum intercalated system exhibiting highest storage capacity for the $AlCl_4$ intercalation, which leads to the formula unit of $(C_3N)_{4.5}AlCl_4$. The obtained capacity 116 mAh/g is higher than that in the previously reported graphite (70 mAh/g) *[34]* and BC_3 (74.37 mAh/g) *[82]* electrodes for Al batteries. Finally to determine the voltage corresponding to C_3N bulk, we have provided the voltage profile diagrams (Figure 2.11) for the intercalation of $AlCl_4$ molecules as function of molar ratio between $AlCl_4$ and C_3N. From the voltage profile of C_3N bulk it is clearly observable that the $AlCl_4$ intercalation in C_3N bulk shows two different kind of intercalation behaviour (Figure 2.11). The first kind is observed when the $AlCl_4$ intercalation is subjected within the same stage, such as stage-1, where the voltage variation for the first intercalation step is quite a bit larger than those of the other successive intercalation steps due to large energy change involved to achieve the interlayer distance of 8.23 Å, resulting in a comparatively higher voltage value. Other successive intercalation steps become easy in the already expanded C_3N layers, subsequently resulting in constant voltage values. The second kind of behaviour is observable when the intercalation is examined through the staging mechanism of $AlCl_4$ intercalation proceeding from pristine C_3N to stage-2 and then finally to the fully intercalated stage-1 and the average charging voltage increases as the $AlCl_4$ intercalation proceeds to form stage-1. The reason being the greater energy change required to open up or fill each interlayer spacing of stage-1 compared to the alternate interlayer spacing of satge-2. Due to the rigidity and structural similarity of C_3N with graphite, this kind of voltage behaviour during the intercalation of $AlCl_4$ anions have also been observed for graphite in previous reports, and for some other anions such as TFSI, PF_6 as well *[72]*. Therefore, the voltage corresponding to fully intercalated C_3N is calculated to be 0.45 V.

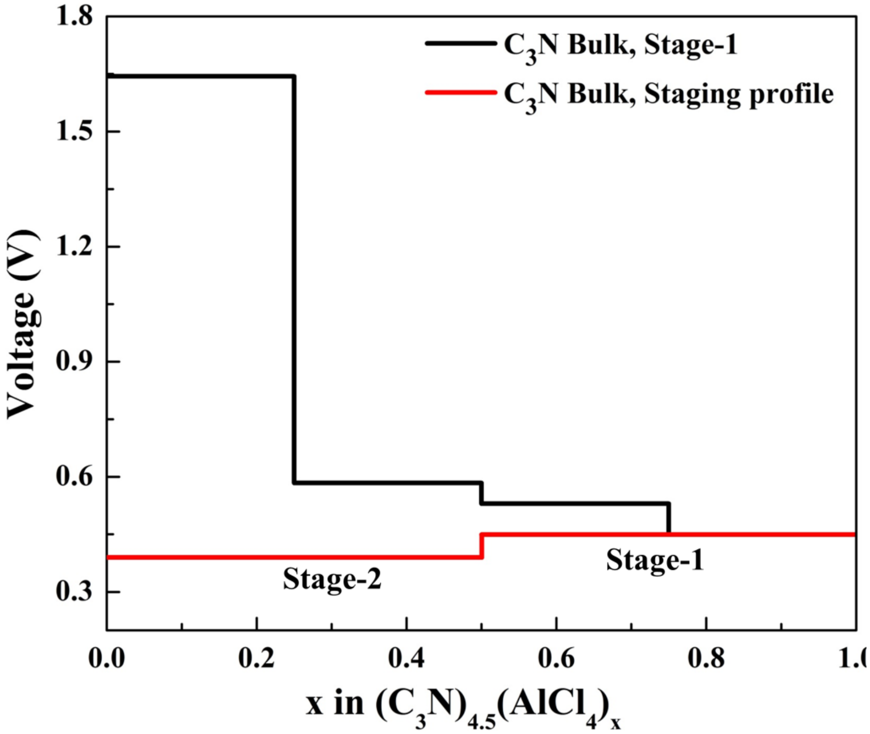

Figure 2.11: Voltage profile diagram of $AlCl_4$ intercalated C_3N system. Here the molar ratio x has different values for each system. The black and red colours represent the voltage profile within the same stage and between two different stages.

2.3.2.5. Stability vs. Voltage for Al Batteries

The stability and voltage are the two very important parameters of a battery. The resultant voltage is directly related with the stability of electrodes, which means upon the extent of interaction between the participating ions (metal ions or anions) and electrodes. In case of metal-ion batteries, such as Li-ion batteries, the participating ions are Li-ion respectively, which intercalate/deintercalate into electrodes during charge/discharge reactions *[78]*. The Al battery works on a different mechanism, where the amount of freely mobile anions ($AlCl_4$ and Al_2Cl_7) in the liquid electrolyte changes with state-of-charge and involves intercalation/deintercalation of $AlCl_4$ anions in cathode *[34, 81-84]*. However, the stability of metal ion or anion-intercalated system plays very important role in evaluating the cell voltage in both types of batteries as suggested by equation 8. In metal-ion batteries, the voltage is calculated based on the reaction equation *[87]*, $Electrode + nM \leftrightarrow M_nElectrode$, and $V = -\frac{(E_{M_nElectrode} - E_{Electrode} - nE_M)}{nze}$, where $E_{M_xElectrode}$ and $E_{Electrode}$ are the total energies of electrode with n metal ions and without metal ions, E_M is the energy per atom in metal bulk form and z is the electronic charge of metal. According to this equation, a more stable cathode system will give higher voltage for the system. However, in Al batteries both the anode Al metal and $AlCl_4$ intercalated cathode appear on the left side of equation 2.13. Therefore, a more stable $AlCl_4$ intercalated system will generate lower voltage in Al battery. Because of this reason, the calculated voltage for fully occupied (by $AlCl_4$) C_3N (0.45 V) is low in comparison of previously reported graphite (2.00 V) *[34]* and BC_3 bulk (2.41 V) *[82]* systems. We observe in our study that the C_3N system strongly interact with the intercalant $AlCl_4$ with the average binding energies of -2.63 eV ($(C_3N)_{4.5}AlCl_4$). The strong binding between $AlCl_4$ and C_3N phases makes the overall $AlCl_4$ intercalated C_3N phases very stable. This decreases the free energy difference between the left and right hand side reactants in equation 2.13, and as a result, according to the voltage equation 2.16, the voltage difference between anode and cathode becomes small, which leads to lower net voltage in Al battery.

The previously reported graphite and BC_3 bulk electrodes have shown high voltage values of 2.00 V, and 2.41 V respectively *[34, 82]*. To compare these results with our results of C_3N phases, we have calculated the binding energy of $AlCl_4$ in graphite, and BC_3 in their maximum $AlCl_4$ concentrated systems, which have the basic formula unit of ($C_{18}AlCl_4$), and ($(BC_3)_8AlCl_4$), respectively. The corresponding $AlCl_4$ binding energies in graphite, and BC_3 are -1.20 eV, and -0.61 eV, respectively. The BC_3 and C_3N systems are structurally similar to graphite, however the replacement of C with electron deficient B or electron efficient N (compared to C), significantly changes the voltage in these systems (increasing for BC_3 and decreasing for C_3N) by affecting the interaction with intercalated $AlCl_4$. The extent of interaction can be understood on the basis of the electronic distribution in graphite, BC_3, and C_3N. In Figure 2.13, we have shown the total electron density plots and the electron localization functions (ELFs) of (001) section of one layer of (a) graphite, (b) BC_3, and (c) C_3N, respectively. We observe that for graphite (Figure 2.12a), electrons are evenly distributed over the entire surface between the C-C bonds. The introduction of electron deficient B (compared to C) leads to the more electron localization around the C_6-hexagons compared to B containing hexagons and overall decrease in electron density of BC_3 surface, which makes it less favourable towards charge transfer to $AlCl_4$ (Figure 2.12b). While in case of C_3N, the one electron rich N increases the overall electron density of the system with extra electron localization on N atoms (Figure 2.12c), which is able to provide higher charge transfer to the intercalant $AlCl_4$ and thus to strong binding with $AlCl_4$. Now, it can be clearly understood that the lower stability of $AlCl_4$ intercalated BC_3 system leads to high voltage (2.41 V) for Al battery. However, the binding should not be very small so that the voltage does not exceed the 2.45 V value, which is the limit of electrochemical stability window of the EMIMCl:$AlCl_3$ electrolyte and after this potential the $AlCl_4$ anion oxidizes to gaseous chlorine (Cl_2), and cannot be reversed back in the next discharge cycle *[27]*. The Al batteries involving the anion intercalation/deintercalation are still in the initial stage of development and very few electrode materials (mainly carbon based) and electrolytes (EMIMCl:$AlCl_3$ and BMIMCl:$AlCl_3$) have been used till now *[88, 89]*. Therefore, this detailed relative discussion of voltage and system stability will be very helpful in developing efficient electrodes for the Al batteries.

The electron rich systems such as C_3N systems can improve the overall stability of the Al battery during various charge/discharge cycles but cannot deliver higher voltage. However, BC_3 like electron deficient systems can certainly improve voltage.

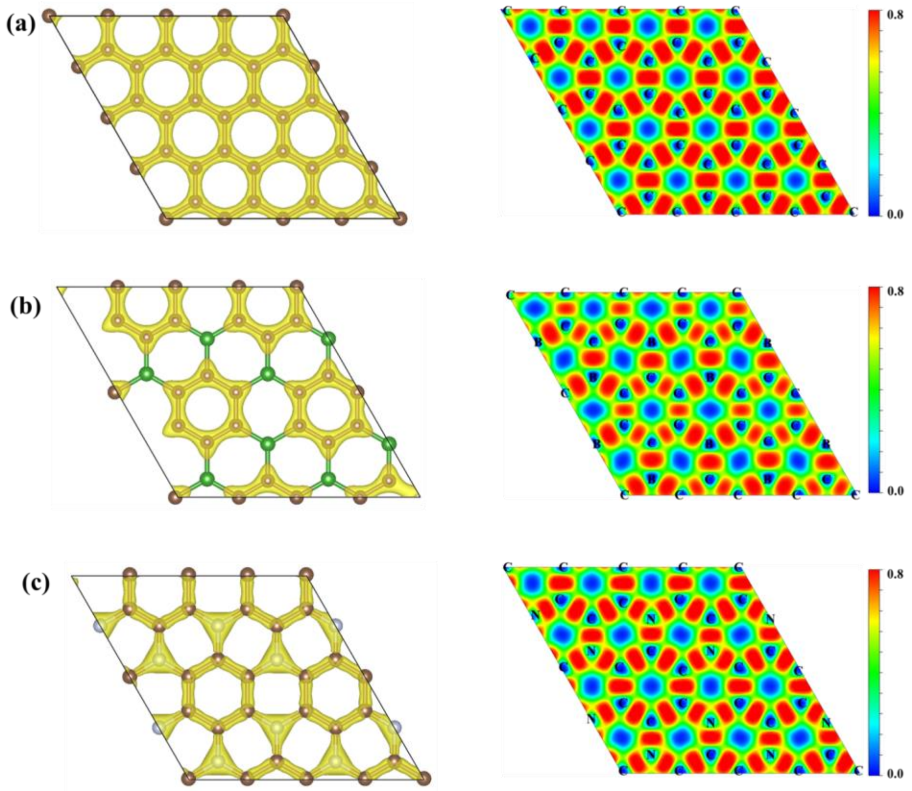

Figure 2.12: Total Charge density plots (Isosurface = 0.25 e/Å^3) and electron localization function plots of (001) section of one layer of (a) graphite, (b) BC_3, and (c) C_3N. The red and blue colours represent charge accumulation and depletion, respectively.

2.4. Conclusion

The staging mechanism is systematically studied for the intercalation of $AlCl_4$ in bulk graphite system. The stability of the $AlCl_4$ intercalated system and the average voltage and average theoretical capacity are calculated for intercalation of $AlCl_4$. Four different stages (stage-1 to stage-4) have been modelled to investigate the intercalation mechanism and to study the electrochemical properties. Our results show that $AlCl_4$ intercalates within the graphite system with its energetically stable tetrahedral form, which gets distorted due to the van der Waals interlayer attraction forces between the host graphite layers. The Al atom takes bridge position between two non-bonded C-atoms and four Cl atoms nearly occupy the center of the hexagon (C_6). Further, we have investigated the thermal stability of $AlCl_4$ intercalated graphite using AIMD at 300-500 K. We find that the graphite retains its stacking and the tetrahedral geometry of $AlCl_4$ also remains unchanged verifying that the $AlCl_4$ intercalated graphite structures considered in our study are stable. Our binding energy calculations suggest that $AlCl_4$ can intercalate in all the four stages. The significant amount of charge transfer from C-atoms of host intercalating layers to the four Cl atoms of $AlCl_4$ indicates the electrochemical oxidation of graphitic carbons by $AlCl_4$ intercalation and confirming the intercalation of $AlCl_4$ is a charging process which is in good agreement with the previous experimental report of Lin et al. The expanded graphite host galleries (interlayer spacing range 8.26 to 8.76 Å) after $AlCl_4$ intercalation makes the diffusion of $AlCl_4$ very easy with the diffusion barrier value ~0.01 eV, which justifies the ultrafast charging rate of experimentally studied graphite based Al-ion battery. We have found from the interlayer spacing of different stages and variation of voltage with $AlCl_4$ concentration that intercalation becomes more and more favourable for higher $AlCl_4$ concentrations for all the stages. Our calculated average voltages (2.01 V - 2.3 V) are in agreement with the experimentally reported voltage plateaus by Lin et al. Moreover, our calculated gravimetric capacities 25.94 mAh/g and 69.62 mAh/g for the partially occupied graphite system (stage-4) and completely intercalated system (stage-1), respectively agrees very well with experiments. Therefore based on our findings, we predict that it will be better to explore graphite-like layered materials as cathode materials which have larger interlayer spacing and greater flexibility. The intercalation and deintercalation of $AlCl_4$ will become easy in such large host galleries, which can increase the efficiency and lifetime of the battery because the structural deformation will be negligible and even the first intercalation step could be an easier one.

In conclusion, we have studied the cathode applicability of 3D bulk C_3N materials for Al batteries by evaluating the binding behaviour, geometry, electronic properties, voltages and storage capacities. It is observed that the C_3N system preferably stabilizes the tetrahedral geometry of $AlCl_4$ showing similar characteristic as previously reported Al battery cathode materials. The total and projected density of states plots show that the $AlCl_4$ intercalated C_3N system is metallic in nature, which insures an excellent electronic conductivity when used as a battery electrode. With the help of voltage profile diagrams, we observe that the variation of voltage shows two different behaviors. For C_3N bulk the voltage decreases when $AlCl_4$ intercalation is examined within the same stage (i.e. stage-1), and the voltage increases when the staging mechanism is followed from pristine C_3N to fully intercalated stage-1 C_3N. This behavior can be explained on the basis of free energy change, which is quite large for the first intercalation step to achieve the interlayer distance of 8.23 Å, resulting in a comparatively higher voltage value compared to the already expanded C_3N layers for the subsequent intercalation steps which permit constant voltage values. While in the staging mechanism the greater energy change required to open up or fill each interlayer spacing of stage-1 compared to the alternate interlayer spacing of satge-2, increases the voltage. In addition, we also observe that in Al batteries involving $AlCl_4$ intercalation/deintercalation, the voltage is inversely related with the stability of the $AlCl_4$ intercalated system. An electrode which can strongly bind $AlCl_4$ with high charge transfer value will produce small net voltage, such as C_3N electrodes. However, electrodes having lower binding energies for $AlCl_4$, can deliver high voltage as in previously studied BC_3 electrode. Therefore, in this regard, a 1D electron deficient system possessing adequate stability towards $AlCl_4$ intercalation will be a superior choice to obtain high voltage in Al battery compared to pristine carbon based systems. Overall, we believe that this detailed relative discussion of voltage and system stability will be helpful in understanding the important attributes to develop the efficient Al batteries.

2.5. References

1. Whittingham M. S. (2008), Materials challenges facing electrical energy storage, MRS Bull., 33, 411−419 (DOI: 10.1557/mrs2008.82)
2. Liu J., Zhang J. G., Yang Z., Lemmon J. P., Imhoff C., Graff G. L., Li L., Hu J., Wang C., Xiao J., Xia G. (2013), Materials science and materials chemistry for large scale electrochemical energy storage: From transportation to electrical grid, Adv. Funct. Mater., 23, 929-946 (DOI: 10.1002/adfm.201200690)
3. Armand M., Tarascon J. M. (2008), Building Better Batteries, Nature, 451, 652-657 (DOI: 10.1038/451652a)
4. Noorden R. V. (2014), The rechargeable revolution: A better battery, Nature, 507, 26-28, (DOI: 10.1038/507026a)
5. Dunn B., Kamath H., Tarascon J. M. (2011), Electrical energy storage for the grid: a battery of choices, Science, 334, 928-935 (DOI: 10.1126/science.1212741)
6. Thackeray M. M., Wolverton C., Isaacs E. D. (2012), Electrical energy storage for transportation—approaching the limits of, and going beyond, lithium-ion batteries, Energy Environ. Sci., 5, 7854-7863 (DOI: 10.1039/C2EE21892E)
7. Goodenough J. B., Kim Y. (2009), Challenges for rechargeable Li batteries, Chem. Mater., 22, 587-603 (DOI: 10.1021/cm901452z)
8. Goodenough J.B., Park K. S. (2013), The Li-ion rechargeable battery: A perspective, J. Am. Chem. Soc., 135, 1167-1176 (DOI: 10.1021/ja3091438)

9. Scrosati B., Garche J. (2010), Lithium batteries: Status, prospects and future, J. Power Sources, 195, 2419-2430 (DOI: 10.1016/j.jpowsour.2009.11.048)
10. Scrosati B., Hassoun J., Sun Y. K. (2011), Lithium-ion batteries. A look into the future, Energy Environ. Sci., 4, 3287-3295 (DOI: 10.1039/C1EE01388B)
11. Ellis B. L., Lee K. T., Nazar L. F. (2010), Positive electrode materials for Li-ion and Li-batteries, Chem. Mater., 22, 691-714 (DOI: 10.1021/cm902696j)
12. Ellis B. L., Nazar L. F. (2012), Sodium and sodium-ion energy storage batteries, Curr. Opin. Solid State Mater. Sci., 16, 168-177 (DOI: 10.1016/j.cossms.2012.04.002)
13. Kim S. W., Seo D. H., Ma X., Ceder G., Kang K. (2012), Electrode materials for rechargeable sodium-ion batteries: potential alternatives to current lithium-ion batteries, Adv. Energy Mater., 2, 710-721 (DOI: 10.1002/aenm.201200026)
14. Palomares V., Serras P., Villaluenga I., Hueso K. B., Carretero-González J., Rojo T. (2012), Na-ion batteries, recent advances and present challenges to become low cost energy storage systems, Energy Environ. Sci., 5, 5884-5901 (DOI: 10.1039/C2EE02781J)
15. Rasul S., Suzuki S., Yamaguchi S., Miyayama M. (2012), High capacity positive electrodes for secondary Mg-ion batteries, Electrochim. Acta, 82, 243-249 (DOI: 10.1016/j.electacta.2012.03.095)
16. Huie M. M., Bock D. C., Takeuchi E. S., Marschilok A. C., Takeuchi K. J. (2015), Cathode materials for magnesium and magnesium-ion based batteries, Coord. Chem. Rev., 287, 15-27 (DOI: 10.1016/j.ccr.2014.11.005)
17. Xu C., Li B., Du H., Kang F. (2012), Energetic zinc ion chemistry: the rechargeable zinc ion battery, Angew. Chem., Int. Ed., 51, 933-935 (DOI: 10.1002/anie.201106307)

18. Lee B., Lee H. R., Kim H., Chung K. Y., Cho B. W., Oh S. H. (2015), Elucidating the intercalation mechanism of zinc ions into α-MnO2 for rechargeable zinc batteries, Chem. Commun., 51, 9265-9268 (DOI: 10.1039/C5CC02585K)
19. Chen Z., Ren Y., Jasen A. N., Lin C., Weng W., Amine K. (2013), New class of nonaqueous electrolytes for long-life and safe lithium-ion batteries, Nat. Commun., 4, 1513 (DOI: 10.1038/ncomms2518)
20. Tepavcevic S., Xiong H., Stamenkovic V. R., Zuo X., Balasubramanian M., Prakapenka V. B., Johnson C. S., Rajh T. (2012), Nanostructured bilayered vanadium oxide electrodes for rechargeable sodium-ion batteries, ACS Nano, 6, 530-538, (DOI: 10.1021/nn203869a)
21. Cheng F., Liang J., Tao Z., Chen J. (2011), Functional materials for rechargeable batteries, Adv. Mater., 23, 1695-1715, (DOI: 10.1002/adma.201003587)
22. Manthiram A. (2011), J. Phys. Chem. Lett., 2, 176-184, (DOI: 10.1021/jz1015422)
23. Mohtadi R., Mizuno F. (2014), Magnesium batteries: Current state of the art, issues and future perspectives, Beilstein J. Nanotechnol., 5, 1291-1311, (DOI: 10.3762/bjnano.5.143)
24. Mori R. A. (2014), A novel aluminium–air secondary battery with long-term stability, RSC Adv., 4, 1982-1987, (DOI: 10.1039/C3RA44659J659J)
25. Li Q., Bjerrum N. J. (2002), Aluminum as anode for energy storage and conversion: a review, J. Power Sources, 110, 1-10, (DOI: 10.1016/S0378-7753(01)01014-X)
26. Singer J., Fielder W. L. (2000), Scientists outline advantages of Al/air cell battery, Am. Met. Mark., 2000, 108, 4
27. Hudak N. S. (2014), Chloroaluminate-doped conducting polymers as positive electrodes in rechargeable aluminum batteries, J. Phys. Chem. C, 118, 5203-5215 (DOI: 10.1021/jp500593d)

28. Gifford P. R., Palmisano J. B. (1988), An aluminum/chlorine rechargeable cell employing a room temperature molten salt electrolyte, J. Electrochem. Soc., 135, 650-654 (DOI: 10.1149/1.2095685)
29. Tang Y., Lu L., Roesky H. W., Wang L., Huang B. (2004), The effect of zinc on the aluminum anode of the aluminum–air battery, J. Power Sources, 138, 313-318 (DOI: 10.1016/j.jpowsour.2004.06.043)
30. Doche M. L., Cattin F. L., Durand R., Rameau J. J. (1997), Characterization of different grades of aluminum anodes for aluminum/air batteries, J. Power Sources, 65, 197-205 (DOI: 10.1016/S0378-7753(97)02473-7)
31. Jayaprakash N., Das S. K., Archer L. A. (2011), The rechargeable aluminum-ion battery, Chem. Commun., 47, 12610-12612 (DOI: 10.1039/C1CC15779E)
32. Rani J. V., Kanakaiah V., Dadmal T., Rao M. S., Bhavanarushi S. (2013), Fluorinated natural graphite cathode for rechargeable ionic liquid based aluminum–ion battery, J. Electrochem. Soc., 160, 1781-1784 (DOI: 10.1149/2.072310jes)
33. Wang W., Jiang B., Xiong W., Sun H., Lin Z., Hu L., Jiao S. (2013), A new cathode material for super-valent battery based on aluminium ion intercalation and deintercalation, Sci. Rep., 3, 3383 (DOI: 10.1038%2Fsrep03383)
34. Lin M. C., Gong M., Lu B., Wu Y., Wang D. Y., Guan M., Angell M., Chen C., Yang J., Hwang B. J., Dai H. (2015), An ultrafast rechargeable aluminium-ion battery, Nature, 520, 324-328 (DOI: 10.1038/nature14340)
35. Noel M., Santhanam R. (1998), Electrochemistry of graphite intercalation compounds, J. Power Sources, 72, 53-65 (DOI: 10.1016/S0378-7753(97)02675-X)

36. Besenhard J. O., Fritz H. P. (1983), The electrochemistry of black carbons, Angew. Chem., Int. Ed. Engl., 22, 950-975 (DOI: 10.1002/anie.198309501)
37. Besenhard J. O., Winter M. (2002), Advances in battery technology: rechargeable magnesium batteries and novel negative-electrode materials for lithium ion batteries, ChemPhysChem, 3, 155-159 (DOI: 10.1002/1439-7641(20020215)3:2%3C155::AID-CPHC155%3E3.0.CO;2-S)
38. Placke T., Fromm O., Lux S. F., Bieker P., Rothermel S., Meyer H. W., Passerini S., Winter M. (2012), Reversible intercalation of Bis(trifluoromethanesulfonyl)imide anions from an ionic liquid electrolyte into graphite for high performance dual-ion cells, J. Electrochem. Soc., 159, 1755-1765 (DOI: 10.1149/2.011211jes)
39. Wu M. S., Xu B., Chen L. Q., Ouyang C. Y. (2016), Geometry and fast diffusion of AlCl4 cluster intercalated in graphite, Electrochim. Acta, 195, 158-165 (DOI: 10.1016/j.electacta.2016.02.144)
40. Jung S. C., Kang Y. J., Yoo D. J., Choi J. W., Han Y. K. (2016), Flexible few-Layered graphene for the ultrafast rechargeable aluminum-ion battery, J. Phys. Chem. C, 120, 13384-13389 (DOI: 10.1021/acs.jpcc.6b03657)
41. Jung S. C., Kang Y. J., Han Y. K. (2017), Comments on “Geometry and fast diffusion of $AlCl_4$ cluster intercalated in graphite [Electrochim. Acta 195 (2016) 158–165]”, Electrochim. Acta, 223, 135–136 (DOI: 10.1016/j.electacta.2016.11.040)
42. Martyna G., Tuckerman M., Tobias D., Klein M. (1996), Explicit reversible integrators for extended systems dynamics, Mol. Phys., 87, 1117-1157 (DOI: 10.1080/00268979600100761)
43. Wang H., Maiyalagam T., Wang X. (2012), Review on recent progress in nitrogen-doped graphene: synthesis, characterization, and its potential applications, ACS Catal., 2, 781-794 (DOI: 10.1021/cs200652y).

44. Liu H., Jia M., Sun N., Cao B., Chen R., Zhu Q., Wu F., Qiao N.(2015),Nitrogen-rich mesoporous carbon as anode material for high-performance sodium-ion batteries, ACS Appl. Mater. Interfaces, 7, 27124-27130 (DOI: 10.1021/acsami.5b06898).
45. Wang Y., Shao Y., Matson D. W., Li J., Lin Y.(2010), Nitrogen-doped graphene and its application in electrochemical biosensing, ACS Nano, 4, 1790-1798 (DOI: 10.1021/nn100315s).
46. Mahmood J., Lee E. K., Jung M., Shin D., Choi J., Seo M., Jung S. M., Kim D., Li F., Lah M. S., Park N., Shin H. J., Oh J. H.(2016), Two-dimensional polyaniline (C3N) from carbonized organic single crystals in solid state, PNAS, 113, 7414 (DOI: 10.1073/pnas.1605318113).
47. Yang S., Li W., Ye C., Wang G., Tian H., Zhu C., He P., Ding G., Xie X., Liu Y., Liftshitz Y., Lee S. T., Kang Z., Jiang M.(2017), C3N—A 2D crystalline, hole-free, tunable-narrow-bandgap semiconductor with ferromagnetic properties, Adv. Mater., 29, 1605625 (DOI: 10.1002/adma.201605625).
48. Shi S., Gao J., Liu Y., Zhao Y., Wu Q., Ju W., Ouyang C., Xiao R. (2016), Theoretical investigation of properties of boron nitride nanocages and nanotubes as high-performance anode materials for lithium-ion batteries, 25, 018212 (DOI: 10.1139/cjc-2017-0070).
49. Kresse G., Furthmüller J. (1996), Efficient iterative schemes for ab initio total-energy calculations using a plane-wave basis set, Phys. Rev. B: Condens. Matter Mater. Phys., 54, 11169-11186 (DOI: 10.1103/PhysRevB.54.11169)
50. Chen Y., Peng F., Yan Y., Wang Z., Sun C., Ma Y. (2013), Exploring high-pressure lithium beryllium hydrides: a new chemical perspective, J. Phys. Chem. C, 117, 13879-13886 (DOI: 10.1021/jp404046g)
51. Perdew J. P., Burke K., Ernzerhof M. (1996), Generalized gradient approximation made simple, Phys. Rev. Lett., 77, 3865–3868 (DOI: 10.1103/PhysRevLett.77.3865)

52. Blöchl P. E. (1994), Projector augmented-wave method, Phys. Rev. B: Condens. Matter Mater. Phys., 50, 17953-17979 (DOI: 10.1103/PhysRevB.50.17953)
53. Grimme S., Antony J., Ehrlich S., Krieg H. (2010), A consistent and accurate ab initio parametrization of density functional dispersion correction (DFT-D) for the 94 elements H-Pu, J. Chem. Phys., 2010, 132, 154104 (DOI: 10.1063/1.3382344)
54. Baskin Y., Meyer L. (1955), Lattice constants of graphite at low temperatures, Phys. Rev., 100, 544 (DOI: 10.1103/PhysRev.100.544)
55. Bader R. F. W. (1991), A quantum theory of molecular structure and its applications, Chem. Rev., 91, 893-928 (DOI: 10.1021/cr00005a013)
56. Henkelman G., Arnaldsson A., Jónsson H. (2006), A fast and robust algorithm for Bader decomposition of charge density, Comput. Mater. Sci., 36, 354-360 (DOI: 10.1016/j.commatsci.2005.04.010)
57. Sanville E., Kenny S. D., Smith R., Henkelman G. J. (2007), Improved grid-based algorithm for Bader charge allocation, Comput. Chem., 28, 899-908 (DOI: 10.1002/jcc.20575)
58. Tang W., Sanville E., Henkelman G. J. (2009), A grid-based Bader analysis algorithm without lattice bias, J. Phys.: Condens. Matter, 21, 084204 (DOI: 10.1088/0953-8984/21/8/084204)
59. Mills G., Jónsson H., Schenter G. K. (1995), Reversible work transition state theory: application to dissociative adsorption of hydrogen, Surf. Sci., 324, 305-337 (DOI: 10.1016/0039-6028(94)00731-4)
60. Seel J. A., Dahn J. R. (2000), Electrochemical intercalation of PF 6 into graphite, J. Electrochem. Soc., 147, 892-898 (DOI: 10.1149/1.1393288)
61. Kouvetakis J., Sasaki T., Shen C., Hagiwara R., Lerner M., Krishnan K. M., Bartlett N. (1990), Novel aspects of graphite intercalation by fluorine and fluorides and new B/C, C/N and B/C/N materials based

on the graphite network, Synth. Met., 34, 1-7 (DOI: 10.1016/0379-6779(89)90355-X)

62. Millman S. E., Kirczenow G., Solenberger D. (1982), Phase diagrams for alkali metal graphite intercalation compounds, J. Phys. C: Solid State Phys., 15, 1269-1276 (DOI: 10.1088%2F0022-3719%2F15%2F36%2F003)
63. Millman S. E., Kirczenow G. (1982), Origin of simple staging in graphite intercalation compounds,Phys. Rev. B: Condens. Matter Mater. Phys., 26, 2310-2313 (DOI: 10.1103/PhysRevB.26.2310)
64. Safran S. A., Hamann D. R. (1980), Coherency strains and staging in graphite intercalation compounds, Phys. B+C, 99, 469-472 (DOI: 10.1016/0378-4363(80)90279-X)
65. Safran S. A. (1980), Phase diagrams for staged intercalation compounds, Phys. Rev. Lett., 44, 937-940 (DOI: 10.1103/PhysRevLett.44.937)
66. Ohzuku T., Iwakoshi Y., Sawai K. (1993), Formation of lithium-graphite intercalation compounds in nonaqueous electrolytes and their application as a negative electrode for a lithium ion (shuttlecock) cell, J. Electrochem. Soc., 140, 2490-2498 (DOI: 10.1149/1.2220849)
67. Dahn J. R. (1991), Phase diagram of Li_xC_6, Phys. Rev. B: Condens. Matter Mater. Phys., 44, 9170-9177 (DOI: 10.1103/PhysRevB.44.9170)
68. Rothermel S., Meister P., Schmuelling G., Fromm O., Meyer H. W., Nowak S., Winter M. Placke T. (2014), Dual-graphite cells based on the reversible intercalation of bis(trifluoromethanesulfonyl)imide anions from an ionic liquid electrolyte, Energy Environ. Sci., 7, 3412-3423 (DOI: 10.1039/C4EE01873G)
69. Okamoto Y. (2013), Density functional theory calculations of alkali metal (Li, Na, and K) graphite intercalation compounds, J. Phys. Chem. C, 118, 16-19 (DOI: 10.1021/jp4063753)

70. Schmuelling G., Placke T., Kloepsch R., Fromm O., Meyer H. W., Passerini S., Winter M. (2013), X-ray diffraction studies of the electrochemical intercalation of bis(trifluoromethanesulfonyl)imide anions into graphite for dual-ion cells, J. Power Sources, 239, 563-571 (DOI: 10.1016/j.jpowsour.2013.03.064)
71. Takahashi S., Koura N., Kohara S., Saboungi M. L., Curtiss L. A. (1999), Technological and scientific issues of room-temperature molten salts, Plasmas Ions, 2, 91-105 (DOI: 10.1016/S1288-3255(99)00105-7)
72. Huesker J. M., Winter M., Placke T. (2015), Dilatometric study of the electrochemical intercalation of bis(trifluoromethanesulfonyl) imide and hexafluorophosphate anions into carbon-based positive electrodes**,** ECS Trans., 69, 9-21 (DOI: 10.1149/06922.0009)
73. Dresselhaus M. S., Dresselhaus G., Intercalation compounds of graphite (2002), Adv. Phys., 51, 1-186 (DOI: 10.1080/00018730110113644)
74. Batsanov S. S. (2001), van der Waals radii of elements, Inorg. Mater., 37, 871-885 (DOI:10.1023/A:1011625728803)
75. Kim D., Tarakeshwar P., Kim K. S. (2004), Theoretical investigations of anion−π interactions: the role of anions and the nature of π systems, J. Phys. Chem. A, 108, 1250-1258 (DOI: 10.1021/jp037631a)
76. Sun H., Wang W., Yu Z., Yuan Y., Wang S., Jiao S. (2015), A new aluminium-ion battery with high voltage, high safety and low cost, Chem. Commun., 51, 11892-11895 (DOI: 10.1039/C5CC00542F)
77. Meunier V., Kephart J., Roland C., Bernholc J. (2002), Ab initio investigations of lithium diffusion in carbon nanotube systems, Phys. Rev. Lett., 88, 075506 (DOI: 10.1103/PhysRevLett.88.075506)
78. Thinius S., Islam M. M., Heitjans P., Bredow T. (2014), Theoretical study of Li migration in lithium–graphite intercalation compounds with dispersion-corrected DFT methods, J. Phys. Chem. C, 118, 2273-2280 (DOI: 10.1021/jp408945j)

79. Aydinol M. K., Kohan A. F., Ceder G., Cho K., Joannopoulos J. (1997), Ab initio study of lithium intercalation in metal oxides and metal dichalcogenides, Phys. Rev. B: Condens. Matter Mater. Phys., 56, 1354-1365 (DOI: 10.1103/PhysRevB.56.1354)
80. Aydinol M. K., Kohan A. F., Ceder G. (1997), Ab initio calculation of the intercalation voltage of lithium-transition-metal oxide electrodes for rechargeable batteries, J. Power Sources, 68, 664-668 (DOI: 10.1016/S0378-7753(96)02638-9)
81. Wang D. Y., Wei C. Y., Lin M. C., Pan C. J., Chou H. L., Chen H. A., Gong M., Wu Y., Yuan C., Angell M., Hsieh Y. J. (2017), Advanced rechargeable aluminium ion battery with a high-quality natural graphite cathode, Nature Commun., 8, 14283 (DOI: 10.1038/ncomms14283)
82. Bhauriyal P., Mahata A., Pathak B. (2017), Hexagonal BC3 Electrode for a High-Voltage Al-Ion Battery, J. Phys. Chem. C, 121, 9748–9756 (DOI: 10.1021/acs.jpcc.7b02290)
83. Jung S. C., Kang Y. J., Yoo D. J., Choi J. W., Han Y. K. (2016), Flexible Few-Layered Graphene for the Ultrafast Rechargeable Aluminium-Ion Battery, J. Phys. Chem. C, 120, 13384 (DOI: 10.1021/acs.jpcc.6b03657)
84. Bhauriyal P., Mahata A., Pathak B.(2017), A Computational Study of a Single-Walled Carbon-Nanotube-Based Ultrafast High-Capacity Aluminium Battery, Chem. Asian J., 12, 1944-1951 (DOI: 10.1002/asia.201700570)
85. Backus E. H. G., Eichler A., Kleyn A. W., Bonn M. (2005) Real-Time Observation of Molecular Motion on a Surface, Science, 310, 1790–1793 (DOI: 10.1126/science.1120693)
86. Tekin A., Hummelshoj J. S., Jacobsen H. S., Sveinbjornsson D., Blanchard D., Norskov J. K., Vegge T. (2010) Ammonia dynamics in magnesium ammine from DFT and neutron scattering, Energy Environ. Sci., 3, 448–456 (DOI: 10.1039/B921442A)

87. Hu J., Xu B., Yang S. A., Guan S., Ouyang C., Yao Y.(2015) 2D electrides as promising anode materials for Na-ion batteries from first-principles study, ACS Appl. Mater. Interfaces, 7, 24016–24022 (DOI: 10.1021/acsami.5b06847)
88. Zafar Z. A., Imtiaz S., Razaq R., Ji S., Huang T., Zhang Z., Huang Y., Anderson J. A. (2017), Cathode materials for rechargeable aluminum batteries: current status and progress, J. Mater. Chem. A, 5, 5646–5660 (DOI: 10.1039/c7ta00282c).
89. Das S. K., Mahapatra S., Lahan H. (2017), Aluminium-ion batteries: developments and challenges, J. Mater. Chem. A, 5, 6347–6367 (DOI: 10.1039/C7TA00228A)

Chapter 3

Graphene/hBN Heterostructure as High-Capacity Cathode with High Voltage for Next-Generation Aluminium Batteries

3.1. Introduction

The continuously increasing world's energy demands as well as rising environmental problems have led to look out for such energy devices which can fulfill the never ending energy needs *[1, 2]*. In this respect, secondary batteries can be regarded as the efficient solution for energy conversion and more importantly its storage *[3, 4]*. The most commercialized Li-ion batteries and lead acid batteries are quite efficient to fulfill the requirements but also have their share of limitations in terms of abundance, environmental effects, manufacturing costs, etc *[5-10]*. Therefore, the desire to overcome the limitations and exploration of more efficient secondary batteries are the two primary objectives of present scenario. In this respect, Al metal based batteries are emerging as the next alternate provider of energy due to the higher abundance of Al in the Earth's crust (~ 8% vs. 0.0065% for Li) *[11]*, three-electron redox properties and a four-fold higher volumetric capacity than Li (~ 8040 mAhcm^{-3} vs. ~ 2000 mAhcm^{-3}) *[12]*. Therefore, due to the small expected size and low cost of Al batteries, the marketing of aluminum battery technology is anticipated to be safer than that of lithium battery technology. One of the very first Al battery is reported by Gifford and Palmisano in 1988 using $AlCl_3$ and 1,2-dimethyl-3-propylimidazolium-chloride (DMPIC) at a molar ratio of 1.5 : 1. They have obtained the average operating voltage of 1.7 V with discharge capacities in the range of 35 to 40 mAh/g, however, the formation of gaseous Cl_2 at the cathode is observed to be problematic for further development of this kind of Al battery *[13]*. Till present, two kinds of working mechanisms have been observed for Al batteries *[14-26]*. The first mechanism is based on the rocking chair batteries, and involves intercalation/deintercalation of Al^{+3} ions into cathode during discharge/charge *[13-16]*. Whereas, in the second mechanism, the participating ion $AlCl_4^-$ intercalates/deintercalates into cathode during charging/discharging and the battery behaves as the dual-ion battery *[17-30]*. Al batteries with the dual-ion battery working mechanism are reported to impart higher average voltage, fast charge/discharge rates, and efficient cycle stability with constant energy density *[19, 27]*. The complete reactions for Al battery involving the intercalation/deintercalation of $AlCl_4^-$ during charging/discharging, respectively can be written as,

Anode: $\mathrm{Al} + 7\mathrm{AlCl}_4^- \rightleftharpoons 4\mathrm{Al}_2\mathrm{Cl}_7^- + 3\mathrm{e}^-$ (3.1)

Cathode: $\mathrm{C}_\mathrm{n}[\mathrm{AlCl}_4] + \mathrm{e}^- \rightleftharpoons \mathrm{C}_\mathrm{n} + \mathrm{AlCl}_4^-$ (3.2)

It has been observed that in these kinds of Al batteries, the choice of cathode plays a quite important role in determining the overall battery efficiency *[22, 23, 28, 29]*. Therefore, choosing a suitable cathode which can deliver higher voltage and efficient storage capacity as well as maintaining the structural stability with fast charge/discharge rate is the primary aim of Al batteries. Till present many carbons based cathodes have been reported experimentally and theoretically, where the suitability is either limited to low capacity and cycle stability or low voltage values *[22, 23, 29, 31-33]*. In our previous study, it is explained that the binding of $AlCl_4$ in cathode inversely affects the charging voltage of the Al battery, and a low dimensional-electron deficient cathode with low binding of $AlCl_4$ can deliver higher voltage and sufficient capacity with high charge/discharge rate *[29]*. In earlier reports, it has been observed that the experimentally reported graphite moderately binds $AlCl_4$ with the binding energy of -1.20 eV (furnishing 2.00 V voltage), whereas the other proposed electrodes such as BC_3 and C_3N offer the binding energies of -0.61 eV (2.41 V) and -2.63 eV (0.45 V), respectively *[19, 21, 23, 29]*. The electron deficiency of BC_3 compared to graphite and C_3N improves the voltage in Al battery, but the stability of the overall $AlCl_4$ intercalated BC_3 system decreases, reaching the maximum charging cutoff voltage at very low storage capacity of 74.37 mAh/*g* *[23]*. Therefore, to acquire the maximum efficiency in Al battery, it becomes important to look for other alternate electrode materials. In that way it can be beneficial to check the suitability of monolayer hexagonal boron nitride (hBN) for Al batteries, which is regarded as ‘white graphene’ having the similar structural characteristic and electronic count *[34]*. However, the inadequately large band gap (5.9 eV) of hBN limits it’s usage as battery electrode which constantly requires high electronic conductivity during charge/discharge processes *[35]*. One of the possible ways to overcome this limitation is constructing a van der Waals heterostructure of hBN with another 2D material. Therefore, we have thought of choosing G/hBN heterostructure, where the hBN layer can reduce the binding energy of $AlCl_4$ to get high voltage due to electron deficient B and electronegative N atom. And, at the same time the graphene along with maintaining constant conductivity can also help in providing the overall stability to system so that the G/hBN heterostructure can furnish high $AlCl_4$ storage as well as providing high voltage. In last few years 2D heterostructures, formed by stacking of different kind of single-layered materials have become a subject of interest due to their uniquely modified physical properties. The 2D heterostructures open new opportunities as they offer the advantages associated with their individual fragments as well as limiting the individual drawbacks *[36-39]*. The improvement of electronic and electrochemical properties have successfully been achieved for Li-ion batteries when the individual monolayer electrode is replaced by heterostructure such as in hBN/graphene *[40]*, black-phosphorene/graphene *[41]*, blue-phosphorene/borophene *[42]*, and other 2D metal heterostructures *[43-45]*. Moreover, the heterostructure of graphene (G) and hexagonal boron nitride (hBN) is of quite importance as it exhibits rich physical properties that include a tunable band gap, ultrahigh electron mobility, and the demonstration of controllable hyperbolic metamaterial characteristics *[39-46]*. The two-layer structured G/hBN is first prepared by Oshima et al. in year 2000 on Ni(111) substrate *[47]*. After that with the help of density functional theory studies, the most stable configuration of G/hBN and its electronic properties are studied *[48]*. Besides, many theoretical studies have also analyzed the stacking behavior and interlayer distance of G/hBN heterostructure and observed that the AB stacking, where B atoms are positioned directly towards the C atoms and N atoms are positioned towards the centre of the graphene hexagon is most stable stacking pattern at various interlayer distances, because of the low electron density at centre and B cation directly above the C atoms of graphene tend to enhance the effect of attraction between graphene and hBN layers *[49, 50]*. The advancement in the properties of graphene/hBN hereostructures may result from the variety of factors such as change in the morphology, tuning of electronic properties, lattice mismatch etc and the hBN layers can serve as good substrates and also as protective covers for graphene *[51]*. Earlier, the graphene/hBN composites have also been used as an anode for Li-ion batteries *[40]*. In that way, it will be interesting to check the graphene/hBN interface towards the interaction with $AlCl_4$, and its effect on overall battery performance.

In this work, we have carried out a systematic investigation of the cathode applicability of graphene/hexagonal boron nitride (G/hBN) heterostructure for Al batteries using the density functional theory (DFT) calculations. For the better understanding, we have made a comparative study between graphene, hBN and G/hBN to evaluate the structural stability, $AlCl_4$ binding properties, and the diffusion characteristics. Moreover, we have also conducted the detailed study of the storage capacity of $AlCl_4$ in G/hBN heterostructure and the corresponding monolayers of graphene and hBN by subjecting the systems to undergo step by step $AlCl_4$ binding. The voltage profiles of graphene, hBN and G/hBN heterostructure are also compared to determine the corresponding charging voltage. Based on the obtained results, we believe that the G/hBN could be a potential cathode material for Al batteries and our study motivates further developments of graphene based heterostructure for Al batteries.

3.2. Computational Details

We have carried out density functional theory calculations by using the projector augmented-wave (PAW) *[52, 53]* method to treat interactions between ion cores and valence electrons as implemented in the Vienna Ab initio Simulation Package (VASP) *[54-57]*. The generalized gradient approximation of Perdew-Burke-Ernzerhof (GGA-PBE) *[58, 59]* is used to describe the exchange-correlation potential and the plane-wave cutoff energy is fixed to 470 eV for the all the calculations. The optimized structures are fully relaxed until the Hellmann−Feynman forces on each atom are less than 0.03 eV/Å and total energy is converged to 10^{-4} eV. The Brillouin zone is sampled with Gamma centred k-point grid of 25 × 25 × 1 and 4 × 4 × 1 for the unit cell and 6 × 6 × 1 supercell calculations. A minimum of 13 Å of vacuum is used along the z-direction to avoid any periodic interactions. The DFT-D3 approach is included for the correction of van der Waals interactions for potential energy and interatomic forces *[60]*. The DFT-D3 level of theory is reliable enough to correlate with the real experimental scenario, because the results obtained in our previous theoretical study *[21]* have been independently justified by a recent experimental report *[61]*.For the electronic calculation, the Brillouin zone is sampled with a k-point grid of 45 × 45 × 1, and 11 × 11 × 1 for the unitcell and supercell, respectively. Bader charge *[62-66]* analysis is performed with the help of the Henkelman programme using near-grid algorithm refine-edge method to understand the charge transfer process between the atoms. We have determined the diffusion barriers using the climbing image nudged elastic band (CI-NEB) method *[67]*. The minimum energy paths (MEP) are initialized by inserting seven image structures between fully optimized initial and final structural geometries and the energy conversion criteria of each image is set to 10^{-3} eV.

The calculated lattice constants are a = b = 2.46 Å, and a = b = 2.51 Å for the monolayer graphene and hBN respectively, which are in agreement with the previous reports *[68]*. In order to minimize the lattice mismatch between graphene and h-BN layers, the hexagonal unit cell of G/hBN heterostructure is modelled by combining 1×1 unit cell of both graphene and hBN unit cells. The hereostructure is the AB-stacked bilayer with B facing C, and N in the hollow site of the graphene hexagon, since it is the most stable configuration for the G/hBN interface. The lattice constants of G/hBN heterostructure are a = b = 2.48 Å *[68-69]*. The lattice mismatch between the graphene and h-BN monolayer is ~0.80 %, which is quite small in comparison to previously studied heterostructures for metal-ion batteries, such as hBN/phosphorene (5%) *[70]*, silicene/graphene (< 4%) *[45]*, phosphorene/borophene (< 2%) *[42]*. Moreover, the interlayer distance 3.32 Å of G/hBN heterostructure layer is also close to previous reports *[71]*.

The stacking stability of G/h-BN heterostructure is calculated using the equation,

$$E_{Stack} = (E_{G/BN} - E_G - E_{BN})/n \tag{3.3}$$

where, E_G , E_{BN} and $E_{G/BN}$ are the total energies of graphene, BN and G/BN heterostructure unit cells respectively, and n is the total number of atoms in the heterostructure. The stacking stability value is -0.04 eV/atom, which indicates towards a stability of G/hBN heterostructure, as it has also been experimentally synthesized.

Having x number of $AlCl_4$ adsorbed/intercalated on G/hBN system the overall reaction can be written as *[21, 22]*,

$$3/x[(AlCl_4)_xG/hBN] + 4(EMI^+AlCl_4^-) + Al \leftrightarrow 3/x(G/hBN) + 4(EMI^+Al_2Cl_7^-) \tag{3.4}$$

The cell voltage can be determined by the Nernst equation *[72]*,

$$V = -\frac{\Delta G_{cell}}{zF} \tag{3.5}$$

where, F is the Faraday constant and z is the number of valence electrons, respectively; ΔG_{cell} is the change in Gibbs free energy for chemical reaction of Al battery. At 0 K due to negligible contribution of entropy (S) and volume effect (V) on the cell voltage, ΔG_{cell} can be approximated to the internal energy ($\Delta G_{cell} = \Delta E + P\Delta V - T\Delta S$). The internal energy change can be computed as,

$$\Delta E = \{{}^{3}/_{x}\, E_{[(AlCl_4)_xG/hBN]} + 4E_{[EMI^+AlCl_4^-]} + E_{Al}\} - \{{}^{3}/_{x}\, E_{G/hBN} + 4E_{[EMI^+Al_2Cl_7^-]}\} \tag{3.6}$$

where, $E_{[(AlCl_4)_xG/hBN]}$, $E_{[EMI^+AlCl_4^-]}$ and $E_{[EMI^+Al_2Cl_7^-]}$ are the total energies of the $AlCl_4$ intercalated G/hBN system, $EMI^+AlCl_4^-$ and $EMI^+Al_2Cl_7^-$, respectively. E_{Al} is the energy per atom in the bulk Al metal and $E_{G/hBN}$ is the total energy of G/hBN. Due to non-availability of crystal structures of $EMI^+AlCl_4^-$ and $EMI^+Al_2Cl_7^-$, $E_{[EMI^+AlCl_4^-]}$ and $E_{[EMI^+Al_2Cl_7^-]}$ are calculated by optimizing the $EMI^+AlCl_4^-$ and $EMI^+Al_2Cl_7^-$ as ion pairs in a box, respectively. We have not considered solvent effects in our calculations as Agiorgousis et al. have shown in their recent study that the difference between the solvation energies of $AlCl_4^-$ and $Al_2Cl_7^-$ anions is very small (~0.1 eV), where the ions are solvated by $EMI^+AlCl_4^-$ *[26]*. Therefore the average voltage (V_{ave}) for the system can be calculated using equation (3.7), where z is the electronic charge.

$$V_{ave} = \left(\frac{\{{}^{3}/_{x}E_{[(AlCl_4)_xG/hBN]} + 4E_{[EMI^+AlCl_4^-]} + E_{Al}\} - \{{}^{3}/_{x}E_{G/hBN} + 4E_{[EMI^+Al_2Cl_7^-]}\}}{z}\right) \tag{3.7}$$

In addition, the specific capacity (C) is calculated as *[73]*,

$$C = \frac{zxF}{M_f} \tag{3.8}$$

where, z is the number of electrons transferred per formula unit, x is the number of $AlCl_4$ molecules involved, F is the Faraday constant, and M_f is the mass of formula unit.

3.3. Results and Discussion

3.3.1. Binding of $AlCl_4$

To study the binding of $AlCl_4$, we have considered a 3 × 3 × 1 supercell of G/hBN heterostructure along with the possibility of binding of both planar and tetrahedral $AlCl_4$ on the surfaces of graphene ($AlCl_4$/G/hBN) and hBN (G/hBN/$AlCl_4$), and in the interlayer spaces (G/$AlCl_4$/hBN). We observe that same as the previous reports *[19-23, 25-26]*. the geometrical preference of $AlCl_4$ is tetrahedral both before and after the adsorption/intercalation in G/hBN heterostructure. To check the most stable binding site of this tetrahedral $AlCl_4$, different sites have been considered for all the binding possibilities, $AlCl_4$/G/hBN, and G/hBN/$AlCl_4$ as well as for the interlayer spaces G/$AlCl_4$/hBN as shown in Figure 3.1. Thus calculated relative energies of the all possible sites are given in Table 3.1 and based on these value we observe that for the surface adsorptions $AlCl_4$/G/hBN, and G/hBN/$AlCl_4$, the most stable sites are the top site of C (site A1), and hollow site (site B3) of hBN, respectively, whereas the $AlCl_4$ intercalation in the interlayer space of G/hBN prefers the bridge site of BN bond (site C4).

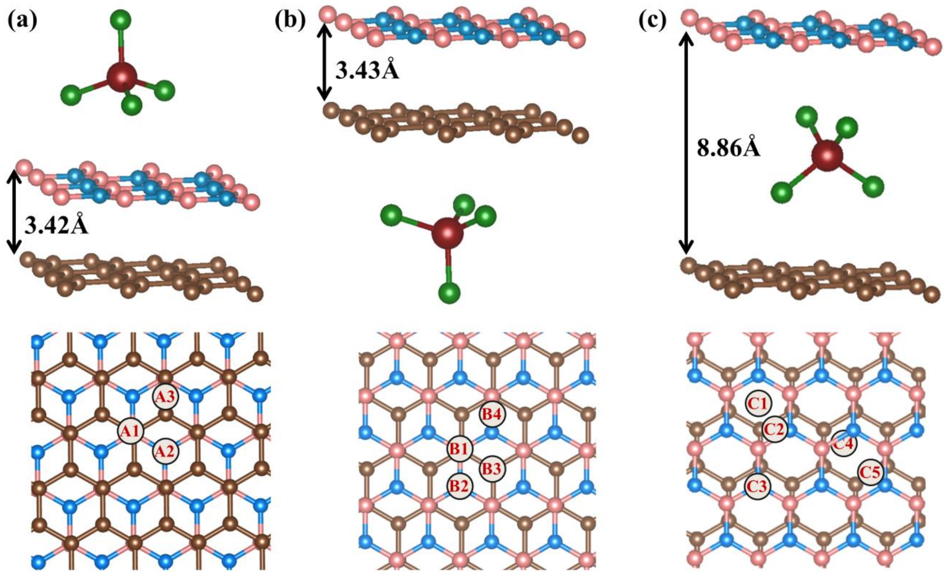

Figure 3.1: Top and side views of $AlCl_4$ adsorption sites in (a) $G/hBN/AlCl_4$, (b) $AlCl_4/G/hBN$, and (c) $G/AlCl_4/hBN$.

Table 3.1: The relative energies (R. E.) of $AlCl_4$ adsorption/intercalation for all the binding possibilities in $AlCl_4/G/hBN$, $G/hBN/AlCl_4$, and $G/AlCl_4/hBN$ systems.

System	**Sites**	**R. E. (meV)**
$AlCl_4$/G/hBN	A1	0.00
	A2	0.24
	A3	5.46
G/hBN/$AlCl_4$	B1	188.63
	B2	175.99
	B3	173.53
	B4	179.88
G/$AlCl_4$/hBN	C1	416.76
	C2	410.12
	C3	410.16
	C4	408.11
	C5	416.52

The binding energies ($\mathrm{E_{binding}}$) corresponding to the most stable sites are calculated as,

$$\mathrm{E_{binding}} = (\mathrm{E_{G/hBN+AlCl_4}} - \mathrm{E_{G/hBN}} - \mathrm{E_{AlCl_4}}) \tag{3.9}$$

where, $\mathrm{E_{G/hBN+AlCl_4}}$ and $\mathrm{E_{G/hBN}}$ are the total energies of G/hBN system with and without $AlCl_4$, respectively, and $\mathrm{E_{AlCl_4}}$ is the total energy of one $AlCl_4$ molecule in the box. The more negative binding energy value means a more stable binding of $AlCl_4$, and Table 3.2 presents the most stable binding sites along with the corresponding binding energies for the ($AlCl_4$/G/hBN), (G/hBN/$AlCl_4$), and (G/$AlCl_4$/hBN) binding possibilities. For comparison, the adsorption of $AlCl_4$ on the surfaces of pristine monolayers of graphene and hBN are also studied (Figure 3.2) and the calculated binding energies of the most stable sites are given in Table 3.2. From the obtained results, it can be concluded that the adsorption of $AlCl_4$ is much stronger on the outer surface of G/hBN/$AlCl_4$ (-1.19 eV) compared to pristine monolayer of hBN (-0.92 eV), while the adsorption energies of $AlCl_4$ are comparable for graphene outer surface in G/hBN heterostructure, $AlCl_4$/G/hBN (-1.37 eV) and pristine graphene (-1.36 eV) (Table 3.2). On the other hand, in G/hBN heterostructure, the binding of $AlCl_4$ is comparatively less favourable in interlayer spaces G/$AlCl_4$/hBN (-0.96 eV), than the outer surfaces of $AlCl_4$/G/hBN and G/hBN/$AlCl_4$, while it is still more favoured compared to the $AlCl_4$ binding in pristine monolayer hBN surface. The results clearly indicate that the binding of $AlCl_4$ has improved in G/hBN heterostructure compared to pristine hBN due to the interaction between the graphene and hBN layers, while maintaining the similar binding strength on outer graphene surface as that of pristine graphene. Therefore, G/hBN heterostructure ensures overall stability of the battery during charge/discharge cycles.

Table 3.2: Binding energy ($E_{binding}$) of the most stable binding sites and the corresponding charge transfer (Δq) values to $AlCl_4$.

System	**Sites**	**$E_{binding}$ (eV)**	**Δq (|e|)**
$AlCl_4$/G	A2 (Hollow)	-1.36	-0.43
$AlCl_4$/hBN	B2 (N-top)	-0.92	-0.36
$AlCl_4$/G/hBN	A1 (Top)	-1.37	-0.43
G/hBN/$AlCl_4$	B3 (Hollow)	-1.19	-0.39
G/$AlCl_4$/hBN	C4 (Bridge-BN)	-0.96	-0.65

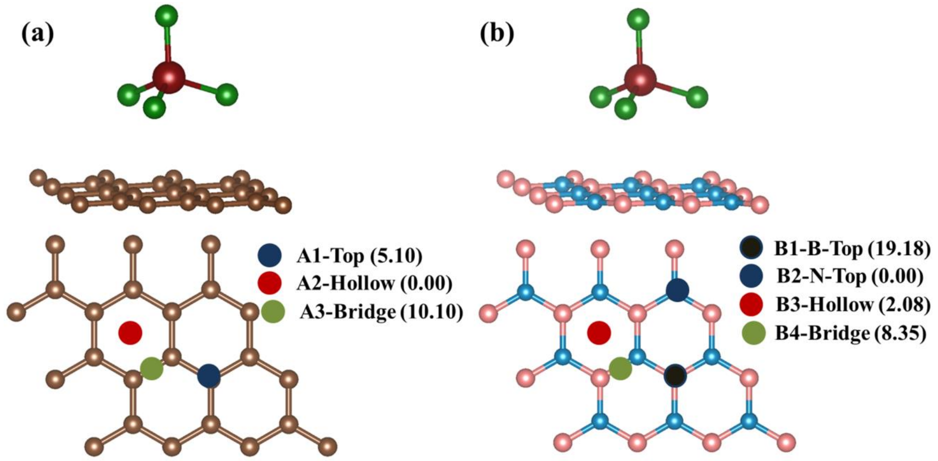

Figure 3.2: Representations of $AlCl_4$ adsorption sites in (a) graphene, and (b) h-BN with their relative energies given in parenthesis in meV.

Next, to study the nature of interaction between $AlCl_4$ and G/hBN heterostructure, we have evaluated the charge density difference (ρ_{CDD}) using following equation,

$$\rho_{CDD} = \rho^{total} - \sum_i \rho_i^{fragments} \tag{3.10}$$

where, the ρ^{total} is the total charge density of the system and $\rho_i^{fragments}$ is the charge density of the individual fragments by which the system is made of. Here, the charge density of the fragments ($\rho_i^{fragments}$) is calculated by a pseudo structure in which fragment part retains the same structure as in the total system but other parts are deleted. The charge density difference plots of the most stable $AlCl_4$ bounded systems are given in Figure 3.3. The nature of the interaction is ionic as there is charge accumulation on the Cl atoms of $AlCl_4$, whereas charge depletion can be seen on the surfaces of graphene and hBN for surface adsorption of $AlCl_4$ in $AlCl_4$/G/hBN and G/hBN/$AlCl_4$ systems, respectively and in the interlayer spaces of G/hBN heterostructures, for interlayer $AlCl_4$ intercalation. The charge density difference plots clearly indicate towards the oxidation of G/h-BN heterostructure on $AlCl_4$ intercalation/adsorption, confirming that G/hBN heterostructure can behave in a similar manner as graphite electrode in Al batteries. The Bader charge analysis *[62-66]* is performed to determine the extent of charge transfer between $AlCl_4$ and G/hBN heterostructure for each stable site on surfaces as well as in interlayer spaces (Table 3.2). For the adsorption of $AlCl_4$ on outside surface of graphene, the amount of charge gain on $AlCl_4$ is -0.43 |e|, while the calculated charges of graphene and hBN are +0.41 |e| and +0.02 |e|. In a similar way, when one $AlCl_4$ is adsorbed on the hBN surface, the charge transferred to $AlCl_4$ and net charge on hBN and graphene are -0.39 |e|, +0.19|e|, and +0.21 |e|, respectively. Here, both hBN and graphene layer influence the adsorption of $AlCl_4$ on hBN outer surface as can be seen from the charge density difference plot (Figure 3.3c), Bader charge calculations as well as the binding energies that significantly improves in G/hBN/$AlCl_4$ compared to $AlCl_4$ binding in pristine hBN (hBN/$AlCl_4$). Moreover, the maximum charge transferred values is obtained for the interlayer binding with the charge transfer of -0.65 |e| to $AlCl_4$, where also both inner surfaces of graphene and hBN layers actively interact with the all four Cl atoms of intercalated $AlCl_4$ via the charge transfer of -0.35 |e| and -0.30 |e|, respectively.

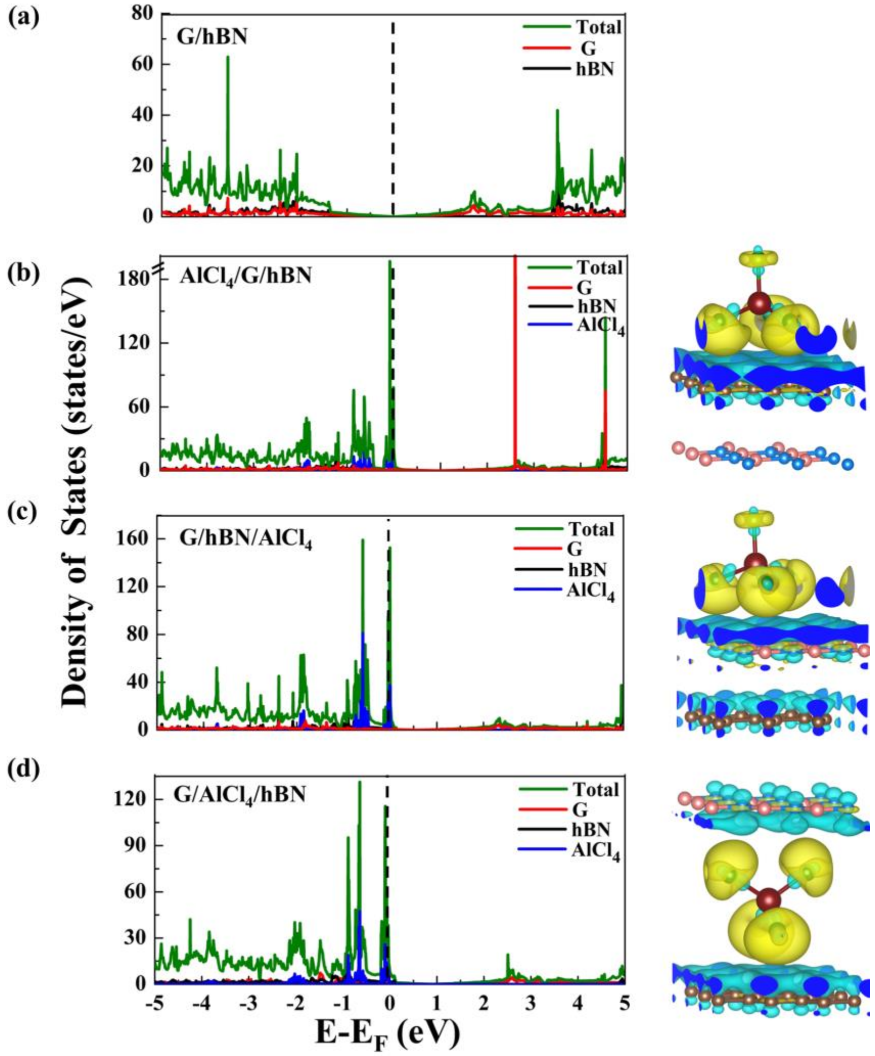

Figure 3.3: The TDOS and PDOS of (a) pristine G/hBN, (b) AlCl$_4$/G/hBN, (c) G/hBN/AlCl$_4$, and (d) G/AlCl$_4$/hBN and the corresponding charge density difference plots.

The important electronic property, which can affect the rate capability of an electrode, is the electronic conductivity. As analysed earlier, the monolayer of graphene and h-BN are zero band gap semimetal and insulator (4.64 eV band gap), respectively (Figure 3.4), whereas, G/hBN at the interlayer distance of 3.32 Å show similar electron density distribution as of graphene (Figure 3.3a) with a band gap of 0.03 eV which is in good agreement with previous report *[74-75]*. Therefore, the G/hBN is capable of showing similar electron conductivity like graphene electrode. The adsorption/intercalation of $AlCl_4$ introduces sizable density of states at the Fermi level due to the charge transfer from G/hBN to $AlCl_4$ and shifts the Fermi level towards the valence band as shown in Figure 3.3 (b, c, d). In all $AlCl_4$ adsorbed/intercalated G/hBN systems, significant overlap between graphen and hBN layer, and bonded $AlCl_4$ can be clearly seen, further indicating the notable interaction between $AlCl_4$ and G/hBN heterostructure. Overall, we can say the $AlCl_4$ adsorbed/intercalated G/hBN system can deliver good electrical conductance which is beneficial for battery applications.

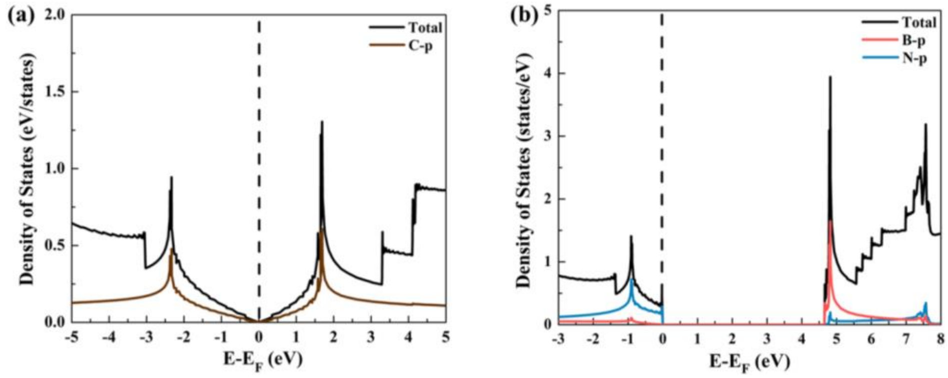

Figure 3.4: Total and projected density of states of (a) graphene, and (b) hBN. The Fermi level is set at zero.

3.3.2. Electrochemical Properties

The electrochemical properties such as voltage and specific storage capacity are the important characteristics to determine the suitability of a working battery. And to analyse these two characteristics, we should know upto which extent of the adsorbed/intercalated ions, the considered electrode is stable. Therefore, we first investigate the total number of $AlCl_4$ which are stable in G/hBN heterostructure, and for this we have considered a 6 × 6 × 1 supercell involving $AlCl_4$ binding in step by step manner. Various binding arrangements of $AlCl_4$ in G/hBN heterostructure are checked and the most stable arrangements are shown in Figure 3.5. The binding energy of $AlCl_4$ in $AlCl_4$/G/hBN is higher than that of

G/hBN/$AlCl_4$ and G/$AlCl_4$/hBN, therefore at lower concentration till $(AlCl_4)_{0.125}[C_9/(hBN)_{4.5}]$ only the sites available on outer graphene surface are occupied. After that the adsorption also initiates at the outer surface of hBN, and as per the optimized structural arrangements and binding energy values, both outer surfaces of graphene and hBN preferably bind $AlCl_4$, reaching to the stoichiometry $(AlCl_4)_{1.00}[C_9/(hBN)_{4.5}]$. On further increase in $AlCl_4$ concentration, the interlayer spaces of G/hBN also start to bind $AlCl_4$ and the G/hBN heterostructure reaches its highest occupation concentration having $(AlCl_4)_{1.50}[C_9/(hBN)_{4.5}]$ stoichiometry.

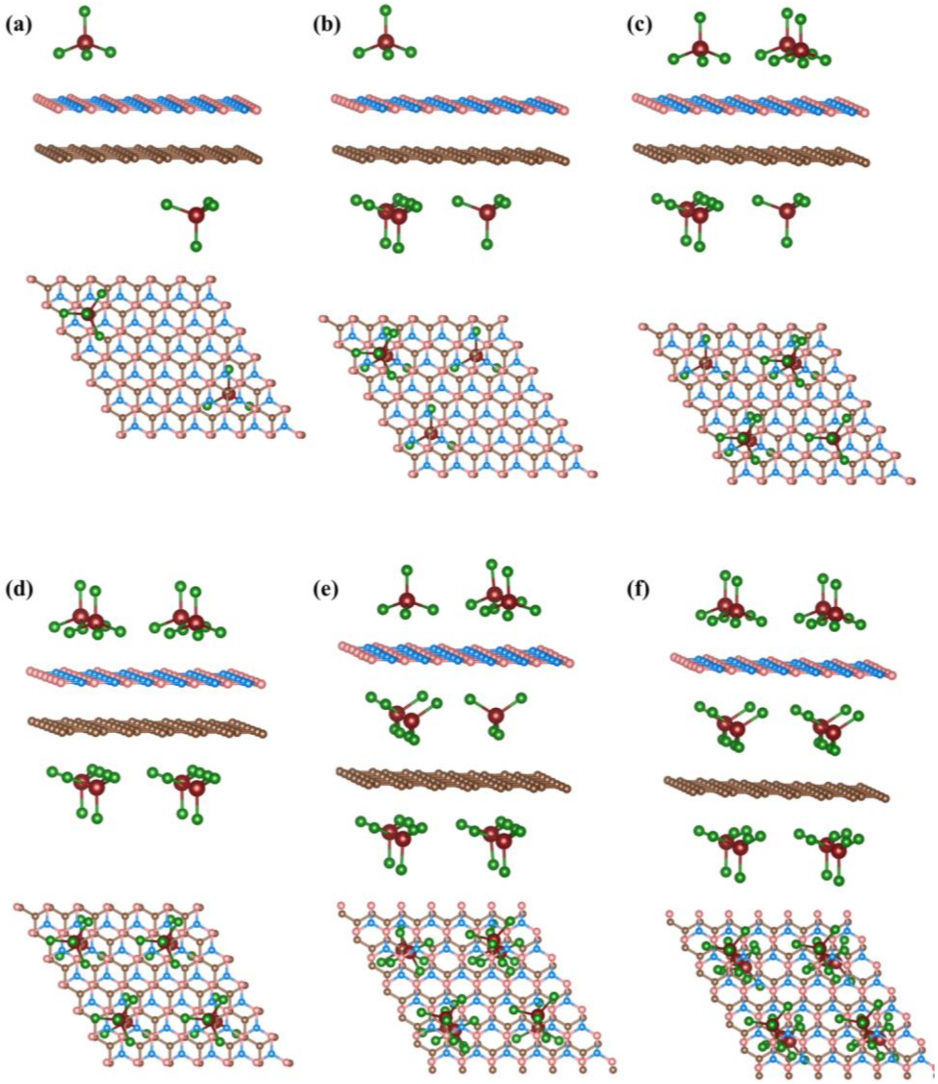

Figure 3.5: The most stable arrangements of $AlCl_4$ in different possible concentrations after geometry optimizations.

To determine the voltage during the $AlCl_4$ adsorption/intercalation process in G/hBN heterostructure, we have analysed the voltage profile diagram for the intercalation of $AlCl_4$ molecules as function of molar ratio between $AlCl_4$ and G/hBN and the voltage has been calculated using equation 8. For comparison, the voltage profiles of pristine graphene and hBN are also be studied by evaluating the $AlCl_4$ adsorption on the 6 × 6 × 1 supercell of each system and are shown with the voltage profile of G/hBN in Figure 3.6. For G/hBN heterostrcture, the voltage varies in the range of 1.46-2.43 V with net average voltage of 2.14 V. The voltage profile of G/hBN heterostructure (represented by green color) show that the highest achievable voltage of 2.43 V at $(AlCl_4)_{1.25}[C_9/(hBN)_{4.5}]$ stoichiometry is obtained when the binding of $AlCl_4$ starts into the interlayer spacing of G/hBN heterostructure. The reason being the large energy change required to open up the partially closed interlayer spaces, resulting into a comparatively higher voltage value. The next successive intercalation step becomes easy in the already expanded G/hBN interspace involving small energy change and comparatively low voltage value. As a result, the voltage further drops to 2.19 V to achieve the stoichiometry of $(AlCl_4)_{1.50}[C_9/(hBN)_{4.5}]$ before exceeding the limit of electrochemical stability window of the EMIMCl:$AlCl_3$ electrolyte (EMIMCl:$AlCl_3$ electrolyte starts oxidizing at 2.45 V) *[19]*. So, the specific capacity which can be achieved with G/hBN heterostructure is 183 mAh/g. On comparing with the voltage profile of hBN, it can be clearly noted that hBN can furnish a maximum voltage of 2.37 V with an average voltage of 2.23 V, however due to its low binding affinity for $AlCl_4$ (compared to graphene and G/hBN heterostructure) the voltage reaches its limiting cutoff at a very low capacity value of 120 mAh/g. On the other hand, graphene due the strong binding with $AlCl_4$ can impart higher capacity of 248 mAh/g providing the possibility of $AlCl_4$ binding ability on both sides of its surface but with a quite less average voltage (1.99 V) compared to its heterostructure G/hBN. Therefore, we can say that G/hBN heterostructure can possibly work as better cathode with higher voltage and better specific capacity compared to pristine graphene and hBN.

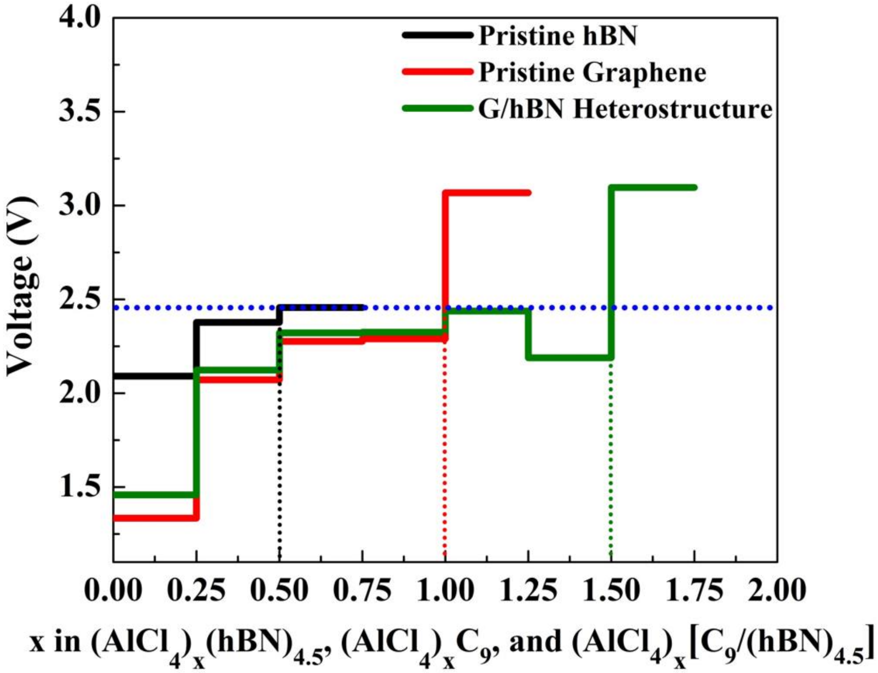

Figure 3.6: The voltage profile as a function of increasing $AlCl_4$ concentration in $(AlCl_4)_xC_9$ (red), $(AlCl_4)_x(hBN)_{4.5}$ (black) and $(AlCl_4)_x[C_9/(hBN)_{4.5}]$ (green). The blue dotted line corresponds to the experimental cut-off voltage (2.45 V) used in Al battery. The black, red, and green dotted lines represent the maximum stable concentration of $AlCl_4$ in pristine hBN, graphene and G/hBN heterostructure, respectively.

Further, we study the variation in the surface area (A) of G/hBN on binding of $AlCl_4$ during the charging process. Small change in the area of electrode with varying $AlCl_4$ is beneficial for the overall cycle stability of the Al battery. The percentage change in the surface area of G/hBN heterostructure can be studied using the equation,

$$\Delta A = (A_{(AlCl_4)_xG/BN} - A_{G/BN})/A_{G/BN} \tag{3.12}$$

where, $A_{(AlCl_4)_x G/BN}$ and $A_{G/BN}$ are the area of the heterostructure with and without $AlCl_4$ binding, respectively. The variation of G/hBN area with increasing $AlCl_4$ concentration is shown in Figure 3.7, Supporting Information, and we can clearly observe that there is only 0.33 % increase for the fully charged system. This confirms the suitability of G/hBN heterostructure for Al batteries.

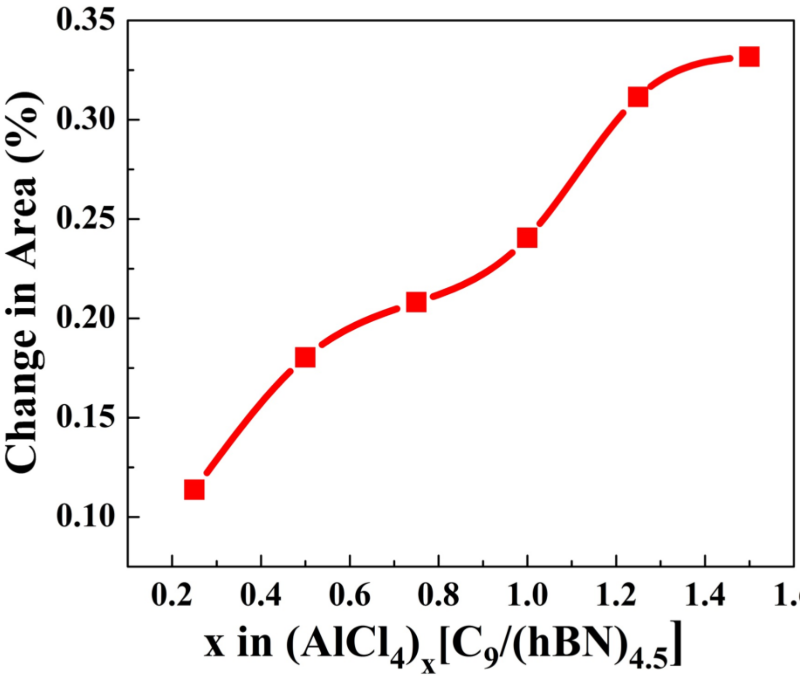

Figure 3.7: The variation of percentage change in area as a function of increasing $AlCl_4$ concentration $(AlCl_4)_x[C_9/(hBN)_{4.5}]$ heterostructure.

3.3.3. Diffusion Properties of $AlCl_4$

The charge/discharge rate of a battery is closely related to the mobility of involved ions, thus we next determine the diffusion barrier for $AlCl_4$ in G/hBN heterostructure using the CI-NEB method *[67]*. Due to the different possibilities of $AlCl_4$ binding (surfaces of G and hBN and interlayer space), three possible cases can be studied for $AlCl_4$ diffusion, (1) $AlCl_4$ diffusion over the surface of graphene in G/hBN system, (2) $AlCl_4$ diffusion over the surface of hBN, and (3) $AlCl_4$ diffusion in the interlayer space of G/hBN. We have used a 6 × 6 × 1 supercell of G/hBN to identify the diffusion paths and the corresponding diffusion barriers as shown in Figure 4. First, we investigate the diffusion of $AlCl_4$ on the surface of graphene ($AlCl_4$/G/hBN), and for this system four diffusion paths (path-1, path-2, path-3, and path-4) are possible along the xy-direction from most stable C-top site to the neighbouring stable top sites as shown in Figure 3.8a. We observe that the path-1 permits the minimum diffusion barrier of 0.02 eV along the x-direction. In a similar way, for the $AlCl_4$ diffusion on outside surface of hBN, four diffusion paths are studied varying along the xy-direction between the neighbouring most stable hollow sites, as presented in Figure 3.8b. The diffusion barriers along these four paths are given in Figure 3.8b, having the minimum value for path-1 which passes through intermediate bridge-BN site with the energy barrier of 0.01 eV. On comparing the surface diffusion of $AlCl_4$ in pristine graphene (0.01eV) (Figure 3.9), there is slight increment in the energy barrier on the outside surfaces of graphene of G/hBN heterostructure, however the diffusion barrier are remains same for G/hBN/$AlCl_4$ outer surface diffusion and pristine hBN (0.01 eV). Similar results have been also reported for Li-ion battery using blue phosphorene/borophene heterostructure *[42]*. This could be explained on the basis of surface reconstruction of G/hBN heterostructure caused by the interaction of graphene and hBN layers. The outer surfaces of G/hBN bind $AlCl_4$ more strongly (-1.37 eV in graphene, and -0.96 eV in hBN) with $AlCl_4$-surface distance of 3.27 Å for graphene and hBN. Whereas, the pristine graphene and hBN surfaces bind $AlCl_4$ with relatively small adsorption energy of -1.36 eV and -0.92 eV at surface-$AlCl_4$ distance of 3.28 Å and 3.32 Å, respectively, which could be the influential factor in determining the energy barrier.

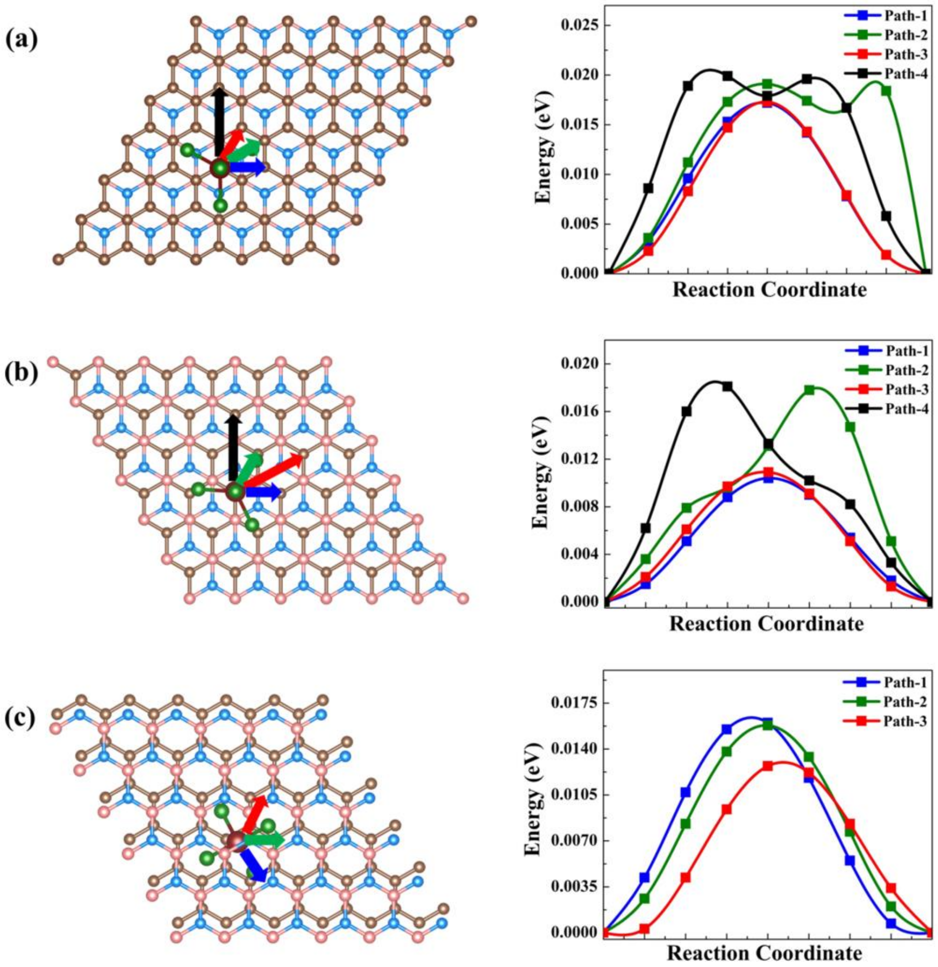

Figure 3.8: Diffusion paths and corresponding energy barriers of $AlCl_4$ diffusion in, (a) $AlCl_4$/G/hBN, (b) G/hBN/$AlCl_4$, and (c) G/$AlCl_4$/hBN.

Similarly, for obtaining the $AlCl_4$ diffusion in the interlayer space of G/hBN (G/$AlCl_4$/hBN), three diffusion paths have been considered represented by path-1, path-2, and path-3 depicted in Figure 3.8c along with the corresponding energy barriers. The minimum diffusion barrier 0.01 eV is obtained for the path-3, compared to 0.02 eV for path-1 and path-2. It is worth noting that the diffusion barrier inside the interlayer space of G/hBN is higher, even the $AlCl_4$ binding energy in interlayer is less than that of outer surface of hBN. This is because of the more restricted environment of interlayer space as compared to surfaces of G/hBN heterostructure. On comparing with previously reported electrode for Al batteries, such as graphite, BC_3, C_3N, it can be seen that the energy barrier of this heterojunction is relatively low *[21,23,29]*. Overall, we can say that the G/hBN is capable of providing excellent rate performance for Al batteries.

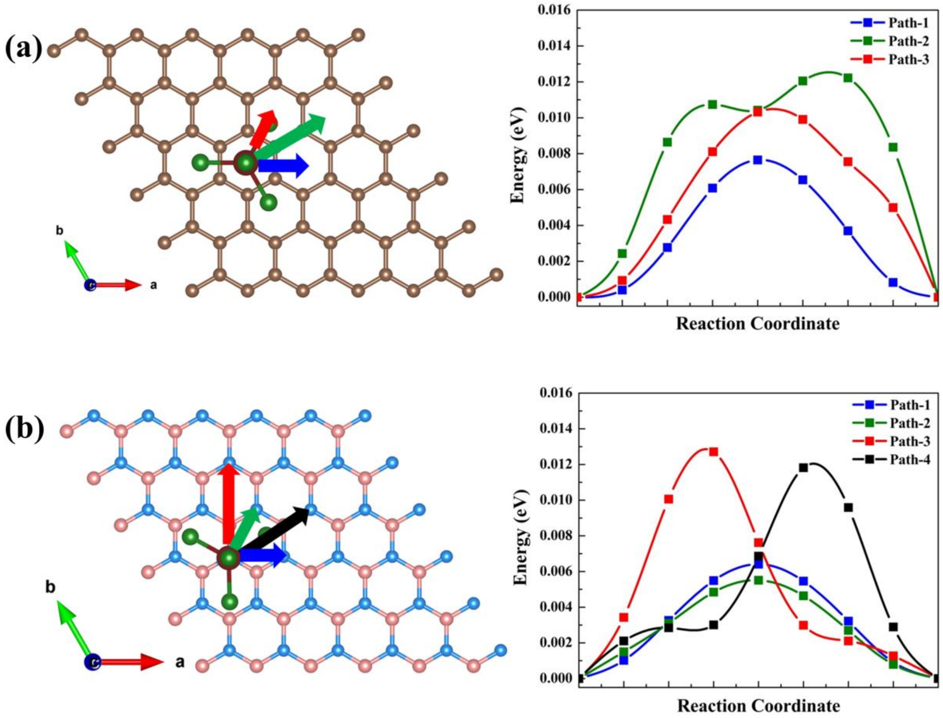

Figure 3.9: Diffusion paths and corresponding energy barriers of $AlCl_4$ diffusion in, (a) garphene, (b) hBN.

3.4. Conclusion

In this work, we have systematically investigated the suitability of G/hBN heterostucture as a cathode material of Al batteries using the first principles calculations. By means of comparative analysis of structural and binding studies, we observe that the binding energy of $AlCl_4$ incorporation into the G/hBN is significantly improved compared to the pristine graphene and hBN. The charge-density difference analysis and Bader charge calculation indicate the oxidation of the G/hBN upon $AlCl_4$ adsorption, which shows a similar electrochemical behaviour to that of $AlCl_4$ intercalation into graphite. The total and projected density of states plots show that the $AlCl_4$ intercalated G/hBN systems is metallic in nature, which insures an excellent electronic conductivity when used as a battery electrode. Moreover, we observe that the G/hBN heterostructure can show diffusion barrier as small as 0.01 eV for the outer hBN surface diffusion, which is comparatively lower than experimentally studied graphite electrode. Moreover, the voltage of 2.14 V and efficient storage capacity of 183 mAh/g obtained in G/hBN heterostructure are larger than that obtained in monolayer graphene which provides high storage capacity (248 mAh/g) but with small voltage (1.99 V) and monolayer hBN imparting a voltage of 2.23 V while having very less capacity (120 mAh/g). All these results suggest that the G/BN heterostructure could be an ideal cathode material choice for Al batteries and other 2D heterostructures should also be examined for Al batteries.

3.5. References

1. Dubal D. P., Ayyad O., Ruiz V., Gómez-Romero P. (2015), Hybrid energy storage: the merging of battery and supercapacitor chemistries, Chem. Soc. Rev., 44, 1777−1790 (DOI: 10.1039/C4CS00266K)
2. Bonaccorso F., Colombo L., Yu G., Stoller M., Tozzini V., Ferrari A. C., Ruoff R. S., Pellegrini V. (2015), Graphene related two dimensional crystals, and hybrid systems for energy conversion and storage, Science, 347, 1246501 (DOI: 10.1126/science.1246501)
3. Armand M., Tarascon J.-M. (2008), Building better batteries, Nature, 451, 652−657 (DOI: 10.1038/451652a)
4. Dunn B., Kamath H., Tarascon, J.-M. (2011), Electrical energy storage for the grid: A battery of choices, Science, 334, 928−935 (DOI: 10.1126/science.1212741)
5. Lee J., Urban A., Li X., Su D., Hautier G., Ceder G. (2014), Unlocking the potential of cation-disordered oxides for rechargeable lithium batteries, Science, 343, 519−522 (DOI: 10.1126/science.1246432)

6. Aurbach D., Lu Z., Schechter A., Gofer Y., Gizbar H., Turgeman R., Cohen Y., Moshkovich M., Levi E. (2000), Prototype systems for rechargeable magnesium batteries, Nature, 407, 724−727 (DOI: 10.1038/35037553)
7. Goodenough J. B., Kim Y. (2009), Challenges for rechargeable Li batteries, Chem. Mater., 22, 587−603 (DOI: 10.1021/cm901452z)
8. Hariprakash B., Mane A. U., Martha S. K., Gaffoor S. A., Shivashankar S. A., Shukla A. K. (2004), A low-cost, high energy-density lead/acid battery, Electrochem. Solid-State Lett., 7, A66 (DOI: 10.1149/1.1645752)
9. May G. J., Davidson A., Monahov B. (2018), Lead batteries for utility energy storage: A Review, J. Energy Storage, 15, 145−157 (DOI: 10.1016/j.est.2017.11.008)
10. Newman R. H. (1994), Advantages and disadvantages of valve-regulated, lead/acid batteries, J. Power Sources, 52, 149−153 (DOI:10.1016/0378-7753(94)01940-1)
11. Fleischer M. (1953), Recent estimates of the abundances of the elements in this earth’s crust, Geological Survey Circular, 285, 1−6 (DOI: 10.3133/cir285)
12. Muldoon J., Bucur C. B., Gregory T. (2014), Quest for nonaqueous multivalent secondary batteries: magnesium and beyond, Chem. Rev., 114, 11683−11720 (DOI: 10.1021/cr500049y)
13. Gifford P. R., Palmisano J. B. (1988), An aluminum/chlorine rechargeable cell employing a room temperature molten salt electrolyte, J. Electrochem. Soc., 135, 650 (DOI: 10.1149/1.2095685)
14. Jayaprakash N., Das S. K., Archer L. A. (2011), The rechargeable aluminum-ion battery, Chem. Commun., 47, 12610 (DOI: 10.1039/C1CC15779E)
15. Rani J. V., Kanakaiah V., Dadmal T., Rao M. S., Bhavanarushi S. (2013), Fluorinated natural graphite cathode for rechargeable ionic

liquid based aluminum-ion battery, J. Electrochem. Soc., 160, A1781−A1784 (DOI: 10.1149/2.072310jes)

16. Ambroz F., Macdonald T. J., Nann T. (2017), Trends in aluminium-based intercalation batteries, Adv. Energy Mater., 7, 1602093 (DOI: 10.1002/aenm.201602093)
17. Li C., Zhang X., He W. (2018), Design and modification of cathode materials for high energy density aluminum-ion batteries: A Review, J. Mater. Sci.: Mater. Electron., 29, 14353−14370 (DOI: 10.1007/s10854-018-9478-1)
18. Hudak N. S. (2014), Chloroaluminate-doped conducting polymers as positive electrodes in rechargeable aluminum batteries, J. Phys. Chem. C, 118, 5203−5215 (DOI: 10.1021/jp500593d)
19. Lin M.-C., Gong M., Lu B., Wu Y., Wang D.-Y., Guan M., Angell M., Chen C., Yang J., Hwang B.-J., et al. (2015), An ultrafast rechargeable aluminium-ion battery, Nature, 520, 324−328 (DOI: 10.1038/nature14340)
20. Sun H., Wang W., Yu Z., Yuan Y., Wang S., Jiao S. (2015), A new aluminium-ion battery with high voltage, high safety and low cost, Chem. Commun., 51, 11892−11895 (DOI: 10.1039/C5CC00542F)
21. Bhauriyal P., Mahata A., Pathak B. (2017), The staging mechanism of AlCl4 intercalation in a graphite electrode for an aluminium-ion battery, Phys. Chem. Chem. Phys., 19, 7980−7989 (DOI: 10.1039/C7CP00453B)
22. Bhauriyal P., Mahata A., Pathak B. (2017), A computational study of a single-walled carbon-nanotube-based ultrafast high-capacity aluminum battery, Chem. Asian J., 12, 1944−1951 (DOI: 10.1002/asia.201700570)
23. Bhauriyal P., Mahata A., Pathak B. (2017), Hexagonal BC3 electrode for a high-voltage Al-ion battery, J. Phys. Chem. C, 121, 9748− 9756 (DOI: 10.1021/acs.jpcc.7b02290)

24. Wu M. S., Xu B., Chen L. Q., Ouyang C. Y. (2016), Geometry and fast diffusion of AlCl4 cluster intercalated in graphite, Electrochim. Acta, 195, 158−165 (DOI: 10.1016/j.electacta.2016.02.144)
25. Jung S. C., Kang Y.-J., Yoo D.-J., Choi J. W., Han Y.-K. (2016), Flexible few-layered graphene for the ultrafast rechargeable aluminum-ion battery, J. Phys. Chem. C, 120, 13384−13389 (DOI: 10.1021/acs.jpcc.6b03657)
26. Agiorgousis M. L., Sun Y.-Y., Zhang S (2017), The role of ionic liquid electrolyte in an aluminum-graphite electrochemical cell, ACS Energy Lett., 2, 689−693 (DOI: 10.1021/acsenergylett.7b00110)
27. Kravchyk K. V., Wang S., Piveteau L., Kovalenko M. V. (2017), Efficient aluminum chloride-natural graphite battery, Chem. Mater., 29, 4484−4492 (DOI: 10.1021/acs.chemmater.7b01060)
28. Zafar Z. A., Imtiaz S., Razaq R., Ji S., Huang T., Zhang Z., Huang Y., Anderson J. A. (2017), Cathode materials for rechargeable aluminum batteries: current status and progress, J. Mater. Chem. A, 5, 5646−5660 (DOI:10.1039/C7TA00282C)
29. Bhauriyal P., Garg P., Patel M., Pathak B. (2018), Electron-rich graphite-like electrode: stability vs. voltage for Al batteries, J. Mater. Chem. A, 6, 10776 (DOI:10.1039/C8TA01820K)
30. Wang S., Kravchyk K. V., Krumeich F., Kovalenko M. V. (2017), Kish graphite flakes as a cathode material for an aluminum chloride-graphite battery, ACS Appl. Mater. Interfaces, 9, 28478−28485 (DOI: 10.1021/acsami.7b07499)
31. Jiao H., Wang C., Tu J., Tian D., Jiao S. (2017), A rechargeable Al-ion battery: Al/molten AlCl3−urea/graphite, Chem. Commun., 53, 2331−2334 (DOI:10.1039/C6CC09825H)
32. Uemura Y., Chen C.-Y., Hashimoto Y., Tsuda T., Matsumoto H., Kuwabata S. (2018), Graphene nanoplatelet composite cathode for a chloroaluminate ionic liquid-based aluminum secondary battery, ACS Appl. Energy Mater., 1, 2269−2274 (DOI: 10.1021/acsaem.8b00341)

33. Wu Y., Gong M., Lin M.-C., Yuan C., Angell M., Huang L., Wang D.-Y., Zhang X., Yang J., Hwang B.-J., et al. (2016), 3D graphitic foams derived from chloroaluminate anion intercalation for ultrafast aluminum-ion battery, Adv. Mater., 28, 9218 (DOI: 10.1002/adma.201602958)
34. Wheelock P. B., Cook B. C., Harringa J. L., Russell A. M. (2004), Phase changes induced in hexagonal boron nitride by high energy mechanical milling, J. Mater. Sci., 39, 343−347 (DOI: 10.1023/B:JMSC.0000008086.48380.01)
35. Cassabois G., Valvin P., Gil B. (2016), Hexagonal boron nitride is an indirect bandgap semiconductor, Nat. Photonics, 10, 262−266 (DOI: 10.1038/nphoton.2015.277)
36. Pomerantseva E., Gogotsi Y. (2017), Two-dimensional heterostructures for energy storage, Nat. Energy, 2, 17089 (DOI: 10.1038/nenergy.2017.89)
37. Sadeghi H., Sangtarash S., Lambert C. J. (2017), Cross-plane enhanced thermoelectricity and phonon suppression in graphene/ MoS2 van der Waals heterostructures, 2D Mater., 4, 015012 (DOI:10.1088/2053-1583/4/1/015012)
38. Chiku M., Takeda H., Matsumura S., Higuchi E., Inoue H. (2015), Amorphous vanadium oxide/carbon composite positive electrode for rechargeable aluminum battery, ACS Appl. Mater. Interfaces, 7, 24385−24389 (DOI: 10.1021/acsami.5b06420)
39. Wang J., Ma F., Liang W., Sun M. (2017), Electrical properties and applications of graphene, hexagonal boron nitride (h-BN), and graphene/h-BN heterostructures, Mater. Today Phys., 2, 6−34 (DOI: 10.1016/j.mtphys.2017.07.001)
40. Shirodkar S. N., Kaxiras E. (2016), Li intercalation at graphene/ hexagonal boron nitride interfaces, Phys. Rev. B: Condens. Matter Mater. Phys., 93, 245438 (DOI: 10.1103/PhysRevB.93.245438)

41. Guo G.-C., Wang D., Wei X.-L., Zhang Q., Liu H., Lau W.-M., Liu L.-M. (2015), First-principles study of phosphorene and graphene heterostructure as anode materials for rechargeable Li batteries, J. Phys. Chem. Lett., 6, 5002−5008 (DOI: 10.1021/acs.jpclett.5b02513)
42. Li Q., Yang J., Zhang L. (2018), Theoretical prediction of blue phosphorene/borophene heterostructure as a promising anode material for lithium-ion batteries, J. Phys. Chem. C, 122, 18294−18303 (DOI: 10.1021/acs.jpcc.8b05076)
43. Mikhaleva N. S., Visotin M. A., Kuzubov A. A., Popov Z. I. (2017), VS2/graphene heterostructures as promising anode material for Li- ion batteries, J. Phys. Chem. C, 121, 24179−24184 (DOI: 10.1021/acs.jpcc.7b07630)
44. Liu H., Huang Z., Wu G., Wu Y., Yuan G., He C., Qi X., Zhong J. (2018), A novel WS2/NbSe2 vdW heterostructure as an ultrafast charging and discharging anode material for lithium-ion batteries, J. Mater. Chem. A, 6, 17040−17048 (DOI:10.1039/C8TA05531A)
45. Shi L., Zhao T. S., Xu A., Xu J. B. (2016), Ab initio prediction of a silicene and graphene heterostructure as an anode material for Li- and Na-ion batteries, J. Mater. Chem. A, 4, 16377−16382 (DOI:10.1039/C6TA06976B)
46. Wang J., Ma F., Sun M. (2017), Graphene, hexagonal boron nitride, and their heterostructures: properties and applications, RSC Adv., 7, 16801−16822 (DOI:10.1039/C7RA00260B)
47. Oshima C., Itoh A., Rokuta E., Tanaka T., Yamashita K., Sakurai T. (2000), A hetero-epitaxial-double-atomic-layer system of monolayer graphene/monolayer h-BN on Ni(111), Solid State Commun., 116, 37−40 (DOI: 10.1016/S0038-1098(00)00268-4)
48. Giovannetti G., Khomyakov P. A., Brocks G., Kelly P. J., van den Brink J. (2007), Substrateinduced band gap in graphene on hexagonal boron nitride: ab initio density functional calculations, Phys. Rev. B:

Condens. Matter Mater. Phys., 76, 073103 (DOI: 10.1103/PhysRevB.76.073103)

49. Fan Y., Zhao M., Wang Z., Zhang X., Zhang H. (2011), Tunable electronic structures of graphene/boron nitride heterobilayers, Appl. Phys. Lett., 98, 083103 (DOI: 10.1063/1.3556640)
50. Zhong X., Yap Y. K., Pandey R., Karna S. P. (2011), First-principles study of strain-induced modulation of energy gaps of graphene/BN and BN bilayers, Phys. Rev. B: Condens. Matter Mater. Phys., 83, 193403 (DOI: 10.1103/PhysRevB.83.193403)
51. Mayorov A. S., Gorbachev R. V., Morozov S. V., Britnell L., Jalil R., Ponomarenko L. A., Blake P., Novoselov K. S., Watanabe K., Taniguchi T. et al. (2011), Micrometer-scale ballistic transport in encapsulated graphene at room temperature, Nano Lett., 11, 2396−2399 (DOI: 10.1021/nl200758b)
52. BlÖchl P. E. (1994), Projector augmented-wave method, Phys. Rev. B: Condens. Matter Mater. Phys., 50, 1795 −17979 (DOI: 10.1103/PhysRevB.50.17953)
53. Kresse G., Joubert D. (1999), From ultrasoft pseudopotentials to the projector augmented-wave method, Phys. Rev. B: Condens. Matter Mater. Phys., 59, 1758 (DOI: 10.1103/PhysRevB.59.1758)
54. Kresse G., Hafner J. (1993), Ab initiomolecular dynamics for liquid metals, Phys. Rev. B: Condens. Matter Mater. Phys., 47, 558 (DOI: 10.1103/PhysRevB.47.558)
55. Kresse G., Hafner J. (1994), Ab initiomolecular-dynamics simulation of the liquid-metal-amorphous-semiconductor transition in germanium, Phys. Rev. B: Condens. Matter Mater. Phys., 49, 14251 (DOI: 10.1103/PhysRevB.49.14251)
56. Kresse G., Furthmüller J. (1996), Efficiency of ab-initio total energy calculations for metals and semiconductors using a plane-wave basis set, Comput. Mater. Sci., 6, 15−50 (DOI: 10.1016/0927-0256(96)00008-0)

57. Kresse G., Furthmüller J. (1996), Efficient iterative schemes for ab initio total-energy calculations using a plane-wave basis set, Phys. Rev. B: Condens. Matter Mater. Phys., 54, 11169−11186 (DOI: 10.1103/PhysRevB.54.11169)
58. Perdew J. P., Burke K., Ernzerhof, M. (1996), Generalized gradient approximation made simple, Phys. Rev. Lett., 77, 3865−3868 (DOI: 10.1103/PhysRevLett.77.3865)
59. Perdew J. P., Burke K., Ernzerhof M. (1996), Generalized gradient approximation made simple, Phys. Rev. Lett. 1997, 78, 1396 (DOI: 10.1103/PhysRevLett.77.3865)
60. Grimme S., Antony J., Ehrlich S., Krieg H. (2010), A consistent and accurate ab initio parametrization of density functional dispersion correction (DFT-D) for the 94 Elements H-Pu, J. Chem. Phys., 132, 154104 (DOI: 10.1063/1.3382344)
61. Wang D. Y., Wei C. Y., Lin M. C., Pan C. J., Chou H. L., Chen H. A., Gong M., Wu Y., Yuan C., Angell M., Hsieh Y. J. (2017), Advanced rechargeable aluminium ion battery with a high-quality natural graphite cathode, Nat. Commun., 8, 14283 (DOI: 10.1038/ncomms14283)
62. Bader R. F. W. (1991), A quantum theory of molecular structure and its applications, Chem. Rev., 91, 893−928 (DOI: 10.1021/cr00005a013)
63. Henkelman G., Arnaldsson A., Jónsson H. (2006), A fast and robust algorithm for Bader decomposition of charge density, Comput. Mater. Sci., 36, 354−360 (DOI: 10.1016/j.commatsci.2005.04.010)
64. Sanville E., Kenny S. D., Smith R., Henkelman G. (2007), Improved grid-based algorithm for Bader charge allocation, J. Comput. Chem., 28, 899−908 (DOI: 10.1002/jcc.20575)
65. Rawat K. S., Mahata A., Pathak B. (2017), Thermochemical and electrochemical CO 2 reduction on octahedral Cu nanocluster: role of

solvent towards product selectivity, J. Catal., 349, 118−127 (DOI:10.1039/C9CP02394A)

66. Tang W., Sanville E., Henkelman G. (2009), A grid-based Bader analysis algorithm without lattice bias, J. Phys.: Condens. Matter, 21, 084204 (DOI: 10.1088/0953-8984/21/8/084204)
67. Henkelman G., Uberuaga B. P., Jónsson H. (2000), A climbing image nudged elastic band method for finding saddle points and minimum energy paths, J. Chem. Phys., 113, 9901−9904 (DOI: 10.1063/1.1329672)
68. Lebedev A. V., Lebedeva I. V., Popov A. M., Knizhnik A. A. (2017), Stacking in incommensurate graphene/hexagonal-boron-nitride heterostructures based on ab initio study of interlayer interaction, Phys. Rev. B, 96, 085432 (DOI: 10.1103/PhysRevB.96.085432)
69. Zhou S., Han J., Dai S., Sun J., Srolovitz D. J. (2015), van der Waals bilayer energetics: generalized stacking-fault energy of graphene, boron nitride, and graphene/boron nitride bilayers, Phys. Rev. B: Condens. Matter Mater. Phys., 92, 155438 (DOI: 10.1103/PhysRevB.92.155438)
70. Chowdhury C., Karmakar S., Datta A. (2016), Capping black phosphorene by h-BN enhances performances in anodes for Li and Na ion batteries, ACS Energy Lett., 1, 253−259 (DOI: 10.1021/acsenergylett.6b00164)
71. Lynch R. W., Drickamer H. G. (1966), Effect of high pressure on the lattice parameters of diamond, graphite, and hexagonal boron nitride, J. Chem. Phys., 44, 181 (DOI: 10.1063/1.1726442)
72. Aydinol M. K., Kohan A. F., Ceder G., Cho K., Joannopoulos J. (1997), Ab initiostudy of lithium intercalation in metal oxides and metal dichalcogenides, Phys. Rev. B: Condens. Matter Mater. Phys., 56, 1354 (DOI: 10.1103/PhysRevB.56.1354)
73. Bhauriyal P., Mahata A., Pathak B. (2018), Graphene-like carbon-nitride monolayer: a potential anode material for Na- and K-ion

batteries, J. Phys. Chem. C, 122, 2481−2489 (DOI: 10.1021/acs.jpcc.7b09433)

74. Choudhuri I., Pathak B. (2018), Ferromagnetism and half-metallicity in a high-band-gap hexagonal boron nitride system, ChemPhysChem, 19, 153−161 (DOI: 10.1002/cphc.201700759)
75. Kan E., Ren H., Wu F., Li Z., Lu R., Xiao C., Deng K., Yang J. (2012), Why the band gap of graphene Is tunable on hexagonal boron nitride, J. Phys. Chem. C, 116, 3142−3146 (DOI: 10.1021/jp2106988)

Chapter 4

A Computational Study of Single-walled Carbon Nanotube Based Ultrafast High Capacity Aluminium Battery

4.1. Introduction

Energy storage is an ever growing technology that satisfies the world's power need from portable electronic devices to electric vehicles and large-scale power grid systems *[1, 2]*. Among the different types of energy storage systems, secondary batteries have received remarkable attention because of their great advantages of compact size and high efficiency *[3-5]*. Secondary batteries also known as rechargeable batteries or storage battery which are potentially consist of reversible cell reactions that allow them to recharge their cell potential through the work done by passing currents of electricity *[3-5]*. A promising way of achieving these goals is the modification of metal-ion batteries that frames the efficiency and energy storage capacity of the secondary batteries *[6-8]*. The world's research interest is moving from the traditional Li-ion batteries, which are associated with the limitations such as safety, production cost, and reactivity *[9-11]* to the newly emerging field of multivalent batteries (Mg *[12-14]*, Zn *[15-16]*, Al *[17-26]*) due to their large natural resources, high energy density, and capacity. Among these developing technologies, aluminium batteries have distinctive advantages because its three electron redox couple provides high theoretical specific capacity 2.89 Ah/g and volumetric charge storage capacity 8.0 Ah/cm^3 *[19, 20]*. Many electrode materials have been studied for aluminium batteries which have essentially played an important role in increasing the efficiency of these batteries as well as opening new doors for further research attentive *[17-18, 20-23, 26]*. An aluminium battery that is comprised of three-dimensional graphitic-foam cathode graphite has attracted a worldwide attention due to its ultrafast charging rate and involvement of intercalation/deintercalation of $AlCl_4$ anions during charging/discharging respectively *[27]*. Soon after that, with the help of dispersion corrected DFT study, we predicted that not only the graphite foam, but the natural graphite can also be used as the cathode material in aluminium batteries, which intercalates tetrahedral $AlCl_4$ forming different stages with an average voltage of 2.3 V *[28]*. At the same time, some recent experimental studies on advanced rechargeable aluminium battery have also produced the similar results with natural graphite *[29-32]*. However, many experimental studies on anion intercalation and the theoretical study conducted by us into graphite electrode have shown that the very first intercalation step (cycle) differs from the other successive steps because it involves kind of activation of partially closed interlayer spaces of graphite layers during the first intercalation of the anion, which results into lower discharge capacities *[30, 33, 34]*. Thus it becomes important to look for other electrode materials which can overcome the interlayer gallery opening difficulty in the first intercalation step in graphite like layered materials *[28, 35]* and increase the battery performance.

Among the various carbon allotropes, carbon nanotubes (CNTs) based materials can be promising for the first intercalation step of aluminium battery. CNTs have been a subject of interest to chemists and physicists ever since discovered by Iijima in 1991 *[36]*. The superior electronic and structural properties of carbon nanotubes (CNTs) have significantly motivated the world's interest for the building blocks in future nanodevices. The literature surveys show that CNTs are considerably feasible for high storage capacity than their corresponding graphite counterparts with hollow structures which possess large surface area, more guest binding sites and easy transmission *[37-47]*. In addition, the tubular structure of CNTs acts as a host for various molecules and atoms that can be encapsulated inside CNTs and the hollow interior cavities provide large space for mitigating the strain associated with the structural change due to repeated guest intercalation/deintercalation, increasing the cycle life of batteries *[40, 48-49]*. Very recently, an aluminium asymmetric capacitor utilizing multi-walled carbon nanotube and Al metal anode is proposed which also involves adsorption/desorption and intercalation/deintercalation of $AlCl_4$ during charging/discharging of the capacitor *[50]*. However, the feasibility of carbon nanotubes for aluminium batteries is still unexplored.

In this present paper, we have studied the great potential of the armchair single-walled carbon nanotubes (SWNTs) to be the high capacity cathode materials for aluminium batteries. The first principles calculations are performed for the systematic study of $AlCl_4$ adsorption on SWNTs with varying diameters and locating different adsorption positions on each tube to evaluate the adsorption behaviour of the system and structural and thermal stability. The density of states, charge density difference *[51-52]*, and Bader charge *[53-59]* calculations are carried out to examine the extent of interaction between adsorbed $AlCl_4$ and the tube. We have also done the detailed investigation to understand the diffusion pathways for $AlCl_4$ diffusion in SWNT. Furthermore, we have also discussed the effect of varying SWNT diameters on the average open-circuit voltage and specific capacity of SWNT based aluminium batteries. Finally, we conclude that the results are promising and promote a potential electrode material for aluminium batteries.

4.2. Computational Details

We have used the density functional theory (DFT) as implemented in the Vienna Ab initio Simulation Package (VASP) in all calculations *[60, 61]*. The exchange-correlation potential is described by using the generalized gradient approximation of Perdew-Burke-Ernzerhof (GGA-PBE) *[62]*. The Projector augmented-wave (PAW) *[63]* method is employed to treat interactions between ion cores and valance electrons. The plane wave cut-off energy is fixed to 470 eV, which is sufficient for the convergence of total energy to 10^{-3} eV. The underlying structure optimizations are carried out using the van der Waals corrected density functional theory (DFT-D3) proposed by Grimme to overcome the deficiencies of DFT in treating dispersion interactions *[64]*. All the optimized structures are obtained by fully relaxing both atomic and lattice positions until the Hellmann-

Feynman forces on all atoms are smaller than 10^{-3} eV/Å. During the relaxation, the Brillouin zone is represented by Monkhorst-Pack special k-point meshes of 1 × 1 × 6 for the SWNTs. To avoid the periodic image interaction between the SWNTs, the inter-tube distances are set to 25 Å and the supercells contain six layers of carbon atoms. The Bader charge analysis is performed to measure the charge transfer between $AlCl_4$ and SWNT *[53-59]*. The density of states calculations are carried out with 1 × 1 × 12 k-point sampling of Monkhorst-Pack grid. The diffusion barriers and the minimum energy paths for $AlCl_4$ hopping between two most stable adsorption sites are obtained by using climbing-image nudged elastic band method (CI-NEB) *[65]*. The minimum energy paths (MEPs) are initialized by considering six image structures between fully optimized initial and final structural geometries, and the energy convergence criteria of each image is set to 10^{-3} eV. Activation barriers are calculated by the energy differences between the transition and initial states and the entropy corrections and Zero point energy (ZPE) correction are included while calculating the diffusion barriers. The ZPE is calculated as: $\mathrm{ZPE} = \sum_i \frac{hv_i}{2}$, where h is Planck's constant and v_i is vibrational frequency. The ZPE of the system is calculated by considering only the degrees of freedom of intercalated $AlCl_4$.

4.3. Results and Discussions

4.3.1. $AlCl_4$ Adsorption, Stability and Electronic Properties

Depending on the way the graphene is rolled, different chiralities are possible which are generally identified by their chiral vector (n,m). The SWNT is metallic, when the difference between two components of the chiral vector (n,m) is a multiple of 3, otherwise it is semiconducting. The metallic and semiconducting SWNTs have different electrochemical properties including the storage property *[66]*. It is well accepted by both theoretical and experimental studies that storage capacity of metallic single-walled CNTs is about 5 times greater than that of the semiconducting ones *[66]*. Therefore, based on their finding we have carried out our study using armchair metallic SWNTs *[67-68]*. Firstly, we have taken (10, 10) SWNT system as an example to study the adsorption behaviour, and electronic properties of $AlCl_4$ adsorbed SWNT. The (10, 10) SWNT is experimentally synthesized and has been immensely studied for Li-ion batteries *[37, 69-70]*.

Firstly, we start by examining the most stable geometry of $AlCl_4$ inside the nanotube, whether it is planar or tetrahedral. We obtained that the tetrahedral geometry of $AlCl_4$ is stable in SWNT and there is a negligible change in the geometry, Al-Cl bond lengths and Cl-Al-Cl bond angle of $AlCl_{4.}$ Also, there is very negligible structural distortion of SWNT after $AlCl_4$ adsorption. However, on examining the system stability with the planar $AlCl_4$ molecule, it is observed that the planar geometry of $AlCl_4$ changes to tetrahedral geometry after optimization. The stability of tetrahedral geometry over planar is in agreement with our gas phase calculations, where the tetrahedral $AlCl_4$ molecule is 0.88 eV more stable than the planar $AlCl_4$ and it is also supported by our earlier report for $AlCl_4$ intercalation in graphite *[28]*. The structural change of $AlCl_4$ from planar to tetrahedral in SWNT after adsorption justifies the energetic results that the tetrahedral $AlCl_4$ is more favourable in SWNT.

Next, we have studied the most stable adsorption site of $AlCl_4$ on the inner and outer surface of SWNT. Unlike the intercalation of $AlCl_4$ in graphite cathode, here the adsorption of $AlCl_4$ occurs on the SWNT surface and this concept of $AlCl_4$ adsorption has also been studied in the previous experimental reports *[20, 71]*. We have set three orientations of $AlCl_4$ adsorption as shown in Figure 4.1a-c. Further, we have considered five adsorption sites (Figure 1d-h): (i) hollow site 1 (H-1), (ii) hollow site 2 (H-2), (iii) top site 1 (T-1), (iv) top site 2 (T-2), and (v) bridge site (B). The binding of $AlCl_4$ on SWNT is studied by calculating the adsorption energy E_{ad} using the equation,

$$\mathrm{E_{ad}} = (\mathrm{E_{SWNT+AlCl_4}} - \mathrm{E_{SWNT}} - \mathrm{E_{AlCl_4}}) \tag{4.1}$$

where, $\mathrm{E_{SWNT+AlCl_4}}$ and $\mathrm{E_{SWNT}}$ and $\mathrm{E_{AlCl_4}}$ are the total energies of SWNT with $AlCl_4$, SWNT, and one $AlCl_4$ molecule in the box, respectively. The negative E_{ad} value means favourable adsorption. Our relative energetic study (Table 4.1) shows that $AlCl_4$ prefers to be adsorbed through 3-Cl orientation (three Cl atoms facing the surface) as shown in Figure 4.1c. This orientation is favourable for $AlCl_4$ adsorption on the inner and outer surfaces. The results show that the H-1 site is the most stable site for $AlCl_4$ adsorption. Similarly, site choices are also observed for other metal ion and anions on SWNTs, graphite and their derivatives *[69]*.

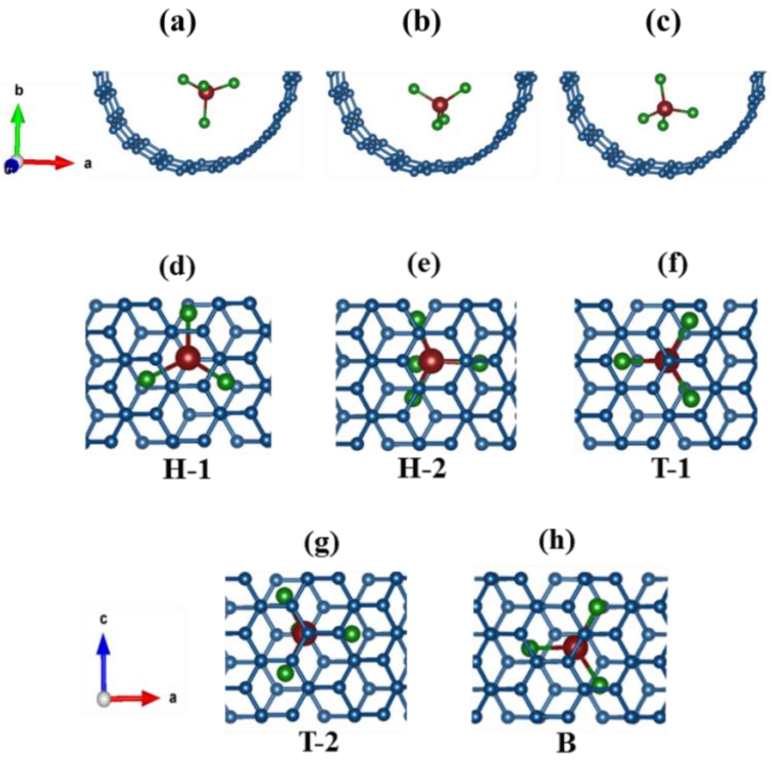

Figure 4.1: Top view of $AlCl_4$ orientations: (a) 1-Cl, (b) 2-Cl, (c) 3-Cl. Side view of the possible adsorption sites for $AlCl_4$ adsorption, (d) Hollow site (H-1), (e) Hollow site (H-2), (f) Top site (T-1), (g) Top site (T-2), (h) Bridge site (B).

Table 4.1: The energy difference (ΔE) between the considered sites for internal side-wall and external side-wall adsorption of $AlCl_4$. H-1 (inner surface) is taken as a reference adsorption site.

Sites	**ΔE (eV)**	
	Inner surface	**Outer surface**
Hollow (H-1)	0.000	0.938
Holoow (H-2)	0.005	0.986
Top (T-1)	0.011	0.921
Top (T-2)	0.010	1.001
Bridge (B)	0.026	0.988

To further understand the adsorption behaviour and nature of interactions between $AlCl_4$ and SWNTs, we have analysed the electronic properties like density of states and charge density difference calculations *[51-52]* (Figure 4.2). The armchair carbon nanotubes are metallic in nature with good electrical conductivity *[67-69]*, which is a deciding factor for investigating the electrochemical properties. The total and projected density of states depicted in Figure 4.2 show that the tube remains metallic on adsorption of $AlCl_4$ on inner as well as on outer surfaces. We observe significant overlap between C_*2p* orbital and Cl_*3p* orbital in -2.5 to 0 eV energy range, indicating towards the interaction between adsorbed $AlCl_4$ and nanotube.

The previous experimental and theoretical reports on graphite electrode conclude that the $AlCl_4$ intercalation results in the oxidation of graphitic carbons with 1|e| charge transfer per $AlCl_4$ molecule intercalated *[27, 28]*. Similarly, to check the nature of bonding between $AlCl_4$ and nanotube, we have calculated the charge density difference, as expressed by the following formula *[51-52]*,

$$\Delta\rho(\mathrm{r}) = \rho_{\mathrm{SWNT+AlCl_4}}(\mathrm{r}) - \rho_{\mathrm{SWNT}}(\mathrm{r}) - \rho_{\mathrm{AlCl_4}}(\mathrm{r}) \tag{4.2}$$

where, $\rho_{\mathrm{SWNT+AlCl_4}}(\mathrm{r})$, $\rho_{\mathrm{SWNT}}(\mathrm{r})$, and $\rho_{\mathrm{AlCl_4}}(\mathrm{r})$ are the charge densities of $AlCl_4$ adsorbed SWNT system, SWNT (without $AlCl_4$) and isolated $AlCl_4$ molecule adsorbed at the same position as in the total system. Figure 4.2b and 4.2d show the charge density difference of the $AlCl_4$ molecules adsorbed at the H-1 site on the inner and outer surfaces, respectively. There is a net gain of electronic charge around each Cl atom of $AlCl_4$ molecule and a net loss of electronic charge on neighbouring C atoms of SWNT surface, indicating the charge transfer from tube towards the Cl atoms of $AlCl_4$ molecule and oxidation of SWNT after $AlCl_4$ adsorption.

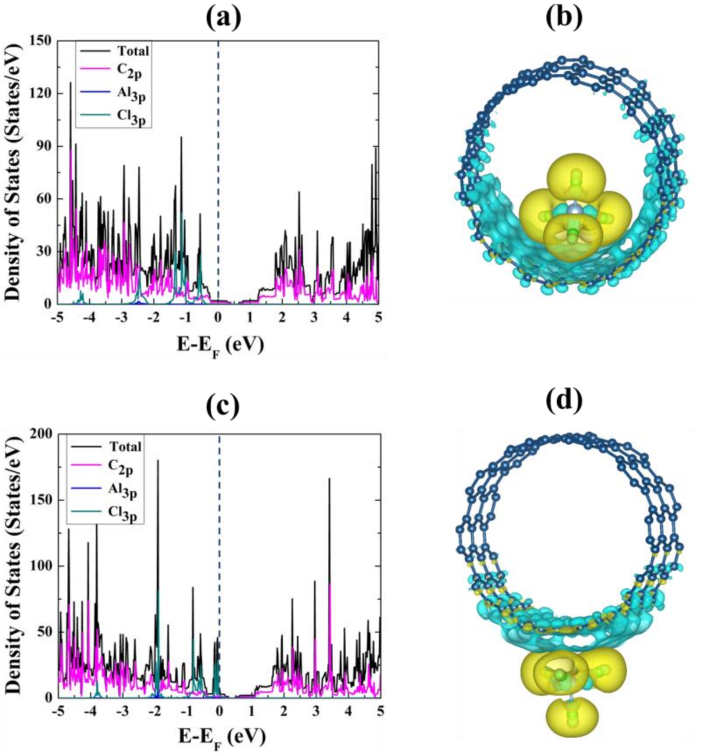

Figure 4.2: Density of states and charge density difference of the $AlCl_4$ adsorbed SWNT for (a-b) inner and (c-d) outer surface adsorption of $AlCl_4$. The Fermi energy is set to zero. Isosurface value is 0.0003; yellow and blue represent $\Delta\rho > 0$ and $\Delta\rho < 0$, respectively.

Next, we have performed the AIMD simulations to investigate the thermal stability of $AlCl_4$ adsorbed (10,10) SWNT using NVT ensemble and Nóse thermostat *[72]*. The analysis is carried out at a temperature range of 300-600 K with the time scale of 1 femtosecond for 5 picoseconds and the observed time evolution of total energy during the simulations is shown in Figure 4.3. The $AlCl_4$ adsorbed on the most stable H-1 adsorption site is considered for the calculations. For the simulation at 300 K temperature, the total energy value reaches the equilibrium very quickly (in 1 ps) and fluctuates near the equilibrium. The structure snapshots in Figure 4.3a show that no structural reconstruction of $AlCl_4$ and SWNT structures occurs at 300 K, however having a lateral shifting of $AlCl_4$ site position and slight distortion of SWNT structure. Furthermore, MD simulations are carried out at higher temperatures 400 K, 500 K and 600 K and the total energy shows larger fluctuations with increasing temperature of the NVT system. We observe that the tetrahedral geometry of $AlCl_4$ is preserved, but the orientation and position of $AlCl_4$ slightly changes from the optimized structure and for SWNT, the structural distortion is similar to lower temperature simulation result. Overall, we can conclude that the $AlCl_4$ intercalated SWNT system is stable even at higher temperatures and shows no structural reconstruction. The second important conclusion that can be inferred is about the rate capability of the battery as the $AlCl_4$ is not strongly bonded to one specific site (very small difference between the possible binding sites) and changes the relative position without changing the nature of chemical bonding with SWNT system. This can lead to lower diffusion barrier for $AlCl_4$ diffusion into SWNT system, providing ultrafast charging rate. Thus, we can also examine SWNT for aluminium battery, which can provide fast charging/discharging rate.

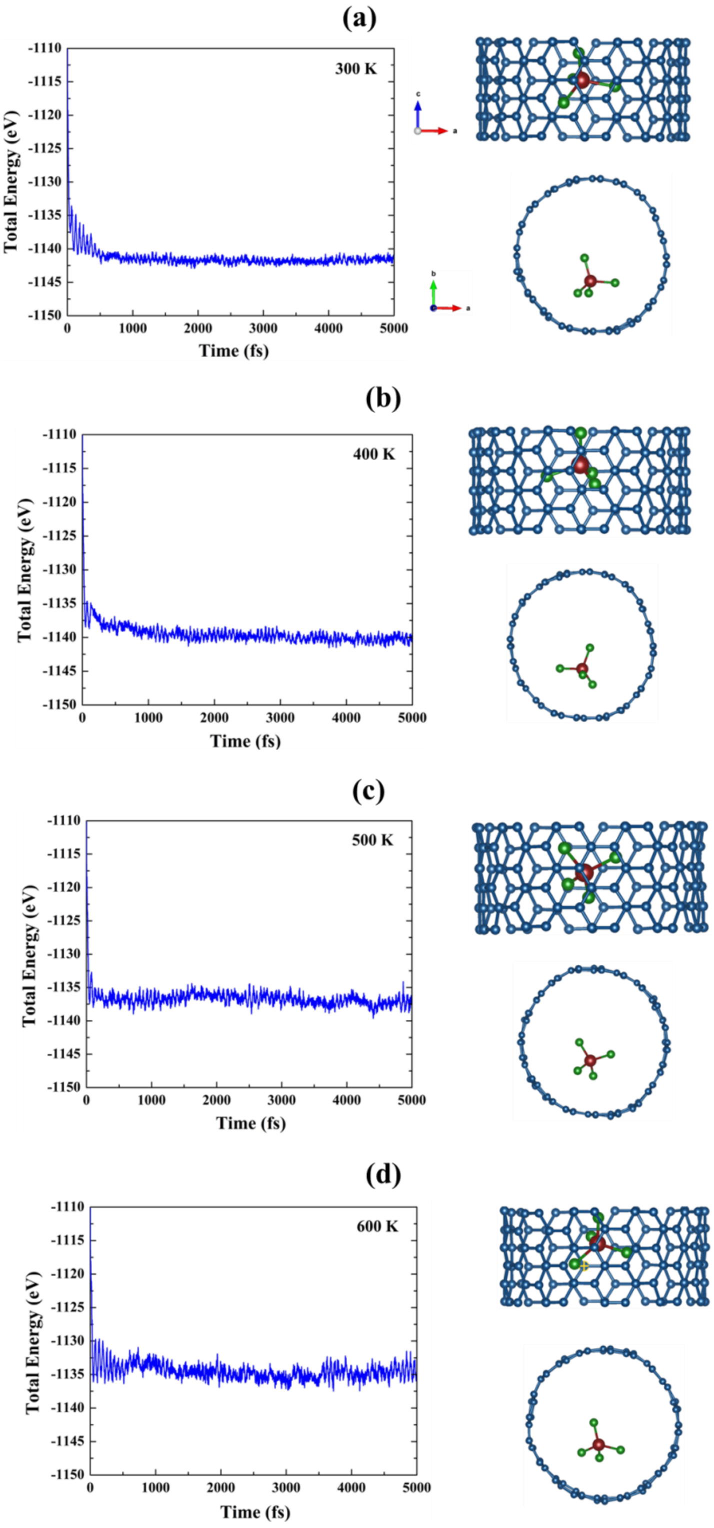

Figure 4.3: Molecular dynamics simulation analysis at different temperatures as a function of time step and the obtained structures, (a) 300K, (b) 400 K, (c) 500 K and (d) 600 K.

Next, we have evaluated the adsorption energies of $AlCl_4$ on the most stable H-1 site for different SWNTs (5, 5), (6, 6), (10, 10), (15, 15), (20, 20) and (25, 25) on the inner surface, the outer surface and at the centre of nanotubes as shown in Figure 4.4. The side views of single-walled SWNTs employed in our study are shown in Figure 4.5 with their respective diameters. In (5, 5) SWNT, we observe that the only possible adsorption is on the outer surface with -1.82 eV adsorption energy because the diameter of SWNT (6.92 Å) is comparatively smaller to accommodate large sized $AlCl_4$ (5.28 Å) *[73]* in the inner cavity. However, both inner and outer surface adsorption patterns are stable for higher SWNTs. Our calculations show that the inner adsorption is very less favourable (-0.70 eV) as compared to the outer adsorption (-1.83 eV) in (6, 6) SWNT. However, for larger SWNTs, the adsorption of $AlCl_4$ on the inner surface becomes more favourable. From Figure 4.4 and Table 4.2, it is clear that as the SWNT diameter increases, the adsorption at the centre of the tube decreases and the difference between inner and outer adsorption becomes less. Initially, for (10, 10) SWNT, the inner surface adsorption energy is largest followed by the adsorption at the tube centre and outer surface adsorption. The inner surface adsorption becomes less favourable while the outer surface adsorption energy increases a little with the increase in diameter and becomes almost equal for (25, 25). Similar trends have also been observed for other metal-ion adsorption and the reason for this behaviour is the flattening of the nanotube with increasing diameters that frames it to behave like a single sheet *[69, 74]*. All these results conclude that both the inner and outer surfaces are capable of storing $AlCl_4$ which can lead to high storage capacity for SWNTs.

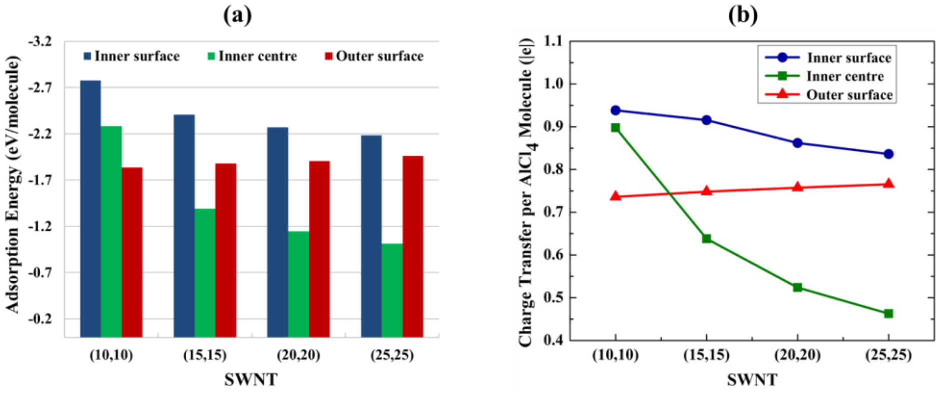

Figure 4.4: (a) Adsorption energies of $AlCl_4$ on the inner, outer surface and on the centre of the inner surface for different single walled SWNTs. (b) Charge transfer per $AlCl_4$ molecule for inner, outer surface and inner centre of different single walled SWNTs.

The Bader charge analysis *[53-59]* is performed for the quantitative estimation of the extent of charge transfer between $AlCl_4$ and the SWNTs. The net effective charges on each Cl atom of adsorbed $AlCl_4$ and nearest C atoms are examined for the (10, 10), (15, 15), (20, 20) and (25, 25) SWNTs for three adsorption possibilities (inner surface, outer surface and inner centre) and the calculated net charge transfer is given in Table 2.2. Further, Figure 4.4 shows the systematic variation with SWNT diameters and the results clearly indicate towards the electrochemical oxidation of SWNTs on $AlCl_4$ adsorption, thus we can say that the electrochemical behaviour of SWNTs will be similar to graphite *[27-28]*, when being used as a cathode for aluminium batteries. The net charge transfer value from nearest C atoms to $AlCl_4$ is high when $AlCl_4$ adsorption is stronger at SWNT surface. The maximum charge transfer occurs in (10, 10) SWNT, when the adsorption of $AlCl_4$ occurs on the inner surface because of the upmost interaction between $AlCl_4$ and the surface Carbons. The charge transfer for the inner surface adsorption deceases with the increasing diameter of SWNTs, and the reverse order is observed for outer surface adsorption.

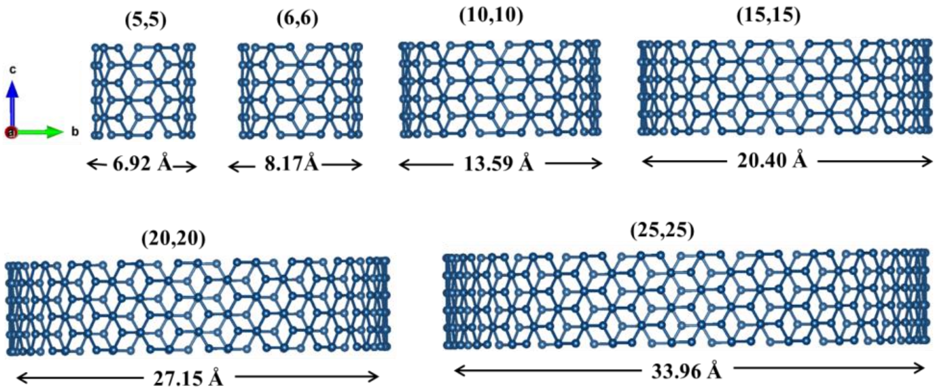

Figure 4.5: The side views of single walled CNTs (5, 5), (6, 6), (10, 10), (15, 15), (20, 20) and (25, 25) with their respective diameters.

Table 4.2: Adsorption energies **(**E_{ad}) of $AlCl_4$ on the internal, external side-wall and on the centre of the internal wall for different SWNTs and net effective charge (Δq) calculated on respective $AlCl_4$ molecule by Bader charge analysis.

SWNT	**Inner surface**		**Inner centre**		**Outer surface**	
	E_{ad} (eV)	**Δq |e|**	**E_{ad} (eV)**	**Δq |e|**	**E_{ad} (eV)**	**Δq |e|**
(10, 10)	-2.77	0.94	-2.29	0.74	-1.84	0.90
(15, 15)	-2.41	0.92	-1.39	0.76	-1.88	0.64
(20, 20)	-2.27	0.86	-1.15	0.76	-1.91	0.52
(25, 25)	-2.19	0.84	-1.01	0.77	-1.96	0.46

4.3.2. $AlCl_4$ Diffusion on (10, 10) SWNT Surface

Mobility of ions is an important factor for determining the rate performance of a particular battery at which the battery can be charged and discharged. In particular, a low diffusion barrier and high mobility are much desired to make a promising electrode material. Therefore, we have investigated the diffusion of $AlCl_4$ on both inner and outer surfaces of SWNT from its neighbouring equivalent sites. We have taken 1 × 1 × 6 supercell of (10, 10) SWNT to investigate the diffusion paths and diffusion barriers. Two different diffusion directions are considered as shown in Figure 4.6a. The associated energy barriers along these paths are calculated and the energy profiles are shown in Figure 4.6b-c. We find that the preferred diffusion pathways of $AlCl_4$ on inner and outer surfaces of SWNTs are quite energetically different. For inner surface diffusion, the preferable path is in the axial direction is path 1-2, showing a diffusion barrier of 0.003 eV, whereas the outside diffusion along the axis (path 1-3) possesses a barrier of 0.006 eV. The saddle point corresponds to a configuration where $AlCl_4$ is below (above) the C-C bridge site for inner (outer) surface diffusion. We observe that the diffusion of $AlCl_4$ inside the tube is more directional as compared to outer surface diffusion with the higher difference in diffusion barrier for path 1-2 selectivity. However, for outer surface diffusion, the difference in diffusion barriers along different pathways is less. On a flat graphite layer, these maximum energies (inside –outside) are equal because of structural symmetry. For the case of SWNTs, however, the asymmetry caused by curvature effect separates these maximum energies, giving rise to different diffusion barriers. The weakening of curvature effect of outer side saturates the diffusion barriers at the same value *[74]*. The second reason could be that we have only investigated an isolated SWNT system and the contributions of interactions between adjacent tubes have not been taken. We would like to mention that the choices of diffusion direction on both inner and outer surfaces agree well with the Li-ion battery on SWNTs, however with smaller diffusion barriers (0.003 eV, 0.006 eV) as compared to diffusion barrier of Li-ion (0.046 eV, 0.147 eV) on SWNT *[74]*. Thus, we believe that the SWNTs with low diffusion barrier along with other desirable properties can ensure high rate performance for aluminium battery.

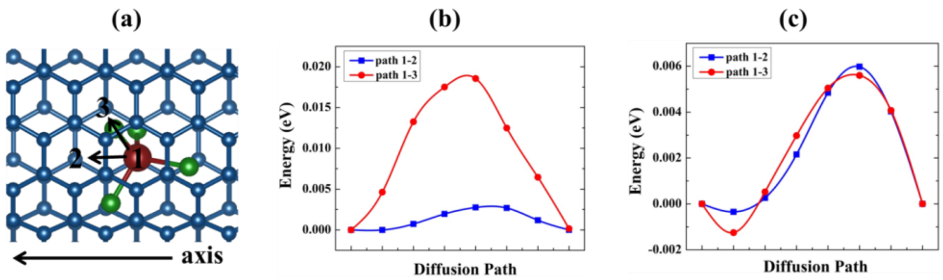

Figure 4.6: (a) Schematic representation of the top view of the considered diffusion paths. Corresponding diffusion barrier profiles for $AlCl_4$ on (10, 10) SWNT (b) Inner surface and (c) Outer surface.

4.3.3. Open-Circuit Voltage and Storage Capacity

The standard chemical reaction involved in ionic liquid electrolyte based aluminium batteries can be described as follows,

Anode: $$Al + 7AlCl_4^- \rightleftharpoons 4Al_2Cl_7^- + 3e^- \quad (4.3)$$

Cathode: $$C_n[AlCl_4] + e^- \rightleftharpoons C_n + AlCl_4^- \quad (4.4)$$

The overall cell reaction can be represented with the given expression *[20]*,

$$3[(AlCl_4)SWNT] + 4(EMI^+AlCl_4^-) + Al \leftrightarrow 3SWNT + 4(EMI^+Al_2Cl_7^-) \quad (4.5)$$

For x number of $AlCl_4$ adsorbed on SWNT the net reaction can be expressed as,

$$3/x[(AlCl_4)_xSWNT] + 4(EMI^+AlCl_4^-) + Al \leftrightarrow 3/x[SWNT] + 4(EMI^+Al_2Cl_7^-) \quad (4.6)$$

The cell voltage can be determined by the Nernst equation *[75-76]*,

$$V = -\frac{\Delta G_{cell}}{zF} \quad (4.7)$$

where z and F are the number of valence electrons during the intercalation process and the Faraday constant, respectively; ΔG_{cell} is the change in Gibbs free energy for chemical reaction of aluminium battery, which can be approximated to the internal energy ($\Delta G_f = \Delta E + P\Delta V - T\Delta S$) at 0 K due to negligible contribution of entropy and volume effect on the cell voltage. Thus, the cell voltage can be calculated by computing the corresponding internal energy change as *[28]*,

$$\Delta E = \{{}^{3}/_{x}\, E_{[(AlCl_4)_x SWNT]} + 4E_{[EMI^{+}AlCl_4^{-}]} + E_{Al}\} - \{{}^{3}/_{x}\, E_{SWNT} + 4E_{[EMI^{+}Al_2Cl_7^{-}]}\} \quad (4.8)$$

where $E_{[(AlCl_4)_x SWNT]}$, $E_{[EMI^{+}AlCl_4^{-}]}$ and $E_{[EMI^{+}Al_2Cl_7^{-}]}$ are the total energies of the $AlCl_4$ adsorbed SWNT system, $EMI^{+}AlCl_4^{-}$ and $EMI^{+}Al_2Cl_7^{-}$, respectively. E_{Al} is the total energy of a single Al atom in a bulk fcc structure and E_{SWNT} is the total energy of SWNT system. $E_{[EMI^{+}AlCl_4^{-}]}$ and $E_{[EMI^{+}Al_2Cl_7^{-}]}$ are calculated by optimizing the $EMI^{+}AlCl_4^{-}$ and $EMI^{+}Al_2Cl_7^{-}$, respectively as a molecular species due to non-availability of their crystal structures.

Therefore the average open circuit voltage (V_{ave}) for the system can be calculated as follows *[28]*,

$$V = \left(\frac{\{{}^{3}/_{x}E_{[(AlCl_4)_x SWNT]} + 4E_{[EMI^{+}AlCl_4^{-}]} + E_{Al}\} - \{{}^{3}/_{x}E_{SWNT} + 4E_{[EMI^{+}Al_2Cl_7^{-}]}\}}{z}\right) \quad (4.9)$$

The average open circuit voltage calculated for (10, 10), (15, 15), (20, 20) and (25, 25) SWNTs are summarized in Table 2.3. It can be seen that average voltage increases with the increase of the tube diameter. For (25, 25) SWNT, the cell voltage becomes 1.96 V which is close to the experimentally reported graphite system (2.00 V) *[27, 32]*, and it can certainly improve for SWNTs with larger diameters leading to better performance in aluminium batteries.

Table 4.3: The average open-circuit voltage (V_{ave}), specific energy and specific capacity of different $AlCl_4$ adsorbed SWNT systems.

SWNTs	V_{ave} (V)	Specific Energy (eV)	Capacity (mAh/g)
(10, 10)	1.70	1.76	223
(15, 15)	1.76	1.86	236
(20, 20)	1.80	1.97	251
(25, 25)	1.96	2.14	275

To investigate the maximum capacity of different SWNTs, we calculated the specific energy of (10, 10), (15, 15), (20, 20), and (25, 25) SWNTs with $AlCl_4$ densities upto $(AlCl_4)C_{10}$, $(AlCl_4)C_{9.47}$, $(AlCl_4)C_{8.89}$, and $(AlCl_4)C_{8.11}$. The specific energy (E_S) is given by the following equation *[77]*,

$$E_s = -(E_{SWNT+AlCl_4} - E_{SWNT})/m \tag{4.10}$$

where, $E_{CNT+AlCl_4}$ and E_{CNT} are the total energies of SWNT with and without $AlCl_4$, and m is the total number of carbon atoms in the supercell. The positive specific energy indicates that the system is stable and can accommodate m number of guest species. The calculated specific energy for each SWNT is given in Table 2.3. On the basis of the E_s value, we conclude that (10, 10), (15, 15), (20, 20) and (25, 25) SWNTs stable up to $AlCl_4)C_{10}$, $(AlCl_4)C_{9.47}$, $(AlCl_4)C_{8.89}$, and $(AlCl_4)C_{8.11}$ unit formulas.

Therefore, based on the above unit formulas, we have further calculated the specific capacity using the following expression,

$$C = \frac{nxF}{M_f} \tag{4.11}$$

where, n is the number of electrons transferred per formula unit, x is the number of $AlCl_4$ molecules involved, F is the Faraday constant, and M_f is the mass of formula unit. The capacity calculated for each tube is listed in Table 2.3. The important point that can be inferred from this Table 2.3 is about the variation of capacity with tube diameter. For (10, 10) SWNT, the calculated capacity is 223 mAh/g, which further increases to 236 to 251 mAh/g for (15, 15) and (20, 20) SWNT respectively, and the specific capacity of as high as 275 mAh/g can be obtained with (25, 25) SWNT. The systematic increase in capacity with increasing tube diameter is in accordance with the earlier studies on Li-ion batteries with SWNT electrodes.[68] The storage capacities obtained for the reported SWNTs are higher than that of the earlier studied graphite cathode (70 mAh/g) *[27-29]*, which promotes the application of SWNTs as superior cathode host for aluminium batteries. Moreover, the level of theory (DFT-D3) used in our calculation is valuable enough to correlate with experimental studies *[64]* because the theoretical results of our previous study *[28]* on natural graphite have also been evaluated in a very recent experimental study *[29, 32]*. Therefore, we believe that a single-walled CNT with precisely large diameter will be able to offer the higher capacity and thus, will be suitable for practical applications.

4.4. Conclusion

In this work, we have investigated the potential applicability of a series of armchair single-walled carbon nanotubes (SWNTs) (10, 10), (15, 15), (20, 20) and (25, 25) for aluminium battery by studying the adsorption behaviour, electronic properties, average open-circuit voltages and storage capacities. It is demonstrated that the SWNTs can act as suitable cathode material for aluminium batteries. Through the structural studies, it is concluded that $AlCl_4$ adsorbs in its stable tetrahedral geometry and the AIMD study show that the $AlCl_4$ adsorbed SWNT system is stable at 300-600 K temperature range. The $AlCl_4$ prefers to adsorb at the hollow site above the centre of the hexagonal ring with the 3-Cl orientation. The studies show that for the small tubes the inner surface adsorption is more favourable than outer surface and inner centre adsorption and as the tube diameter increases the possibility of inner and outer surface adsorption becomes equal due to flattening of the tube and inner centre adsorption energy decrease due to increasing distance between tube surface and centre. The density of states calculations show the $AlCl_4$ adsorbed armchair SWNT system preserves its metallic nature, which is important for the electrode material. The charge density difference and Bader charge calculation indicate the oxidation of tube on $AlCl_4$ adsorption, showing a similar electrochemical behaviour as $AlCl_4$ intercalation into graphite. Moreover, our results show that SWNT shows very small diffusion barriers of 0.003 and 0.006 eV for $AlCl_4$ diffusion on inner and outer tube surface, respectively exhibiting excellent charge/discharge rates for aluminium battery. The average open-circuit voltages are in the range of 1.96 V which can further improve with the increase in diameter of SWNTs. In addition, our work reveals high specific capacities (more than 200 mAh/g) for SWNTs which increases with tube diameter and can be as high as 275 mAh/g in (25, 25) tube, which is far better than the capacity of graphite cathode (70 mAh/g). Our findings give a direction to explore carbon nanotube materials for aluminium batteries with large capacities, compatible voltages and high charge/discharge rates.

4.5. References

1. Whittingham M. S. (2008), Materials challenges facing electrical energy storage, MRS Bull., 33, 411–419 (DOI: 10.1557/mrs2008.82)
2. Liu J., Zhang J. G., Yang Z., Lemmon J. P., Imhoff C., Graff G. L., Li L., Hu J., Wang C., Xiao J., Xia G. (2013), Materials science and materials chemistry for large scale electrochemical energy storage: From transportation to electrical grid, Adv. Funct. Mater., 23, 929–946 (DOI: 10.1002/adfm.201200690)

3. Armand M., Taracson J. M. (2008), Issues and challenges facing rechargeable lithium batteries, Nature, 451, 652–657 (DOI: 10.1142/9789814317665_0024)
4. Noorden R. Van (2014), The rechargeable revolution: A better battery, Nature, 507, 26–28 (DOI: 10.1038/507026a)
5. Dunn B., Kamath H., Taracson J. M. (2011), Electrical energy storage for the grid: A battery of choices, Science, 334, 928–935 (DOI: 10.1126/science.1212741)
6. Goodenough J. B., Park K. S. (2013), The Li-ion rechargeable battery: A perspective, J. Am. Chem. Soc., 135, 1167–1176 (DOI: 10.1021/ja3091438)
7. Scrosati B., Hassoun J., Sun Y.K. (2011), Lithium-ion batteries. A look into the future, Energy Environ. Sci., 4, 3287–3295 (DOI: 10.1039/C1EE01388B)
8. Ellis B.L., Lee K.T., Nazar L.F. (2010), Positive electrode materials for Li-ion and Li-batteries, Chem. Mater., 22, 691–714 (DOI: 10.1021/cm902696j)
9. Thackeray M. M., Wolverton C., Isaacs E. D. (2012), Electrical energy storage for transportation-approaching the limits of, and going beyond, lithium-ion batteries, Energy Environ. Sci., 5, 7854–7863 (DOI: 10.1039/C2EE21892E)
10. Goodenough J. B., Kim Y. (2009), Challenges for rechargeable Li batteries, Chem. Mater., 22, 587–603 (DOI: 10.1021/cm901452z)
11. Manthiram A. (2011), Materials challenges and opportunities of lithium ion batteries, J. Phys. Chem. Lett., 2, 176–184 (DOI: 10.1021/jz1015422)
12. Mohtadi R., Mizuno F. (2014), Magnesium batteries: Current state of the art, issues and future perspectives, Beilstein J. Nanotechnol., 5, 1291–1311 (DOI: 10.3762/bjnano.5.143)
13. Rasul S., Suzuki S., Yamaguchi S., Miyayama M. (2012), High capacity positive electrodes for secondary Mg-ion batteries,

Electrochim. Acta, 82, 243–249 (DOI: 10.1016/j.electacta.2012.03.095)

14. Huie M. M., Bock D. C., Takeuchi E. S., Marschilok A. C., Takeuchi K. J. (2015), Cathode materials for magnesium and magnesium-ion based batteries, Coord. Chem. Rev., 287, 15–27 (DOI: 10.1016/j.ccr.2014.11.005)
15. Xu C., Li B., Du H., Kang F. (2012), A long-cycle-life self-doped polyaniline cathode for rechargeable aqueous zinc batteries, Angew. Chem., 124, 957–959 (DOI: 10.1002/ange.201808886)
16. Lee B., Lee H. R., Kim H., Chung K. Y., Cho B. W., Oh S. H. (2015), Elucidating the intercalation mechanism of zinc ions into α-MnO_2 for rechargeable zinc batteries, Chem. Commun., 51, 9265–9268 (DOI: 10.1039/C5CC02585K)
17. Liu S., Hu J. J., Yan N. F., Pan G. L., Li G. R., Gao X. P. (2012), Aluminum storage behavior of anatase TiO_2 nanotubearrays in aqueous solution for aluminum ion batteries, Energy Environ. Sci., 5, 9743–9746 (DOI: 10.1039/C2EE22987K)
18. Geng L., Lv G., Xing X., Guo J. (2015), Reversible electrochemical intercalation of aluminum in Mo_6S_8 , Chem. Mater., 27, 4926–4929 (DOI: 10.1021/acs.chemmater.5b01918)
19. Li Q., Bjerrum N. J. (2002), Aluminum as anode for energy storage and conversion: a review, J. Power Sources, 110, 1–10 (DOI: 10.1016/S0378-7753(01)01014-X)
20. Hudak N. S. (2014), Chloroaluminate-doped conducting polymers as positive electrodes in rechargeable aluminum batteries, J. Phys. Chem. C, 118, 5203–5215 (DOI: 10.1021/jp500593d)
21. Reed L. D., Ortiz S. N., Xiong M., Menke E. J. (2015), A rechargeable aluminum-ion battery utilizing a copper hexacyanoferrate cathode in an organic electrolyte, Chem. Commun., 51, 14397–14400 (DOI: 10.1039/C5CC06053B)

22. Jayaprakash N., Das S. K., Archer L. A. (2011), The rechargeable aluminum-ion battery, Chem. Commun., 47, 12610 – 12612 (DOI: 10.1039/C1CC15779E)
23. Rani J. V., Kanakaiah V., Dadmal T., Rao M. S., Bhavanarushi S. (2013), Fluorinated natural graphite cathode for rechargeable ionic liquid based aluminum–ion battery, J. Electrochem., 160, A1781–A1784 (DOI: 10.1149/2.072310jes)
24. Gifford P. R., Palmisano J. B. (1988), An aluminum/chlorine rechargeable cell employing a room temperature molten salt electrolyte, J. Electrochem. Soc., 135, 650–654 (DOI: 10.1149/1.2095685)
25. Xia S., Zhang X. M., Huang K., Chen Y. L., Wu Y. T. (2015), Ionic liquid electrolytes for aluminium secondary battery: Influence of organic solvents, J. Electroanal. Chem., 757, 167–175 (DOI: 10.1016/j.jelechem.2015.09.022)
26. Chiku M., Takeda H., Matsumura S., Higuchi E., Inoue H. (2015), Amorphous vanadium oxide/carbon composite positive electrode for rechargeable aluminum battery, ACS Appl. Mater. Interfaces, 7, 24385–24389 (DOI: 10.1021/acsami.5b06420)
27. Lin M. C., Gong M., Lu B., Wu Y., Wang D. Y., Guan M., Angell M., Chen C., Yang J., Hwang B. J., Dai H. (2015), An ultrafast rechargeable aluminium-ion battery, Nature, 520, 324–328 (DOI: 10.1038/nature14340)
28. Bhauriyal P., Mahata A., Pathak B. (2017), The staging mechanism of $AlCl_4$intercalation in a graphite electrode for an aluminium-ion battery, Phys. Chem. Chem. Phys., 19, 7980–7989 (DOI: 10.1039/C7CP00453B)
29. Wang D. Y., Wei C. Y., Lin M. C., Pan C. J., Chou H. L., Chen H. A., Gong M., Wu Y., Yuan C., Angell M., Hseih Y. J. (2017), Advanced rechargeable aluminium ion battery with a high-quality natural

graphite cathode, Nat. Commun., 8, 14283 (DOI: 10.1038/ncomms14283)

30. Sun H., Wang W., Yu Z., Yuan Y., Wang S., Jiao S. (2015), A new aluminium-ion battery with high voltage, high safety and low cost, Chem. Commun., 51, 11892–11895 (DOI: 10.1039/C5CC00542F)
31. Song Y., Jiao S., Tu J., Wang J., Liu Y., Jiao H., Mao X., Guo Z., Fray D. J. (2017), A long-life rechargeable Al ion battery based on molten salts, J. Mater. Chem. A, 5, 1282–1291 (DOI: 10.1039/C6TA09829K)
32. 32.Kravchyk K. V., Wang S., Piveteau L., Kovalenko M. V. (2017), Efficient aluminum chloride–natural graphite battery, Chem. Mater., 29, 4484-4492 (DOI: 10.1021/acs.chemmater.7b01060)
33. Schmuelling G., Placke T., Kloepsch R., Fromm O., Meyer H. W., Passerini S., Winter M. (2013), X-ray diffraction studies of the electrochemical intercalation of bis(trifluoromethanesulfonyl)imide anions into graphite for dual-ion cells, J. Power Sources, 239, 563–571 (DOI: 10.1016/j.jpowsour.2013.03.064)
34. Placke T., Rothermel S., Fromm O., Meister P., Lux S. F., Huesker J., Meyer H. W., Winter M. (2013), Influence of graphite characteristics on the electrochemical intercalation of bis(trifluoromethanesulfonyl) imide anions into a graphite-based cathode, J. Electrochem. Soc., 160, A1979–A1991 (DOI: 10.1149/2.027311jes)
35. Bhauriyal P., Mahata A., Pathak B. (2017), The staging mechanism of $AlCl_4$ intercalation in a graphite electrode for an aluminium-ion battery, J. Phys. Chem. C, 121, 9748−9756 (DOI: 10.1021/acs.jpcc.7b02290)
36. Iijima S. (1991), Helical microtubules of graphitic carbon, Nature, 354, 56 (DOI: 10.1038/354056a0)
37. Britz D. A., Khlobystov A. N. (2006), Noncovalent interactions of molecules with single walled carbon nanotubes, Chem. Soc. Rev., 35, 637–659 (DOI: 10.1039/B507451G)

38. Fatemi S. M., Foroutan M. (2016), Review on carbon nanotubes and carbon nanotube bundles for gas/ion separation and water purification studied by molecular dynamics simulation, Int. J. Environ. Sci. Technol., 13, 457–470 (DOI: 10.1007/s13762-015-0918-7)
39. Zhao Q., Nardelli M. B., Bernholc J. (2002), Ultimate strength of carbon nanotubes: A theoretical study, Phys. Rev. B, 65, 144105 (DOI: 10.1103/PhysRevB.65.144105)
40. Lee S. W., Yabuuchi N., Gallant B. M., Chen S., Kim B. S., Hammond P. T., Shao-Horn Y. (2010), High-power lithium batteries from functionalized carbon-nanotube electrodes, Nat. Nanotechnol., 5, 531–537 (DOI: 10.1038/nnano.2010.116)
41. Gao B., Bower C., Lorentzen J. D., Fleming L., Kleinhammes A., Tang X. P., Mcneil L. E., Wu Y., Zhou O. (2000), Enhanced saturation lithium composition in ball-milled single-walled carbon nanotubes, Chem. Phys. Lett., 327, 69–75 (DOI: 10.1016/S0009-2614(00)00851-4)
42. Gao B., Kleinhammes A., Tang X. P., Bower C., Fleming L., Wu Y., Zhou O (1999), Electrochemical intercalation of single-walled carbon nanotubes with lithium, Chem. Phys. Lett., 307, 153–157 (DOI: 10.1016/S0009-2614(99)00486-8)
43. Morris R. S., Dixon B. Gennett T., Raffaelle R., Heben M. J. (2004), High-energy, rechargeable Li-ion battery based on carbon nanotube technology, J. Power Sources, 138, 277–280 (DOI: 10.1016/j.jpowsour.2004.06.014)
44. Ng S. H., Wang J., Guo Z. P., Chen J., Wang G. X., Liu H. K. (2005), Single wall carbon nanotube paper as anode for lithium-ion battery, Electrochim. Acta, 51, 23–28 (DOI: 10.1016/j.electacta.2005.04.045)
45. Shimoda H., Gao B., Tang X. P., Kleinhammes A., Fleming L., Wu Y., Zhou O. (2001), Lithium intercalation into opened single-wall carbon nanotubes: Storage capacity and electronic properties, Phys. Rev. Lett., 88, 015502 (DOI: 10.1103/PhysRevLett.88.015502)

46. Frackowiak E., Gautier S., Gaucher H., Bonnamy S., Beguin F. (1999), Electrochemical storage of lithium in multiwalled carbon nanotubes, Carbon, 37, 61–69 (DOI: 10.1016/S0008-6223(98)00187-0)
47. Centi G., Perathoner S. (2011), Carbon nanotubes for sustainable energy applications, ChemSusChem, 4, 913–925 (DOI: 10.1002/cssc.201100084)
48. Iijima S., Brabec C., Maiti A., Bernholc J. (1996), Structural flexibility of carbon nanotubes, J. Chem. Phys., 104, 2089–2092 (DOI: 10.1063/1.470966)
49. Eliseev A. A., Yashina L. V., Brzhezinskaya M. M., Chernysheva M. V., Kharlamova M. V., Verbitsky N. I., Lukashin A. V., Kiselev N. A., Kumskov A. S., Zakalyuhin R. M., Hutchison J. L., Freitag B., Vinogradav A. S. (2010), Structure and electronic properties of AgX (X = Cl, Br, I)-intercalated single-walled carbon nanotubes, Carbon, 48, 2708–2721 (DOI: 10.1016/j.carbon.2010.02.037)
50. Jiao H., Wang J., Tu J., Lei H., Jiao S. (2016), Aluminum-ion asymmetric supercapacitor incorporating carbon nanotubes and an ionic liquid electrolyte: Al/$AlCl_3$-[EMIm]Cl/CNTs, Energy Technol., 4, 1112–1118 (DOI: 10.1002/ente.201600125)
51. Kumar S., Choudhari I., Pathak B. (2016), An atomically thin ferromagnetic half-metallic pyrazine-fused Mn-porphyrin sheet: a slow spin relaxation system, J. Mater. Chem. C, 4, 9069–9077 (DOI: 10.1039/C6TC03438A)
52. Garg P., Kumar S., Choudhari I., Mahata A., Pathak B. (2016), Hexagonal planar CdS monolayer sheet for visible light photocatalysis, J. Phys. Chem. C, 120, 7052–7060 (DOI: 10.1021/acs.jpcc.6b01622)
53. Bader R. F. W. (1991), Atoms in molecules, Chem. Rev., 91, 893–928 (DOI: 10.1021/ar00109a003)

54. Henkelman G., Arnaldsson A., Jonsson H. (2006), A fast and robust algorithm for Bader decomposition of charge density, Comput. Mater. Sci., 36, 354–360 (DOI: 10.1016/j.commatsci.2005.04.010)
55. Sanville E., Kenny S. D., Smith R., Henkelman G. J. (2007), Improved grid-based algorithm for Bader charge allocation, Comput. Chem., 28, 899–908 (DOI: 10.1002/jcc.20575)
56. Tang W., Ssanville E., Henkelman G. J. (2009), A grid-based Bader analysis algorithm without lattice bias, J. Phys. Condens. Matter, 21, 084204 (DOI: 10.1088/0953-8984/21/8/084204)
57. Mahata A., Bhauriyal P., Rawat K. S., Pathak B. (2016), Pt_3Ti ($Ti_{19}@Pt_{60}$)-based cuboctahedral core–shell nanocluster favors a direct over indirect oxygen reduction reaction, ACS Energy Lett., 1, 797–805 (DOI: 10.1021/acsenergylett.6b00385)
58. Mahata A., Rawat K. S., Choudhari I., Pathak B. (2016), Single-layered platinum nanocage: a highly selective and efficient catalyst for fuel cells, J. Mater. Chem. A, 4, 12756–12767 (DOI: 10.1039/C6TA03245A)
59. Choudhari I., Kumar S., Mahata A., Rawat K. S., Pathak B. (2016), Transition-metal embedded carbon nitride monolayers: high-temperature ferromagnetism and half-metallicity, Nanoscale, 8, 14117–14126 (DOI: 10.1039/C6NR03282F)
60. Chen Y., Peng F., Yan Y., Wang Z., Sun C., Ma Y. (2013), Exploring high-pressure lithium beryllium hydrides: A new chemical perspective, J. Phys. Chem. C, 117, 13879–13886 (DOI: 10.1021/jp404046g)
61. Kresse G., Furthmuller J. (1996), Efficient iterative schemes for ab initio total-energy calculations using a plane-wave basis set, Phys. Rev. B: Condens. Matter Mater. Phys., 54, 11169–11186 (DOI: 10.1103/PhysRevB.54.11169)
62. Blochl P. E. (1994), Projector augmented-wave method, Phys. Rev. B: Condens. Matter Mater. Phys., 50, 50, 17953 (DOI: 10.1103/PhysRevB.50.17953)

63. Perdew J. P., Burke K., Ernzerhof M. (1996), Generalized gradient approximation made simple, Phys. Rev. Lett., 77, 3865 – 3868 (DOI: 10.1103/PhysRevLett.77.3865)
64. Grimme S., Antony J., Ehrlich S., Kreig H. (2010), A consistent and accurate ab initio parametrization of density functional dispersion correction (DFT-D) for the 94 elements H-Pu, J. Chem. Phys., 132, 154104 (DOI: 10.1063/1.3382344)
65. Mills G., Jansson H., Schenter G. K. (1995), Reversible work transition state theory: application to dissociative adsorption of hydrogen, Surf. Sci., 324, 305–337 (DOI: 10.1016/0039-6028(94)00731-4)
66. Kawasaki S., Hara T., Iwai Y., Suzuki Y. (2008), Metallic and semiconducting single-walled carbon nanotubes as the anode material of Li ion secondary battery, Mater. Lett., 62, 2917–2920 (DOI: 10.1016/j.matlet.2008.01.088)
67. Sun G. Y., Kurti J., Kertesz M., Baughman R. H. (2003), Variations of the geometries and band gaps of single-walled carbon nanotubes and the effect of charge injection, J. Phys. Chem. B, 107, 6924–6931 (DOI: 10.1021/jp022629p)
68. Cabria I., Mintmire J. W., White C. T. (2003), Metallic and semiconducting narrow carbon nanotubes, Phys. Rev. B, 67, 121406 (DOI: 10.1103/PhysRevB.67.121406)
69. Gao S., Shi G., Fang H. (2016), Impact of cation–π interactions on the cell voltage of carbon nanotube-based Li batteries, Nanoscale, 8, 1451 (DOI: 10.1039/C5NR06456B)
70. Kong J., Soh H. T., Cassell A. M., Quate C. F., Dai H. (1998), Synthesis of individual single-walled carbon nanotubes on patterned silicon wafers, Nature, 395, 878–881 (DOI: 10.1038/27632)
71. Stadie N. P., Wang S., Kravchyk K. V., Kovalenko M. V. (2017), Zeolite-templated carbon as an ordered microporous electrode for

aluminum batteries, ACS Nano, 11, 1911–1919 (DOI: 10.1021/acsnano.6b07995)

72. Martyna G., Tuckerman M., Tobias D., Klein M. (1996), Explicit reversible integrators for extended systems dynamics, 87, 1117–1157 (DOI: 10.1080/00268979600100761)
73. Takahashi S., Koura N., Kohara S., Saboungi M. L., Curtiss L. A. (1999), Technological and scientific issues of room-temperature molten salts, 2, 91 (DOI: 10.1016/S1288-3255(99)00105-7)
74. Zhao M., XiaY., Mei L. (2005), Diffusion and condensation of lithium atoms in single-walled carbon nanotubes, 71, 165413 (DOI: 10.1103/PhysRevB.71.165413)
75. Aydinol M. K., Kohan A. F., Ceder G., Joannopoulos K. C. (1997), Ab initio study of lithium intercalation in metal oxides and metal dichalcogenides, Phys. Rev. B: Condens. Matter Mater. Phys., 56, 1354 (DOI: 10.1103/PhysRevB.56.1354)
76. Aydinol M. K., Kohan A. F., Ceder G. (1997), Ab initio calculation of the intercalation voltage of lithium-transition-metal oxide electrodes for rechargeable batteries, 68, 664–668 (DOI: 10.1016/S0378-7753(96)02638-9)
77. Larsson P., Ahuja R., Nyten A., Thomas J. O. (2006), An ab initio study of the Li-ion battery cathode material Li2FeSiO4, 8, 797–800 (DOI:10.1016/j.elecom.2006.03.012)

Chapter 5

Investigation of Charge and Discharge Processes in Aluminium-Sulfur Batteries

5.1. Introduction

The never-ending need of energy, which is increasing with each passing year, has given the scientists a new challenge to look beyond the commercial Li-ion batteries due to their low energy density, high cost and safety concerns *[1-6]*. In this regard, the metal-sulfur batteries have emerged as the promising alternative of commercial batteries as they have the benefit of low cost, and eco-friendly sulfur cathode offering a maximum theoretical capacity of 1675 mAh/g, which is the highest of all known solid cathode materials. Amongst various metal-S batteries, rechargeable Li-S batteries were the first to be investigated in year 1940's and are the most studied till present *[7]*. The working mechanism of Li-S battery involves the reversible oxidation of Li anode and the reduction of sulfur cathode during discharging process. The sulfur reduction results in a series of polysulfides S_x^{2-}, $1 \leq x \leq 6$ to give the final product Li_2S. The working behavior and chemistry of Li-S batteries have been considered as the basis of the all the other types of developing metal-sulfur batteries, although they operate differently. While comparing amongst various metal-S batteries such as Li-S *[8-12]*, Na-S *[13-15]*, K-S *[16]*, Mg-S *[17-20]*, Al-S *[21]*, and Ca-S *[22]*, the Al-S batteries stand out as the most advantageous ones because of the high abundance and trivalent oxidation state of aluminium to provide high gravimetric (2.90 Ah/g) and volumetric capacity (3.80 Ah/g) as Al metal anode *[23-25]*. Overall, Al-S batteries can deliver high energy density of 1300 Wh/Kg *[26]* with the theoretical voltage of 1.30 V. Al-S batteries with non-aqueous ionic-liquid electrolyte show huge advantages over aqueous electrolytes in terms of reversibility. In 2015, Cohn et al. made a successful attempt to develop a primary non-aqueous Al-S battery having capacity of 1400 mAh/g sulfur, more than 80% of the theoretical capacity for a sulfur cathode-based system *[27]*. Very recently, the first reversible Al-S battery is proposed by Gao et al. *[26]*, comprising an ionic liquid (IL) electrolyte of $AlCl_3$ with EMIC (1-ethyl-3-methylimidazolium chloride) with sulfur undergoing a solid-state conversion reaction. However, it suffered from a sluggish electrochemical kinetics due to the lack of a facile sulfur cathode. Therefore, to overcome these challenges, more advanced reversible ambient-temperature Al-S batteries are studied with strategically designing the sulfur cathodes *[28,29]* or by inclusion of additive in Al[EMI]Cl_4 ionic liquid electrolyte *[30]*. All of these studies have tried to offer new promising ways to enhance the stability and reversibility of Al–S batteries, and involve almost the same working mechanism. The overall cell reaction during discharge can be written as follows,

Anode: $2Al + 14AlCl_4^- \leftrightarrow 8Al_2Cl_7^- + 6e^-$ (5.1)
Cathode: $8Al_2Cl_7^- + 6e^- + 3S \leftrightarrow Al_2S_3 + 14AlCl_4^-$ (5.2)
Overall: $2Al + 3S \leftrightarrow Al_2S_3$ (5.3)

At cathode, the involved reaction steps resulting into the final discharge product Al_2S_3 are proposed to undergo similar polysulfide sequence formation as of Li-S batteries that are S_x^{2-} $1 \leq x < 6$ *[28-30]*. However in Li-S batteries, due to a large number of reported and on-going studies, the understanding of complex reaction mechanism is quite clear. The computational methodologies have played a huge role in understanding of complex electrochemical reactions during charge and discharge processes. Especially, molecular dynamics (MD) simulation compared to other density function theory (DFT) calculations have been reported to be a powerful tool to study the dynamics involved in the reaction, characterize surface reactions and reduction mechanisms in metal-S batteries. Such theoretical studies could be very important for Al-S batteries that are just being investigated from last two-three year, to get a better understanding of their working and to build advanced Al-S batteries. To the best of our knowledge there are no such theoretical study reported as per now. Therefore, it becomes necessary to evaluate the complex electrochemical reactions occurring during charge/discharge process with the help of *ab initio* molecular dynamics (AIMD) simulation.

Here, in this work, we have used the most stable S_8-ionic liquid electrolyte interface system to understand the discharging process by systematic addition of Al atoms along the top interface of S_8 surface and the structural insights regarding the formation of various Al polysulfides are illustrated. Along with that, the voltage profile is drawn with a relative comparison with the experimental discharge voltage behavior. The charging process is also studied by considering the most stable surface of the final discharged product Al_2S_3 by making an interface with ionic liquid electrolyte. Our results provide detailed insights into the atomistic changes occurring in terms of reduction steps of sulfur cathode into Al polysulfides via formation of various cationic and anionic polysulfide intermediates as well as illustrating the variation of charging and discharging voltage profile with respect to resulting structural variation in Al_2S_3 and S_8 systems.

5.2. Computational Details and System Modeling

The density functional theory calculations are carried out by using the projector augmented-wave (PAW) method *[31-32]* to treat interactions between ion cores and valence electrons as implemented in the Vienna Ab initio Simulation Package (VASP) *[33-36]*. The generalized gradient approximation of Perdew-Burke-Ernzerhof (GGA-PBE) *[37-38]* is used to describe the exchange-correlation potential and the plane-wave cutoff energy is fixed to 470 eV for the all the calculations. The optimized structures are fully relaxed until the Hellmann−Feynman forces on each atom are less than 0.01 eV/Å and total energy is converged to 10^{-4} eV. The DFT-D3 approach is included for the correction of van der Waals interactions for potential energy and interatomic forces *[39]*. All the AIMD simulations are performed in NVT ensemble at 300 K and the temperature control is achieved by a Nosé thermostat model *[40]*.

To construct the cathode/electrolyte interfaces in order to study the discharging and charging process, we first determine the low energy surfaces of both S_8 and Al_2S_3 systems. Surface energies are calculated using the following equation,

$$\sigma = \frac{1}{A}[E_{slab} - nE_{bulk}] \qquad (5.4)$$

where, σ is the surface energy, A is the total area of the surface in the slab model, E_{slab} is the total energy of the slab model for the surface, E_{bulk} is the energy of one atom in the bulk, and n is the number of atoms in the slab model.

We observe that for the S_8 system, the possible surface (100), (001), (110), (011) and (111) have very small difference in their relative surface energies (Table 5.1), which in accordance with the previous report *[41]*. The most stable surface is obtained to be (001) surface, which is considered for further study. Whereas, in case of Al_2S_3, the surface energies are much larger because of the stronger inter-atomic bonding in bulk Al_2S_3, and the most stable surface termination is (001). These stable surfaces for S_8 and Al_2S_3 are presented in Figure 5.1.

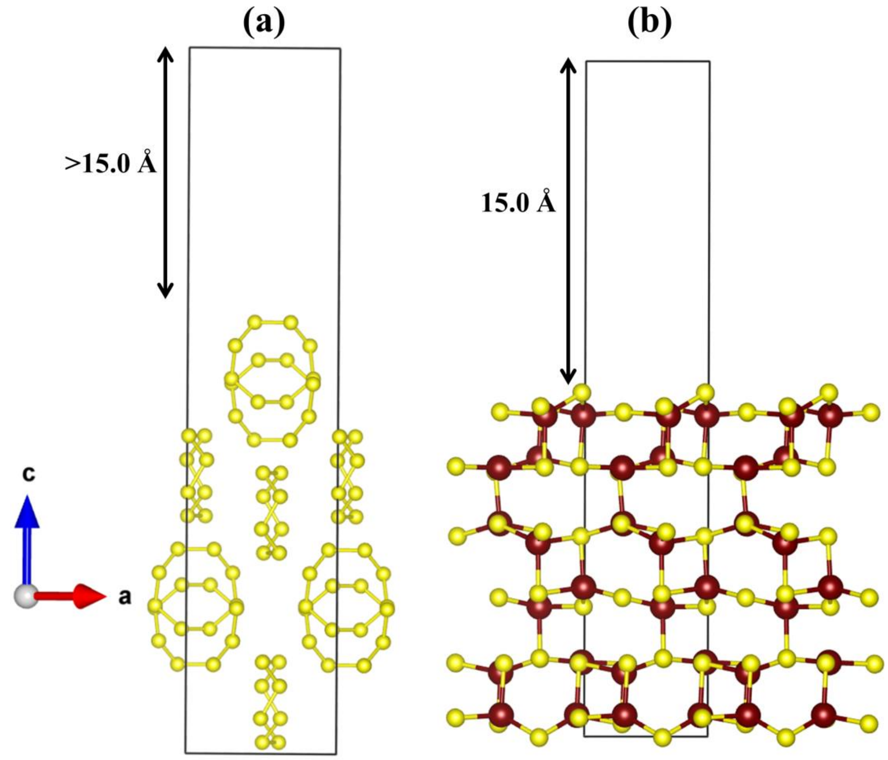

Figure 5.1: Most stable surfaces, (a) S_8(001), and (b) Al_2S_3(001).

Table 5.1: Calculated surface energies for various possible planes of S_8 and Al_2S_3 surfaces.

System	Surface	Surface Energy (meV/Å^2)	Band Gap (eV)
S_8	(100)	13	2.03
	(001)	12	2.07
	(110)	19	2.02
	(011)	20	1.65
	(111)	21	1.64
Al_2S_3	(100)	74	1.15
	(001)	21	2.88
	(011)	120	2.60
	(110)	144	2.23
	(111)	130	1.81

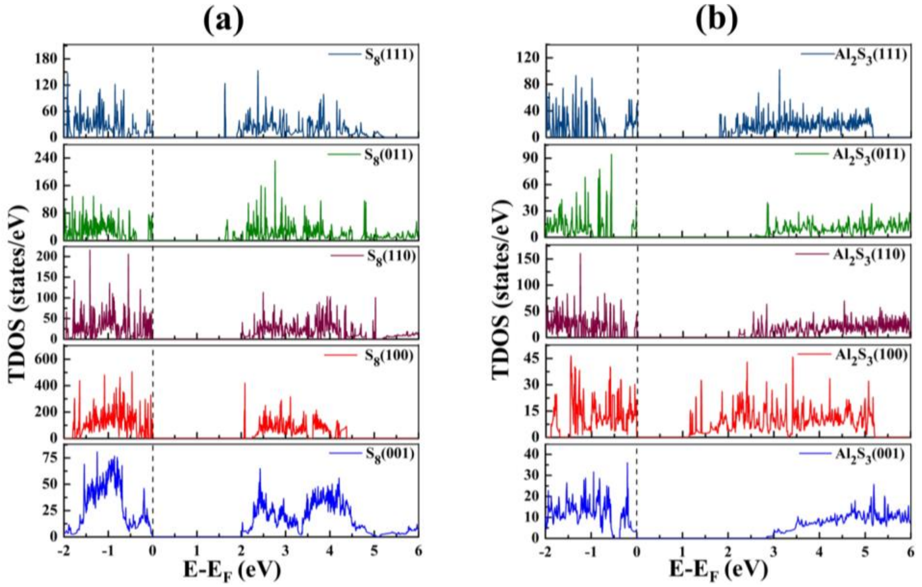

Figure 5.2: Density of states for the surfaces (001), (100), (110), (011) and (111) of (a) S_8 and (b) Al_2S_3. The Fermi level is set to zero and is indicated by black dashed line.

To investigate the electric properties of the possible surfaces of both S_8 and Al_2S_3 systems, we have studied the density of state as shown in Figure 5.2. The DOS reveals that all of the considered surfaces (001), (100), (110), (011) and (111) of both S_8 and Al_2S_3 show sizable band gap. For S_8 system, the nature of DOS is quite similar for all of the considered surfaces, where the valence and conduction bands are well separated by the large band gap ranging between 1.63 eV to 2.07 eV (Table 5.1), accounting for the semiconductor nature of these S_8 surfaces. The optimized surfaces of Al_2S_3 also exhibit wide band gap range of 1.15-2.88 eV, having the maximum band gap value of 2.88 eV for the most stable Al_2S_3(001) surface. To best of our knowledge, there are no previous reports on the band gaps of S_8 and Al_2S_3 surface, however the band gaps of the bulk forms of orthorhombic-sulfur and Al_2S_3 are reported to be 2.79 eV *[42]* and 2.81 eV *[43]*, respectively. As, the electrical conductivity (σ_i) is given by,

$$\sigma_i = \sqrt{N_c N_v} \exp\left(-\frac{E_g}{k_B T}\right) e(\mu_e + \mu_h) \tag{5.5}$$

where, N_c and N_v are the effective density of states at the band edges, which are dependent on temperature and the effective mass of the electron and holes respectively. E_g is the band gap and μ_e and μ_h are the mobilities of electron and hole, respectively. So, the higher mobility and lower band gap value will lead to higher electrical conductivity in a system.

Therefore, based on the observed band gap values, the order of conductivity for the surfaces of S_8 and Al_2S_3 systems can be given as (111)>(011)>(110)>(001)>(100) and (100)>(111)>(110)>(011)>(001).

In practical experimental scenario, the active S cathode material is embedded in a carbon based cathode host, which mainly provides necessary conductivity in the system as S and polysulfides are poor conductors. Here, we have considered only the elemental sulphur towards its interaction with the ionic liquid electrolyte ($AlCl_3$ with EMIC) to investigate the reaction patterns in Al-S battery. It is also supported by the fact that the sulphur reduction mechanism to give Al_2S_3 is not much effected by the choice of cathode host where the charge/discharge steps are following the similar paths. Other than that, in Al-S batteries, the involved ionic liquid electrolyte plays a critical role in not only providing medium for ion transport but undergoes active concentration changes in the electrochemical reactions during the course of charge/dis-charge processes. The previous Al-S battery reports with the detailed explanation of the reaction mechanism show that the active component $Al_2Cl_7^-$ undergoes a two-step conversion reaction to give Al^{3+} at the cathode surface, which reacts with S cathode to form the final product Al_2S_3 via several Al polysulfides formations in a chain reaction. So, to understand these chain reactions and to identify their role in charge and discharge, the effects of electrolyte are included explicitly in our simulations by constructing the cathode/electrolyte interface. The computational setups which are used to investigate the charge and discharge process in Al-S battery including the electrolyte are given in Figure 5.3. The dimension of the crystalline region is around 25 Å, whereas that of the electrolyte is around 15 Å. The ionic liquid electrolyte structure is generated by randomly adding electrolyte molecules to the system at the experimental density and the structure is allowed to relax with the solid surface part frozen, followed by a gradual temperature raise of the liquid to 300 K for 2 ps using AIMD calculations. To allow for cathode-electrolyte interaction, the crystalline part, except for the bottom 10 Å of the crystal, is relaxed together with the liquid for another 2 ps to form the equilibrium cathode/electrolyte interface. The frozen bottom crystal is used to simulate the bulk environment.

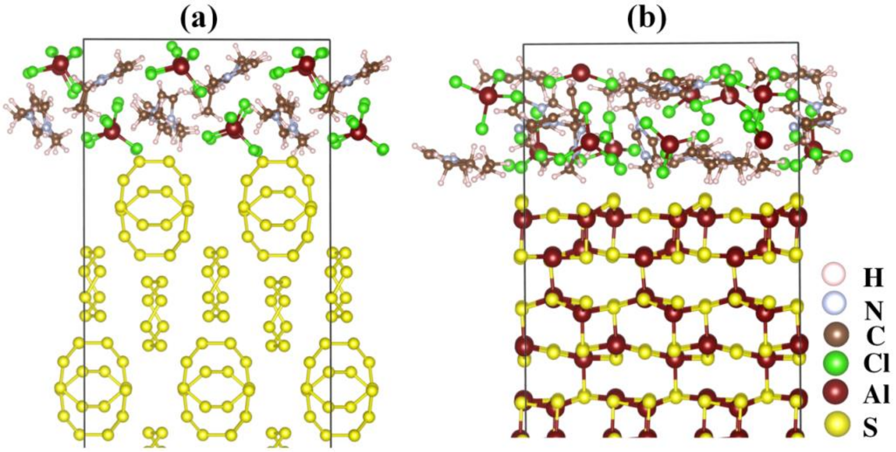

Figure 5.3: Structure of the supercells used in the calculations, (a) S_8(001)/[EMIM]$AlCl_4$-electrolyte, (b) Al_2S_3(001)/[EMIM]$AlCl_4$ electrolyte interfaces.

In this computational setup, the discharging and charging processes (corresponding to Al deposition into cathode to form Al polysulfides and vice versa) are studied only along the top interface. As, we have discussed earlier that ionic liquid electrolyte undergoes conversion reaction to provide Al ion deposition, so to study the discharging, Al atoms are added randomly along the top interface, and during charging, randomly selected Al atoms are removed. After each Al atom addition/removal, the system is equilibrated for a total of 2 ps. To ensure that the statistical errors of simulations are minimum, we have also tested the time period of 5 ps along with 2 ps. The time period of 2 ps is chosen for the equilibration after verifying that the structural configurations are quite similar for both time periods. And, 2 ps is suitable enough to ensure that the interface system evolves structurally and reaches the new equilibrium state, and at the same time the computational cost is reasonable. Similar kind of simulation time periods have also been used for Li-S batteries *[41]* and other previous theoretical studies *[44-45]*, where the reaction patterns are obtained to be reliable.

5.3. Results and Discussion

5.3.1. Discharging Process on the S_8(001) Surface

To study the discharging process, we have taken a 2 × 2 × 1 supercell of (001) surface of S_8 system, having the surface length of ~25 Å and electrolyte length of ~15 Å. To allow the interaction of the interface of S_8(001) surface and electrolyte, the system is equilibrated for 2 ps using AIMD simulations by relaxing the ~15 Å of S_8(001) with electrolyte and keeping the bottom 10 Å fixed. We observe that at this point, there is not much interaction between the electrolyte and the surface, which indicates towards the stability of the elemental sulfur S_8 in Al-S battery. To initiate the discharging process, one Al atom is added to the system and simulated for 2 ps to allow it to interact with the S_8(001) surface. The structural analysis indicates towards the interfacial reactions, where few of the S-S bonds are cleaved to open up the S_8 rings, but overall ring systems remain unaltered (Figure 5.4). Also, we do not observe any Al-S bond formation, as at such low Al atom concentration Al-polysulfide formation is not possible. To check the accuracy of this random addition of Al atom and to ensure convergence in the averaged energies, a different configuration is also studied. However, we observe that in both of these configurations, Al atom has similar interaction approach towards the S_8 rings at the interface as can be seen from the Figure 5.4. Therefore, on considering the computational costs, we have analyzed only one configuration for further Al atom additions.

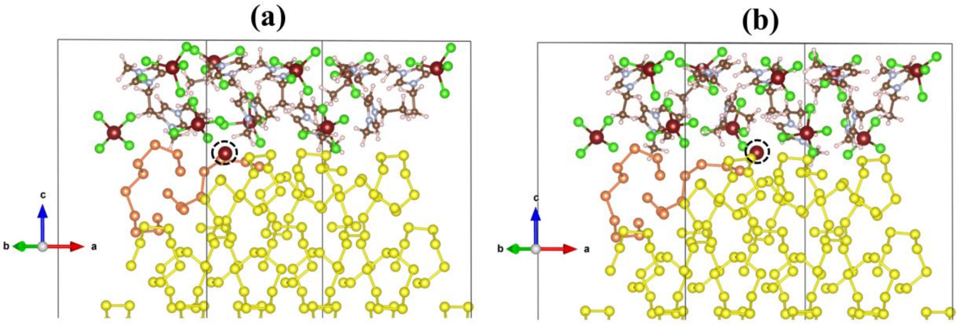

Figure 5.4: Representative structures of the S_8(001)/[EMIM]$AlCl_4$-electrolyte interfaces with 1 Al ion in two different orientations. Black dotted circle represents the added Al atom.

Furthermore, to check the statistical uncertainty of the AIMD simulation, we have also analyzed the equilibration with the time period of 5 ps for the very first Al atom and the 3rd Al atom addition by evaluating the total energy vs time plots and corresponding structural configurations. From the Figures 5.5 and 5.6, we can clearly observe that the nature of total energy variation for 5 ps timescale is quite same as that of 2 ps, and it fluctuates in the same total energy range on continuation of simulation even after 2 ps. For the 1st Al atom added S_8(001)/EMIM-$AlCl_4$-electrolyte interface system, the small fluctuations in total energy throughout the equilibration indicate that the overall ring systems remain unaltered except few S-S bonds being cleaved (Figure 5.5a-b). However, the observed energy spikes indicate towards comparatively unstable intermediate structures, such as Figure 5.5c, Supporting Information, presents the snapshot of the unstable intermediate structure obtained at 581 fs with various sulfur clusters: S_2, S_5, S_6, and S_{10}. For 3rd Al atom addition, the total energy plots for both time periods show an initial sharp decrease, which may correspond to the breaking of the S_8 rings at the interface of S_8(001)/EMIM-$AlCl_4$-

electrolyte system, followed by a smooth decrease corresponding to Al plolysulfides formation alongside the S-S bond breaking (Figure 5.6a). The MD plots as well as the formed intermediate Al polysulfides indicate that structural configurations remain almost same even after 5 ps simulation. Therefore, based on these observations, the time step of 2 ps per Al atom addition/removal is chosen for further discharge/charge calculations.

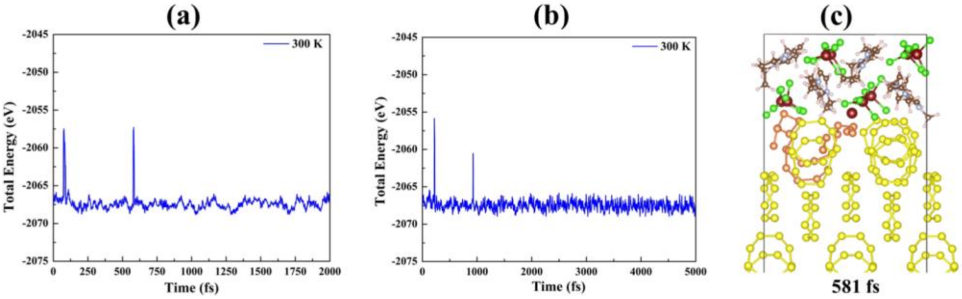

Figure 5.5: AIMD simulations of 1 Al added S_8(001)/EMIM-$AlCl_4$-electrolyte system for (a) 2 ps and (b) 5 ps timescale. (c) Snapshot of 1 Al added S_8(001)/EMIM-$AlCl_4$-electrolyte system at 581 fs.

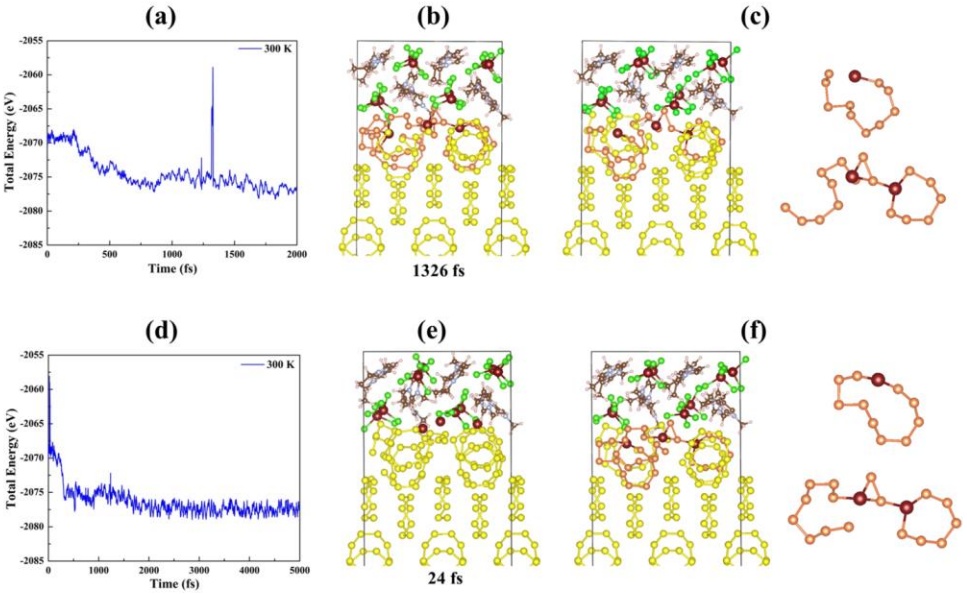

Figure 5.6: AIMD simulations of 3 Al atoms added S_8(001)/EMIM-$AlCl_4$-electrolyte system for (a) 2 ps and (d) 5 ps timescale. Snapshots of the system at (b) 1326 fs of 2 ps timescale, and (e) 24 fs of 5 ps timescale. Representative structures of S_8(001)/[EMIM]$AlCl_4$-electrolyte interface with the corresponding Al polysulfides formed upon completion of (c) 2 ps and (f) 5 ps simulations. The sulfur atoms involved in Al polysulfide formations are shown in orange color.

Further, as more Al atoms are added, electrochemical reduction of sulfur to Al polysulfides is initiated. At initial stages when Al atom concentration is low, upto 5 Al atom simulations, higher order Al polysulfides are expected to form. In our simulations, various reaction products are formed having the form of Al_xS_y, such as $(AlS_9)^{-3}$ and $(Al_2S_{17})^{+1/3}$, which have an overall stoichiometries close to the polysulfides $Al_2(S_3)_3$ and $Al_2(S_6)_3$, respectively (Figure 5.7).

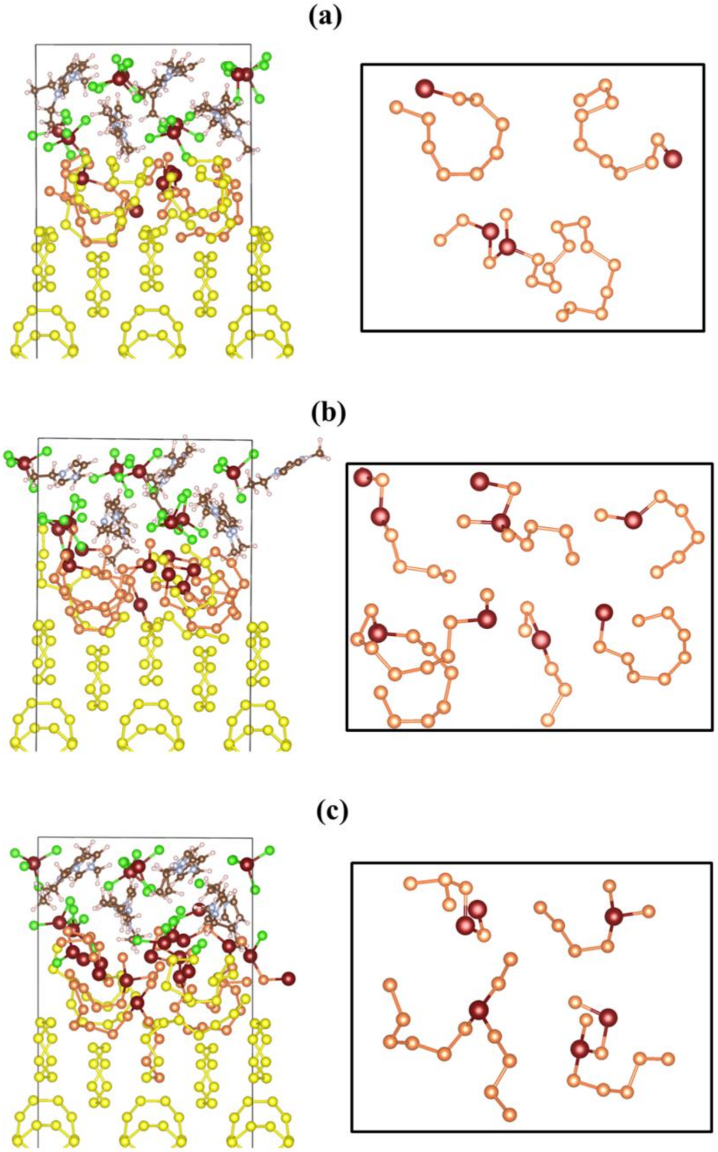

Figure 5.7: Representative structures of S_8(001)/[EMIM]$AlCl_4$-electrolyte interface during discharging reaction with (a) 5, (b) 10, (c) 15 numbers of Al atoms. The rectangular boxes show the corresponding Al polysulfides formed during the course of simulation.

As more number of Al atoms are added into simulations, various other reaction products are also formed AlS_{15}, $(Al_2S_5)^{+1}$, $(Al_2S_7)^{-1}$, $(AlS_6)^{-3}$, $(AlS_{12})^{-3}$, and $(Al_2S_8)^{-2/3}$ having a closer stoichiometries as of higher order polysulfides as shown in Figure 3 for 10 and 15 number of Al atom addition. The formation of these anionic and cationic reaction products during the course of reaction is a result of deficiency of Al^{3+} and availability of extra Al^{3+}, respectively. In experiments, the intermediate polysulfides (undergoing the reversible chain reactions to give the final product Al_2S_3) which are expected to form are of the form of S_x^{2-} ($1 \leq x < 6$), but we observe that the reduction of S_8 can follow a different mechanism, which depends upon the availability of the local Al atom concentration. It is suggested that the due to the presence of different Al atom concentrations around different S_8 rings, the reduction of rings can lead to reaction products such as anionic, cationic and neutral. These are short lived intermediates that give rise to a net electric field that drives the migration of these molecules, leading to the formation of thermodynamically more stable neutral Al polysulfide species and this kind of driving forces have also been observed for previously studied Li-S batteries *[41]*. Moreover, from Figure 5.7, we observe that as more number of Al atoms are added, the higher polysulfides are further reduced and these Al polysulfides starts diffusing into electrolyte due to ionic interactions. This can be more clearly observed in a systematic manner from Figure 5.8, where electrolyte can be seen diffusing into the second layer of S_8 rings, indicating the dissolution of higher order Al polysulfide into the electrolyte. This is in accordance with the experimental observations, where the higher order Al polysulfides, S_x^{2-}, $x \geq 6$ are soluble in ionic liquid electrolyte *[26]*.

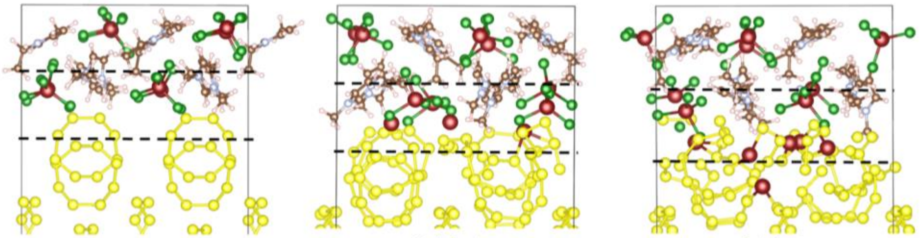

Interface model 3 Al atoms 6 Al atoms

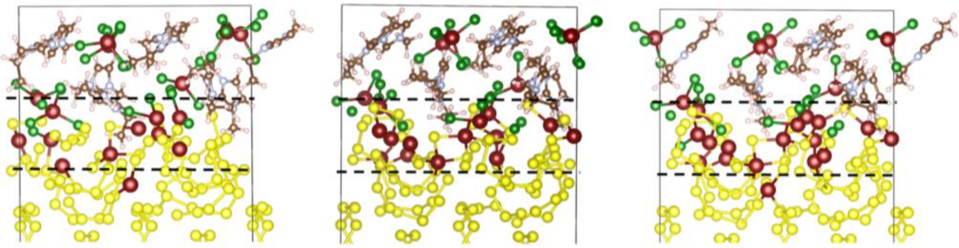

9 Al atoms 12 Al atoms 15 Al atoms

Figure 5.8: Schematic presentation of Al polysulfides diffusion into the electrolyte with the course of AIMD simulation.

After evaluating the structural changes during the discharge process, we have next investigated the variation of voltage relative to number of Al atoms added in the simulations and compare it with experimental values. The correct determination of theoretical voltage is mainly dependent upon the voltage equation used. As, in case of earlier studied Al dual-ion batteries, the energy of electrolyte is also included in calculation of voltage because of the involvement of electrolyte in the net reaction equation, $C_n[AlCl_4] + 4AlCl_4^- + Al \leftrightarrow C_n + 4Al_2Cl_7^-$ in their overall reaction mechanism *[46-48]*. However, in case of Al-S batteries, as we can see from equation 5.3, $2Al + 3S \leftrightarrow Al_2S_3$, the ionic liquid electrolyte does act as Al^{3+} ion carrier between cathode and anode via undergoing conversion reactions involving $AlCl_4^-$ and $Al_2Cl_7^-$ anions (equation 5.1 and 5.3), but does not actively participate in the determination of electrochemical properties, such as cell voltage. This behavior is quite similar to Al batteries involving the intercalation of Al^{3+} ions from the ionic liquid electrolytes *[49-51]*. Therefore, we have considered the following equation (5.6) to determine the reaction voltage,

$$V\ (x_1, x_2) = -\left(\frac{E_{system+x_2Al} - (x_2 - x_1)E_{Al} - E_{system+x_1Al}}{(x_2 - x_1)}\right) \qquad (5.6)$$

where, $E_{system+x_1Al}$ is the energy of S_8(001)/EMIM-$AlCl_4$ interface system with x_1 number of Al atoms and $E_{system+x_2Al}$ is the energy of interface with x_2 of Al atoms after the addition of $(x_2 - x_1)$ Al atoms. Here, both total energies, $E_{system+x_1Al}$ and $E_{system+x_2Al}$ are taken after optimizations of the structural configurations obtained on 2 ps AIMD simulations and similar concept is followed for the charging voltage profile study. E_{Al} is the energy of face centered cubic Al bulk. The voltage plot presenting the variation in discharging voltage is shown in Figure 5.9.

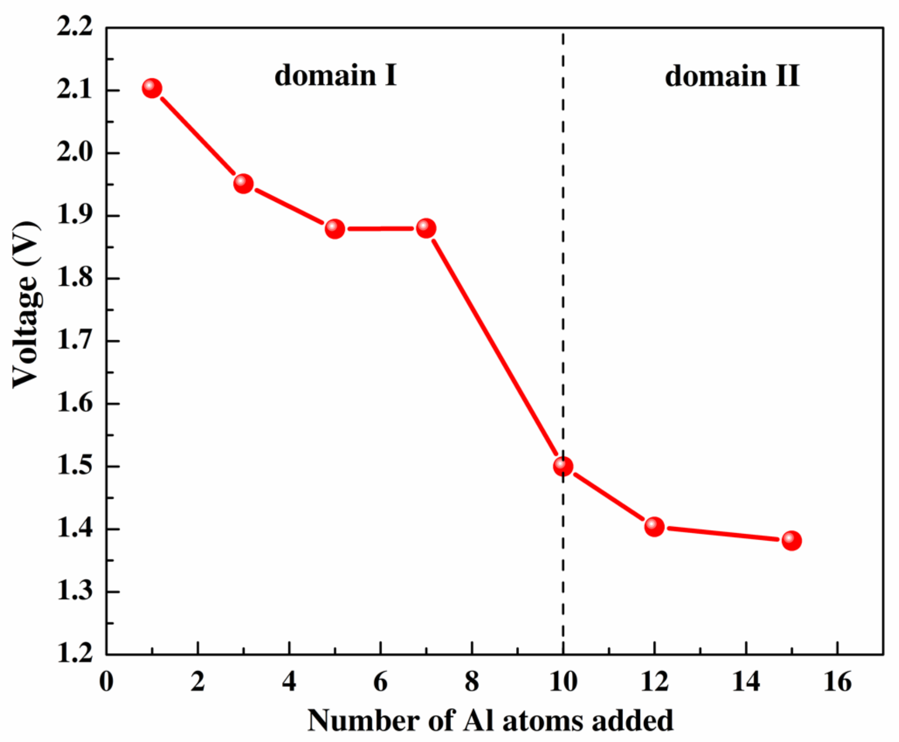

Figure 5.9: The discharging voltage profile as a function of number of Al atoms added to S_8(001)/ EMIM-$AlCl_4$ electrolyte interface.

From the voltage plot, we can observe two different voltage domains, which indicate toward the involvement of different reaction mechanisms.

The first voltage region is of higher voltage values as compared to the upper-limit of experimental discharge voltage 1.30 V. However, the initial high voltage of 1.95-2.10 V corresponding to the addition of 1 and 3 Al atoms can be explained as a consequence of the interface effects of S_8 surface-electrolyte and position of Al atoms along the interface as only few S_8 rings are opened up with small energy penalty and thus high voltage value are observed. The voltage slightly decreases to 1.87-1.88 V as more Al atoms are added, which extends from 5 to 7 in number. Here, the reduction of few of the S_8 rings starts taking place, leading to the formation of higher order Al polysulfides as discussed earlier and can been seen from the representative Figure 5.7. Such higher order cathodic cell voltage than the theoretical cell voltage of 1.30 V of Al-S battery has also been observed by Yu et al. *[28]* in their recent experimental study, where they attributed this behavior to the solvation effect, viscosity, and volatility of the electrolytes. Also, similar phenomenon has been observed for Li-S batteries, where the first reduction peak of current-voltage curve is occurred above the theoretical cell voltage of 2.60 V *[52]*. As more number of Al atoms (10 to 15 atoms) are added into the S_8(001)/electrolyte system, the discharge voltage reaches the second voltage domain of 1.38-1.50 V. From this point, our observed voltage range starts approaching the experimental voltage range of ~1.30 V *[28]*. Experimentally, at this first discharge voltage plateau of 1.30 V, electrochemical reduction comes into consideration and dissociation of elemental sulfur into long chain Al polysulfides start occurring *[28]*. The behavior of S_8 ring reduction into Al polysulfides intermediates has also been observed in our study as discussed earlier, which is in accordance with the experimental observations. However, in experiment *[28]*, a lower voltage plateau is also observed ~0.75 V, which corresponds to the reduction of higher order polysulfides to lower order polysulfides such as Al_2S_6 and the final discharge product Al_2S_3. Overall, these atomistic insights suggest the importance of local Al concentration, and the variation in such a concentration leads to the formation of various intermediate species, the competition of different reaction mechanisms, and thus the overall reaction pattern. It also explains the variation in the experimentally observed charge/discharge profiles as the local Al concentration cannot be precisely controlled experimentally.

5.3.2. Charging Process on Al_2S_3(001) Surface

After the evaluation of the discharging processes on the interface of S_8-electrolyte, we next investigate the charging process, which basically involves $Al_2S_3 \rightarrow 3S + 2Al$ conversion reaction via a chain of polysulfide formation reactions. In charging process, an external voltage is required to pullout the Al atoms from the Al_2S_3 system. The charging process is modeled by removing the Al atoms along the Al_2S_3(001)/[EMIM]$AlCl_4$-electrolyte interface at the same rate as discharging. The Al_2S_3(001) surface is studied being the most stable surface and the representative Al_2S_3(001)/[EMIM]$AlCl_4$-electrolyte model is given in Figure 5.3b. As the charging process proceeds, Al atoms are removed from the top interface of Al_2S_3(001)/[EMIM]$AlCl_4$-electrolyte system followed by AIMD simulations of 2 ps timescale. The corresponding voltage values to these equilibrated systems are calculated using the following equation (5.7),

$$V\,(y_1, y_2) = -\left(\frac{E_{system+y_1Al} - (y_1 - y_2)E_{Al} - E_{system+y_2Al}}{(y_1 - y_2)}\right) \tag{5.7}$$

where, $E_{system+y_1Al}$ is the energy of Al_2S_3(001)/[EMIM]$AlCl_4$-electrolyte system with y_1 number of Al atoms and $E_{system+y_2Al}$ is the energy of interface system with remaining y_2 number of Al atoms after removal of $(y_1$-$y_2)$ Al atoms. The voltages values obtained using equation 5.7, are plotted against the number of Al atoms removed and the charging voltage profile is shown in Figure 5.10.

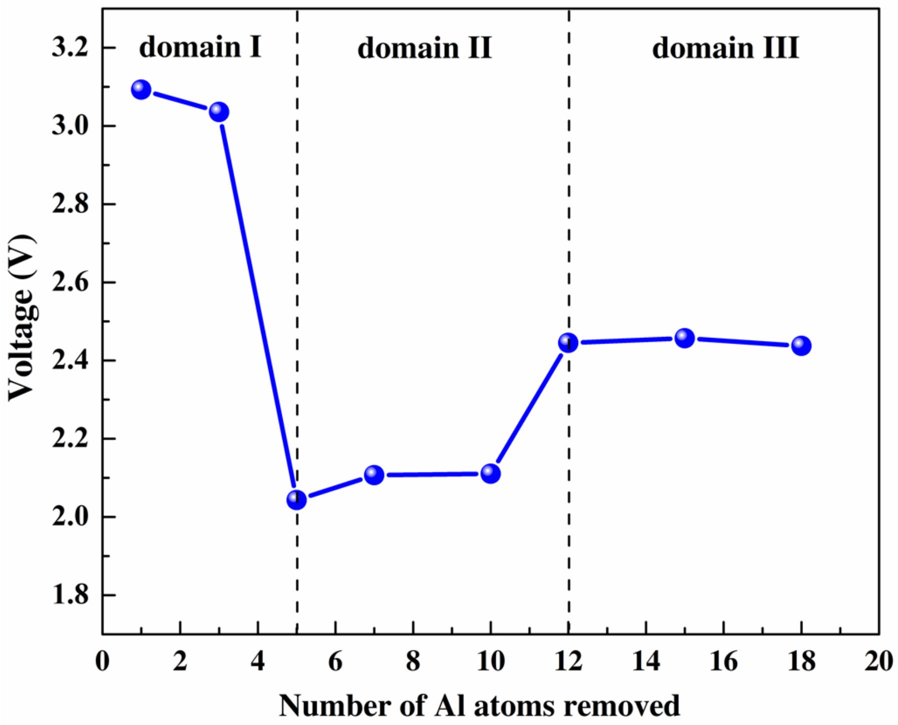

Figure 5.10: The charging voltage profile as a function of number of Al atoms removed from Al_2S_3(001)/[EMIM]$AlCl_4$-electrolyte interface.

In the modeled Al_2S_3(001) system, the stoichiometry of sulfur is more compared to Al, having few of the sulfur atoms residing out of the plane, and the Al atoms are removed from the first atomic layers, which consist of 18 Al atoms. Therefore, we have carried out the simulations to the maximum of 18 Al ions removal. The obtained charging voltage profile is presented in Figure 5.10 and consists of three voltage domains. The charging process starts with the high voltage range of 3.03-3.09 V (domain I), which corresponds to the removal of upto 3 Al atoms. During this voltage range, few of Al-S bonds are cleaved as shown in the representative structure in Figure 5.11a.

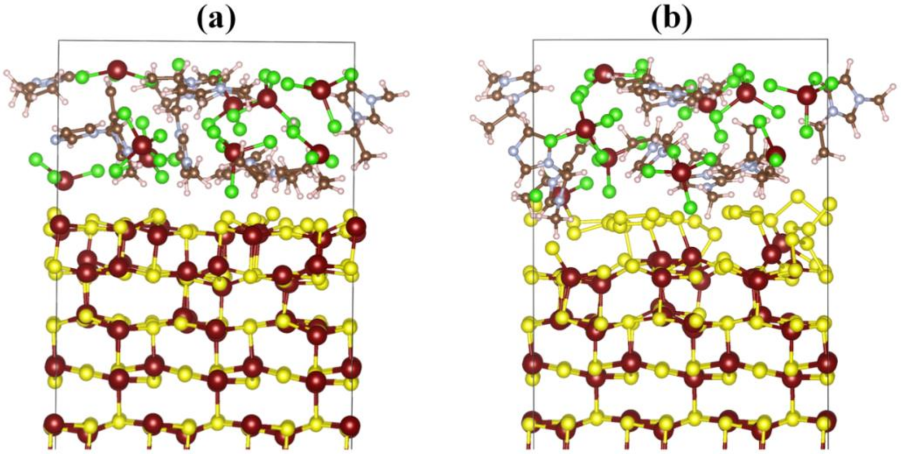

Figure 5.11: Representative structures of Al_2S_3(001)/[EMIM]$AlCl_4$-electrolyte during charging reaction with (a) 3, and (b) 18 numbers of Al atoms removed.

This higher voltage domain may correspond to the higher outer potential required to allow destruction in a stable crystal structure of Al_2S_3(001) surface. As more number of Al atoms (upto 10) are removed from the interface, the charging voltage drops to 2.04-2.11 V range, and we have notified this change as voltage domain II. Here in this domain, the Al atoms are being removed from the already defected Al_2S_3(001) system, which could require lower outer potential and also the energy required to break Al-S bonds gets compensated by S-S bond formation. Thus, decreasing the charging voltage. From the structural point of view, we observe that Al atom removal does not affect the overall structural stability of Al_2S_3 system, and structural distortions are mainly limited to the layer from where Al atoms are removed. This voltage range can be compared to the experimental charge voltage plateau of ~1.75 V *[28]*, which is observed to be the transition of lower order polysulfides S_x^{2-} ($1 \leq x < 6$). The voltage further increases to a plateau of 2.43-2.45 V, as all of Al atoms are removed from the top atomic layer and the Al-S bond cleavage is more prominent than S-S bond formation. This forms domain III of charging voltage profile. We observe that even after all the 18 Al atoms removal from the top Al containing layer of Al_2S_3(001) system

(Figure 5.11b), the inner atomic layer still maintains its structural stability and distortions are mainly narrowed to the top atomic layer. This corresponds towards the layer by layer dissociation behavior of Al_2S_3 system in charging process, which can lead to an overall low electrochemical activity. This observed behavior partially explains the higher charging voltage and the overall large voltage hysteresis (~0.7-1.0 V) observed in experimental studies *[28-30]* other than the kinetic limitation of solid-state sulfur conversion reaction.

5.4. Conclusion

We have used the *ab initio* molecular dynamics (AIMD) simulations to investigate the charging and discharging processes in currently developing Al-S battery. The atomistic structure and reaction voltage as a function of the number of Al atoms are determined with stable S_8 and Al_2S_3 surface-ionic liquid electrolyte systems. After observing the S_8(001) surface to be most stable, the S_8(001)/[EMIM]$AlCl_4$-electrolyte interface system is used to study the discharging process by subsequently adding the Al atoms along the interface followed by MD simulation. The reduction of S_8 follows layer by layer mechanism and involves the formation of various cationic and anionic intermediate species (Al_xS_y) which drives the formation of Al polysulfides during the course of discharging process. The discharge voltage profile shows two voltage domains, where the highest voltage range 1.95-2.10 V is the consequence of the interface effects of S_8 surface-electrolyte and position of Al atoms along the interface. The second voltage domain 1.38-1.50 V which starts coinciding with the experimental values involves the reduction of S_8 to higher order polysulfides. We also observe the diffusion of these higher order Al polysulfides to electrolyte, which is in accordance with the experimental observed solvation of higher order Al poylsulfides into electrolyte. Moreover, the investigation of the charging process on a Al_2S_3(001)/electrolyte interface shows that the top atomic sublayer structural distortions are mainly limited to the layer from where Al atoms are removed and not the other inner atomic layers, which can lead to low electrochemical activity and an increase in the overall charging voltage of Al-S battery. Overall, our investigation provides a detailed microscopic insights into the electrochemical reactions involved in Al−S batteries, and the new atomistic insights obtained, including the formation of various intermediate species, the competition of different reaction mechanisms, and the importance of local Al concentration, could help to improve our understanding of the complex electrochemical processes observed in these batteries.

5.5. References

1. Goodenough J. B., Park K. S. (2013), The Li-ion rechargeable battery: a perspective, J. Am. Chem. Soc., 135, 1167–1176 (DOI: 10.1021/ja3091438)
2. Goodenough J. B., Kim Y. (2010), Challenges for rechargeable Li batteries, Chem. Mater. 22 587–603 (DOI: 10.1021/cm901452z)
3. Bruce P. G., Freunberger S. A., Hardwick L. J., Tarascon J.M. (2012), Erratum: Li–O_2 and Li–S batteries with high energy storage, Nat. Mater. 11, 19–29 (DOI:10.1038/nmat3237)
4. Lu Y. C., Xu Z. C., Gasteiger H. A., Chen S., Hamad-Schifferli K., Shao-Horn Y. (2010), Platinum−gold nanoparticles: a highly active bifunctional electrocatalyst for rechargeable lithium−air batteries, J. Am. Chem. Soc., 132, 12170–12171 (DOI: 10.1021/ja1036572)
5. Liu Y., Wang L. P., Cao L. J., Shang C. Q., Wang Z. Y., Wang H. E., He L. Q., Yang J. Y., Cheng H., Li J. Z., Lu Z. G. (2017), Understanding and suppressing side reactions in Li–air batteries, Mater. Chem. Front., 1, 2495–2510 (DOI: 10.1039/C7QM00353F)
6. Wu S. F., Wang W. X., Li M. C., Cao L. J., Lyu F. C., Yang M. Y., Wang Z. Y., Shi Y., Nan B., Yu S. C., Sun Z. F., Liu Y., Lu Z. (2016), Highly durable organic electrode for sodium-ion batteries via a

stabilized α-C radical intermediate, Nat. Commun., 7, 13318 (DOI: 10.1038/ncomms13318)

7. Ji X. L., Nazar L. F. Advances in Li-S batteries, J. Mater. Chem. 2010, 20, 9821−9826 (DOI: 10.1039/B925751A)
8. Manthiram A., Fu Y., Chung S. H., Zu C., Su Y. (2014), Rechargeable lithium-sulfur batteries, Chem. Rev., 114, 11751–11787 (DOI: 10.1021/cr500062v)
9. Manthiram A., Fu Y., Su Y. (2013), Challenges and prospects of lithium-sulfur batteries, Acc. Chem. Res., 46, 1125–1134 (DOI: 10.1021/ar300179v)
10. Pang Q., Liang X., Kwok C. Y., Nazar L. F. (2016), Advances in lithium-sulfur batteries based on multifunctional cathodes and electrolytes, Nat. Energy, 1, 16132 (DOI: 10.1038/nenergy.2016.132)
11. Fu Y. Z., Zu C. X., Manthiram A. (2013), In situ-formed Li2S in lithiated graphite electrodes for lithium-sulfur batteries, J. Am. Chem. Soc., 135, 18044–18047 (DOI: 10.1021/ja409705u)
12. Klein M. J., Veith G. M., Manthiram A. (2017), Chemistry of sputter-deposited lithium sulfide films, J. Am. Chem. Soc., 139, 10669–10676 (DOI: 10.1021/jacs.7b03379)
13. Manthiram A., Yu X. W. (2015), Ambient temperature sodium-sulfur batteries, Small, 11, 2108–2114 (DOI: 10.1002/smll.201403257)
14. Wei S. Y., Xu S. M., Agrawral A., Choudhury S., Lu Y.Y., Tu Z. Y., Ma L., Archer L. A. (2016), A stable room-temperature sodium-sulfur battery. Nat. Commun., 7, 1172 (DOI: 10.1038/ncomms11722)
15. Xin S., Yin Y. X., Guo Y. G., Wan L. J. (2014), A high-energy room-temperature sodium-sulfur battery, Adv. Mater., 26, 1261– 1265 (DOI: 10.1002/adma.201304126)
16. Zhao Q., Hu Y. X., Zhang K., Chen J. (2014), Potassium-sulfur batteries: a new member of room-temperature rechargeable metal-sulfur batteries, Inorg. Chem., 53, 9000– 9005 (DOI: 10.1021/ic500919e)

17. Gao T., Noked M., Pearse A. J., Gillette E., Fan X. L., Zhu Y. J., Luo C., Suo L. M., Schroeder M. A., Xu K., et al. (2015), Enhancing the reversibility of Mg/S battery chemistry through Li+ mediation, J. Am. Chem. Soc., 137, 12388–12393 (DOI: 10.1021/jacs.5b07820)
18. Kim H. S., Arthur T. S., Allred G. D., Zajicek J., Newman J. G., Rodnyansky A. E., Oliver A. G., Boggess W. C., Muldoon J. (2011), Structure and compatibility of a magnesium electrolyte with a sulphur cathode, Nat. Commun., 2, 427 (DOI: 10.1038/ncomms1435)
19. Li W. F., Cheng S., Wang J., Qiu Y. C., Zheng Z. Z., Lin H. Z., Nanda S., Ma Q., Xu Y., Ye F. M., et al. (2016), Synthesis, crystal structure, and electrochemical properties of a simple magnesium electrolyte for magnesium/sulfur batteries, Angew. Chem. Int. Ed., 55, 6406– 6410 (DOI: 10.1002/anie.201600256)
20. Manthiram A., Yu X.W. (2016), Performance enhancement and mechanistic studies of Magnesium-Sulfur cells with an advanced cathode structure, ACS Energy Lett., 1, 431–437 (DOI: 10.1021/acsenergylett.6b00213)
21. Zhu J., Zou J., Cheng H., Gu Y., Lu Z. (2019), High energy batteries based on sulfur cathode, Green Energy & Environment, 4, 345-359 (DOI: 10.1016/j.gee.2018.07.001)
22. See K. A., Gerbec J. A., Jun Y. S., Wudl F., Stucky G. D., Seshadri R. (2013), A high capacity calcium primary cell based on the Ca- S system, Adv. Energy Mater., 3, 1300160 (DOI: 10.1002/aenm.201300160)
23. Elia G. A., Marquardt K., Hoeppner K., Fantini S., Lin R., Knipping E., Peters W., Drillet J. F., Passerini S., Hahn R. (2016), An overview and future perspectives of aluminum batteries, Adv. Mater., 28, 7564–7579 (DOI: 10.1002/adma.201601357)
24. Wang Y., Chen R., Chen T., Lv H., Zhu G., Ma L., Wang C., Jin Z., Liu J. (2016), Emerging non-lithium ion batteries, Energy Storage Mater., 4, 103–129 (DOI: 10.1016/j.ensm.2016.04.001)

25. Sadat W. I. A., Archer L. A. (2016), The O_2-assisted Al/CO_2 electrochemical cell: A system for CO_2capture/conversion and electric power generation, Sci. Adv., 2, e1600968 (DOI: 10.1126/sciadv.1600968)
26. Gao T., Li X., Wang X., Hu J., Han F., Fan X., Suo L., Pearse A. J., Lee S. B., Rubloff G. W., Gaskell K. J., Noked M., Wang C. (2016), A rechargeable Al/S battery with an ionic-liquid electrolyte, Angew. Chem. Int. Ed., 55, 9898–9901; Angew. Chem., 128, 10052–10055 (DOI: 10.1002/anie.201603531)
27. Cohn G., Ma L., Archer L. A., (2015), A novel non-aqueous aluminum sulfur battery J. Power Sources, 283, 416 – 422 (DOI: 10.1016/j.jpowsour.2015.02.131)
28. Yu X., Manthiram A., (2017), Electrochemical energy storage with a reversible nonaqueous room-temperature aluminum–sulfur chemistry, Adv. Energy Mater., 7, 1700561 (DOI: 10.1002/aenm.201700561)
29. Yu X., Boyer M. J., Hwang G. S., Manthiram A., (2018), Room-temperature aluminum-sulfur batteries with a lithium-ion-mediated ionic liquid electrolyte, Chem, 4, 586–598 (DOI: https://doi.org/10.1016/j.chempr.2017.12.029)
30. Guo Y., Jin H., Qi Z., Hu Z., Ji H., Wan L.-J. (2019), Carbonized-MOF as a sulfur host for aluminum–sulfur batteries with enhanced capacity and cycling life, Adv. Funct. Mater., 29, 1807676 (DOI:10.1002/adfm.201807676)
31. BlÖchl P. E. (1994), Projector augmented-wave method, Phys. Rev. B: Condens. Matter Mater. Phys., 50, 1795 −17979. (DOI: 10.1103/PhysRevB.50.17953)
32. Kresse G., Joubert D. (1999), From ultrasoft pseudopotentials to the projector augmented-wave method, Phys. Rev. B: Condens. Matter Mater. Phys., 59, 1758. (DOI: 10.1103/PhysRevB.59.1758)

33. Kresse G., Hafner J. (1993), Ab initiomolecular dynamics for liquid metals, Phys. Rev. B: Condens. Matter Mater. Phys., 47, 558. (DOI: 10.1103/PhysRevB.47.558)
34. Kresse G., Hafner J. (1994), Ab initiomolecular-dynamics simulation of the liquid-metal-amorphous-semiconductor transition in germanium, Phys. Rev. B: Condens. Matter Mater. Phys., 49, 14251. (DOI: 10.1103/PhysRevB.49.14251)
35. Kresse G., Furthmüller J. (1996), Efficiency of ab-initio total energy calculations for metals and semiconductors using a plane-wave basis set, Comput. Mater. Sci., 6, 15−50. (DOI: 10.1016/0927-0256(96)00008-0)
36. Kresse G., Furthmüller J. (1996), Efficient iterative schemes for ab initio total-energy calculations using a plane-wave basis set, Phys. Rev. B: Condens. Matter Mater. Phys., 54, 11169−11186. (DOI: 10.1103/PhysRevB.54.11169)
37. Perdew J. P., Burke K., Ernzerhof, M. (1996), Generalized gradient approximation made simple, Phys. Rev. Lett., 77, 3865−3868. (DOI: 10.1103/PhysRevLett.77.3865)
38. Perdew J. P., Burke K., Ernzerhof M. (1996), Generalized gradient approximation made simple, Phys. Rev. Lett., 1997, 78, 1396. (DOI: 10.1103/PhysRevLett.77.3865)
39. Grimme S., Antony J., Ehrlich S., Krieg H. (2010), A consistent and accurate ab initio parametrization of density functional dispersion correction (DFT-D) for the 94 Elements H-Pu, J. Chem. Phys., 132, 154104. (DOI: 10.1063/1.3382344)
40. Nosé S., (1984), A unified formulation of the constant temperature molecular dynamics methods, J. Chem. Phys., 81, 511. (DOI: 10.1063/1.447334)
41. Arneson C., Wawrzyniakowski Z. D., Postlewaite J. T., Ma Y. (2018), Lithiation and delithiation processes in lithium–sulfur batteries from

ab initio molecular dynamics simulations, J. Phys. Chem. C, 122, 16, 8769-8779. (DOI: 10.1021/acs.jpcc.8b00478)

42. Liu G., Niu P., Yin L., Cheng H.-M. (2012), α-Sulfur Crystals as a Visible-Light-Active Photocatalyst. J. Am. Chem. Soc., 134, 9070-9073. (DOI: 10.1021/ja302897b)
43. Persson K. (2014), Materials Data on Al_2S_3 (SG:169) by Materials Project., 10.17188/1201189.
44. Ma Y., Garofalini S. H. (2017), Reactive molecular dynamics simulations of the conversion and reconversion reactions in FeF2 nanoparticles, J. Phys. Chem. C, 121, 15002−15007. (DOI: 10.1021/acs.jpcc.7b02412)
45. Ma Y., Garofalini S. H. (2012), Atomistic insights into the conversion reaction in iron fluoride: a dynamically adaptive force field approach, J. Am. Chem. Soc., 134, 8205−8211 (DOI: 10.1021/ja301637c)
46. Lin M. C., Gong M., Lu B., Wu Y., Wang D. Y., Guan M., Angell M., Chen C., Yang J., Hwang B. J., Dai H. (2015), An ultrafast rechargeable aluminium-ion battery, Nature, 520, 324-328 (DOI: 10.1038/nature14340)
47. Bhauriyal P., Mahata A., Pathak B. (2017), The staging mechanism of $AlCl_4$ intercalation in graphite electrode for aluminium-ion battery, Phys. Chem. Chem. Phys., 19, 7980–7989 (DOI: 10.1039/c7cp00453b)
48. Bhauriyal P., Garg P., Patel M., Pathak B. (2018), Electron-rich graphite-like electrode: stability vs. voltage for Al batteries, J. Mater. Chem. A, 6, 10776-10786 (DOI: 10.1039/c8ta01820k)
49. Jayaprakash N., Das S. K., Archer L. A. (2011), The rechargeable aluminum-ion battery, Chem. Commun., 47, 12610–12612 (DOI: 10.1039/C1CC15779E)
50. Geng L., Lv G., Xing X., Guo J. (2015), Reversible electrochemical intercalation of aluminum in Mo_6S_8, Chem. Mater., 27, 4926–4929 (DOI: 10.1021/acs.chemmater.5b01918)

51. Wang S., Yu Z., Tu J., Wang J., Tian D., Liu Y., Jiao S. (2016), A Novel aluminum-ion battery: Al/$AlCl_3$-[EMIm]Cl/Ni_3S_2@graphene, Adv. Energy Mater., 6, 1600137 (DOI: 10.1002/aenm.201600137)
52. Yu X., Manthiram A. (2015), A class of polysulfide catholytes for lithium–sulfur batteries: energy density, cyclability, and voltage enhancement, Phys. Chem. Chem. Phys., 17, 2127- 2136 (DOI: 10.1039/c4cp04895d)

Chapter 6

Superior Anchoring Effect of Cu-Benzenehexathial MOF as Aluminium-Sulfur Battery Cathode Host

6.1. Introduction

The high abundance of aluminium (Al) in earth crust, the high volumetric (8.05 Ah/cm^3) and gravimetric capacity (2.98 Ah/g) associated with 3e^- redox reaction and excellent safety, make Al one of the most advantageous element and Al-metal based batteries to be the future of leading energy storage systems *[1-3]*. The use of ionic liquid-based electrolytes has increased the efficiency and stability of Al batteries via easing the reversible Al deposition/stripping with high Coulombic efficiency and thus has become necessary choice of current Al batteries *[4-5]*. These ionic liquid based Al batteries are proposed to work in two distinctive reversible energy storage mechanisms depending upon the applicability of the cathode materials, one is intercalation reactions and another is conversion reactions. As the chloroaluminate ionic liquid electrolyte consists of Al ion in the form of both cation and anions, so both Al^{3+} and $AlCl_4^-$ can undergo intercalation in rocking chair type Al batteries *[6-16]* and Al dual-ion batteries *[17-30]*, respectively. The rocking chair Al batteries are reported to furnish high capacity (~300 mAh/g) but are limited by their small cycle life (<20 cycles), coulombic efficiency and cell voltage range (~0.6 V), whereas Al dual-ion batteries can deliver higher voltage (~2.0 V) with fast charge/discharge rates, but have low storage capacity (<120 mAh/g) and involve large volume expansion due to the involvement of large sized anion *[31]*, which can cause irreversible damage to the battery. On the other hand, the conversion reaction mechanism has been reported in case of Ni and Fe-based sulfides *[32-35]*, which can hold higher storage capacities for initial charge/discharge cycles, but abruptly drop for long term usage due to destruction of cathode lattice with continuous charge/discharge cycles *[33]*. Also, the low conductivity is a big obstacle in the application of these conversion based Al batteries. However, the sulfur shows quite good advantages, when used as conversion cathode as it can undergo multi-electron transfer during electrochemical reactions to provide high specific capacity of 1675 mAh/g and is light weight. These sulfur cathodes have been quite explored in Li-S *[36-39]*, Na-S *[40-41]*, and Mg-S *[42-43]* batteries but the field of Al-S batteries is still very new. Till present, limited numbers of studies *[44-48]* have been reported for non-aqueous electrolyte based Al-S batteries after getting a successful initiation from primary Al-S battery in year 2015 *[44]*. The involved charge/discharge process are suggested to be following the given reaction mechanism,

Anode: $2Al + 14AlCl_4^- \leftrightarrow 8Al_2Cl_7^- + 6e^-$ (6.1)

Cathode: $8Al_2Cl_7^- + 6e^- + 3S \leftrightarrow Al_2S_3 + 14AlCl_4^-$ (6.2)

Overall: $2Al + 3S \leftrightarrow Al_2S_3$ (6.3)

In order to improve the battery efficiency, these studies either include the advancement of the cathode host material such as employing an activated carbon cloth/sulfur composite *[45]*, and constructing cathode matrix by dispersing a sulfur/Al[EMI]Cl_4 slurry onto free-standing carbon nanofiber (CNF) paper with coating of single-wall carbon nanotube paper on the separator to slow down the diffusion of polysulfide *[46]*. Or, by using lithium-ion (Li^+-ion)-mediated ionic liquid electrolyte *[47]*. However, these room-temperature Al-S batteries still observed to either show an extremely poor reversibility or suffered from a sluggish electrochemical kinetics due to the lack of a facile sulfur cathode host. In this regard, very recently, a composite of S on a carbonized HKUST-1 (Hong Kong University of Science and Technology) matrix (S@HKUST-1-C) is reported for Al–S batteries *[48]*, which maintains a reversible capacity of 600 mAh/g at the 75th cycle and a reversible capacity of 460 mAh/g at the 500th cycle with a Coulombic efficiency of around 95%. The better efficiency of this battery is credited to the presence of Cu in the electrochemical process to form an ionic cluster with polysulfide that facilitates the electrochemical reaction and improves the reversibility of S during charge/discharge. Additionally, Cu increases the electron conductivity at the HKUST-1-C/S interface. Such Cu based metal organic frameworks (MOFs) have also been explored for the development of more efficient Li-S batteries, both experimentally and theoretically *[49-52]*. Therefore, for the effective growth of Al-S batteries, it is necessary to take inspiration from more developed Li-S batteries as Al-S batteries may also follow the similar kind of working mechanism. Moreover, it is also important to investigate the reason behind the superior anchoring effect of Cu-metal based materials compared to the other experimentally studied carbonaceous host materials in Al-S batteries.

Therefore, in this study, we have investigated a two-dimensional (2D) copper-based MOF (Cu-BHT) monolayer to be used as the potential cathode support in Al-S batteries *[53]*, which has been recently synthesized having benzenehexathial (BHT) ligands, where Cu ions are connected in an extremely dense fashion. To investigate how a MOF could act as a better cathode host than the experimentally reported carbon based cathode hosts, we have carried out a comparative study of Cu-BHT monolayer with respect to graphene, a representative of carbonaceous hosts. We have analysed the corresponding cathode systems on the basis of detailed binding characteristics of sulfur and Al polysulfides, electronic properties, electrolyte interactions as well as Al polysulfide deposition behaviour. Our results show that Cu-BHT could be one of the promising cathode hosts that can be used in Al-S batteries.

6.2. Computational Details

The density functional theory (DFT) as implemented in the Vienna Ab initio Simulation Package (VASP) is used to perform the calculations *[54-57]*. The exchange-correlation potential is described by using the generalized gradient approximation of Perdew-Burke-Ernzerhof (GGA-PBE) *[58-59]*. The interactions between ion cores and valence electrons are treated by employing projector augmented-wave (PAW) method *[60-61]*. The plane wave cut-off energy is fixed to 470 eV and the total energy is converged to 10^{-5} eV. To optimize the structures, atomic positions are fully relaxed until the Hellmann-Feynman forces on all atoms are smaller than 0.01 eV/Å. Moreover, all the structure optimizations are carried out using the van der Waals corrected density functional theory (DFT-D3) to overcome the deficiencies of DFT in treating dispersion interactions *[62]*. A 2 × 2 × 1 supercell of Cu-BHT monolayer and 7 × 7 × 1 supercell of graphene having the lattice parameters a = b = 17.51 Å and a = b = 17.27 Å, respectively are used for the calculations and the Brillouin zone is represented by Monkhorst-k-point grid of 5 × 5 × 1 for both systems. To avoid the periodic image interaction between the two nearest neighbour unit cells, the vacuum is set to 20 Å in the z-direction. For the electronic structure calculations, the Brillouin zone is sampled with a k-point grid of 15 × 15 × 1.

6.3. Results and Discussion

6.3.1. Adsorption Characteristics of Sulfur (S_8) and Al Polysulfides (Al_2S_x) on Cu-BHT Monolayer and Graphene

It has been observed that in Al-S batteries, the charging and discharging processes proceed through the formation of Al polysulfide intermediates as given by equations 6.4 and 6.5,

$$\left(\frac{1}{8}\right)S_8 + \left(\frac{1}{3}\right)e^- \rightarrow \left(\frac{1}{6}\right)S_6^{2-} \tag{6.4}$$

$$\left(\frac{1}{6}\right)S_6^{2-} + \left(\frac{2}{x} - \frac{1}{3}\right)e^- \leftrightarrow \left(\frac{1}{x}\right)S_x^{2-} \quad (1 \leq x < 6) \tag{6.5}$$

These Al polysulfides molecules can be represented with the formula unit of Al_2S_x. Therefore, to study the adsorption behavior of these Al polysulfides on Cu-BHT monolayer and graphene, we have to first find out the stable structures of the set of S-containing species, $Al_2(S_6)_3$ or Al_2S_{18}, $Al_2(S_4)_3$ or Al_2S_{12}, $Al_2(S_2)_3$ or Al_2S_6, $Al_2(S)_3$ or Al_2S_3 along with

S_8. Out of all the possible structures studied, the most stable structures are presented in Figure 6.1.

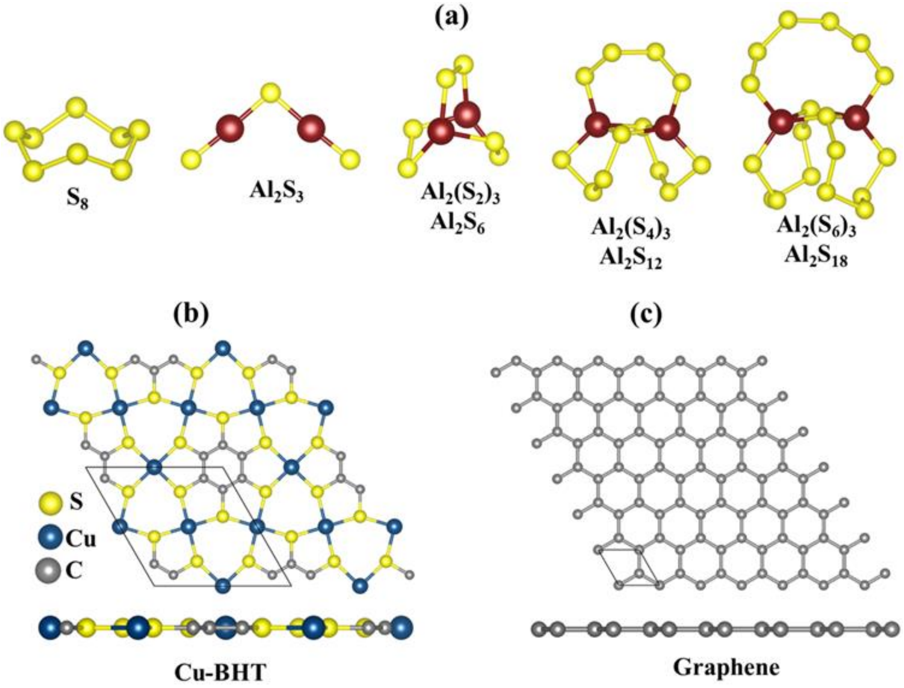

Figure 6.1: (a) Most stable molecular structures of S_8 and Al_2S_x (x = 3, 6, 12 and 18). Top and side views of fully optimized structure of (b) Cu-BHT and (c) graphene monolayer surfaces.

The S_8 molecule stabilizes in its most stable allotrope form at room temperature, which is a 3D crown like orthorhombic α-S_8 structure, whereas Al_2S_3 prefers planar bent structure compared to linear structure with S atom taking the centre position with side S-Al-S and centre Al-S-Al bond angle of 179.9^o and 100^o respectively, which is in close accordance with a previous study (179.2^o and 101.7^o, respectively) *[63, 64]*. For higher order Al_2S_x with more S atoms, the 3D cluster shapes are stable compared to the 2D chains with Al or S atoms at the terminal, which can effectively avoid the dangling bonds observed in Al_2S_3 and contribute to the structure stability. Similar results have also been observed for higher order Li polysulfides in Li-S batteries *[65]*. On a closer observation, we find that all the S atoms in these Al_2S_x molecules are not equivalent in their binding nature, having S-S and Al-S bond lengths range of 2.02-2.14 Å and 2.18-2.38 Å, respectively. Also, as the size of Al_2S_x molecule increases, the average Al-S bond length increases from Al_2S_3 (2.09 Å) to Al_2S_{18} (2.27 Å), which could lead to easy dissociation of Al-S bond in higher order Al_2S_x molecules compared to lower order Al polysulfides. This could be one of reasons for the higher irreversibility observed in the charging process in Al-S batteries, which involves conversion of lower order to higher order Al_2S_x *[45-46]*.

The Cu-BHT monolayer possesses a hexagonal planar structure, where the Cu atoms and BHT are connected together by Cu-S covalent bonds (2.28 Å) as shown in Figure 6.1a. Our optimized lattice constant 8.76 Å is in good agreement with the previous reported values (8.76 Å and 8.80 Å) *[53, 66]*. The monolayer of Cu-BHT MOF has intrinsic metallic nature mainly contributed from the electronic states of C 2p, S 3p, and Cu 3d orbitals at the Fermi level and is dynamically stable *[67]*. This metallic characteristic of Cu-BHT could be quite beneficial in improving the rate performance of Al-S battery. The graphene monolayer optimized for the comparative study is also shown in Figure 1c with the lattice parameters (a = b = 2.46 Å) in good accordance with the experimental data for graphite.

To investigate the reason behind the poor performance of carbonaceous based cathode host for Al-S batteries, we have systematically compared the binding behavior of S_8 and the corresponding Al_2S_x molecules on graphene surface as well as on Cu-BHT monolayer. Various initial structures of S_8 and Al_2S_x molecules are investigated at possible binding sites on both Cu-BHT and graphene monolayer and the corresponding binding energies are calculated using the following equation,

$$E_{Binding} = \left(E_{System} - E_{Host} - E_M\right) \tag{6.6}$$

where, E_{System}, and E_{Host} are the total energies of Cu-BHT or graphene monolayer with and without adsorbed molecules, respectively. E_M is the total energy of an isolated S_8 or Al_2S_x molecule. Here, the more negative binding energy means a more favorable binding of molecule. The plot of the corresponding binding energies for both Cu-BHT and graphene monolayer are presented in Figure 6.2 along with the most stable binding configurations on Cu-BHT and graphene monolayer are presented in "with vdW" (with van der Waals functional involved) of Figure 6.3c and d.

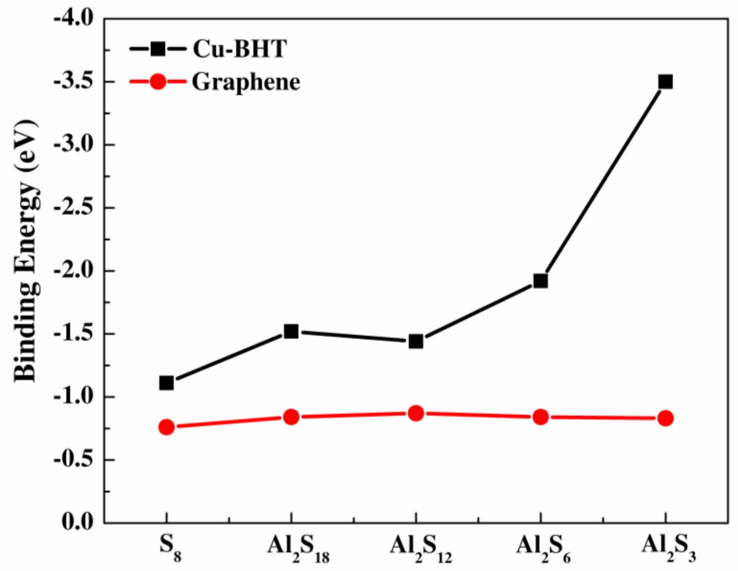

Figure 6.2: (a) Binding energies for S_8 and Al_2S_x (x = 3, 6, 12, and 18) on Cu-BHT and graphene monolayers.

We observe that the graphene has constantly quite low binding affinity towards S_8 (-0.76 eV) and Al_2S_x molecules (-0.83 to -0.87). Whereas, for Cu-BHT monolayer, the binding strength has remarkably increased and opposite to the graphene, in Cu-BHT monolayer, the binding energy is not constant but increases from S_8 (-1.11 eV) molecule to Al_2S_x molecules with maximum being for Al_2S_3 (-3.56 eV). Our results reveal that the binding energy of Al_2S_x molecules varies in the range of -1.44 to -3.56 eV and this stronger binding strength for lower order Al polysulfides could be because of the closer binding approach of the optimized structures forming $Al\text{-}S_{Cu\text{-}BHT}$ (S of Cu-BHT) and $Cu\text{-}S_M$ (S of Al_2S_x molecule) bonds as shown in “with vdW” side in Figure 6.3c. This overall increase in the binding strength on Cu-BHT monolayer compared to graphene indicates towards its improved anchoring effect as a cathode host in Al-S battery.

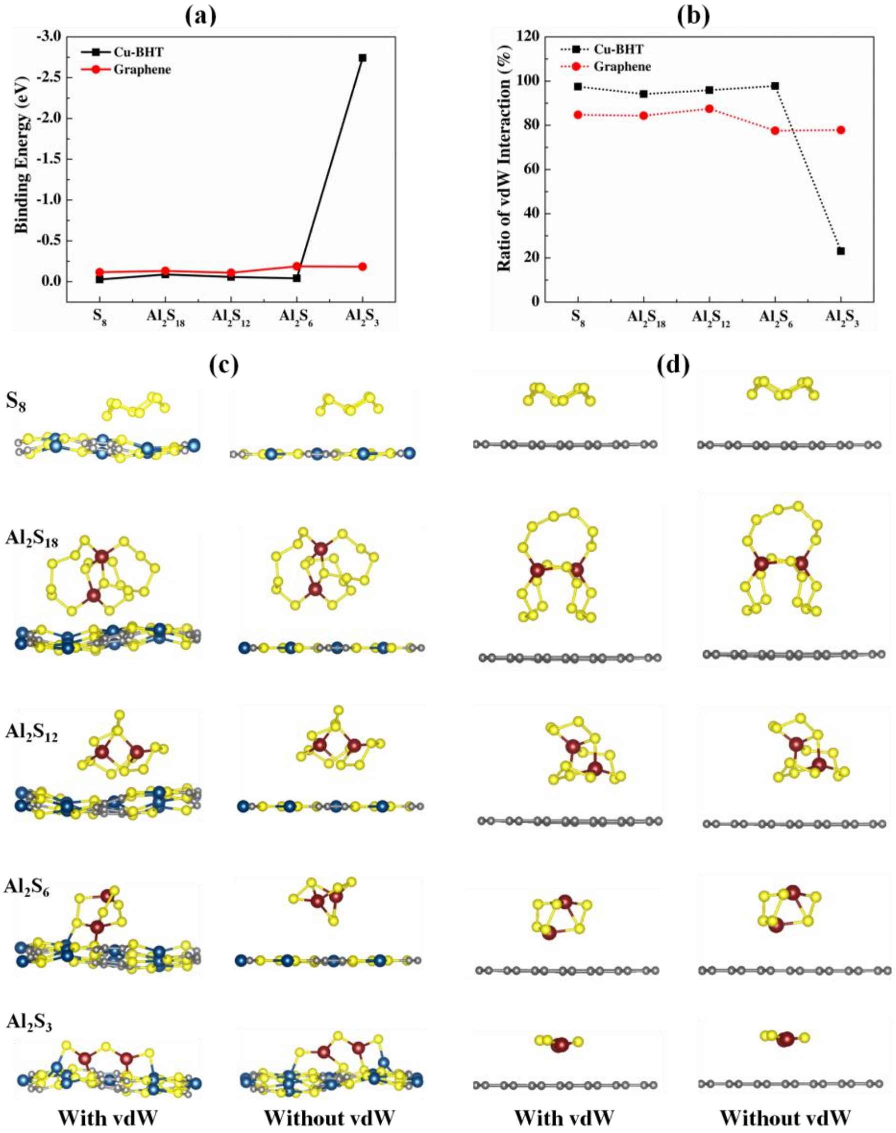

Figure 6.3: (a) Binding energies for S_8 and Al_2S_x (x = 3, 6, 12, and 18) on Cu-BHT and graphene monolayers without vdW functional, and (b) the corresponding ratio (r%) for vdW interaction for Cu-BHT and graphene monolayers. Optimized configurations S_8 and Al_2S_x (x = 3, 6, 12, and 18) molecules on (c) Cu-BHT monolayer, and (d) graphene monolayer, simulated with and without vdW functional.

Further, to get more valuable insights into the anchoring effects of Cu-BHT and graphene, we have evaluated the contribution of the physisorption (given by vdW interactions) and chemisorption to the net binding strengths of S_8 and Al_2S_x molecules. The percentage ratio of the vdW interaction in can be calculated using, $r = \left(\frac{E_b^{vdW} - E_b^{without-vdW}}{E_b^{vdW}}\right)$, where E_b^{vdW} and $E_b^{without-vdW}$ are the binding energies with and without van der Waals corrections. Figure 6.3b shows the variation in the van der Waals contributions for binding of S_8 and other Al_2S_x molecules on graphene and Cu-BHT monolayers. For graphene, the physisorption dominates for the whole process of binding, maximum being for S_8 and higher order Al_2S_{18} molecule, Al_2S_{12} (85-87 %) and reduces to 78 % for lower order Al_2S_6 and Al_2S_3 systems. From here, we can conclude that the physisorption are mainly contributed from the S content and promote the binding of S_8, Al_2S_{18}, and Al_2S_{12}, however for lower order Al_2S_6 and Al_2S_3 the chemisorption also start contributing. For the case of graphene, the contributions from vdW functional do not change the nature of interactions of S_8 and Al_2S_x (Figure 6.3d), other than decreasing the binding distance values from 3.31-4.34 Å to 3.17-3.83 Å. However, the overall binding energies remain quite constant for graphene host through-out the charge/discharge process. On the other hand, for Cu-BHT monolayer, the physisorption play a major role for S_8 and higher order Al polysulfides with the range of 94-97 %, but for Al_2S_3, the chemisorption dominate having vdW ratio of 23 %. The role of vdW interaction in the binding of S_8 and Al_2S_x molecules can further be understood by evaluating the binding structures with and with-vdW interaction as presented in Figure 6.3c. The influence of vdW functional is observed in three ways, (1) induced buckling of the Cu-BHT monolayer compared to planar layer in without-vdW functional, which offers a suitable binding space to enhance the physisorption with S_8 and other Al_2S_x molecules, and (2) decrease in the binding distance between these molecules and Cu-BHT monolayer. These two factors can be clearly seen for the binding of S_8, Al_2S_{18}, Al_2S_{12}, and Al_2S_6. However, factor (3) which involves changes in the binding conformation is primarily observed in case of Al_2S_6 by inclusion of vdW functional to form Al-$S_{\text{Cu-BHT}}$ and Cu-S_M bonds and leading to a overall increased binding energy (-1.92 eV). For Al_2S_3, the binding structures are almost the same after adding vdW functional indicating towards more dominating chemisoption, which is in accordance with the vdW ratio plot in Figure 6.3b.

To get more insights into the interaction mechanism between Cu-BHT and Al polysulfides, we have analysed the charge density difference (ρ_{CDD}), as expressed by the following equation,

$$\rho_{CDD} = \rho^{total} - \sum_i \rho_i^{fragments} \tag{6.7}$$

where, the ρ^{total} is the total charge density of the system and $\rho_i^{fragments}$ is the charge density of the individual fragments by which the system is made of. Here, the charge density of the fragments ($\rho_i^{fragments}$) is calculated by a pseudo structure in which fragment part retains the same structure as in the total system but other parts are deleted. The charge density difference plot presented in Figure 6.4a clearly shows charge distribution between Al_2S_x molecules and Cu-BHT monolayer, where the pink and green colours represent charge accumulation and depletion, respectively. The extent of charge transfer follows a general trend of increment from Al_2S_{18} to Al_2S_3 but is lowest for Al_2S_{12} system, which is in accordance with the binding energy values (Figure 6.2). The large charge exchange between Al_2S_3 and Cu-BHT monolayer indicates towards the involvement of strong chemical interactions, which decrease as extent of S increases to form higher Al polysulfides. Overall, two opposite charge transfer channels, (1) $S_{\text{Cu-BHT}}$-Al and (2) S_M-Cu, are contributing to the chemical interactions and the dominance of one of these two charge transfer channels determines the net direction of charge transfer. The quantitative charge transfer values calculated using the Bader charge analysis *[68-71]* (Table 6.1), further support the results of charge density difference analysis, where Al_2S_{12} system involves 0.05 electronic charge transfer from Cu-BHT monolayer to Al_2S_{12} molecule. The Bader charge transfer values increases from Al_2S_{18} (0.05 |e|) to Al_2S_6 (0.24 |e|), to finally Al_2S_3 (0.73 |e|), which is in accordance with the binding energy trend and such increased charge transfer is the reason for the improved chemical binding strength. The overall improvement in the binding of Cu-BHT monolayer with Al_2S_x molecules can be associated with the probability of Cu ions having Lewis acid nature (due to empty 3d orbitals) to interact with soft Lewis base S_M atoms of Al_2S_x (having electron lone pairs) along with the Lewis base $S_{Cu\text{-}BHT}$ to strongly interact with Al cations of Al_2S_x molecules.

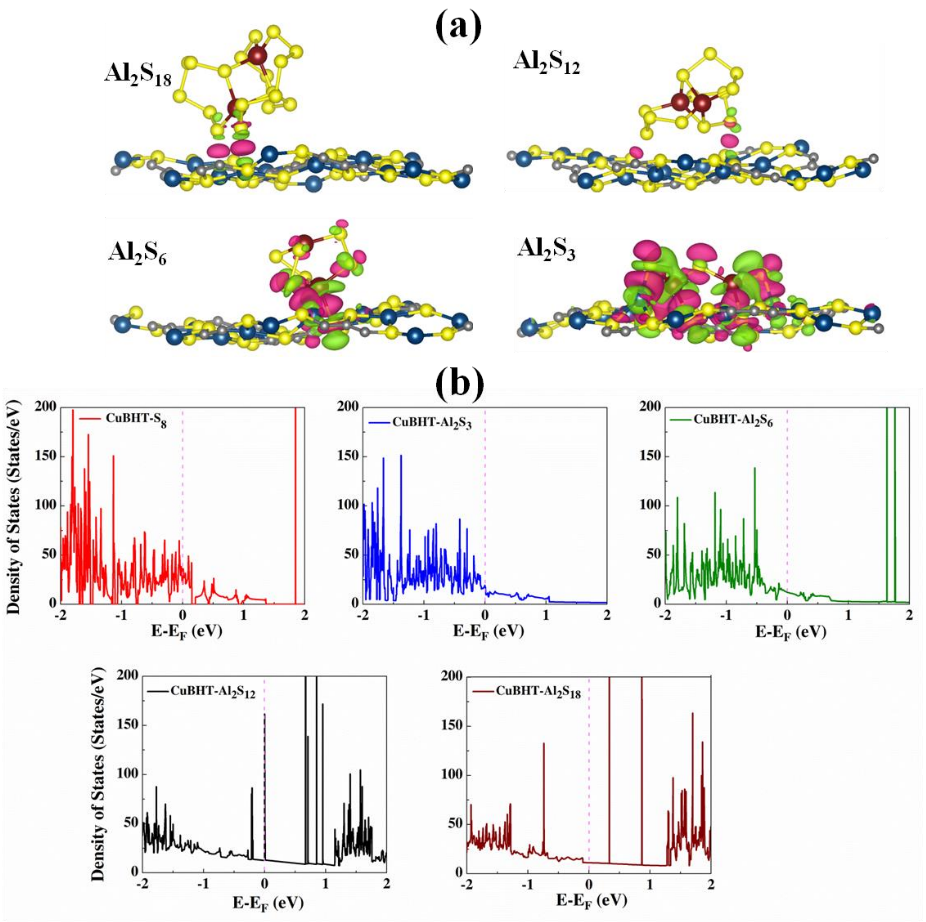

Figure 6.4: (a) Charge density difference (ρ_{CDD}) plots for Al_2S_x molecules adsorbed on Cu-BHT monolayer surface (isosurface value = 0.0015 e/Å^3). Here, the pink and green colors represent charge accumulation and depletion, respectively. (b) Total density of states for S_8 and Al_2S_x molecules adsorbed on Cu-BHT monolayer surface. The Fermi level is set to zero.

Table 6.1: Charge transfer between Al_2S_x molecules and Cu-BHT monolayer. Here, the negative value indicates towards the charge transfer from Cu-BHT to Al_2S_x molecules.

System	**Al_2S_{18}**	**Al_2S_{12}**	**Al_2S_6**	**Al_2S_3**
Charge Transfer (|e|)	0.05	-0.05	0.24	0.73

Further, to evaluate the suitability of Cu-BHT monolayer as cathode host in Al-S batteries, it is important to check whether it is able to overcome the insulating nature of S cathode and the corresponding Al polysulfides formed during charging and discharging processes to provide constant conductivity in the system. The Cu-BHT is superconducting in nature with T_c ~ 3 K *[72]*. Figure 6.4b, shows that all S_8 and Al_2S_x containing Cu-BHT monolayer systems have abundant density of states at the Fermi level, leading to the metallic character in these systems. This metallic nature is suitable to provide electron conduction in whole system making a path for electrons to participate into the redox reactions of adsorbed S_8 and Al polysulfides during charge/discharge reactions. The Cu-BHT works in a similar manner like experimentally studied S@HKUST-1-C system *[48]*, where, a significant decrease in the kinetic barrier for the conversion of sulfur species during battery operation is observed due to presence of Cu atoms.

6.3.2. Interaction with Electrolyte

One of the primary concerns of sulfur based batteries is the low confinement of elemental sulfur and polysulfides in the cathode host compared to their increased attraction towards the involved electrolyte, which leads to shuttle reactions to give poor cycle life, high self-discharge rate and low Columbic efficiency in sulfur batteries. In Al-S batteries, the carbonaceous cathode host (S@C) is also observed to show pronounced shuttling effects of Al polysulfides from cathode to anode and showing fast capacity decay, indicating poorer S utilization, and low reversibility *[48]*. In a similar way, we observe that graphene monolayer shows slightly stronger binding of S_8 (-0.76 eV), Al_2S_{18} (-0.84 eV), and Al_2S_{12} (-0.87 eV) molecules compared to 1-ethyl-3-methylimidazolium tetrachloroaluminate ($EMIM^+AlCl_4^-$) ionic liquid electrolyte (-0.30 to -0.53 eV) as can been seen from Figure 6.5 along with the most stable binding configurations. However, the interaction of electrolyte for Al_2S_6 (-1.62 eV) dominated by

Cl atom of EMIM$^+$AlCl$_4^-$ electrolyte and Al of Al_2S_6 exceeds that of the graphene (-0.84 eV). Moreover, we also observe that the electrolyte itself shows stronger binding on the graphene surface with the binding energy of -0.95 eV, much higher than those of S_8 and Al_2S_x molecules on graphene. Based on these results we can conclude that the carbonaceous materials do not make suitable anchoring host for Al-S batteries, as they not only able to bind elemental sulfur and Al-polysulfides strongly, but the involved ionic liquid electrolyte also competes to bind over carbonaceous host. And, all of these reasons lead to shutting effect of intermediate polysulfides, observed in experimental applications of carbon based cathode hosts *[48]*.

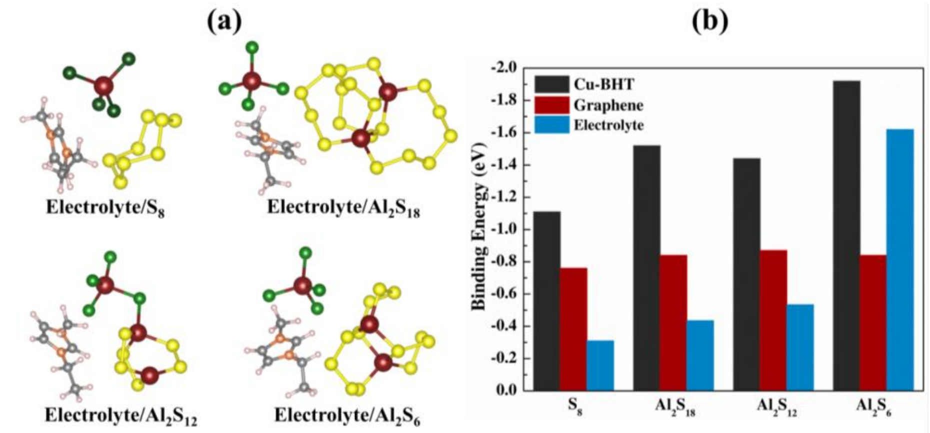

Figure 6.5: (a) Optimized binding configurations S_8 and Al_2S_x (x = 6, 12, and 18) molecules with EMIM$^+$AlCl$_4^-$ ionic liquid electrolyte, and (b) comparative binding energies of S_8 and Al_2S_x (x = 6, 12, and 18) molecules with graphene, Cu-BHT monolayer and EMIM$^+$AlCl$_4^-$ electrolyte.

Whereas, for Cu-BHT monolayer systems, it is highly unlikely for S_8 and Al_2S_x molecules to dissolve into electrolyte, because of the comparatively poor binding compared to Cu-BHT host ranging from -1.11 eV to -1.92 eV. In addition, the EMIM$^+$AlCl$_4^-$ electrolyte also observed to have lower interaction (-0.98 eV) with the Cu-BHT monolayer host in comparison with the Al polysulfides. The stronger binding is a resultant of soft acid-base interactions between S atoms (Lewis base) of Al polysulfides and Cu(I) atoms (Lewis acid) of Cu-BHT monolayer compared to Cl atoms of $EMIM^+AlCl_4^-$ electrolyte (Figure 6.2). Therefore, we can expect that the Cu-BHT monolayer material can act as the potential anchoring host with reduced polysulfide shuttling compared to carbonaceous host to provide improved cycle life in Al-S batteries. In a similar way, vital effect of Cu has also been observed in a recent experimental report of HKUST-1-C/S cathode for Al-S battery *[48]*. Where, in the electrochemical process, Cu forms an ionic cluster with polysulfide and facilitates the electrochemical reaction and shows improved the reversibility of S during charging/ discharging process.

6.3.3. Deposition of Al_2S_3 on Cu-BHT Monolayer Surface

Several experimental and theoretical reports on Li-S batteries have realized that a cathode host material able to regulate uniform deposition of the discharge product Li_2S is useful to reduce the cell resistance as well as manifests a rapid kinetics in redox reaction of Li polysulfides *[67, 73-74]*. Therefore, to check the suitability of Cu-BHT as anchoring material in Al-S batteries, we investigated the deposition behavior of Al_2S_3 molecules on Cu-BHT monolayer surface. We have compared the binding energies of various possible initial configurations of two and then three Al_2S_3 molecules adsorbed on surface of Cu-BHT monolayer. Figure 6.6 shows the most stable configurations of the isolated Al_2S_3 molecules and in agglomeration network for both two and three Al_2S_3 molecules depositions. The relative energies of these configurations show that Al_2S_3 molecules are more inclined to form the agglomerated network and the network size further increases as more Al_2S_3 molecules are deposited on Cu-BHT surface (Figure 6.6c). This uniform deposition of Al_2S_3 on Cu-BHT monolayer is a result of synergistic dual interactions through Al-$S_{Cu\text{-}BHT}$ and Cu-S_M, which enhances the affinity Cu-BHT to have an electrical contact with Al_2S_x. And, as result Cu-BHT can reduce the kinetic barrier of Al polysulfide redox reactions. Moreover, this uniform deposition of Al_2S_3 increases the surface utilization of Cu-BHT monolayer as shown in Figure 6.6c.

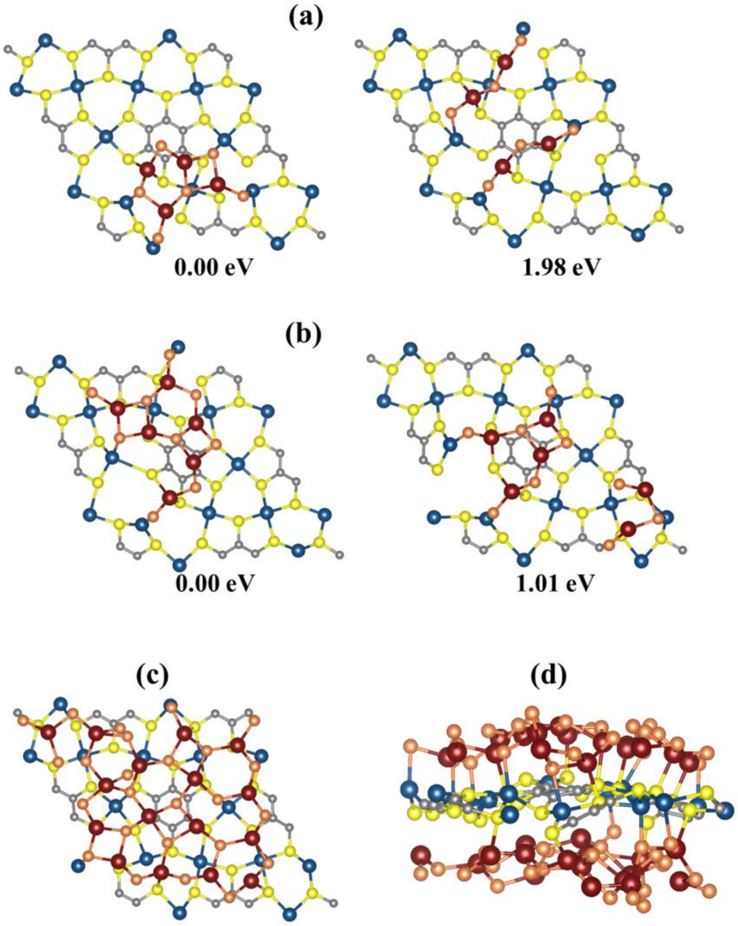

Figure 6.6: Optimized configurations of (a) two Al_2S_3 and (b) three Al_2S_3 molecules on Cu-BHT mnolayer with their relative energies, situated near and far from each other. (c) Uniform Al_2S_3 layer deposition on Cu-BHT monolayer surface. (d) Side view of the optimized configuration with maximum stable loading of Al_2S_3 molecules on Cu-BHT monolayer surface. Here, for the clear understanding, the sulfur atoms of Al_2S_3 molecules and Cu-BHT monolayer surface are shown in orange and yellow colors, respectively.

Further to check the capacity retention in Al-S battery, we have calculated the amount of sulfur which can be incorporated in Cu-BHT monolayer host. The Al_2S_3 molecules are allowed to bind on both sides of 2 × 2 × 1 Cu-BHT monolayer to get the energetically stable system. We observe that Al_2S_3 molecules bind in a layered framework on both sides of Cu-BHT monolayer (Figure 6.6c and d) with average binding energies of -5.36 eV and -5.18 eV for one side and both sides of Cu-BHT, respectively. On allowing the binding of third layer of Al_2S_3 molecules, the system becomes energetically unstable, favouring the binding of 16 Al_2S_3 molecules in 2 × 2 × 1 Cu-BHT monolayer host. Therefore, the maximum amount of sulfur which can be incorporated in Cu-BHT monolayer is 45.81 weight percentage (wt%) of sulfur. The capacity of Cu-BHT monolayer is quite higher than the experimentally studied S@HKUST-1-C host which holds 34 wt% of sulfur *[48]*.

In both HKUST and Cu-BHT MOFs, the structure along with the presence of Cu plays quite important role in Al-S battery by enhancing the stability of sulfur and Al_2S_x molecules, and improving reaction reversibility and electronic conductivity. However, the Cu-BHT MOF emerges as a more suitable cathode host for Al-S batteries furishing higher sulfur capacity.

6.4. Conclusion

In this work, we have investigated the preferential applicability of 2D Cu-benzenehexathial (Cu-BHT) metal organic framework to be used a potential anchoring cathode host for Al-S batteries as compared to carbonaceous host such as graphene. We observe that the favourable electrical conductivity of Cu-BHT eliminates the insulating nature of S_8 and other Al polysulfide (Al_2S_x) molecules and could be helpful in supporting the cathode charge/discharge processes. From the binding calculations of S_8 and Al_2S_x molecules, we observe that graphene shows constantly low binding energies, where the physisorption dominates throughout the whole process of binding (78-87 %). Whereas, the Cu-BHT monolayer furnishes improved binding of Al polysulfides (-1.44 to -3.56 eV), because of the presence of copper and sulfur, which results into increased charge transfer to Al polysulfides. Moreover, from the comparative study of S_8 and Al_2S_x molecules binding with graphene, Cu-BHT and $EMIM^+AlCl_4^-$ electrolyte, we conclude that with the relatively stronger binding of S_8 and Al_2S_x molecules, Al-S battery with Cu-BHT monolayer host cathode can reduce the overall dissolution of Al polysulfide into electrolyte compared to carbonaceous host to provide improved cycle life. The Cu-BHT MOF permits synergic dual interaction based on the Al-S (of sulfur host) bond and S (of Al polysulfide)-Cu bond leading to uniform deposition of insoluble Al_2S_3 over the Cu-BHT surface. This improves the utilization of the active cathode host, allowing better sulfur incorporation of 45.81 wt% of sulfur in Cu-BHT host, which is even higher compared to HKUST MOF (34 wt%) studied in a most recent experimental report. Overall, all of these results suggest that that Cu-BHT monolayer can be used as a promising anchoring cathode host compared to graphene in Al-S batteries.

6.5. References

1. Elia G. A., Marquardt K., Hoeppner K., Fantini S., Lin R., Knipping E., Peters W., Drillet J.-F., Passerini S., Hahn R. (2016), An overview and future perspectives of aluminum batteries, Adv. Mater., 28, 7564–7579 (DOI: 10.1002/adma.201601357)
2. 24. Wang Y., Chen R., Chen T., Lv H., Zhu G., Ma L., Wang C., Jin Z., Liu J. (2016), Emerging non-lithium ion batteries, Energy Storage Mater., 4, 103–129 (DOI: 10.1016/j.ensm.2016.04.001)
3. Sadat W. I. A., Archer L. A. (2016), The O_2-assisted Al/CO_2 electrochemical cell: A system for CO_2capture/conversion and electric power generation, Sci. Adv., 2, e1600968 (DOI: 10.1126/sciadv.1600968)

4. Bai L. (1990), Complex behavior of Al dissolution in non-aqueous medium as tevealed by impedance spectroscopy, J. Electrochem. Soc., 137, 3737 (DOI: 10.1149/1.2086295)
5. Suneesh P. V., Satheesh Babu T. G., Ramachandran T. (2013), Electrodeposition of aluminium and aluminium-copper alloys from a room temperature ionic liquid electrolyte containing aluminium chloride and triethylamine hydrochloride, Inter. J. Min. Met. Mater., 20, 909–916 (DOI: 10.1007/s12613-013-0814-4)
6. Wang W., Jiang B., Xiong W., Sun H., Lin Z., Hu L., Tu J., Hou J., Zhu H., Jiao S. (2013), A new cathode material for super-valent battery based on aluminium ion intercalation and deintercalation, Sci. Rep., 3, 3383 (DOI: 10.1038/srep03383)
7. Chiku M., Takeda H., Matsumura S., Higuchi E., Inoue H. (2015), Amorphous vanadium oxide/carbon composite positive electrode for rechargeable aluminum battery, ACS Appl. Mater. Interfaces, 7, 24385–24389 (DOI: 10.1021/acsami.5b06420)
8. Wang H., Bai Y., Chen S., Luo X., Wu C., Wu F., Lu J., Amine K. (2015), Binder-free V_2O_5 cathode for greener rechargeable aluminum battery, ACS Appl. Mater. Interfaces, 7, 80–84 (DOI: 10.1021/am508001h)
9. Wang H., Bi X., Bai Y., Wu C., Gu S., Chen S., Wu F., Amine K., Lu J. (2017), Open-Structured $V_2O_5 \cdot nH_2O$ Nanoflakes as highly reversible cathode material for monovalent and multivalent intercalation batteries, Adv. Energy Mater., 7, 1602720 (DOI: 10.1002/aenm.201602720)
10. Jiang J., Li H., Huang J., Li K., Zeng J., Yang Y., Li J., Wang Y., Wang J., Zhao J. (2017), Investigation of the reversible intercalation/deintercalation of Al into the novel Li_3VO_4@C microsphere composite cathode material for aAluminum-ion batteries, ACS Appl. Mater. Interfaces, 9, 28486–28494 (DOI: 10.1021/acsami.7b07503)

11. Kaveevivitchai W., Huq A., Wang S., Park M. J., Manthiram A. (2017), Rechargeable aluminum-Ion batteries based on an open-tunnel framework, Small, 13, 1701296 (DOI: 10.1002/smll.201701296)
12. Mei L., Xu J., Wei Z., Liu H., Li Y., Ma J., Dou S. (2017), Chevrel Phase Mo_6T_8 (T = S, Se) as electrodes for advanced energy storage, Small, 13, 1701441 (DOI: 10.1002/smll.201701441)
13. Li Z., Niu B., Liu J., Li J., Kang F. (2018), Rechargeable aluminum-ion battery based on MoS_2 microsphere cathode, ACS Appl. Mater. Interfaces, 10, 9451–9459 (DOI:10.1021/acsami.8b00100)
14. Geng L., Scheifers J. P., Fu C., Zhang J., Fokwa B. P. T., Guo J. (2017), Titanium sulfides as intercalation-type cathode materials for rechargeable aluminum batteries, ACS Appl. Mater. Interfaces, 9, 21251–21257 (DOI: 10.1021/acsami.7b04161)
15. Vahid M. A., Hadjikhani A., Shahbazmohamadi S., Beidaghi M. (2017), Two-dimensional vanadium carbide (MXene) as a high-capacity cathode material for rechargeable aluminum batteries, ACS Nano, 11, 11135–11144 (DOI: 10.1021/acsnano.7b05350)
16. Liu S., Hu J. J., Yan N. F., Pan G. L., Li G. R., Gao X. P. (2012), Aluminum storage behavior of anatase TiO2 nanotube arrays in aqueous solution for aluminum ion batteries, Energy Environ. Sci., 5, 9743-9746 (DOI: 10.1039/c2ee22987k)
17. Lin M. C., Gong M., Lu B., Wu Y., Wang D. Y., Guan M., Angell M., Chen C., Yang J., Hwang B. J., Dai H. (2015), An ultrafast rechargeable aluminium-ion battery, Nature, 520, 324-328 (DOI: 10.1038/nature14340)
18. Kravchyk K. V., Wang S., Piveteau L., Kovalenko M. V. (2017), Efficient aluminum chloride–aatural graphite battery, Chem. Mater., 29, 4484–4492 (DOI: 10.1021/acs.chemmater.7b01060)
19. Bhauriyal P., Mahata A., Pathak B. (2017), The staging mechanism of $AlCl_4$ intercalation in graphite Eelectrode for aluminium-ion battery,

Phys. Chem. Chem. Phys., 19, 7980–7989 (DOI: 10.1039/c7cp00453b)

20. Wang S., Kravchyk K. V., Krumeich F., Kovalenko M. V. (2017), Kish Ggraphite flakes as a cathode material for an aluminum chloride–graphite battery, ACS Appl. Mater. Interfaces, 9, 28478–28485 (DOI: 10.1021/acsami.7b07499)
21. Stadie N. P., Wang S., Kravchyk K. V., Kovalenko M. V. (2017), Zeolite-templated carbon as an ordered microporous electrode for aluminum batteries, ACS Nano, 11, 1911–1919 (DOI: 10.1021/acsnano.6b07995)
22. Childress A. S., Parajuli P., Zhu J., Podila R., Rao A. M. (2017), A Raman Spectroscopic Study of Graphene Cathodes in High-Performance Aluminum Ion Batteries, Nano Energy, 39, 69–76 (DOI: 10.1016/j.nanoen.2017.06.038)
23. Chen H., Xu H., Wang S., Huang T., Xi J., Cai S., Guo F., Xu Z., Gao W., Gao C. (2017), Ultrafast all-climate aluminum-graphene battery with quarter-million cycle life, Sci. Adv., 3, eaao7233 (DOI: 10.1126/sciadv.aao7233)
24. Chen H., Guo F., Liu Y., Huang T., Zheng B., Ananth, N., Xu Z., Gao W., Gao C. (2017), A defect-free principle for advanced graphene cathode of aluminum-ion battery, Adv. Mater., 29, 1605958 (DOI: 10.1002/adma.201605958)
25. Wu Y., Gong M., Lin M.-C., Yuan C., Angell M., Huang L., Wang D.-Y., Zhang X., Yang J., Hwang B.-J., et al. (2016), 3D graphitic foams derived from chloroaluminate anion iIntercalation for ultrafast aluminum-ion battery, Adv. Mater., 28, 9218–9222 (DOI:10.1002/adma.201602958)
26. Bhauriyal P., Mahata A., Pathak B. (2017), Hexagonal BC_3 electrode for a high-voltage Al-ion battery, J. Phys. Chem. C, 121, 9748–9756 (DOI:10.1021/acs.jpcc.7b02290)

27. Bhauriyal P., Mahata A., Pathak B. (2017), A computational study of a single-walled carbon-nanotube-based ultrafast high-capacity aluminum battery, Chem. Asian J., 12, 1944–1951 (DOI: 10.1002/asia.201700570)
28. Bhauriyal P., Garg P., Patel M., Pathak B. (2018), Electron-rich graphite-like electrode: stability vs. voltage for Al batteries, J. Mater. Chem. A, 6, 10776-10786 (DOI: 10.1039/c8ta01820k)
29. Bhauriyal P., Bhattacharyya G., Rawat K. S., Pathak B. (2019), Graphene/hBN heterostructures as high-Capacity cathodes with high voltage for next-generation aluminum batteries, J. Phys. Chem. C, 123, 3959–3967 (DOI: 10.1021/acs.jpcc.8b10550)
30. Hudak, N. S. (2014), Chloroaluminate-doped conducting polymers as positive electrodes in rechargeable aluminum batteries, J. Phys. Chem. C, 118, 5203–5215 (DOI: 10.1021/jp500593d)
31. Zafar Z. A., Imtiaz S., Razaq R., Ji S., Huang T., Zhang Z., Huang Y., Anderson J. A. (2017), Cathode materials for rechargeable aluminum batteries: current status and progress, J. Mater. Chem. A, 5, 5646–5660 (DOI: 10.1039/C7TA00282C)
32. Mori T., Orikasa Y., Nakanishi K., Kezheng C., Hattori M., Ohta T., Uchimoto Y. (2016), Discharge/charge reaction mechanisms of FeS2 cathode material for aluminum rechargeable batteries at 55°C, J. Power Sources, 313, 9–14 (DOI: 10.1016/j.jpowsour.2016.02.062)
33. Wang S., Yu Z., Tu J., Wang J., Tian D., Liu Y., Jiao S. (2016), A novel aluminum-ion battery: Al/AlCl-[EMIm]Cl/NiS@graphene, Adv. Energy Mater., 6, 1600137 (DOI: 10.1002/aenm.201600137)
34. Yu Z., Kang Z., Hu Z., Lu J., Zhou Z., Jiao S. (2016), Hexagonal NiS nanobelts as advanced cathode materials for rechargeable Al-ion batteries, Chem. Commun., 52, 10427–10430 (DOI: 10.1039/C6CC05974K)
35. Wang S., Jiao S., Wang J., Chen H.-S., Tian D., Lei H., Fang D.-N. (2017), High-performance aluminum-ion battery with CuS@C

microsphere composite cathode, ACS Nano, 11, 469–477 (DOI: 10.1021/acsnano.6b06446)

36. Manthiram A., Fu Y., Chung S.-H., Zu C., Su Y.-S., (2014), Rechargeable lithium–sulfur batteries, Chem. Rev., 114, 23, 11751-11787 (DOI: 10.1021/cr500062v)
37. Manthiram A., Fu Y., Su Y.-S., (2013), Challenges and prospects of lithium–sulfur batteries, Acc. Chem. Res., 46, 5, 1125-1134 (DOI: 10.1021/ar300179v)
38. Klein M. J., Veith G. M., Manthiram A., (2017), Chemistry of sputter-deposited lithium sulfide films, J. Am. Chem. Soc., 139, 31, 10669-10676 (DOI: 10.1021/jacs.7b03379)
39. Pang Q., Liang X., Kwok C. et al. (2016), Advances in lithium–sulfur batteries based on multifunctional cathodes and electrolytes, Nat Energy, 1, 16132 (DOI:10.1038/nenergy.2016.132)
40. Xin S., Yin Y.-X., Guo Y.-G., Wan L.-J., (2014), A high-energy room-temperature Sodium-Sulfur Battery, 26, 1261-1265 (DOI: 10.1002/adma.201304126)
41. Wenzel S., Metelmann H., Raiß C., Dürr A. K., Janek J., Adelhelm P., (2013), Thermodynamics and cell chemistry of room temperature sodium/sulfur cells with liquid and liquid/solid electrolyte, J. Power Sources, 243, 758-765 (DOI: 10.1016/j.jpowsour.2013.05.194)
42. Gao T., Noked M., Pearse A. J., Gillette E., Fan X., Zhu Y., Luo C., Suo L., Schroeder M. A., Xu K., et al. (2015), Enhancing the reversibility of Mg/S battery chemistry through Li+ mediation, J. Am. Chem. Soc., 137, 12388-12393 (DOI: 10.1021/jacs.5b07820)
43. Li W., Cheng S., Wang J., Qiu Y., Zheng Z., Lin H., Nanda S., Ma Q., Xu Y., Ye F., Liu M., Zhou L., Zhang Y. (2016), Synthesis, crystal structure, and electrochemical properties of a simple magnesium electrolyte for magnesium/sulfur batteries, Angew. Chem. Int. Ed., 55, 6406 (DOI: 10.1002/anie.201600256)

44. Cohn G., Ma L., Archer L. A., (2015), A novel non-aqueous aluminum sulfur battery J. Power Sources, 283, 416 – 422 (DOI: 10.1016/j.jpowsour.2015.02.131)
45. Gao T., Li X., Wang X., Hu J., Han F., Fan X., Suo L., Pearse A. J., Lee S. B., Rubloff G. W., Gaskell K. J., Noked M., Wang C. (2016), A rechargeable Al/S battery with an ionic-liquid electrolyte, Angew. Chem. Int. Ed., 55, 9898–9901; Angew. Chem., 128, 10052–10055 (DOI: 10.1002/anie.201603531)
46. Yu X., Manthiram A., (2017), Electrochemical energy storage with a reversible nonaqueous room-temperature aluminum–sulfur chemistry, Adv. Energy Mater., 7, 1700561 (DOI: 10.1002/aenm.201700561)
47. Yu X., Boyer M. J., Hwang G. S., Manthiram A., (2018), Room-temperature aluminum-sulfur batteries with a lithium-ion-mediated ionic liquid electrolyte, Chem, 4, 586–598 (DOI: https://doi.org/10.1016/j.chempr.2017.12.029)
48. Guo Y., Jin H., Qi Z., Hu Z., Ji H., Wan L.-J. (2019), Carbonized-MOF as a sulfur host for aluminum–sulfur batteries with enhanced capacity and cycling life, Adv. Funct. Mater., 29, 1807676 (DOI:10.1002/adfm.201807676)
49. Wang Z., Wang B., Yang Y., Cui Y., Wang Z., Chen B., Qian G. (2015), Mixed-metal–organic framework with effective Lewis acidic sites for sulfur confinement in high-performance lithium–sulfur batteries, ACS Appl. Mater. Interfaces, 7, 20999-21004 (DOI: 10.1021/acsami.5b07024)
50. Hao G.-P., Tang C., Zhang E., Zhai P.-Y., Yin J., Zhu W., Zhang Q., Kaskel S. (2017), Thermal exfoliation of layered metal–organic frameworks into ultrahydrophilic graphene stacks and their applications in Li–S batteries, Adv. Mater., 29, 1702829 (DOI: 10.1002/adma.201702829)
51. Mao Y., Li G., Guo Y., Li Z., Liang C., Peng X., Lin Z. (2017), Foldable interpenetrated metal-organic frameworks/carbon nanotubes

thin film for lithium–sulfur batteries, Nat. Commun. 8, 14628 (DOI: 10.1038/ncomms14628)

52. Zhou J., Li R., Fan X., Chen Y., Han R., Li W., Zheng J., Wang B., Li X. (2014), Rational design of a metal–organic framework host for sulfur storage in fast, long-cycle Li–S batteries, Energy Environ. Sci**., 7**, 2715-2724 (DOI:10.1039/C4EE01382D)
53. Huang X., Sheng P., Tu Z., Zhang F., Wang J., Geng, H., Zou Y., Di C.-an., Yi Y., Sun Y., Xu W., Zhu D. (2015), A two-dimensional π–d conjugated coordination polymer with extremely high electrical conductivity and ambipolar transport behavior, Nat Commun., 6, 7408 (DOI: 10.1038/ncomms8408)
54. Kresse G., Hafner J. (1993), Ab initiomolecular dynamics for liquid metals, Phys. Rev. B: Condens. Matter Mater. Phys., 47, 558 (DOI: 10.1103/PhysRevB.47.558)
55. Kresse G., Hafner J. (1994), Ab initiomolecular-dynamics simulation of the liquid-metal-amorphous-semiconductor transition in germanium, Phys. Rev. B: Condens. Matter Mater. Phys., 49, 14251 (DOI: 10.1103/PhysRevB.49.14251)
56. Kresse G., Furthmüller J. (1996), Efficiency of ab-initio total energy calculations for metals and semiconductors using a plane-wave basis set, Comput. Mater. Sci., 6, 15−50 (DOI: 10.1016/0927-0256(96)00008-0)
57. Kresse G., Furthmüller J. (1996), Efficient iterative schemes for ab initio total-energy calculations using a plane-wave basis set, Phys. Rev. B: Condens. Matter Mater. Phys., 54, 11169−11186 (DOI: 10.1103/PhysRevB.54.11169
58. Perdew J. P., Burke K., Ernzerhof, M. (1996), Generalized gradient approximation made simple, Phys. Rev. Lett., 77, 3865−3868 (DOI: 10.1103/PhysRevLett.77.3865)

59. Perdew J. P., Burke K., Ernzerhof M. (1996), Generalized gradient approximation made simple, Phys. Rev. Lett., 1997, 78, 1396 (DOI: 10.1103/PhysRevLett.77.3865)
60. BlÖchl P. E. (1994), Projector augmented-wave method, Phys. Rev. B: Condens. Matter Mater. Phys., 50, 1795 −17979 (DOI: 10.1103/PhysRevB.50.17953)
61. Kresse G., Joubert D. (1999), From ultrasoft pseudopotentials to the projector augmented-wave method, Phys. Rev. B: Condens. Matter Mater. Phys., 59, 1758 (DOI: 10.1103/PhysRevB.59.1758)
62. Grimme S., Antony J., Ehrlich S., Krieg H. (2010), A consistent and accurate ab initio parametrization of density functional dispersion correction (DFT-D) for the 94 Elements H-Pu, J. Chem. Phys., 132, 154104 (DOI: 10.1063/1.3382344)
63. Jemmis, E. D., Giju, K. T. and Leszczynski, J. (1997), Ionic to covalent bonding: a density functional theory study of linear and bent X_2Y_3 monomers (X = B, Al, Ga, In; Y = O, S, Se). Electron. J. Theor. Chem., 2: 130-138 (DOI:10.1002/ejtc.37)
64. Zhang N., Shi Y., Gao Z., Kong F., Zhu Q. (1994), Aluminum–sulfur cluster ions: Formation and photolysis, J. Chem. Phys., 101, 1219 (DOI: 10.1063/1.467814)
65. Yu T., Li F., Liu C., Zhang S., Xu H., Yang G. (2017), Understanding the role of lithium sulfide clusters in lithium–sulfur batteries, J. Mater. Chem. A, 5, 9293-9298 (DOI: 10.1039/C7TA01006K)
66. Zhang X., Zhou Y., Cui B., Zhao M., Liu F., Theoretical discovery of a superconducting two-dimensional metal−organic framework, Nano Lett., 2017, 17, 6166−6170 (DOI: 10.1021/acs.nanolett.7b02795)
67. Li F., Zhang X., Liu X., Zhao M. (2018), Novel conductive metal–organic framework for a high-performance lithium–sulfur battery host: 2D Cu-benzenehexathial (BHT), ACS Appl. Mater. Interfaces, 10, 15012-15020 (DOI: 10.1021/acsami.8b00942)

68. Bader R. F. W. (1991), Atoms in molecules, 91, 893–928 (DOI: 10.1021/ar00109a003)
69. Henkelman G., Arnaldsson A., Jonsson H. (2006), A fast and robust algorithm for Bader decomposition of charge density, Comput. Mater. Sci, 36, 354–360 (DOI: 10.1016/j.commatsci.2005.04.010)
70. Sanville E., Kenny S. D., Smith R., Henkelman G. J. (2007), Improved grid-based algorithm for Bader charge allocation, J. Comput. Chem., 28, 899–908 (DOI: 10.1002/jcc.20575)
71. Tang W., Ssanville E., Henkelman G. J. (2009), A grid-based Bader analysis algorithm without lattice bias, J. Condens. Matter Phys., 21, 084204 (DOI: 10.1088/0953-8984/21/8/084204)
72. Huang X., Zhang S., Liu L., Yu L., Chen G., Xu W., Zhu D. (2018), Superconductivity in a copper(II)-based coordination polymer with perfect Kagome structure, Angew. Chem. Int. Ed., 57, 146 (DOI: 10.1002/anie.201707568)
73. Kong L., Chen X., Li B.-Q., Peng H.-J., Huang J.-Q., Xie J., Zhang Q., (2018), A bifunctional perovskite promoter for polysulfide regulation toward stable lithium–sulfur batteries, Adv. Mater., 30, 1705219 (DOI: 10.1002/adma.201705219)
74. Zhao J., Yang Y., Katiyar R. S., Chen Z. (2016), Phosphorene as a promising anchoring material for lithium–sulfur batteries: a computational study, J. Mater. Chem. A, 4, 6124-6130 (DOI: 10.1039/C6TA00871B)

Chapter 7

Scope for Future Works

7.1. Scope for Future Works

This present doctoral thesis involves the detailed understanding of the working mechanism of non-aqueous Al dual-ion batteries as well as valuable insights into the charge/discharge reaction in Al-S battery. Moreover, we have also identified suitable cathode materials for Al dual-ion batteries such as graphene/hBN heterostructure and carbon nanotubes, able to provide efficient electronic and electrochemical properties, along with exploring Cu-BHT monolayer to be a potential cathode host material in Al-S batteries.

Our understanding of the preferable requirements for designing suitable cathode materials can also be utilised to further carry on the exploration of novel cathode materials. Various anion hosting materials with easily reversible intercalation/deintercalation of anions, such as organic cathodes can be tested for Al based batteries. MOFs present another wide scope of usage as cathode materials due to availability of stable structures with large pores to host bulky anionic species. Moreover, some other possibilities are also there for exploring dual-ion batteries based on other anions like PF_6^-, $TFSI^-$, FSI^- or BF_4^- etc. These anions are supposed to have similar working mechanisms as for $AlCl_4^-$, but result in different battery performance depending on size of the anions. Hence, insights from this thesis work can be used to establish output characteristics for dual ion batteries involving such anions by performing first-principle calculations. Another important future research aspect can be based on exploration of potential electrolytes in rechargeable Al based batteries. Presently, the battery performance is limited to room temperature ionic liquid electrolyte, $EMIM^+AlCl_4^-$, where the electrochemical outputs are restricted by the oxidation limit of $AlCl_4^-$ anion and amount of electrolyte present in cell. Therefore, a deep understanding is further required in future to choose better ionic liquid electrolytes on the basis of their electrochemical windows, relative interaction of electrolytes with the corresponding cathode and anode, and interatomic characteristic such as conductivity.

For the case of non-aqueous Al-S batteries, which are just being explored from year 2015, and are experimentally observed to be suffering from sluggish kinetics and poor reversibility of electrochemical reactions, the first principle calculations can provide a more systematic investigation approach.